DISSERTATION

SUBMITTED TO THE

COMBINED FACULTIES FOR THE NATURAL SCIENCES AND FOR MATHEMATICS

OF THE RUPERTO-CAROLA UNIVERSITY OF HEIDELBERG, GERMANY

FOR THE DEGREE OF

DOCTOR OF NATURAL SCIENCES

PRESENTED BY

M.SC. ANNABELLE SCHLÜTER

BORN IN: WOLFENBÜTTEL, GERMANY

ORAL-EXAMINATION: 29.11. 2016

THE LOCALIZATION, REGULATION AND FUNCTION OF

SYNAPTOPODIN AND THE CISTERNAL ORGANELLE IN THE AXON INITIAL SEGMENT DURING

MURINE VISUAL SYSTEM DEVELOPMENT

REFEREES: PROF. DR. STEPHAN FRINGS

PROF. DR. CHRISTIAN SCHULTZ

"Imagination is the only weapon in the war against reality."

(The Cheshire Cat)

<u>Contents</u>

I. Summary

Activity-dependent development of neurons during critical periods of plasticity is a hallmark feature of visual system maturation. Synaptopodin (synpo) is an actin-associated protein and an essential component of the cisternal organelle (CO), localized in the axon initial segment (AIS). The CO is a putative Ca^{2+} store and potentially plays a role in Ca^{2+} current regulation of the AIS. The CO is the structural correlate of the spine apparatus in dendritic spines, which is a dynamic structure and exhibits striking plasticity depending on synpo expression. The AIS undergoes activity-dependent plasticity during visual cortex development, yet, how this plasticity is regulated remains to be elucidated. Furthermore, the structure of the AIS in retinal ganglion cells (RGCs) and its ability to undergo plasticity during retinal development is largely unknown. Therefore, the current thesis investigates the putative role of the CO in AIS structural plasticity in the murine visual system.

For this purpose, the developmental regulation of synpo/CO expression in AIS was examined utilizing semi-quantitative immunofluorescence. Confocal microscopy and self-programmed macros were utilized to analyze synpo/CO cluster remodeling in AIS in the visual cortex and the retina. Activity-dependent regulation of synpo/CO expression was tested by performing visual deprivation experiments. The impact of synpo/CO expression on AIS maturation under normal and visual deprivation conditions was investigated in wildtype and synpo KO mice. The precise subcellular localization of synpo/CO in retinal AIS was determined applying super resolution microscopy.

It was found that synpo/CO expression is dynamically regulated in an activity-dependent manner in a subset of visual cortex neurons and RGCs during visual system development. Dark-rearing of mice resulted in a significant increase in size and number of synpo/CO clusters in the AIS. Furthermore, a correlation between synpo/CO and structural AIS length maturation was found in the visual cortex. Visual deprivation led to the maintenance of elongated AIS with juvenile characteristics in adult wildtype, and to AIS shortening in synpo KO mice. This indicates a potential role for synpo/CO in AIS structural maturation. Super resolution analysis of retinal AIS revealed gaps in the AIS scaffold where synpo/CO clusters are located. In summary, the present thesis highlights that synpo/CO expression is regulated in an activity-dependent manner during visual system development and that the presence of synpo/CO influences structural AIS plasticity in the visual cortex.

II. Zusammenfassung

Die Reifung des visuellen Systems zeichnet sich durch eine aktivitätsabhängige Entwicklung von Neuronen während kritischer Perioden der Plastizität aus. Synaptopodin (synpo) ist ein Aktin-assoziiertes Protein und essentieller Bestandteil der Cisternalen Organelle (CO) im Axoninitialsegment (AIS). Die CO dient vermutlich als Ca^{2+} Speicher sowie der lokalen Ca^{2+} Regulation im AIS. Die CO ist das strukturelle Korrelat des Spineapparats, dessen dynamische Struktur eine synpo-abhängige Plastizität aufzeigt. Während der Entwicklung des visuellen Cortex durchläuft das AIS Perioden aktivitätsabhängiger Plastizität, dessen Regulierung nur unzureichend verstanden ist. In retinalen Ganglienzellen (RGCs) ist die Struktur sowie Plastizität des AIS vollständig unbekannt. Die vorliegende Arbeit untersucht die mögliche Rolle der CO in der strukturellen AIS Plastizität im murinen visuellen System.

Zu diesem Zweck wurde die Expression von synpo/CO während der Entwicklung unter Verwendung von semi-quantitativer Immunfluoreszenz analysiert. Konfokale Mikroskopie und eigenständig programmierte Makros dienten der synpo/CO Cluster Analyse im AIS des visuellen Cortex und der Retina. Eine aktivitätsabhängige synpo/CO Expression wurde durch Anwendung visueller Deprivationsexperimente getestet. Die Auswirkung der synpo/CO Expression auf die kortikale AIS Reifung wurde unter normalen Bedingungen und nach visueller Deprivation in Wildtypen sowie in synpo KO Mäusen untersucht. Die genaue subzelluläre Lokalisierung von synpo/CO im AIS von RGCs wurde durch superauflösende Mikroskopie bestimmt.

Die vorliegende Arbeit zeigt, dass synpo/CO während der Entwicklung dynamisch und aktivitätsabhängig in einer Subpopulation von kortikalen Neuronen (V1) sowie in RGCs reguliert wird. Visuelle Deprivation resultierte in einer signifikanten Zunahme von Anzahl und Größe der synpo/CO Cluster im AIS. Im visuellen Cortex wurde eine Korrelation zwischen synpo/CO Expression und struktureller AIS Reifung gefunden. Visuelle Deprivation führte zu langen AIS mit juvenilen Eigenschaften, während in synpo KO Mäusen eine AIS Verkürzung auftrat. Dies weist auf eine Rolle für synpo/CO in der Regulation der AIS Plastizität hin. In RGCs wurden subzelluläre Lücken im AIS Gerüst aufgedeckt, in denen Synpo/CO Cluster lokalisiert sind. Zusammenfassend zeigen diese Ergebnisse, dass synpo/CO während der Entwicklung des visuellen Systems aktivitätsabhängig exprimiert wird sowie dass synpo/CO die strukturelle Reifung des AIS im visuellen Cortex beeinflusst.

III.   List of figures

IV.   List of abbreviations

abbreviation	definition
%	percent
°	degree
°C	degree Celsius
μl	micro liter
μm	micrometer
μm^2	square micrometers
2D	two dimensional
3D	three dimensional
5-HT	5-hydroxytryptamine, serotonin
A	adenine
A	Ampere
α	alpha
aa	amino acids
AAS	axo-axonic synapse
AIS	axon initial segment
ankG	ankyrin-G
AP	action potential
ATP	adenosine triphosphate
bp	base pairs
BSA	bovine serum albumin
BW	body weight
C	cytosine
CA1	cornu ammonis area 1
Ca^{2+}	calcium ion
CA3	Cornu Ammonis region 3
CAM	cell adhesion molecule
CaMK	Ca^{2+}/calmodulin-dependent protein kinase
Ca$_V$	voltage-gated calcium channel
cdk	cyclin-dependent kinase
cDNA	complementary deoxyribonucleic acid
CFP	cyan fluorescent protein
ch	chicken

ChC	Chandelier cell
CICR	calcium induced calcium release
CK	casein kinase
cm	centimeter
cm^2	square centimeters
CO	cisternal organelle
CP	critical period
DAPI	4′,6-diamidino-2-phenylindole
DCN	dorsal cochlear nucleus
ddH$_2$O	double-distilled water
dLGN	dorsolateral geniculate nucleus
DNA	deoxyribonucleic acid
E	embryonic day
EB	end binding protein
EDTA	ethylenediaminetetraacetic acid
ER	endoplasmic reticulum
FGF	fibroblast growth factor
G	guanine
GABA	γ-aminobutyric acid
GCL	ganglion cell layer
GFP	green fluorescent protein
gp	guinea pig
GSK	glycogen synthase kinase
GSO	giant saccular organelle
gt	goat
H	heavy chain
HPRT1	hypoxanthine phosphoribosyltransferase 1
HRP	horseradish peroxidase
hrs	hours
IgG	immunoglobulin G
IgY	immunoglobulins Y
IHC	immunohistochemistry
IP3R	inositol 1,4,5-trisphosphate receptor Ca^{2+} channel
IR$^+$	immunoreactive positive
K$^+$	potassium ion

kDa	kilo Dalton
KLH	keyhole limpet hemocyanin
KO	knockout
K_V	voltage-gated potassium channel
kW	kilo Watt
L	light chain
mA	milli-Ampere
mAb	monoclonal antibody
min	minutes
mm	millimeter
MP	milk powder
mRNA	messenger ribonucleic acid
ms	mouse
msec	milliseconds
MW	molecular weight
mW	milli-Watt
n	number
Na^+	sodium ion
Na_V	voltage-gated sodium channel
NeuN	neuron-specific nuclear protein
NF	neurofascin
NFL	nerve fiber layer
nm	nanometer
NMDA	N-methyl-D-aspartic acid
NrCAM	neuronal cell adhesion molecule
OD	ocular dominance
OD	optical density
P	postnatal day
p	confidence level
pAb	polyclonal antibody
PAEZ	pre-axonal exclusion zone
PAGE	polyacrylamide gel electrophoresis
PBS	phosphate buffered saline
PBS-T	phosphate buffered saline - Tween20
PCR	polymerase chain reaction

PFA	paraformaldehyde
preCP	pre-critical period
PSD	postsynaptic density protein
PVDF	polyvinylidene fluoride
qPCR	quantitative polymerase chain reaction
rb	rabbit
RGC	retinal ganglion cell
RNA	ribonucleic acid
ROI	region of interest
rpm	revolutions per minute
RT	reverse transcriptase
RyR	ryanodine receptor
S.E.M.	standard error of the mean
SA	spine apparatus
sAHP	slow afterhyperpolarization
SCHIP1	schwannomin-interacting protein 1
SDS	sodium dodecyl sulfate
SERCA	sarcoplasmic/endoplasmic reticulum Ca^{2+} ATPase

1 Introduction

The axon initial segment (AIS) is a specialized axonal compartment crucial for proper neuronal function. The AIS can undergo dynamic structural changes in response to alterations in neuronal network activity (reviewed in: Adachi et al. 2015; Petersen et al. 2016). This AIS plasticity has been shown to modulate neuronal excitability by either increasing or decreasing physiological parameters of single neurons (Grubb and Burrone 2010a; Kuba et al. 2010; Wefelmeyer et al. 2015; Gulledge and Bravo 2016). The AIS of a subset of cortical and hippocampal projection neurons contains the endoplasmic reticulum (ER) derived cisternal organelle (CO). The CO is a putative Ca^{2+} storing and sequestering organelle and is suggested to have functions in local AIS Ca^{2+} trafficking (Benedeczky et al. 1994; King et al. 2014). The CO might therefore contribute to AIS plasticity and neuronal excitability.

The current thesis focuses on the analysis of the structural maturation and activity-regulated expression of the CO during the development of the murine retina and visual cortex. The aim of this thesis is to elucidate the putative role of the CO for AIS structural maturation and plasticity during visual system development. The impact of the CO on AIS maturation and plasticity has not been explored before and might therefore contribute to our understanding of how AIS structural plasticity is regulated.

1.1 The axon initial segment

Mature neurons are functionally and structurally polarized cells with distinct compartments, typically a single axon as well as multiple dendrites. Both the axonal and somatodendritic compartments are crucial for action potential (AP) initiation, propagation, and neuronal function (Yoshimura and Rasband 2014). A structurally and molecularly specialized axonal region, the AIS, contains a layer of electron-dense material beneath the plasma membrane and fascicles of microtubules, both allowing its identification at the ultrastructural level and its distinction from dendrites (Palay et al. 1968; Peters et al. 1968). The AIS separates somatodendritic and axonal domains in a physiological and physical way

(also see section 1.1.4: The axon initial segment cytoskeleton;(Song et al. 2009; Grubb and Burrone 2010b; Rasband 2010; Watanabe et al. 2012).

Usually, the AIS is characterized by a thin unmyelinated region of approximately 10µm to 60µm length located between its origin at the axon hillock and the beginning of myelination in cortical principal neurons (Figure 1; Kole and Stuart 2012). However, the characteristics of the AIS can vary dependent on type and function of the corresponding neuron. For example, neurons with unmyelinated axons also contain AIS, which exhibit a similar molecular composition of those in myelinated axons (Boiko et al. 2003). Furthermore, several studies also demonstrated a more distal location of the AIS at basal dendrites (Martina et al. 2000; Herde et al. 2013; Thome et al. 2014) or apical dendrites several microns away from the soma (Hausser et al. 1995). Thus, the AIS is indeed a highly specialized structure, but can be diverse in regard to its location and molecular composition. In general, the AIS is considered to be the primary site of AP generation (Bender and Trussell 2012). This is accomplished by a high density of voltage-gated ion channels that are clustered in the axonal membrane by the scaffolding protein ankyrin-G (ankG). AnkG binds to ßIV-spectrin, which links the AIS protein complex to the actin cytoskeleton (Figure 2). Both, ankG and ßIV-spectrin, molecularly define the AIS (Zhang and Rasband 2016).

Although the AIS is relatively small in size, it exhibits high Na^+ conductance lowering the threshold for AP generation at the AIS. In contrast, the soma is large in size and therefore has large electrical loads in relation to membrane capacitance and K^+ conductance, which affects AP generation at the AIS (Adachi et al. 2015). AIS length, distance from the soma, and also density of voltage-gated ion channel expression all determines the optimal location for the minimum threshold current in the axon. Ion channels at the AIS can vary considerably across different neuronal cell types in regard to ion channel density, distribution and subunit type (Lorincz and Nusser 2008). An increase in the distance of the AIS from the soma reduces the effect of the large electrical soma load, which results in a higher excitably of the neuron. However, further distal location of the AIS in turn reduces cell excitability. The optimal distance between soma and AIS represents a minimum threshold current, which enables a specified value of electrical charges to reach the AIS and simultaneously isolate it from the soma (Adachi et al. 2015). Length of AIS affects K^+ conductance,

membrane capacitance, and Na⁺ conductance. With longer AIS, Na⁺ / K⁺ conductance and membrane capacitance increase, thereby enhancing neuron excitability through overcoming the electrical loads of the soma. This increases electrical loads at the AIS itself and leads to AIS membrane potentials close to AP threshold. Small distances between AIS and soma become preferable for long AIS, whereas long distances are optimal for shorter AIS (Adachi et al. 2015). A recent modeling study utilizing reconstructed data from realistic neurons additionally showed that somatodendritic morphology modulates AIS performance. Specifically, small neurons have a higher excitability when AIS are of intermediate length and located proximal to the soma. In comparison, large neurons are more excitable when AIS are long and located distally from the soma (Gulledge and Bravo 2016).
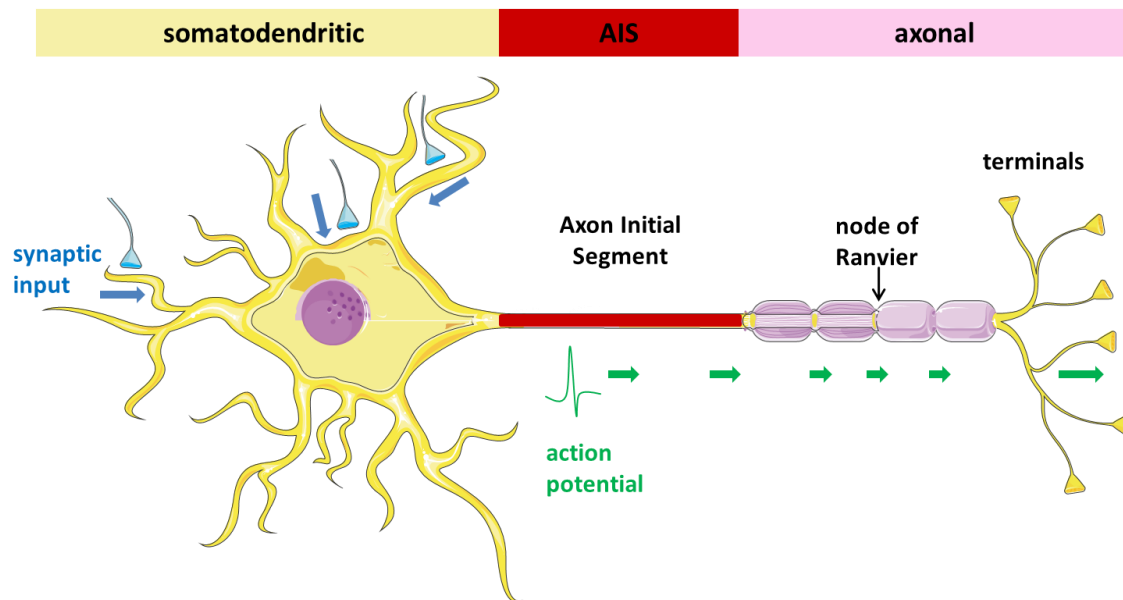
Figure 1: Schematic illustration of the localization of the axon initial segment (AIS).
In most principal neurons, the AIS (red) is an unmyelinated region located proximal to the soma at the beginning of the axon. Synaptic input (blue) received in the somatodendritic compartment (yellow) is integrated and summed in the soma. The AIS generates action potentials (APs) and transmits the cellular output along the axon in saltatoric manner utilizing nodes of Ranvier (at myelinated axons). Structurally, nodes of Ranvier are similar to the AIS, characterized by clustering of voltage-gated ion-channels. Ultimately, APs generated at the AIS lead to neurotransmitter release at axon terminals (Figures were produced using "Servier Medical Art", www.servier.com).

1.1.1 Ion channels at the axon initial segment

As outlined above, voltage-gated sodium channels (Na_V) are clustered at high densities at the AIS, which provides the structural basis for the generation of APs (Figure 2; Kole and Stuart 2008). Of the nine known members of the sodium channel family, three ($Na_V1.1$, $Na_V1.2$, and $Na_V1.6$) are enriched in the AIS membrane (Yoshimura and Rasband 2014). AP generation is assumed to occur in the distal end of the AIS, which shows a precise localization of distinct Na_V channels (Petersen et al. 2016). $Na_V1.1$ channels are localized at the proximal AIS of interneurons in the neocortex, cerebellum, at retinal ganglion cells (RGCs), CA3 pyramidal neurons in the hippocampus, and spinal motoneurons (Petersen et al. 2016). $Na_V1.2$ channels are mainly expressed in unmyelinated neurons early in development and in adults (Jarnot and Corbett 1995; Boiko et al. 2003), such as in AIS of RGCs (Boiko et al. 2003), and in the proximal AIS of cortical and hippocampal pyramidal neurons (Hu et al. 2009). Both, $Na_V1.1$ and $Na_V1.2$ channels are proposed to shape firing behavior of individual neurons (Adachi et al. 2015). $Na_V1.6$ channels are predominantly located distally in the AIS of cortical pyramidal cells and RGCs. They are crucial in lowering AP thresholds at the AIS of mature neurons (Van Wart et al. 2007; Lorincz and Nusser 2008; Hu et al. 2009).

Voltage-gated potassium (K_V) channels localized at the AIS (Figure 2 and 5) also play a major role in neuron excitability since they are crucial for producing the AP repolarization phase as well as for setting AP thresholds and interspike intervals (Petersen et al. 2016). As a result, K_V channels significantly modulate the firing frequency of the neuron. In most neuronal types, the major subtypes of K_V channels at the AIS are K_V1 channels, including the $K_V1.1$ and $K_V1.2$ channels (Kole and Stuart 2012). These channels counteract the depolarizing effect of Na_V channels due to their rapid kinetics and hyperpolarized voltage dependence for activation. Thus, they regulate threshold and promote repolarization of APs (Adachi et al. 2015). $K_V1.4$ channels at the AIS produce fast transient outward A-currents, which regulate neuronal firing frequency by enhancing the interspike interval (Connor and Stevens 1971). However, they do not adapt firing frequency (Petersen et al. 2016). K_V7 channels stabilize the resting membrane potential and increase availability of Na_V channels for AP generation (Adachi et al. 2015). They generate low-voltage activating and non-activating M-type currents, show slow kinetics and get activated during repetitive firing

(Petersen et al. 2016). The K_V7.2 and K_V7.3 subtypes are found in high densities at the distal part of AIS in pyramidal neurons (Kole and Stuart 2012). In addition, K_V2.1 and K_V2.2 channels are expressed in the AIS membrane. K_V2.2 channels are localized to the AIS of principal neurons of the medial nucleus of the trapezoid body, a part of the auditory pathway. K_V2.2 possibly regulates spike intervals during repetitive firing (Bender and Trussell 2012). The K_V2.1 channel is clustered at the AIS (Sarmiere et al. 2008; King et al. 2014), but is also expressed at the soma and proximal dendrites (Trimmer 1991; Lim et al. 2000). K_V2.1 is regulated in a rapid activity-dependent manner through reversible changes in the posttranslational modifications of the channel, which homeostatically regulates intrinsic neuronal excitability (Misonou et al. 2006; Mohapatra et al. 2009). At the AIS of e.g. cortical and hippocampal pyramidal neurons, K_V2.1 is clustered at gaps in the AIS scaffold, where ankG expression is absent (Figure 2 and 5; King et al. 2014). Phosphorylated K_V2.1 is predominantly located at the proximal AIS and dephosphorylated K_V2.1 is clustered at the more distal part of the AIS (King et al. 2014). Dephosphorylation of K_V2.1 is regulated in an activity-dependent manner by calcineurin, which causes suppression of neuronal excitability (Misonou et al. 2006).

Voltage-gated calcium (Ca_V) channels are usually expressed in somatodendritic compartments and axon terminals. Yet several subtypes were also found at the AIS (Figure 2), where they modulate neuronal firing patterns and thus, excitability of the neuron (Petersen et al. 2016). T-type (Ca_V3) Ca^{2+} channels are clustered at the AIS of dentate gyrus granule cells (Martinello et al. 2015) and in cartwheel interneurons from the dorsal cochlear nucleus. Cartwheel cells also express R-type (Ca_V2.3) Ca^{2+} channels at the AIS (Bender and Trussell 2009). Both, T-type and R-type Ca^{2+} channels, produce low-threshold spikes that trigger burst firing of APs (Bender and Trussell 2012; Martinello et al. 2015). P/Q-type (Ca_V2.1) Ca^{2+} channels are located at AIS of Purkinje cells in the cerebellum (Callewaert et al. 1996) and at AIS of pyramidal neurons (Yu et al. 2010). Pyramidal cells also express N-type (Ca_V2.2) Ca^{2+} channels. Both, N-type and P/Q-type Ca^{2+} channels are activated after depolarization during APs. In turn, they cause fast repolarization of APs by triggering Ca^{2+} dependent K^+ conductance (Yu et al. 2010).

1.1.2 Receptors at the axon initial segment

Many cortical and hippocampal pyramidal neurons receive γ-aminobutyric acid (GABA)-ergic input at the AIS, often exclusively mediated by axo-axonic Chandelier cells (ChC). ChC are fast-spiking cortical interneurons modulating neuron excitability (Inan and Anderson 2014). ChC have the ability to either inhibit or depolarize neurons depending on the membrane potential of the targeted neuron (Woodruff et al. 2010; Wang et al. 2016b). At the axo-axonic synapse (AAS), the AIS represents the postsynaptic site. GABA binds to the α2 subunit of GABA-A receptors located at the AIS (Figure 2 and 5; Howard et al. 2005). In contrast, cerebellar Purkinje cells receive GABAergic "pinceau synapses" at the AIS by basket cells, which are inhibitory (Ango et al. 2004).

Monoamine receptors are also located the AIS. Serotonin (5-hydroxytryptamine, 5-HT) activates 5-HT_{1A} receptors at the AIS of some pyramidal cells in human and non-human primates (DeFelipe et al. 2001), spinal motoneurons and several other types of interneurons (reviewed in Petersen et al. 2016). 5-HT_{1A} receptors are proposed to modulate neuronal activity by inhibition through interaction with GABAergic terminals of ChC and basket cells (Czyrak et al. 2003) as well as hyperpolarization and cyclic-nucleotide-gated channels (Ko et al. 2016). Dopamine D_3 receptors are found at the AIS of cartwheel interneurons in the dorsal cochlear nucleus. They reduce neuronal output through the modulation of T-type Ca^{2+} channels (Bender et al. 2010).

1.1.3 Cell adhesion molecules at the axon initial segment

Transmembrane cell adhesion molecules (CAMs) play a role in assembling AAS and are located at the AIS (Figure 2). The 186 kDa isoform of neurofascin (NF186) regulates GABAergic Pinceau synapse formation at AIS of cerebellar Purkinje cells and of hippocampal pyramidal neurons by distally increasing a NF186 gradient along the AIS. NF186 has additional functions in maintaining neuronal polarity in Purkinje neurons (Buffington and Rasband 2011). Both, NF186 and the neuronal CAM (NrCAM) bind to ankG. The function of NrCAM is not completely understood. It is likely that NrCAM plays a role in Na_V channels clustering, which has been shown for nodes of Ranvier in the peripheral nervous system (Rasband 2011).

1.1.4 The axon initial segment cytoskeleton

The AIS has a specialized cytoskeletal organization, establishing a dense meshwork underneath the plasma membrane (Jones et al. 2014). This meshwork is essential for building and maintaining functional AIS. The AIS is thought to act as a diffusion barrier as well as filter and sorting machinery that contributes to the establishment of neuronal polarity (Sobotzik et al. 2009; Rasband 2011; Leterrier and Dargent 2014; Yoshimura and Rasband 2014; Jenkins et al. 2015). Formation and maintenance of the AIS is determined by the membrane scaffolding protein ankyrin-G (ankG) (Jenkins et al. 2015; Rasband 2010).

The AIS diffusion barrier ensures that proteins and lipids are restricted to either the axonal or somatodendritic compartment, and active transport of dendritic cargoes is prevented from entering the axon (Kevenaar and Hoogenraad 2015). AnkG has distinct binding motifs for transmembrane proteins such as Na_V channels and ßIV-spectrin, and links these proteins to the actin and microtubule cytoskeleton (Pan et al. 2006; Grubb and Burrone 2010b; Rasband 2010). Patches of actin filaments in AIS are suggested to act as a barrier or filter where dendritic vesicle transport stops (Watanabe et al. 2012). In contrast, other studies suppose that targeted axonal trafficking relies on the interaction of selective motor proteins with microtubules and vesicles (Petersen et al. 2014; Farias et al. 2015). Furthermore, microtubule interacting end-binding (EB) proteins are selectively associated with the 480kDa isoform of ankG (Figure 2; Freal et al. 2016). This binding is crucial for AIS formation and neuronal polarity in cultured hippocampal neurons.

Super resolution imaging via stochastic optical reconstruction microscopy (STORM) revealed a periodicity of axonal actin filaments that form submembranous rings regularly spaced along the axonal shaft (Zhong et al. 2014; Leterrier et al. 2015). These rings form immediately after axon specification, have a spacing of ~190nm, colocalize with the actin capping protein adducin, and alternate with ßII-spectrin. Similar to ßIV-spectrin, ßII-spectrin is an actin binding protein (Zhong et al. 2014). Spectrins have predicted lengths of ~190nm suggesting that they prearrange the periodic cytoskeleton organization (Zhong et al. 2014), which is supposed to provide flexibility and elasticity to the axon (Jones and Svitkina 2016; Zhang and Rasband 2016). Furthermore, ankG, ßIV-spectrin, Na_V channels, and NF186 were also found to have similar periodic arrangements. ßIV-spectrin subunits

associate with the N-terminus of ankG in a head-to-head orientation, both located in the submembrane cytoskeleton (Leterrier and Dargent 2014). AnkG spatially extends into the axoplasm with its C-terminus that is proposed to bind intracellular proteins (Figure 2; Leterrier et al. 2015). The ankG C-terminus is also suggested to have functions in assembling the AIS (Jenkins et al. 2015). In contrast, ankG is supposed to be restricted to the proximal axon through a boundary located at the distal axon. This distal submembranous axonal cytoskeleton contains ankyrin-B, αII-spectrin, and βII-spectrin (Galiano et al. 2012). Thus, AIS definition might not exclusively be dependent on ankG.

Furthermore, a recent study in cultured hippocampal neurons has shown that most somatodendritic-specific organelles, e.g. somatodendritic carriers, the Golgi complex and the rough ER are hindered to enter the axon at so-called pre-axonal exclusion zones (PAEZ), (Farias et al. 2015). Those PAEZs are suggested to be located in the axon hillock or at the base of axons originating from dendrites. The sorting mechanisms rely on coupling of a somatodendritic cargo protein to an axonally directed kinesin-1-binding peptide (Farias et al. 2015).
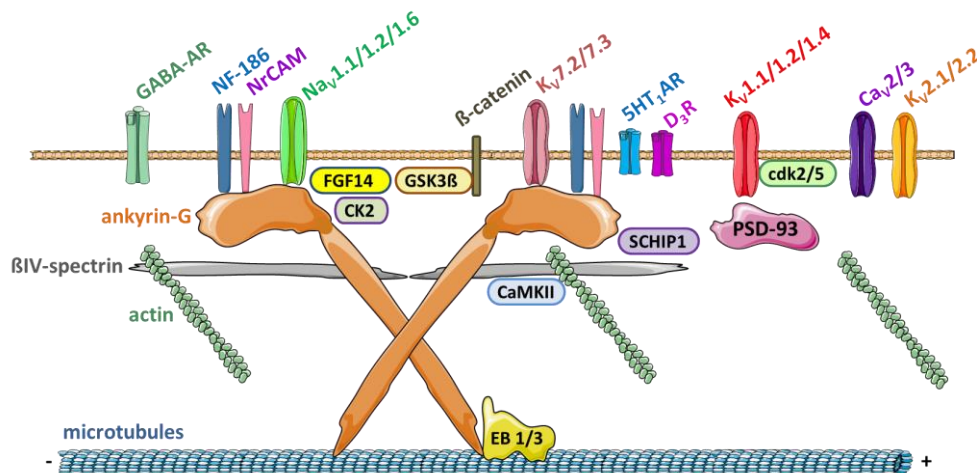
Figure 2: Schematic illustration of molecular components and cytoskeleton scaffold in the AIS.
Ankyrin-G (ankG) (orange) is the main membrane scaffolding protein at the AIS and is crucial for determining and maintaining AIS structure. AnkG binds to ßIV-spectrin (grey), which in turn binds to actin filaments (green). AnkG clusters $Na_V1.1$, $Na_V1.2$ and $Na_V1.6$ channels (green), $K_V7.2$ and $K_V7.3$ channels (light red), NrCAM (pink) and neurofascin-186kDa (NF-186) (blue). AnkG is linked to microtubules (blue/white) via end binding proteins (EB1/3) (yellow) and also binds to SCHIP1 (violet). Other voltage-gated ion channels present at the AIS are $Ca_V2/3$ channels (purple), $K_V1.1$, $K_V1.2$ and $K_V1.4$ channels (red) linked to PSD-93 (pink) as well as $K_V2.1$ and $K_V2.2$ (orange). The 5-HT$_1$A receptor (5-HT$_1$AR) (blue) and dopamine D_3 receptor (D_3R) (pink) are also located at the AIS. Furthermore, the non-secreted protein FGF-14 (yellow) and the kinases GSK3ß (orange), CK2 (green), cdk2/5 (green) and CaMKII (blue) are expressed at the AIS (Figures were produced using "Servier Medical Art", www.servier.com).

1.2 Plasticity of the axon initial segment

During central nervous system development, plasticity in the brain occurs that is driven by many pre- and postnatal events such as experience, age, and disease. This neuronal plasticity is greatly enhanced during so called critical periods (CP), when the brain responds and adapts to specific internal and external stimuli (Hensch 2005b). Among other events, plasticity relies on activity-dependent alterations within the developing brain and involves a wide range of molecular and cellular processes that are essential for development and circuit formation (Holtmaat and Svoboda 2009; Maggio and Vlachos 2014). Synaptic plasticity has been the focus of neuroscience for many years and its mechanisms are fairly well understood. Synaptic plasticity plays a critical role in a variety of physiological processes. For instance, long-term memory formation involves dynamic reconstruction of synapses based on protein proteolysis and synthesis, respectively, as well as cytoskeletal arrangements (Citri and Malenka 2008). The adjustment of neural circuits at an optimal range is mediated by homeostatic plasticity, which constitutes a negative feedback mechanism. Thus, it is the counterpart of positive-feedback mechanisms such as long-term potentiation and depression, also known as Hebbian plasticity (Nelson and Turrigiano 2008).

Already in 1968, it was postulated that AIS structural changes might contribute to dynamically modulate neuron excitability (Palay et al. 1968). Structural changes at the AIS are associated with various pathological conditions, such as brain trauma, ischemia, cognitive disorders, or epilepsy (reviewed in Adachi et al. 2015). Moreover, the concept of homeostatic plasticity at the AIS has become a focus for researchers in the past few years. It has been revealed that the AIS is capable of regulating neuron excitability and activity through structural remodeling (Adachi et al. 2015).

During central nervous system development, the AIS undergoes structural changes during CPs that are correlated with changes in neuron excitability (reviewed in Petersen et al. 2016). For example, neurons in the avian *nucleus laminaris* receive synaptic input from both ears and are essential for sound localization (Kuba 2007). AIS of those neurons appear prior to the reception of synaptic input from the auditory nerve and elongate with the onset of hearing independent of neuronal activity. Later, the auditory input triggers AIS

remodeling in an activity-dependent and cell-specific way. Short and distal AIS in neurons of the rostromedial part of the *nucleus laminaris* respond to higher sound frequencies. Longer and more proximal AIS of neurons in the caudolateral part of the nucleus respond to lower frequencies (Kuba et al. 2006; Kuba et al. 2014). Auditory deprivation prevents this AIS remodeling and leads to AIS lengthening (Kuba et al. 2010; Kuba et al. 2014). Simultaneously, increased neuronal excitability and modified K_V channel expression is observed, whereas $K_V1.1$ channels are replaced by $K_V7.2$ channels (Kuba et al. 2015).

Most recently, AIS structural plasticity was also examined in the rodent visual system (Figure 3; also see section 1.4: The visual system). AnkG-positive AIS of neurons in the developing primary visual cortex (V1) first appear at embryonic day (E) 14.5 and undergo a tri-phasic AIS length maturation during further postnatal development (Gutzmann et al. 2014). In phase 1, AIS significantly elongate shortly before eye-opening around postnatal day (P) 13-14. In phase 2, AIS shorten around the peak of CP at P28 (in mice), suggesting a neuroprotective effect due to high sensitivity to input imbalances during this period. In phase 3, AIS re-elongate with the closure of the CP at P35 reaching a plateau in adulthood. This dynamic and tri-phasic AIS length maturation is activity-dependent since AIS lengthening was impaired in P28 mice after visual deprivation (Gutzmann et al. 2014). Developmental AIS plasticity has also been studied in the primate prefrontal cortex (Cruz et al. 2009). This study showed that AIS length declines during early postnatal development and then remains stable through adolescence and into adulthood.
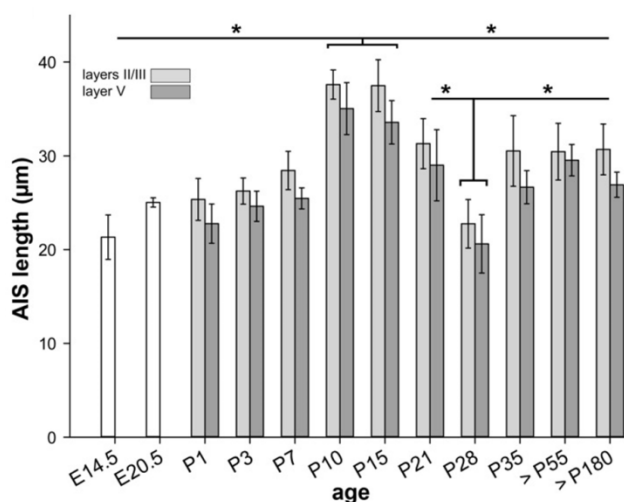
Figure 3: AIS length maturation in the primary visual cortex (V1).
AIS in V1 undergo a tri-phasic length maturation during development. During early ages from E14.5-P7, AIS are short. AIS increase during eye-opening around P13-14 (phase 1). Afterwards, AIS significantly shorten during the peak of the CP at P28 (phase2). AIS re-increase during the closure of the CP at P35 (phase3). In adulthood, AIS lengths stabilize. (Adapted from Gutzmann et al. 2014).

Several additional studies have shown that, besides developmental AIS plasticity during CPs, structural modifications of the AIS can also occur in response to the level of neuronal activity within a network (reviewed in Petersen et al. 2016). Neuronal excitability can be adapted by dynamically regulating AIS-specific parameters, such as length, distance from the soma, and ion channel expression. These modifications are suggested to maintain the level of network activity. In the retina, RGCs with different firing properties exhibit differences in AIS length and position (Fried et al. 2009). Relocation of the AIS can be induced in cultured dissociated neurons by chronic depolarization with K^+ or by photostimulation (Grubb and Burrone 2010a). Under these conditions, the AIS relocates distally, which is reversible and correlates with alterations in current threshold for AP spiking. In olfactory bulb dopaminergic interneurons *in vitro*, the AIS is short und located distally (Chand et al. 2015). Chronic depolarization leads to a proximal relocation and AIS elongation, which is the exact opposite in non-GABAergic olfactory bulb neurons (Chand et al. 2015). This diversity of AIS modification is suggested to facilitate the flexible adaptation of neuronal networks to dysfunctional activity in a cell-specific and cell-function dependent manner. In a model for a traumatic brain injury utilizing blast wave exposure in rats, cortical and hippocampal AIS length is decreased (Baalman et al. 2013). This shortening is thought to lead to increased threshold and interspike intervals of repetitively firing neurons. Furthermore, focal cortical stroke in forelimb motor cortex as well as white matter stroke cause AIS length shortening from the distal end, accompanied by decreased GABA-A $\alpha2$ receptor expression at the AIS (Hinman et al. 2013).

Developmental and structural AIS plasticity occurs on time scales ranging from minutes or hours to days and to weeks (reviewed in Petersen et al. 2016). Several Ca^{2+}-dependent mechanisms were identified to play a role in long-term as well as short-term and rapid homeostatic plasticity of the AIS. For example, AIS relocation and length changes after chronic depolarization depend on increased intracellular Ca^{2+} concentrations through the activation of T- and L-type Ca^{2+} channels within hours or days (Grubb and Burrone 2010a; Evans et al. 2013; Muir and Kittler 2014; Evans et al. 2015). However, Ca^{2+} entry at the AIS is not sufficient for relocation since it is mediated by activation of the Ca^{2+} sensitive phosphatase calcineurin (Evans et al. 2013). Rapid endocytosis of $K_V7.2$ and $K_V7.3$ channels at the AIS of dissociated hippocampal neurons is mediated by Ca^{2+} influx through N-Methyl-

D-aspartic acid (NMDA) receptors and subsequent activation of the Ca^{2+}-dependent cysteine protease calpain within minutes (Benned-Jensen et al. 2016). Calpain in turn has previously been shown to cause an irreversible proteolysis of the AIS cytoskeletal proteins ankG and ßIV-spectrin after ischemic injury and optic nerve crush within hours (Schafer et al. 2009).

In summary, the AIS is a highly dynamic structure contributing to the state of neuronal excitability. The AIS is sensitive to perturbations and to activity changes in surrounding neuronal networks. Homeostatic and structural AIS plasticity has a direct impact on neuronal output and thus, activity in the brain. AIS plasticity is probably also essential for maintaining normal neuronal function and limiting damage caused by pathological insults to the brain (reviewed in Adachi et al. 2015; Petersen et al. 2016). So far, however, the precise mechanisms and consequences of this form of plasticity remain unknown. How is homeostatic AIS plasticity regulated, and which factors promote or suppress this dynamic structural change?

1.3 The cisternal organelle

During APs, Na^+ and K^+ inward currents as well as activity-dependent transmembrane Ca^{2+} entry occur. Subsequently, Ca^{2+} levels are transiently elevated in the AIS. These Ca^{2+} currents modulate the generation and timing of APs (see section 1.1.1 and 1.2; Bender and Trussell 2012) and must therefore be temporally and spatially regulated. It has long been determined that a specialized organelle with implicated roles in Ca^{2+} trafficking is localized in the AIS of pyramidal neurons (Peters et al. 1968). This so-called cisternal organelle (CO) consists of stacks of flattened smooth ER cisternae alternating with plates of electron-dense material (Figure 4; Peters et al. 1968; Benedeczky et al. 1994). The CO is located in close approximation with the AIS plasma membrane (Kosaka 1980; Benedeczky et al. 1994; Bas Orth et al. 2007; Sanchez-Ponce et al. 2012) and show structural and presumable functional similarities to the spine apparatus (SA) in dendritic spines (Peters et al. 1968; Kosaka 1980; Spacek 1985; Benedeczky et al. 1994).
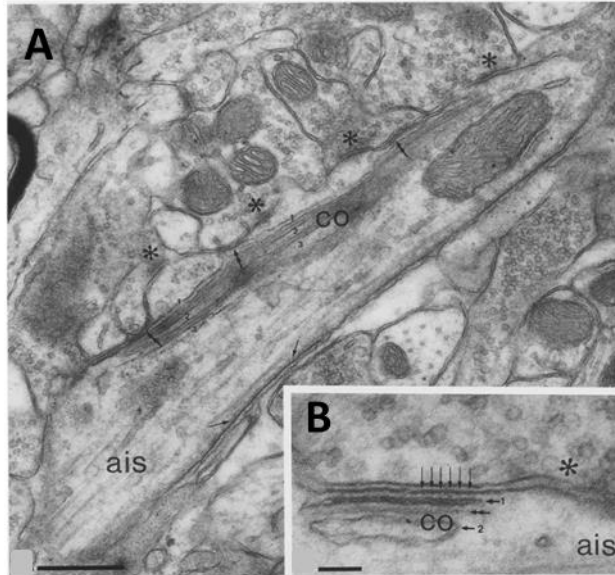
Figure 4: Ultrastructure of the cisternal organelle (CO) revealed by electron microscopy.
COs are present in AIS of pyramidal neurons in CA1 of the rat hippocampus as shown by electron microscopy. The AIS is identified by its electron-dense membrane undercoating displayed in longitudinal **(A)** and cross-sections **(B)**. COs consist of stacks of smooth ER forming cisternae as well as interdigitating plates of electron dense material (double arrow) **(B)**. COs are closely associated to the plasma membrane (double arrows) **(A, B)**, which is connected to the outermost cisternal membrane of the CO through periodic bridges (vertical arrows) **(B)**. COs are present in close approximation to synaptic contacts with the AIS (asterisks, **A**, **B**).
Scale bars=0.5µm **(A)** and 0.1µm **(B).** (adapted from Benedeczky et al. 1994).

Synaptopodin (synpo) is an α-actinin and actin binding protein (Mundel et al. 1997; Kremerskothen et al. 2005), which was first observed to be expressed in foot processes of renal podocytes and in a subset of telencephalic dendritic spines (Mundel et al. 1997; Deller et al. 2000). Later, synpo expression was also found in the CO and SA (Deller et al. 2000; Bas Orth et al. 2007). It has been suggested that synpo links the CO and SA to the actin cytoskeleton and might therefore play a role in actin-based plasticity (Deller et al. 2000).

The synpo gene encodes three protein isoforms: synpo-long (903aa), synpo-short (685aa) and synpo-T (181aa). The long isoform of synpo and synpo-T are exclusively expressed in podocytes. The short isoform of synpo is only found in the brain (Asanuma et al. 2005). The expression of the neuronal synpo isoform is essential for the formation of SAs and COs as demonstrated by studies of synpo-deficient mice that do not develop these organelles in dendritic spines and the AIS, respectively (Deller et al. 2003; Bas Orth et al. 2007). Synpo-deficient mice additionally show deficits in synaptic plasticity and spatial learning (Deller et al. 2003; Jedlicka et al. 2008; Jedlicka et al. 2009; Zhang et al. 2013; Korkotian et al. 2014). Further studies suggest an important role for synpo and the SA in homeostatic synaptic plasticity (Vlachos et al. 2013), in neuronal systemic inflammation (Strehl et al. 2014), in membrane protein diffusion (Wang et al. 2016a), and in stabilizing spine head protrusions that may modulate activity-dependent rewiring of microcircuits (Verbich et al. 2016). Vlachos and colleagues have further shown that synpo/SA has a function in homeostatic

synaptic plasticity. The authors observed that deafferented granule cells of the hippocampus could compensate for the loss of input with an increase in excitatory synaptic strength, which is dependent of the expression of synpo (Vlachos et al. 2013). This homeostatic synaptic scaling is additionally combined with an increase in synpo cluster and stability as well as in SA size. These observations provide evidence for an activity-dependent modulation of synpo/SA employing a negative feedback mechanism responding to changes in network activity (Vlachos 2012; Vlachos et al. 2013). On the other hand, further functions for synpo and the CO in AIS morphology, function, and plasticity still remain elusive to date. It seems reasonable to imply synpo and the CO in Ca^{2+} regulation in the AIS and thus, in modulation of APs. Indeed, several proteins and channels involved in Ca^{2+} signaling were found to be associated with synpo/CO: the sarcoplasmic/endoplasmic reticulum Ca^{2+} ATPase (SERCA) (Benedeczky et al. 1994; Anton-Fernandez et al. 2015), the inositol 1,4,5-trisphosphate (IP_3) receptor Ca^{2+} channel type 1 (IP_3R) (Sanchez-Ponce et al. 2011; King et al. 2014; Anton-Fernandez et al. 2015), the ryanodine receptor (RyR), the Ca^{2+} binding protein annexin6 (Sanchez-Ponce et al. 2011) and the $K_V2.1$ channel (King et al. 2014). The $K_V2.1$ channel is also involved in Ca^{2+} signaling pathways (Misonou et al. 2004; Misonou et al. 2005). Furthermore, synpo/CO is mainly localized closely to synaptic junctions of GABAergic AAS and thus, might play a role in GABAergic transmission of such synapses (Kosaka 1980; Benedeczky et al. 1994; King et al. 2014).

A recent study applying structured illumination microscopy (SIM) revealed putative gaps in the AIS scaffold that are deficient of ankG, $K_V1.2$ and $Na_V1.6$ (Figure 5; King et al. 2014). These gaps have been identified as sites for the clustering of e.g. $K_V2.1$ channels, synpo/CO, RyR, the GABA-A receptor subunits $\alpha1$, ß1 and ß3, the GABA-A receptor scaffolding protein gephyrin, and the presynaptic terminal marker VGAT (Figure 5). These subdomains in the ankG meshwork are suggested to be important for allowing the CO to come in close contact to the plasma membrane and to play a role in Ca^{2+}/calcineurin-dependent modulation of $K_V2.1$ (King et al. 2014).
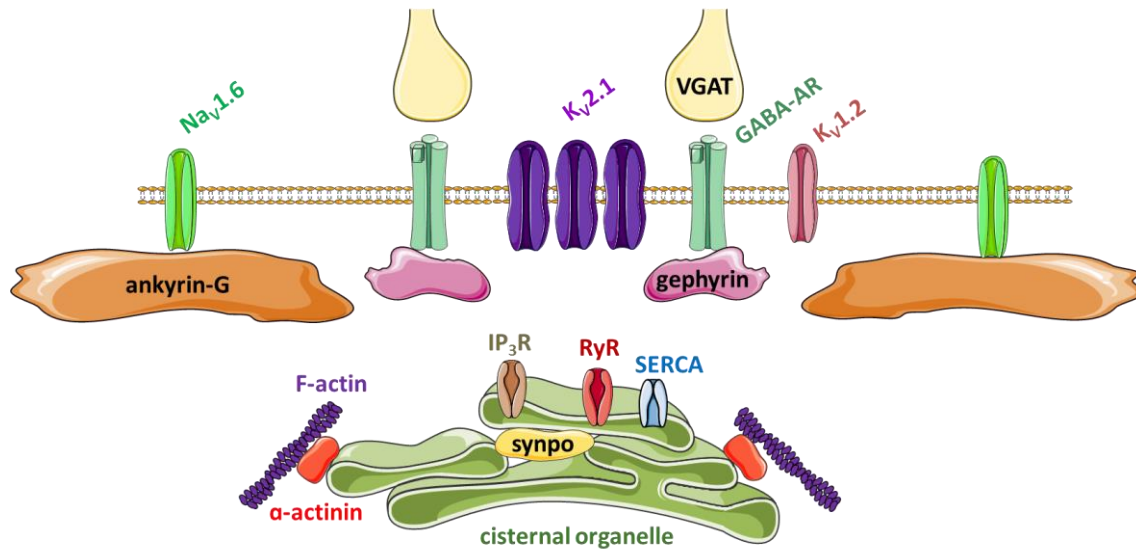
Figure 5: Schematic illustration of synaptopodin (synpo) and cisternal organelle (CO) localization in the axon initial segment (AIS).
The CO (green) is localized in gaps of the AIS meshwork and clusters at sites where ankyrin-G (orange) is absent. The voltage-gated ion channels $K_V1.2$ (pink) and $N_V1.6$ (green) are also absent at these sites. CO and synpo (yellow) are linked to F-actin via α-actinin. The Ca^{2+}-sensitive receptors ryanodine receptor (RyR, brown), IP_3 receptor (IP_3R, red), SERCA type 2 ATPase (blue) are expressed in the CO membrane. IP_3R localizes at AIS scaffold gaps as well. GABAergic synapses and CO cluster together at ankG-deficient sites, as shown by localization of gephyrin (pink), the GABA-A receptor subunits $\alpha1$, ß1 and ß3 (green), and the vesicular GABA transporter (VGAT, yellow). (Figures were produced using "Servier Medical Art", www.servier.com).

Furthermore, a conspicuous elongated organelle was identified in AIS of a subpopulation of layer V type I pyramidal neurons that project to subcortical non-thalamic brain areas (striatum, superior colliculus, thoracic spinal cord, and pontine nuclei) (Sanchez-Ponce et al. 2012; Anton-Fernandez et al. 2015). This organelle extends along the entire AIS and was termed the "giant saccular organelle". In contrast to the CO, giant saccular organelles are centered in the AIS, but are most likely correspond to a variant of the smaller COs since they also contain synpo, α-actinin and Ca^{2+}-related proteins.

1.4 The visual system

In the context of cortical development, the visual system has been extensively studied for decades, in various species, and provides major advantages to investigate developmental processes and dynamic events, especially in the context of activity-dependence (Espinosa and Stryker 2012). It was therefore chosen as the model system for the current thesis.

1.4.1 The retina

The visual system includes the eyes along with the visual pathways that provide connections for visual stimuli to reach the brain. The encoding of visual information in the eye is achieved by neurons of the retina (Hoon et al. 2014). The major excitatory neuron of the retina is the retinal ganglion cell (RGC). RGCs are responsible for transmitting visual information from photoreceptors to the visual centers in the brain (Erskine and Herrera 2014). The retina contains seven major cell types that can be distinguished based on function, morphology, and molecular markers. They are organized into a layered and organized structure, whereas individual cell subtypes can be identified by their laminar position (Byerly and Blackshaw 2009). All cell types form morphologically and functionally distinct circuits working in parallel and in combination to generate complex patterns of visual output (Hoon et al. 2014). In rodents, rod photoreceptors represent the majority of all cells, approximately 72%. Bipolar and amacrine cells make up 10% and 8%, respectively. Cone photoreceptors, Müller glia cells and RGCs each account for only 2-3%. Horizontal cells make up only 0.3% of all cells in the rodent retina (Cepko et al. 1996).

The retinal neuroepithelium derives from the ventral diencephalon during central nervous system development. The major cell types of the retina are generated exclusively from local retinal progenitor cells (Moshiri et al. 2004). In the murine retina, RGCs are born from E10 to P1, with a peak at E13 (Byerly and Blackshaw 2009). RGCs are the output neurons of the retina with their axons forming the optic nerve, projecting to higher visual centers in the brain. RGC excitation is modulated by amacrine cells in two ways through inhibition mediated by GABA and glycine. This results in direct feedforward inhibition from amacrine cell synapses or in indirect feedback inhibition, in which amacrine cells contact axon terminals of bipolar cells first (Hoon et al. 2014).

RGCs are selectively tuned to detect visual scene "trigger features", such as color, size, direction, and speed of motion. Transmembrane receptors of RGCs transform chemical signals from bipolar and amacrine cells into intracellular electrical signals. These are in turn integrated within RGC dendrites and the cell body, and transformed into APs probably in the AIS (Carras et al. 1992). Approximately 30 RGC types have been described based on morphological, molecular, and functional criteria (Sanes and Masland 2015). Individual types are important for distinct retinal circuits and specifically project to targets in the brain depending on the visual trigger features they encode (Erskine and Herrera 2014).

To date, only limited information on the development and characteristics of the AIS in RGC is available. Therefore, the current thesis investigates the developmental and activity-regulated expression of the CO as well as its precise localization in AIS of RGCs in the murine retina.

1.4.2 The visual cortex

The visual cortex is comprised of primary and secondary regions (V1, V2) as well as higher association fields (V3-V5) that contribute to visual perception and process information such as shape, orientation, color, movement, and size of objects.

The primary visual cortex (V1), or area 17, is the main entrance for thalamocortical projections and is organized into functional modules: Neurons with similar receptive fields are organized into columns. Additionally, afferents from the left and right eye, respectively, are separated into alternating columns of cortical tissue, the ocular dominance (OD) columns. These OD columns are particularly prominent at the cortical layer IV, which receives afferents from the dorsolateral geniculate nucleus (dLGN) (Bachatene et al. 2012).

Lamination and major cell types of the primary visual cortex

V1 is comprised of six layers (Figure 6). Layer I contains only a few neurons, but a large number of processes projecting to deeper layers, where they have a direct impact on the firing properties of pyramidal cells. Layer I mainly contains synapses formed between the apical dendrites of layer II-VB pyramidal cells and input from different subcortical regions. Pyramidal cells are excitatory neurons located in the supragranular layers II, IIIA and IIIB as well as in the infragranular layers V and VI. Their general morphology is stereotypical. In

addition to a pyramidal shaped soma, they have basal dendritic extensions and a long apical dendritic tree (Bachatene et al. 2012). The morphology and size of pyramidal neurons as well as the morphology of their AIS vary depending on the specific location of the cells in distinct cortex layers. The diversity of the AIS morphology within the lamination of V1 is shown in Figure 6B.

The small stellate cells are excitatory interneurons mainly located in layer IV (Bachatene et al. 2012). Inhibitory interneurons are predominantly located in layer II/III, IV and V (Peters et al. 1982; Naka and Adesnik 2016; van Versendaal and Levelt 2016). Parvalbumin-expressing interneurons are most abundant in layer IV and V, and are predominantly innervating proximal dendrites and somata of pyramidal neurons. A small proportion of parvalbumin-expressing interneurons is constituted by ChCs, which form AAS at the AIS of pyramidal cells potentially regulating their output (see section 1.1.2: Receptors at the axon initial segment; van Versendaal and Levelt 2016). ChCs are most abundant in layer II/III, but are also present in all other layers (Inan and Anderson 2014). Somatostatin-expressing interneurons are typically Martinotti cells that are most numerous in layer II/III and V. They form inhibitory synapses on dendritic tufts in layer I and on distal dendrites in other cortical layers (van Versendaal and Levelt 2016).

In primates and humans, the laminar organization of V1 is highly specialized (Callaway 1998; Preuss and Coleman 2002). Layers II/III and IV are further subdivided, whereas layer IVC is analogous to layer IV in other cortical areas, and layers II-IVB are analogous to layer II/III. Subdivisions are closely related to direct and indirect inputs from functionally different dLGN afferent pathways (Callaway 1998).
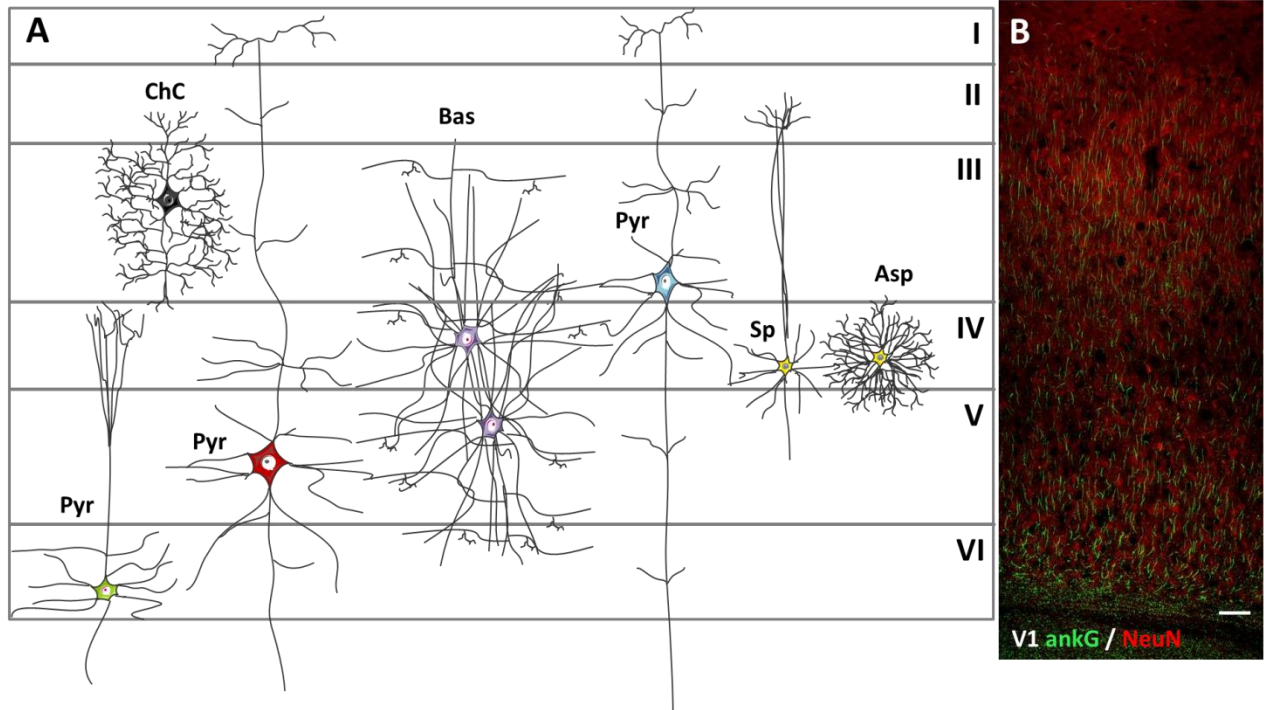
Figure 6: Lamination and schematic illustration of representative major cell types of the primary visual cortex (V1).
(A) Scheme of lamination and major cell types in V1. Dendrites of pyramidal cells in layer II/III (Pyr, blue) and layer V (Pyr, red) extend into layer I. Dendrites of layer VI pyramidal neurons (Pyr, green) extend only into layer IV. Chandelier cells (ChC, dark grey) are mainly located in layer II/III, but can largely project into other layers within V1. Basket cells (Bas, purple) are predominantly localized to layers IV and V, while collectively sending their axons into all cortical layers. Aspiny (Asp, yellow) and spiny (Sp, yellow) stellate neurons are located in layer IV, but send their processes into other layers as well. **(B)** Lamination of adult murine V1 visualized by labeling of pyramidal cells with antibodies against neuron-specific nuclear protein (NeuN, red) and the AIS marker ankyrin-G (ankG, green). Scale bar = 50µm (Figures were produced using "Servier Medical Art", www.servier.com).

1.4.3   From the retina to the primary visual cortex

The processing of visual information involves feedforward connections and a series of reciprocal feedback connections across a hierarchy of cortical areas (Gilbert and Li 2013). The optic nerve collects all RGC axons, which are directed to the specific visual centers and transmit visual information to the main image-forming nuclei. Main targets of RGC axons are the dLGN, the visual part of the thalamus, and the superior colliculus (Nelson 1995; Erskine and Herrera 2014). The pathway of RGC axons from the retina through the dLGN and into V1 is the most direct one for visual information reaching the cortex (Callaway 1998).

The optic nerves from both eyes meet at the optic chiasm localized at the base of the hypothalamus, where RGC axons from the nasal retina cross over to contralateral. RGC axons from the temporal retina remain ipsilateral. Following the optic chiasm, ipsilateral and contralateral axons together form the optic tract. The majority of RGC projections terminate in the dLGN. In carnivores and primates, the dLGN consist of six layers. Each layer receives information from the retinal hemi-field of one eye (Erskine and Herrera 2014). The dLGN of rodents lack this lamination pattern, but retinal projections are organized into complementary non-overlapping eye-specific domains (Godement et al. 1984). RGC axon terminals projecting to each layer form a precise retinotopic map. This retinotopy denotes the spatial organization of neuronal responses to visual stimuli and thus reflects the visual image detected by the retina (Bachatene et al. 2012; Erskine and Herrera 2014). Axons projecting from the dLGN to V1 are organized into thalamocortical fibers forming the optic radiation. The distribution of these fibers in V1 can reproduce the visual field in the corresponding cortical layer. Stellate interneurons in layer IV in V1 receive synaptic connections from afferents of neurons from the dLGN. Specific zones of layer IV receive input from corresponding zones in the dLGN, which in turn receive input from different types of RGCs of distinct functional properties. This provides the organization of V1 into functional maps of orientation, direction (spatial and temporal frequency) and OD, where neurons favor one eye or the other, in higher mammals (Bachatene et al. 2012).

1.4.4 Plasticity of the primary visual cortex

The development of neuronal circuits in V1 occurs in a series of stages. Several studies in V1 of mice have demonstrated similarities to V1 of cats and monkeys (reviewed in Espinosa and Stryker 2012), in e.g. spatial organization of receptive fields (Niell and Stryker 2008). However, corresponding orientation columns and OD columns are lacking in mice. Instead, neurons selective for different stimulus orientations or for different eyes are randomly scattered throughout V1 of mice (Hooks and Chen 2007).

The CP is a sensitive period in early development of an animal wherein experience is absolutely required for subsequent normal structural and functional development. The timing of CP onset and closure can be regulated by physiological and molecular parameters

(Fagiolini et al. 1994; Hanover et al. 1999; Huang et al. 1999). During the CP, neuronal plasticity is greatly enhanced. Three phases of plasticity define the CP: First, the precritical period occurs (preCP; until P19 in mice), when neuronal circuits are initially formed independent of visual experience. Second, the CP follows (peaks around P28 in mice), which is characterized by a distinct onset of robust plasticity in response to visual experience when initially formed circuits can be modified by experience. Third and finally, the closure of the CP occurs (around P35 in mice), when the same visual experience no longer provokes the same degree of plasticity (Hooks and Chen 2007). After CP closure, V1 circuitry and responses appear mature and generally remain stable throughout life (Espinosa and Stryker 2012). However, many studies in V1 have revealed a substantial degree of plasticity in the mature brain, which can be reactivated by modifications of sensory input or sensory motor actions. As a result, level and pattern of activity in cortical circuits are altered (Hubener and Bonhoeffer 2014).

In general, the proper development, refinement and maintenance of special neuronal features in V1 relies on visual experience (Hooks and Chen 2007). During the preCP, the immature patterning of the visual cortex occurs prenatally (Espinosa and Stryker 2012), which is driven by genetic mechanisms (O'Leary et al. 2007). Afterwards, connections between neurons in the dLGN and subplate are formed (Kanold and Luhmann 2010). Later, subplate neurons grow into layer IV of V1 and thus, topographic maps are established, which precisely represent the visual field and provide the proper function of V1. The refinement of these maps occurs before eye-opening and is guided by molecular signaling in the cortex as well as spontaneous neural activity (Feldheim and O'Leary 2010). At this time point, RGCs are only excited through cholinergic mechanisms generating retinal waves that propagate across the retina (Wong et al. 1993). These waves are crucial for map refinement in V1 (Cang et al. 2005). The beginning of the CP is not exclusively activity-dependent; it also relies on the complexity of the neural circuit in V1 (Hooks and Chen 2007). Columns for orientation selectivity and OD appear around eye-opening (Hubel and Wiesel 1963; Des Rosiers et al. 1978; Chapman and Stryker 1993; Chapman et al. 1996; Horton and Hocking 1996). Spontaneous neural activity is the driving factor for this development, however, visual experience is necessary for its maintenance (Espinosa and Stryker 2012). In rodents, OD plasticity begins after 5-10 days of eye-opening and OD can be modified in response to

visual experience during the CP (Hubel and Wiesel 1963; LeVay et al. 1980; Fagiolini et al. 1994). The preCP for OD is still ongoing when vision is present. Onset of the CP for OD can be delayed by dark-rearing (Cynader et al. 1976; Mower 1991; Fagiolini et al. 1994). In comparison, the CP for direction sensitivity in kittens appears before eye-opening (Daw and Wyatt 1976). After dark-rearing during the CP, development of direction sensitivity is disturbed (Li et al. 2006). Direction selectivity becomes fixed after its development and closure of the CP. For orientation selectivity, a discrete period dependent on visual experience seems to be required that maintain once developed neuronal connections. Most studies agree that prolonged visual deprivation of cats and ferrets for more than 3 weeks disrupts orientation selectivity (Pettigrew 1974; Buisseret and Imbert 1976; Sherk and Stryker 1976; Crair et al. 1998; White et al. 2001). In summary, plasticity for OD, orientation and direction selectivity are likely to be differently dependent on visual experience (Hooks and Chen 2007).

The mechanisms underlying the regulation of opening and closure of CPs have been studied extensively in V1. In this context, GABAergic inhibitory innervation is a crucial factor since a transient decrease in inhibition is essential for plasticity (van Versendaal and Levelt 2016). Dark-rearing of cats and rodents leads to the disruption of the excitation and inhibition balance in V1, and delays the peak of the CP into adulthood by directly preventing the maturation of GABA-mediated transmission (Hensch 2005b). Furthermore, dark rearing of rats leads to high rates of spontaneous activity in the visual cortex (Benevento et al. 1992). Recent studies also demonstrated axonal changes (Medini 2014) as well as AIS structural plasticity under dark-rearing conditions (Gutzmann et al. 2014). The AIS can fine-tune neuronal excitability (Gulledge and Bravo 2016), thereby modulating neuronal output and network activity of neuronal circuits. It was also suggested that the CO and Ca^{2+} might be involved in the modulation of GABA-A receptors at the AIS (Llano et al. 1991; Benedeczky et al. 1994; King et al. 2014). This implies a putative function of the AIS and the CO to contribute to neuronal plasticity during visual system development.

2 Aims of the thesis

As detailed above, the development, maintenance and refinement of circuits in the visual system have been extensively explored in the context of neuronal plasticity. Activity-driven axonal plasticity, especially of the AIS, has been shown to be important in shaping neuronal circuits during development (reviewed in Yoshimura and Rasband 2014). During visual cortex development, the AIS has been recently shown to undergo plastic changes in length in response to altered visual activity (Gutzmann et al. 2014). AIS plasticity is supposed to act as a homeostatic mechanism to fine-tune neuronal excitability through changes in AIS length and position from the soma (Gulledge and Bravo 2016). However, the underlying mechanisms of this structural plasticity of AIS are still poorly understood. As outlined earlier (see section 1.3: The cisternal organelle), the CO is a potential structural and functional homologue of the SA in dendritic spines with putative functions in Ca^{2+} current regulation in the AIS. Similar to the dynamic properties of the SA and its function in dendritic spine plasticity in the hippocampus (Vlachos et al. 2013), the CO might be a dynamically expressed organelle during visual system development. Furthermore, the CO might be a potential regulator for AIS structural plasticity.

Currently, the developmental characteristics of the CO as well as the impact of CO expression on AIS structural plasticity still remain elusive. Therefore, the current thesis focuses on the well-studied visual system that is quite accessible for manipulation of visually driven synaptic input onto neurons in the retina and the visual cortex. The activity-regulated plasticity of the CO and the AIS as well as the role of the CO in AIS structural plasticity are further investigated during murine visual system development.

In particular, the following specific questions are addressed in the present thesis:

- Does the CO undergo a dynamic structural maturation during the development of the murine retina and visual cortex?
- Is the expression and maturation of the CO influenced by visual activity?
- What is the impact of CO expression on AIS maturation and AIS structural plasticity during visual cortex development and after visual deprivation?
- What is the precise subcellular localization of the CO with regard to the AIS scaffold in RGCs?

3 Material and Methods

3.1 Animals

All animal protocols were approved by the Heidelberg University, Medical Faculty Mannheim Animal Research Board as well as the State of Baden-Württemberg, Germany and were conducted in accordance with Heidelberg University Guidelines on the Care of Laboratory Animals. The following mouse and rat strains were used: wildtype RjHan:SD rats (Janvier Labs, France), wildtype C57BL/6JRj mice (Janvier Labs, France), synpo-deficient (synpo KO mice, see below), and a transgenic mouse line expressing CFP-tagged (CFP-synpo, see below) or GFP-tagged synpo under the control of the Thy1.2 promoter (GFP-synpo, see below). CFP-synpo mice (official strain designation Thy1-CFP/SP, unpublished), GFP-synpo mice (official strain designation Thy1-GFP/SP, Vlachos et al. 2013) and Synpo KO mice (official strain designation C57BL/6-Synpotm1Mif, Deller et al. 2003) were originally obtained from a colony at Goethe University Frankfurt (Deller group, Clinical Neuroanatomy, Goethe-University Frankfurt, Germany), bred and raised at a local animal facility. Two transcript variants of CFP-synpo mice and three transcript variants of GFP-synpo mice were processed in the current thesis (GFP-synpo-A, GFP-synpo-E, and GFP-synpo-F, as well as CFP-synpo-D and CFP-synpo-G) Heterozygous synpo KO mice were intercrossed to generate homozygous KO mice. The line was maintained in a 129/C57BL6 mixed genetic background. Homozygous KO mice were bred back for >20 generations. Animals of mixed gender from RjHan:SD strain, C57BL/6JRj strain and synpo KO strain were maintained with food and water *ad libitum* on a regular 12h light/dark cycle. C57BL/6JRj mice and synpo KO mice were additionally used for deprivation studies, reared on a 24h dark cycle as outlined below. Animals of mixed gender from CFP-synpo and GFP-synpo strain were kept at a local animal facility. For experiments outlined in this thesis, age groups ranging from P1 to P>55 of wildtype mice and synpo KO mice as well as age groups of P>55 of wildtype rats, CFP-synpo mice and GFP-synpo mice were processed.

3.2 Developmental study

To analyze normal development of synpo/CO expression and AIS structural maturation subject to synpo/CO expression, a total of 6 brains were analyzed in each of the following age groups: P7, P10, P12, P15, P21, P28, P35, P>55 for wildtype and P1, P7, P10, P15, P21, P28, P35, P>55 for synpo KO mice. A total of 6 retinae were analyzed in each of the following age groups of wildtype mice: P8, P10, P15, P21, P28, P35, P>55. Over 100 AIS per animal were examined in the retina and in the primary visual cortex in layers II/III and V, respectively.

3.3 Visual deprivation

Wildtype and synpo KO mice at various ages were kept in completely dark cages with food and water *ad libitum*. Total absence of light was controlled for by exposure of photographic paper located in the cages. Groups of 6 mice each were reared in complete darkness from P0-21, P0-28 and P0-35. Additional rescue experiments were performed by exposing P28 dark-reared mice to light for 1 week until P35. Analyses then proceeded immediately after that period of visual deprivation. Data from the developmental study also served as controls for deprivation experiments. A summary of all experimental groups is given in Table 1.

Table 1: Experimental and control groups used in the current thesis with indication of age of animal, mouse strain, period of visual deprivation and treatment of tissue for immunofluorescence.

Mouse strain	Control	Visual deprivation	Fixation (1% PFA)
Wildtype C57Bl/6JRj	P1		Immersion
	P10, P12, P15		Perfusion
	P21	From birth (P0-21)	Perfusion
	P28	From birth (P0-28)	Perfusion
		From birth (P0-28)/ Rescue in light (P28-35)	
	P35	From birth (P0-35)	Perfusion
	P>55		Perfusion
Synpo KO 129/C57Bl6	P1, P7		Immersion
	P10, P15		Perfusion
	P21	From birth (P0-21)	Perfusion
	P28	From birth (P0-28)	Perfusion
		From birth (P0-28)/ Rescue in light (P28-35)	
	P35	From birth (P0-35)	Perfusion
	P>55		Perfusion

3.4 Immunofluorescence

All chemicals and solutions used for immunostaining are described in Table 2 and Table 3. A summary of all primary antibodies used in this thesis along is shown in Table 4. Secondary antibodies are listed in Table 5.

3.4.1 Chemicals and solutions

Table 2: Chemicals used for immunofluorescence

Type	Specific compound	Source
Embedding media	Tissue Tek® Roti®-Mount FluorCare ProLong® Gold Antifade Mountant Vectashield Antifade Mounting Medium	Sakura Finetek, Alphe, Netherlands Carl Roth, Karlsruhe, Germany Thermo Fisher Scientific, Waltham, MA USA Vector Laboratories, Inc., Burlingame, CA USA
Fluorescent beads	FluoSpheres® Fluorescent Color Kit, Carboxylate-Modified Microspheres, 0.04 μm, four colors	ThermoFisher Scientific, Rockford, USA
Isopentane	2-methylbutane	AppliChem, Darmstadt, Germany
Ketamine Xylazine Isoflurane	Ketamine (10%) Rompun® (10%) 1-Chloro-2,2,2-trifluoroethyl difluoromethyl ether	Medistar GmbH, Ascheberg, Germany Bayer AG, Leverkusen, Germany AbbVie Inc., North Chicago, IL, USA
Nuclear staining	TO-PRO®-3 (To-Pro®-3-iodide) DAPI (4′,6-4′,6-diamidino-2-phenylindole)	Thermo Fisher Scientific, Waltham, MA USA Santa Cruz, Heidelberg, Germany

Table 3: Solutions used for immunofluorescence

Solution	Composition	Source
phosphate buffered saline (PBS, 1x)	in ddH$_2$O (pH 7.4): 10 mM Na$_2$HPO4 * 2H$_2$O 1.47 mM KH$_2$PO$_4$ 130 mM NaCl 2.68 mM KCl	Carl Roth, Karlsruhe, Germany Carl Roth, Karlsruhe, Germany Carl Roth, Karlsruhe, Germany Carl Roth, Karlsruhe, Germany
Saline (0.9%)	in ddH$_2$O: 0.9% NaCl	Carl Roth, Karlsruhe, Germany
Paraformaldehyde (PFA, 1%/4%)	in 1x PBS (pH 7.4): 1%/4% PFA filtered	Carl Roth, Karlsruhe, Germany
Blocking buffer (retina whole mount staining)	in 1xPBS: 0.5% Triton X-100 0.2% bovine serum albumin 0.02% sodium azide	Carl Roth, Karlsruhe, Germany GE Healthcare, Little Chalfont, UK AppliChem, Darmstadt, Germany
Dilution buffer (retina whole mount staining)	in 1xPBS: 1% Triton X-100 10% fetal calf serum 0.02% sodium azide	Carl Roth, Karlsruhe, Germany PAN-Biotech, Aidenbach, Germany AppliChem, Darmstadt, Germany
Sucrose (10%/20%/30%)	in ddH$_2$0: 10%/20%/30% Sucrose	Carl Roth, Karlsruhe, Germany
Switching buffer (50mM)	10% ddH$_2$0 10% 1xPBS 80% glycerol 0.1M cysteamine 100u glucose oxidase (Type VII from *Aspergillus niger*) 800u catalase (from bovine liver) 0.1M D-(+)-glucose	Carl Roth, Karlsruhe, Germany Sigma, St. Louis, Missouri, USA Sigma, St. Louis, Missouri, USA Sigma, St. Louis, Missouri, USA Sigma, St. Louis, Missouri, USA

3.4.2 Antibodies

Table 4: Primary antibodies used for immunofluorescence with indication of clone/type, catalog number, host-species, working dilution, fixation of tissue, previously conducted controls, sources and references where available.

rb: rabbit, ms: mouse, ch. chicken, gp: guinea pig, synpo: synaptopodin, ankG: ankyrin-G, NeuN: Neuronal Nuclei, IP_3R: inositol 1,4,5-trisphosphate receptor, ryanodineR: ryanodine receptor, SERCA2 ATPase: sarcoplasmic/endoplasmic reticulum calcium type 2 adenosine triphosphatase, K_V: voltage-gated potassium channel, NF: neurofilament, KLH: keyhole limpet hemocyanin, mAb: monoclonal antibody, pAb: polyclonal antibody, IgG: immunoglobulin G, IgY: immunoglobulin Y, aa: amino acids, KO: absence of immunostainings in knock out animals, IHC: immunohistochemistry, IP: immunoprecipitation, WB: western blot.

Antibody (host) Clone/type Catalog number	Immunogen	Dilution (PFA fix)	KO	IHC	IP	WB	Source Reference
synpo (gp) pAb 163 004	recombinant mouse synpo, aa 331 - 452 in isoform 2	1:500 1% /4%	X	X		X	Synaptic Systems GmbH, Göttingen, Germany Datasheet
synpo (rb) pAb 163 002	recombinant mouse synpo, aa 331 - 452 in isoform 2	1:500 1% /4%		X		X	Synaptic Systems GmbH, Göttingen, Germany Datasheet
synpo (ms) G1D4, mAb (IgG1) BM5086P	isolated rat kidney glomeruli	1:100 1%	X	X		X	Acris Antibodies GmbH, Herford, Germany (King et al. 2014)
synpo (rb) SE-19, pAb (IgG) S 9442	synthetic peptide corresponding to aa184-202 of rat synpo conjugated to KLH	1:500 1%	X	X		X	Sigma-Aldrich Chemie GmbH, Munich, Germany (Bas Orth et al. 2007)
ankG (rb) H-215, pAb (IgG) sc-28561	aa 4163-4377 of ankG of human origin, C-terminus	1:500 1% /4%	X	X	X	X	Santa Cruz, Heidelberg, Germany (Engelhardt et al. 2013)
ankG (ms) N106/36, mAb (IgG1ϰ) 73-146	recombinant protein corresponding to human ankG	1:250 1% /4%	X	X		X	UC Davis/NIH NeuroMab Facility, CA, USA (Engelhardt et al. 2013)
ßIV-spectrin (rb) pAb (IgG)	aa 2237-2256 of human ßIV-spectrin	1:500 1% /4%	X	X		X	Selfmade (Gutzmann et al. 2014)
NeuN (ms) A60, mAb (IgG1) MAB377	purified cell nuclei from mouse brain	1:250 1%		X		X	Millipore, Temecula, USA (Gutzmann et al. 2014)
NeuN (ch) pAb(IgY) 266 006	recombinant protein, aa 1-97 of mouse NeuN	1:100 1%		X			Synaptic Systems GmbH, Göttingen, Germany (Ott et al. 2015)
α-actinin (ms) H-2, mAb (IgG1ϰ) sc-17829	aa 593-892 of α-actinin-1 of human origin	1:500 1%		X	X	X	Santa Cruz, Heidelberg, Germany Datasheet
α-actinin (ms) EA-53, mAb (IgG1)	rabbit skeletal α-actinin	1:100 1%		X		X	Sigma-Aldrich Chemie GmbH, Munich, Germany

A7811						(King et al. 2014)
IP$_3$R type 1 (ms) L24/18, mAb (IgG1) 75-035	fusion protein aa 2680-2749 of rat type 1 IP$_3$R, cytoplasmic carboxyl terminus	1:100 1%	X		X	UC Davis/NIH NeuroMab Facility, CA, USA Datasheet
ryanodineR (ms) clone 34C, mAb (IgG1) MA3-925	partially purified chicken pectoral muscle ryanodineR	1:500 1%	X	X	X	Thermo Fisher Scientific, Waltham, MA USA (King et al. 2014)
SERCA2 ATPase (ms) IID8, mAb (IgG1) MA3-910	purified canine cardiac sarcoplasmic reticulum	1:500 1%	X	X	X	Thermo Fisher Scientific, Waltham, MA USA Datasheet
K$_V$2.1 (ms) K89/34, mAb (IgG1) 75-014	synthetic peptide aa 837-853, of rat Kv2.1, cytoplasmic C-terminus	1:100 4% (without postfix)	X		X	UC Davis/NIH NeuroMab Facility, CA, USA (King et al. 2014)
200kDa NF (ch) pAb ab72996	full length protein, purified, cow	1:1000 1%/4%		X	X	Abcam Cambridge, UK Datasheet

Table 5: Secondary antibodies used for immunofluorescence with indication of target species, target class, host species, conjugate, working dilution and sources.
rb: rabbit, ms: mouse, gp: guinea pig, ch: chicken, gt: goat, IgG: Immunoglobulin G.

Target species	Target class	Host	Conjugate	Dilution	Source
rb	IgG	gt	Alexa Fluor® 488	1:1000	Life Technologies, Carlsbad, USA
ms	IgG	gt	Alexa Fluor® 488	1:1000	Life Technologies, Carlsbad, USA
gp	IgG	gt	Alexa Fluor® 488	1:1000	Life Technologies, Carlsbad, USA
rb	IgG	gt	Alexa Fluor® 568	1:1000	Life Technologies, Carlsbad, USA
ms	IgG	gt	Alexa Fluor® 568	1:1000	Life Technologies, Carlsbad, USA
gp	IgG	gt	Alexa Fluor® 568	1:1000	Life Technologies, Carlsbad, USA
ch	IgG	gt	Alexa Fluor® 647	1:1000	Life Technologies, Carlsbad, USA
rb	IgG	gt	Alexa Fluor® 647	1:1000	Life Technologies, Carlsbad, USA
ms	IgG	gt	Alexa Fluor® 647	1:1000	Life Technologies, Carlsbad, USA
gp	IgG	gt	Alexa Fluor® 647	1:1000	Life Technologies, Carlsbad, USA

3.4.3   Fixation of tissue

All animals were euthanized by either decapitation or exsanguination according to approved protocols. Brains and eyes from P1-P7 mice as well as P1-P3 rats were dissected in ice-cold 1xPBS. Brains were subsequently fixed overnight by immersion in 1% or 4% PFA at 4°C. Sucrose treatment as outlined below was applied. Mice P10 and older were exsanguinated with 0.9% saline under deep anesthesia with ketamin (120 mg/kg BW) / xylazine (16 mg/kg BW). Rats P7 and older were exsanguinated with 0.9% saline under deep anesthesia with ketamine (100mg/kg BW) / xylazine (3 mg/kg BW). Animals were then perfusion-fixed with ice-cold 1% or 4% PFA. Eyes were processed for retinal immunostaining as outlined below. After overnight immersion in 1% or 4% PFA at 4°C, brains were cryoprotected in 30% sucrose overnight. Tissue was trimmed to a block including visual cortex and was embedded in Tissue Tek® (Table 2). Blocks were flash-frozen in isopentane cooled by liquid nitrogen.

3.4.4   Immunostaining of retinae

Double and triple immunofluorescence was performed on free-floating whole retinae or on sagittal retina cryostat sections directly stained on slides. In a first step, eyes were enucleated from both eye sockets with fine curved forceps and were transferred into a 5cm culture dish containing ice-cold 1xPBS. Retinae were dissected under a stereomicroscope with an internal light source. The eye was held in place with a pair of Dumont forceps. A hole was cut into the eye at the corneal limbus by using a pair of fine spring scissors. After a circumferential incision along the limbus, the cornea, iris, vitreous body, and lens were removed *in toto* by using a pair of Dumont forceps. For preparation of sagittal retinal sections, retinae were kept in the eye cup along with the sclera and pigment epithelium. Tissues were fixed for 10min in 4% PFA, washed three times with 1xPBS and cryoprotected in 30% sucrose for 5hrs. Afterwards, the entire eye cup along with the optic nerve was embedded in Tissue Tek® (Table 2) and frozen in isopentane cooled by liquid nitrogen. 10μm-20μm sagittal retina cryosections were prepared and immediately immunostained according to the protocol used for brain slices as described below. For retinal whole-mount immunostaining, the retina was extracted from the eye cup by carefully tearing the surrounding layers of the sclera and the pigment epithelium away. Retinae were fixed in

4%PFA for 10min and were washed three times in 1xPBS. Retinae were blocked for 24hrs in blocking buffer (Table 3) at 4°C. Primary antibodies (Table 4) were diluted in dilution buffer (Table 3) according to previously validated concentrations. Retinae were incubated with primary antibodies for 24hrs at 4°C. Afterwards, tissues were washed three times in 1xPBS for 15min each. Retinae were then incubated with fluorophore-conjugated secondary antibodies (Table 5) diluted in dilution buffer for 24hrs at 4°C, followed by additional washing steps (3x in 1xPBS, 15min each). For nuclear staining, tissues were incubated in 1xPBS with either TO-PRO®-3 or DAPI (Table 2) followed by a washing step (1x in 1xPBS, 5min). Prior to mounting, retinae were fixed for 10min in 4%PFA and washed in 1xPBS (2x for 5min). Tissue was then cut from the rim to 1/3 of the radial length with fine spring scissors and was then flat-mounted on slides in ddH$_2$0. Retinae were embedded in Roti®-Mount FluorCare mounting medium (Table 2). For imaging of retinae from transgenic mice expressing CFP- or GFP-tagged synpo, Vectashield mounting medium was used (Table 2). For super resolution microscopy, ProLong® Gold mounting medium or switching buffer (Table 2) was used. For shift correction, 1μl of fluorescent beads (Table 2) was transferred near the edge of the slide. Coverslips were sealed onto slides using transparent nail polish.

All stainings were accompanied by negative controls, in which omitting the primary antibody completely abolished all stainings.

3.4.5   Immunostaining of brain slices

Double and triple immunofluorescence was performed on free-floating 40μm thick cryosections prepared for age groups P10 and older. Sections (20μm) from younger age groups were stained directly on slides. After cryosectioning, sections were washed in 1xPBS three times for 5min each. Afterwards, sections were incubated in blocking buffer (Table 3) for 90 min. Sections were incubated overnight at 4°C with primary antibodies (Table 4) diluted in dilution buffer (Table 3) according to previously validated concentrations. Afterwards, sections were washed (3x in 1xPBS, 5min each) and incubated with fluorophore-conjugated secondary antibodies (Table 5) in dilution buffer for 90min at room temperature. For nuclear staining, tissues were incubated in 1xPBS with either TO-PRO®-3 or DAPI (Table 2) followed by a washing step (1x in 1xPBS, 5min). Sections were then

washed in 1xPBS for 5min three times each. Free-floating sections were mounted on slides in ddH$_2$0. Slices were embedded in Roti®-Mount FluorCare mounting medium (Table 2). For imaging of slices from transgenic mice expressing CFP- or GFP-tagged synpo, Vectashield mounting medium was used (Table 2). Again, omitting the primary antibody completely abolished all stainings.

3.5   Microscopy

3.5.1   Confocal laser-scanning microscopy

Confocal laser-scanning microscopy analysis was carried out on a C1 Nikon confocal microscope with a 60x objective (oil immersion, numerical aperture of 1.4) and a Leica SP5 confocal microscope with a 63x objective (oil immersion, numerical aperture of 1.4). To increase the number of in-focus immunoreactive structures, stacks of images were merged into a maximum intensity projection and saved as jpeg and tiff format. Thickness of single optical sections was 0.5μm in stacks of 10-20μm total depth for brain slices. For retinae, stack size was 3-5μm with steps of 0.2-0.3μm. For quantification of synpo/CO clusters and AIS length, confocal x-y-resolution was constantly kept at 0.21μm per pixel. Images for qualitative analysis were evaluated and enhanced for contrast in Fiji (ImageJ; see Table 13 in appendix) and Photoshop C5 (Adobe Systems, see Table 13 in appendix).

3.5.2   Super resolution microscopy

For super resolution imaging of AIS and synpo/CO clusters in retinal ganglion cells *in vivo*, a microscope setup combining structured illumination microscopy (SIM) and single molecule localization microscopy (SMLM) was used. The setup was provided by the Kirchhoff Institute of Physics at Heidelberg University (for reference see "A novel combined Structured Illumination and Single Molecule Localization Microscope and its application to Retinal Structures", http://www.ub.uni-heidelberg.de/archiv/17079 (Dr. Sabrina Rossberger 2014), and also Rossberger et al. 2013b).

For AIS labeling (ßIV-spectrin or ankG, Alexa Fluor® 568) the 568nm laser line was used for excitation. For synpo/CO labeling (synpo, Alexa Fluor® 647) the 671nm laser line was applied. Prior to SIM and SMLM acquisition, a conventional wide field fluorescence image for each wavelength was recorded. In order to correct for the chromatic shift, an additional wide field image was recorded using the 568nm laser line and a 610nm/75nm band pass filter. These wide field images show the relative position of both color signals and thus allows for correction of the two color channels later. For all imaging, a 63x/1.4 oil objective was used, which resulted in a pixel size of 64.5nm for all raw images (for detailed information see Table 12 in appendix).

3.5.2.1 Structured illumination microscopy (SIM)

Method: SIM is a high resolution fluorescence microscopy technique using a specially modulated wide field illumination. In general, SIM provides a lateral resolution that is twice as high as in commonly used wide field microscopy, where lateral resolution is limited to approximately half of the wavelength of the excitation light due to the diffraction limit (Heintzmann and Cremer 1999; Rossberger et al. 2013a).

The sample structure is illuminated with a well-defined illumination pattern, which is generated by using a Twyman-Green interferometer that allows modifying the grating in its phase and orientation.

An intuitive way to describe the resolution improvement with SIM can be conducted with the Moiré effect. The acquired image is a composition of the unknown fine sample structure and the fine but known illumination pattern. The resulting coarse composition can be resolved and is therefore known. Thus, the fine but unknown sample structure can be calculated, which results in a resolution improvement (Rossberger et al. 2013a).

Imaging: Samples were illuminated with a sinusoidal illumination pattern (350nm period). The grating was phase-shifted by 1/3x350nm along the direction of modulation (perpendicular to the grating stripes). Three different spatial orientations of the grating (0°, 60°, -60°) were captured for each of these three phase positions to achieve an isotropic resolution. This resulted in a total of nine raw images in order to generate one high resolution image for each z-position. 3D-SIM stacks were recorded sequentially for each

wavelength starting with the longer wavelength to avoid bleaching (integration time: 50msec/image, focal plane intensity: $\sim(46.8\pm2.7)$W/cm^2). The total z-stack size was 3-5µm with a step size of 200nm between two z-layers.

Image-reconstruction: Highly resolved 3D images were reconstructed by applying either a conventional frequency space based reconstruction algorithm (Heintzmann and Cremer 1999) to the raw SIM-images or by applying a recently developed pixel-sorting based deconvolution algorithm in position space. Pixel size was 32.25nm (For reference see "Development of a Structured Illumination Ophthalmoscope for High Resolution Imaging of the Human Eyeground and Improvements to Structured Illumination Microscopy", http://www.ub.uni-heidelberg.de/archiv/17100 (Dr. Best 2014)).

3.5.2.2 Single molecule localization microscopy (SMLM)

Method: SMLM is a wide field, super resolution microscopy technique based on the activation and detection of photons from individual fluorophores. SMLM improves the spatial resolution compared to standard wide field fluorescence microscopy up to the 10nm range (Rossberger et al. 2013b; Nienhaus and Nienhaus 2016). In conventional wide field microscopy, the entire amount of fluorophores in an immunolabeled sample is excited simultaneously. In SMLM, only a sparse subset of fluorophores emits photons at the same time. Ideally, within a diffraction limited area, only one fluorophore is excited and thus detected. This is achieved by different spectral signatures such as fluorescence lifetime, photo-switching behavior and photobleaching (Nienhaus and Nienhaus 2016). Thus, photoactivatable fluorophores can be switched between an inactive "off" state and an active "on" state. As fluorophore signals located apart with a distance greater than the diffraction limit, the measured point spread functions of these signals can be optically isolated on the detector. Instead of the full width of half maximum, the center of maximum intensity (center of mass) can be computed precisely as an estimate of the fluorophore location. The final image is reconstructed from a time series of camera frames, where every frame consists of signals from different fluororophores. By superimposing all measured fluorophore locations a final 2D super resolution position image is generated. This results in an enhanced resolution up to a factor of approximately 10 for biological samples due to

the dependence on signal, background and noise levels (Rossberger et al. 2013b; Nienhaus and Nienhaus 2016).

Imaging: In the current thesis, the illumination path of the used SIM/SMLM microscope setup was switched to SMLM-mode after recording 3D-SIM images (described above) without moving the specimen. The focal layer for SMLM imaging was selected corresponding to the middle layer of the SIM stack. For each wavelength, a 2D-SMLM time series was recorded (~2000 frames; integration time: 50 msec/image; focal plane intensity: ~(3.84±0.1) kW/cm^2).

Image-reconstruction: Positions of optically isolated SMLM signals were determined using the open source software PYME (see Table 13 in appendix). The mean localization accuracy for the datasets was Δx=10.6nm. SMLM data was visualized using a triangulation algorithm provided in PYME, which translates fluorophore distance inversely into intensity (pixel size=32.25nm for combined SIM/SMLM mode, 5nm for SMLM imaging only). For smoothing of edges, fluorophore positions were jittered randomly (100 times) in order to generate slightly varying triangulated images. Overlaying these images results in smoother edges of the visualized structure. Further image processing and 3D visualization were performed using Matlab, ImageJ and Vaa3D (Table 13 in appendix) (for reference see "A novel combined Structured Illumination and Single Molecule Localization Microscope and its application to Retinal Structures", http://www.ub.uni-heidelberg.de/archiv/17079 (Dr. Sabrina Rossberger 2014), and also Rossberger et al. 2013b).

3.6 Analysis

3.6.1 AIS and synpo expression analysis

AIS lengths were analyzed using self-written macros (Figure 7) (adapted and modified after Gutzmann et al. 2014) in Fiji (ImageJ; see Table 13 in appendix) and Visual Basic for Applications (VBA, Excel, Microsoft; see Table 13 in appendix). The codes of the used macros are described in Table 14 and Table 15 (see appendix). AIS were only quantified if the ßIV-spectrin immunosignal was visible along a single AIS within the recorded stack.

Each AIS was manually selected by a line overlapping the proximal and distal area of the AIS (Figure 7A and B). AIS were straightened, zoomed and plotted by a line extending into the proximal and distal region past the AIS (Figure 7C). Fluorescence intensity profiles of AIS immunosignals were generated using the "Color Profiler" plugin of Fiji and saved as an Excel (Microsoft) file including measured fluorescence intensity for each plotted pixel of immunolabeled AIS (Figure 7D and E). Data of each AIS were stored in an individual file. AIS lengths were calculated in Visual Basic for Applications (VBA, Excel, Microsoft). Maximum fluorescence intensities per pixel of immunolabeled AIS were determined for each individual AIS. The beginning and end of each AIS was set to 10% of maximum fluorescence intensity of AIS to cut-off background noise. Pixels that exceed the 10% fluorescence intensity cut-off were defined for determining start and end point of the AIS, respectively. Length of AIS was calculated using the following formula:

$$AIS\ length\ [\mu m] = \frac{0.21\mu m \cdot n\ pixel}{pixel}.$$

The macro for AIS length measuring was extended by functions for analyzing number and size of synpo/CO clusters for each analyzed AIS in a second step (Figure 7F-H). AIS containing synpo/CO-positive immunofluorescence signals were manually outlined (Figure 7F). Synpo/CO signals in the background beyond the AIS, mainly due to expression in dendritic spines, were eliminated by using the "Clear Outside" function in Fiji. For cluster analysis, the "Color Threshold" option was used. Threshold level was set to 55 and minimum size of pixels was 5 (Figure 7G and H). Both values were kept constant during measurements. All objects defined by these parameters were measured automatically by the "Analyze Particle" function in ImageJ (Figure 7I and J). The mean number and size (in pixels) of synpo/CO-positive clusters per AIS were automatically calculated. For cluster sizes, mean pixel values were translated into μm² applying the following formula:

$$area[\mu m^2] = area[pixel] \cdot (\frac{0.21\mu m}{pixel})^2.$$

Percentage of synpo/CO-expressing AIS was determined by manually counting the total number of AIS in each image, which was analyzed in regard to synpo/CO clusters per AIS as well as AIS length. The number of analyzed AIS for each image frame as described above represented the number of synpo/CO-expressing AIS in the particular image.

The following formula was applied:

$$synpoCO\ expressing\ AIS[\%] = \frac{n\ of\ analyzed\ AIS\ (synpoCO\ expressing\ AIS)per\ image}{total\ n\ of\ AIS\ per\ image} \cdot 100\%$$

A minimum of 3 images was analyzed for each age and layer. The total number of counted AIS is outlined in Table 16 (appendix).

Number, total area, and mean fluorescence intensity of synpo positive immunoreactive (IR+) signals in layer IV of the visual cortex that might correspond to synpo IR+ SAs were manually measured by using the "Analyze Particles" function in Fiji (ImageJ). To exclude synpo IR+ COs from measurement, only particles of sizes ranging from 5 to 30 pixels were measured. Threshold level was set to 55. All values were kept constant during measurements. 6 image frames for each age and condition (n=6 animals) were quantified.
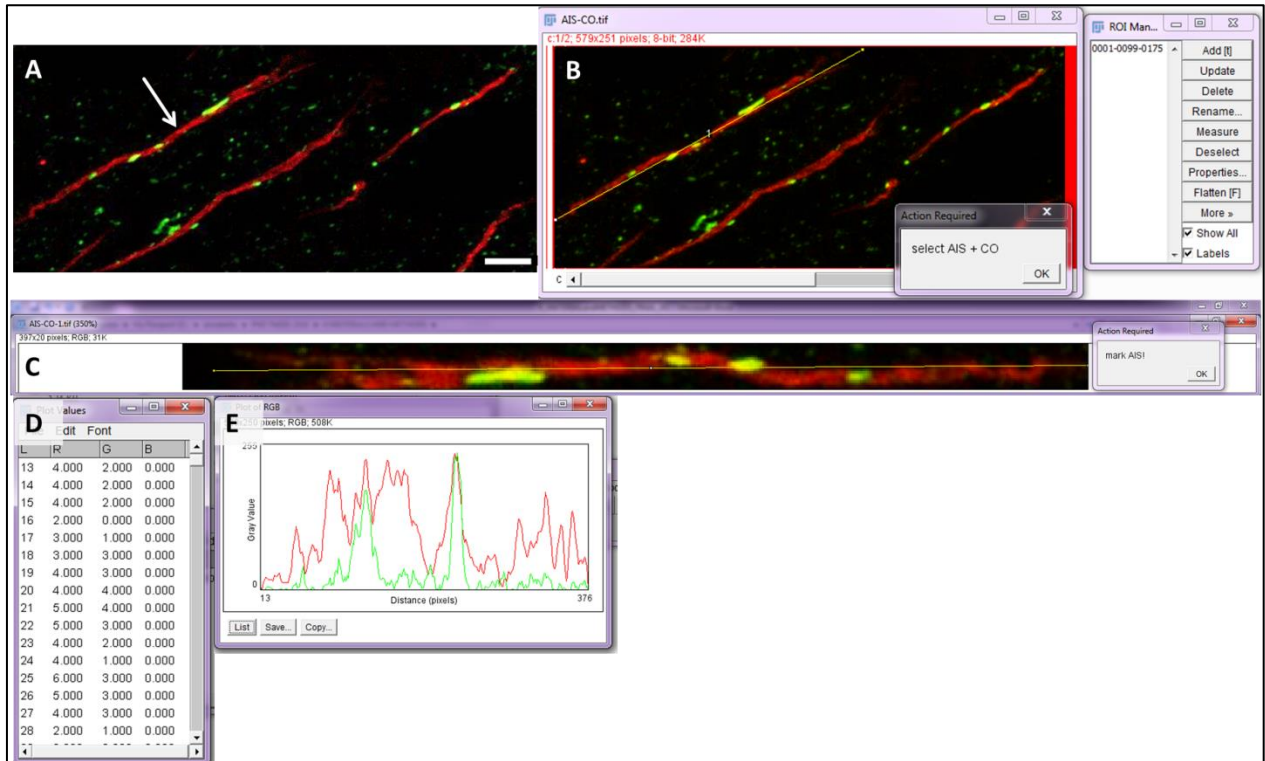
Figure 7: AIS length and synpo/CO cluster analysis in Fiji (ImageJ).
(A) Image of maximum intensity projection of visual cortex AIS expressing synpo/CO. Selected AIS for demonstration of AIS length and synpo/CO cluster analysis is indicated by an arrow. **(B)** The AIS was manually selected by a line (yellow) overlapping the proximal and distal region past the AIS. Selections were saved as region of interests (ROIs) in the "ROI manager" (window on the right in **B**). **(C)** The labeled AIS was straightened and zoomed into in a new window. The AIS was again plotted by a line extending into the proximal and distal regions spanning the AIS. The plugin "Color Profiler" was applied plotting fluorescence intensities of AIS and synpo/CO versus pixel values (plot values, **D**) as well as an intensity profile of AIS and synpo/CO immunofluorescence signals (plot, **E**). The AIS was then bordered using the "Polygon Selection" **(F).** Background signals were eliminated applying the "Clear Outside" function **(G)**. Threshold was set using the "Color Threshold" option **(H)**. Synpo/CO clusters were automatically measured applying the "Analyze Particles" function. Only clusters with sizes ≥5 pixels were included into analysis. **(I)-(J)** Synpo/CO clusters were analyzed in regard to size (area), number (count) and fluorescence intensity (mean). Measurements were saved for each individual analyzed cluster per AIS **(I)** as well as summarized for each analyzed AIS **(J)**. Scale bar = 5μm.

3.6.2 Statistical analysis

Median values and standard error of the mean (S.E.M.) of AIS length as well as size and number of synpo/CO clusters per AIS were calculated in Excel (Microsoft), and plotted and analyzed in GraphPad Prism 7 software, GraphPad InStat3 software, or Sigma Plot 12.5 software. Applied software is shown in Table 13 (appendix). Wilcoxon rank-sum test was carried out for comparison of only two groups. Kruskal-Wallis one-way analysis was applied for comparing three or more groups. Post hoc correction was performed by Dunn's post test. Horizontal bars of box plot diagrams indicate the median. Boxes extend from the

25th to 75th percentiles. Whisker bars indicate minimum and maximum data points. Dots represent individual data points of each median from a total of n=6 animals. Error bars indicate S.E.M. between the 6 mean values of each group/age. Asterisks indicate significant differences (*$p \leq 0.05$). A minimum of 100 AIS per age and animal were analyzed. For frequency histograms of AIS length, different bin-centers were classified: The entire range of AIS length values (10-60μm) was divided into a series of disjoint intervals with steps of 2μm. AIS were then counted and assigned to each interval. For visual cortex data, Spearman rank correlation was performed to measure how synpo/CO number and size vary with AIS length, age and condition, respectively. To predict AIS length from age, condition and cortex layer, a linear multiple regression model ($y=x_1+x_2+x_3$) was applied. The function describes how the y-variable AIS length relates to the three independent x-variables age, condition and cortex layer. For retina data, Spearman rank correlation was performed to measure how synpo/CO number varies with synpo/CO cluster size. To predict synpo/CO cluster number and size, respectively, from age and condition, a linear multiple regression model ($y=x_1+x_2$) was applied. The function describes how the y-variable synpo/CO cluster number or size relates to the two independent x-variables age and condition.

3.7 Quantitative polymerase chain reaction

3.7.1 Chemicals and solutions

Table 6: Chemicals and solutions for agarose gel electrophoresis

Type	Specific compound	Source
TBE (1x)	in ddH$_2$O (pH 8.3): 89 mM Tris 89mM boric acid 2 mM EDTA	 Carl Roth, Karlsruhe, Germany Sigma, St. Louis, Missouri, USA Carl Roth, Karlsruhe, Germany
Agarose (3%)	in 1xTBE: 3% agarose	 Carl Roth, Karlsruhe, Germany
Loading dye (6x)	DNA Gel Loading Dye	Thermo scientific, Rockford, USA
DNA marker	GeneRuler Ultra Low Range DNA Ladder, ready-to-use	Thermo scientific, Rockford, USA
Ethidium bromide staining solution	in 1xTAE: 0,5μg/ml ethidium bromide	 Thermo scientific, Rockford, USA

Table 7: Kits used for RNA preparation, cDNA synthesis and qPCR

Application	Kit	Source
RNA preparation	RNeasy Mini Kit	Qiagen, Venlo, Netherlands
cDNA synthesis	SuperScript III First-Strand Synthesis System for RT-PCR	Life Technologies, Carlsbad, USA
PCR	Taq PCR Master Mix kit	Qiagen, Venlo, Netherlands
qPCR	Brilliant II SYBR® Green QPCR Master Mix	Agilent technologies, Santa Clara, CA, USA

Table 8: Gene-specific primers used for qPCR.
synpo: Synaptopodin, HPRT1: hypoxanthin-phosphoribosyl-transferase 1, T: temperature, A: adenine, C: cytosine, G: guanine, T: thymine, bp: base pairs, T_m: annealing temperature.

Gene (species mouse)	Primer nucleotide sequence (forward/reverse)	T_m (°C) (calculated)	T_m (°C) (optimized / tested)	Product size (bp)
synpo (transcript variant A/B) #1	TCCTCACCTAATGCCACACTC GCTGGAGGGTTTTGGTTGATA	59,8 57,9	60	86
synpo (transcript variant A/B) #2	CTGCATCCGTGGTCAACAG GGGACTCCTATCCGCCATAC	58,8 61,4	61	149
synpo (transcript variant A/B) #3	CCACAGAGGCACATAATGTCC GGATACAGAGTGGAGTAAGAGGG	59,8 62,4	62	185
synpo (transcript variant A)	TTGCTTAGGGCGCTGAGTGG TGGCCTCCTTCAGGTCGTTT	61,4 59,4	61	183
synpo (transcript variant B) #1	AAGAGGCCGATTGACAGAGCA CTGCAATCTGCTGGCTCCTC	59,8 61,4	61	131
synpo (transcript variant B) #2	GGGAAGAGGCCGATTGACAGA TTGGCCTCCTTCAGGTCGTT	61,8 59,4	61	111
HPRT1 #1	GCGTTGGGCTTACCTCACT ATCGCTAATCACGACGCTGG	58,8 59,4	60	132
HPRT1 #2	AGCGTTGGGCTTACCTCAC TCGCTAATCACGACGCTGG	58,8 58,8	59	132
HPRT1 #3	TGGGCTTACCTCACTGCTTTC CATCGCTAATCACGACGCTGG	59,8 61,8	62	129

3.7.2 Procedure

Quantitative polymerase chain reaction (qPCR) was applied to measure synpo RNA levels in retinal samples of mice for different ages of E16.5, P1, P3, P7, P14, P21, P28, P>55. Four animals per age groups were processed. Kits used for RNA preparation, cDNA synthesis, PCR and qPCR are described in Table 7. Gene-specific primers were designed using NCBI/ Primer-BLAST (http://www.ncbi.nlm.nih.gov/tools/primer-blast/) and synthesized via Eurofins MWG Operon Ecommerce (Eurofins Genomics, Luxemburg). Primer design criteria were annealing temperatures (T_m) between 58°C and 61°C (≤2°C difference in the primer pair), primer length of 19-24bp, GC contents of 45-55%, and PCR amplicon length of 100bp-200bp. Primers were chosen to span exon-exon junctions for the amplification of only mRNA. Primer pairs are described in Table 8. Primers were tested in regard to T_m, DNA amplification and DNA reaction side products by performing PCR using a PCR master mix (Table 7). The amplification program was composed of the following steps:

    1x   - 3min at 94°C (denaturation)

    40x   - 30sec at 94°C (primer hybridization)

                - 30sec at T_m (primer annealing)

                - 30sec at 72°C (extension)

    1x   - 10min at 72°C (completion)

Reaction products were visualized by performing agarose gel electrophoresis with 3% agarose gels in 1xTBE buffer for 1hr at constant voltage of 100V. Gels were incubated in ethidium bromide solution for 5min for detection. Chemicals and solutions used for electrophoresis are shown in Table 6.

RNA isolation and purification of retina and brain tissue was performed by using a RNA preparation kit (Table 7) including additional DNA digestion step. 600μl lysis buffer was applied to 20-30μg tissue. RNA concentrations were measured using a NanoDrop (Table 12 in appendix). Only RNA samples with concentrations >100ng/μl and a ratio of the 260/280nm and the 260/230nm absorbance <2.0 were used for further analysis. cDNA was synthesized using a RT-PCR kit (Table 7). Oligo(dT)$_{20}$ primers were used to convert 1μg

RNA into cDNA. qPCR was performed applying a SYBR green I dye master mix (Table 7) including a reference dye (ROX), an optimized RT-PCR buffer, MgCl$_2$, nucleotides (G,A,U,C), SureStart Taq DNA polymerase, SYBR Green and stabilizers. 1µl cDNA as well as 200nM of forward and reverse primers, respectively, were applied to the reaction mix. qPCR was performed by using the Mx3000P QPCR System (Table 12 and 13 in appendix). Comparative quantitation experiment type was performed to relatively quantitate mRNA levels of synpo gene in unknown samples. Synpo and HPRT1 mRNA amounts were determined in regard to an internal standard curve for both gene targets containing different dilutions of a cDNA pool of all samples of known concentration. The following dilutions for standard curve determination were used: 1:2, 1:10, 1:50, 1:250, and 1:1250). Amplification efficiency of each gene target (used primer pairs) was simultaneously determined through standard curves. To normalize mRNA levels, mRNA of the house-keeping gene hypoxanthine phosphoribosyltransferase 1 (HPRT1) was additionally quantified for each sample. "No template controls" (without cDNA) were generated for each used primer pair. Three replicates for each well were prepared and measured. Normal 2 Step qPCR was performed:

  1x   - 10min at 95°C (denaturation)

  40x   - 30sec at 95°C (primer hybridization)

             - 60sec at T$_m$ (combined primer annealing / extension)

  1x   - 1min at 95°C (DNA melting)

             - 30sec at 55°C (stepwise ramp up to 95°C, melting curve measurement)

             - 30sec at 95°C

3.8   Western blot

3.8.1   Chemicals and solutions

Table 9: Chemicals used for Western blot

Type	Specific compound	Source
Bradford assay reagent (5x)	Roti® Quant	Carl Roth, Karlsruhe, Germany
Chemiluminescent substrate	Pierce ECL Western Blotting Substrate	Thermo scientific, Rockford, USA
Protease inhibitor (10x)	cOmplete™, Mini, EDTA-free Protease Inhibitor Cocktail	Sigma, St. Louis, Missouri, USA
Phosphatase inhibitor (10x)	PhosSTOP™	Sigma, St. Louis, Missouri, USA
Protein marker (10–180 kDa)	PageRuler™ Prestained Protein Ladder	Thermo scientific, Rockford, USA
Protein marker (30–460 kDa)	HiMark™ Pre-Stained Protein Standard	Thermo scientific, Rockford, USA
Stripping buffer	Restore™ Western Blot Stripping Buffer	Thermo scientific, Rockford, USA

Table 10: Solutions used for Western blot

Solution	Composition	Source
Homogenization buffer	in ddH$_2$O (pH 7.5): 20 mM Tris 500 mM NaCl 0.5% CHAPS 5 mM EDTA	Carl Roth, Karlsruhe, Germany Carl Roth, Karlsruhe, Germany AppliChem, Darmstadt, Germany Carl Roth, Karlsruhe, Germany
Laemmli sample buffer (5x)	in ddH$_2$O: 5% SDS 25% glycerol 10% 2-mercaptoethanol 0.004% bromphenol blue 0.125M Tris HCl	Carl Roth, Karlsruhe, Germany Carl Roth, Karlsruhe, Germany Carl Roth, Karlsruhe, Germany Merck KGaA, Darmstadt, Germany Carl Roth, Karlsruhe, Germany
Separating gel (8%)	in ddH$_2$O (pH 8.8): 8% acrylamide 0.4M Tris 0.1% SDS 0.1% ammonium persulfate 0.06% TEMED	AppliChem, Darmstadt, Germany Carl Roth, Karlsruhe, Germany Carl Roth, Karlsruhe, Germany Sigma, St. Louis, Missouri, USA Carl Roth, Karlsruhe, Germany
Stacking gel (5%)	in ddH$_2$O (pH 6.8): 5% acrylamide 0.125M Tris	AppliChem, Darmstadt, Germany Carl Roth, Karlsruhe, Germany

	0.1% SDS	Carl Roth, Karlsruhe, Germany
	0.1% ammonium persulfate	Sigma, St. Louis, Missouri, USA
	0.1% TEMED	Carl Roth, Karlsruhe, Germany
Tris-glycine buffer - SDS PAGE running buffer (1x) for 8% gels	in ddH$_2$O: 25mM Tris 192mM glycine 0.1% SDS	Carl Roth, Karlsruhe, Germany Carl Roth, Karlsruhe, Germany Carl Roth, Karlsruhe, Germany
Tris-acetate buffer - SDS PAGE running buffer (1x) for gradient gels	in ddH$_2$O: 50mM tricine 50mM Tris 0.1% SDS	AppliChem, Darmstadt, Germany Carl Roth, Karlsruhe, Germany Carl Roth, Karlsruhe, Germany
Tris-glycine blotting buffer (1x) for semi-dry blot system	in ddH$_2$O: 25mM Tris 192mM glycine 10% methanol	Carl Roth, Karlsruhe, Germany Carl Roth, Karlsruhe, Germany Carl Roth, Karlsruhe, Germany
Tris-glycine blotting buffer #1 (1x) for tank-blot system	in ddH$_2$O: 25mM Tris 192mM glycine 20% methanol	Carl Roth, Karlsruhe, Germany Carl Roth, Karlsruhe, Germany Carl Roth, Karlsruhe, Germany
Tris-glycine blotting buffer #2 (1x) for tank-blot system	in ddH$_2$O: 25mM Tris 192mM glycine 15% methanol 0.05% SDS	Carl Roth, Karlsruhe, Germany Carl Roth, Karlsruhe, Germany Carl Roth, Karlsruhe, Germany Carl Roth, Karlsruhe, Germany
Tris-glycine blotting buffer #3 (1x) for tank-blot system	in ddH$_2$O: 25mM Tris 192mM glycine 0.1% SDS	Carl Roth, Karlsruhe, Germany Carl Roth, Karlsruhe, Germany Carl Roth, Karlsruhe, Germany
PBS-T (1x)	in 1xPBS 1% Tween 20	Carl Roth, Karlsruhe, Germany
BSA blocking buffer	in 1xPBS-T 5% bovine serum albumin	GE Healthcare, Little Chalfont, UK
MP blocking buffer	in 1xPBS-T 5% milk powder	Carl Roth, Karlsruhe, Germany

3.8.2 Antibodies

Table 11: Antibodies used for Western blot with indication of clone/type, catalog number, host-species, working dilution, previously conducted controls, sources and references where available.
rb: rabbit, ms: mouse, ch: chicken, gp: guinea pig, gt: goat, HRP: horseradish, aa: amino acids, IgG: immunoglobulin G, H: heavy chain, L: light chain, mAb: monoclonal antibody, pAb: polyclonal antibody, KO: absence of immunostainings in knock out animals, IHC: immunohistochemistry, IP: immunoprecipitation, WB: western blot.

Antibody (host) Clone/type Catalog number	Immunogen	Dilution in WB	Reported specificity				Source Reference
			KO	IHC	IP	WB	
synpo (rb) pAb 163 002	recombinant mouse synpo, aa 331 - 452 in isoform 2	1:2000		X		X	Synaptic Systems GmbH, Göttingen, Germany Datasheet
synpo (rb) pAb PAB19339	A synthetic peptide corresponding to 17 amino acids near C-terminus of human SYNPO	1:2000		X		X	Abnova GmbH, Taipei City, Taiwan
IP$_3$R type 1 (ms) L24/18, mAb (IgG1) 75-035	fusion protein aa 2680-2749 of rat type 1 IP$_3$R, cytoplasmic carboxyl terminus	1:5000		X		X	UC Davis/NIH NeuroMab Facility, CA, USA Datasheet
Actin (rb) I-19, pAb (IgG) sc-1616-R	epitope at the C-terminus of Actin of human origin	1:1000		X	X	X	Santa Cruz, Heidelberg, Germany Datasheet
αß-tubulin #2148, pAb (IgG)	synthetic peptide corresponding to the sequence of human α- and β-tubulin	1:1000		X		X	Cell Signaling Technology®, Danvers, MA, USA Datasheet
anti-rb (H+L) IgG (gt) -HRP		1:5000					Agilent Technologies, Santa Clara, CA, USA Datasheet
anti-ms (H+L) IgG (gt) -HRP		1:5000					Agilent Technologies, Santa Clara, CA, USA Datasheet

3.8.3   Sample preparation and lysis

All chemicals and solutions used for Western blot are described in Table 9 and

Table 10. Two brains per age group of control mice (wildtype; P7, P10, P14, P21, P28, P35), dark-reared mice (P0-28, P0-35), and of synpo KO mice (P35) were analyzed by Western blot. Two pooled samples of a total of 6 retinae each were analyzed for control mice (wildtype, E16.5, P1, P3, P7, P14, P21, P>55). All animals were euthanized by decapitation with preceding anaesthetization. All dissecting steps were performed on ice. Retina was isolated as described in section 3.4.4. For visual cortex preparation, white matter was eliminated and the visual cortex was isolated under a stereomicroscope with an internal light source using Dumont forceps and fine spring scissors. Tissues were shock-frozen in liquid nitrogen and either stored at -80°C or immediately processed for Western blotting. 50mg of tissue was incubated with 250µl chilled lysis buffer supplemented with 1x phosphatase and 1x protease inhibitor. Subsequently, ultrasonic disruption was applied and the samples were lysed for 1hr at 330rpm and 4°C. Afterwards, samples were centrifuged for 30min at 13.000rpm and 4°C. The supernatant was transferred to a fresh, chilled Eppendorf tube.

3.8.4   Bradford protein assay

Bradford protein assay was applied to determine protein amount in lysed samples. Standard solutions for standard curve determination consisted of 0, 10, 20, 40, 60, 80 and 100µg/ml BSA in ddH$_2$O. 1:100 dilutions (in ddH$_2$O) of lysed cortical and retinal samples were used. 50µl triplets of each standard and protein sample were pipetted into a 96-well plate. 200µl 1x Roti® Quant was transferred to each well. After a maximum incubation time of 5min, samples were measured using an Infinite M200 TECAN reader (Table 12 in appendix). Absorbance was measured at 450nm (OD450) and 590nm (OD590), respectively. Ratio of OD590/OD450 was calculated to determine the standard curve. The linear function of the standard curve was used to determine unknown concentrations of cortical and retinal protein solutions. Afterwards, protein stock solutions of a total volume of 300µl containing 200µg protein, 1x Laemmli sample buffer and ddH$_2$O were produced.

Samples were incubated for 10min at 70°C and subsequently chilled on ice. Aliquots of 30µl were stored at -80°C for long-term storage.

3.8.5 Sodium dodecyl sulphate polyacrylamide gel electrophoresis (SDS PAGE)

For SDS PAGE, 8% polyacrylamide gels (with 5% stacking gel) were cast and used to separate proteins of molecular weights (MW) ranging from 40-200kDa. 10µg of each protein lysate and 10µl of protein marker (range: 10-180kDa) were loaded to the gel wells. SDS-PAGE was performed in 1x Tris-glycine buffer for 20min at 50V and subsequently for 60min at 110V at constant electric current of 300mA. To separate proteins of MW ranging from 40kDa-500kDa range, 3-8% Tris-Acetate gradient gels were used. 20µg of each protein lysate and 15µl of protein marker (range: 30-460kDa) were loaded to the gel wells. SDS PAGE was performed in 1x Tris-acetate buffer at constant voltage of 150V for 55min.

3.8.6 Protein transfer

Proteins were transferred to a polyvinylidene fluoride (PVDF) membrane using the semi-dry blot system (protein MW range: 40-150kDa) or tank-blot system (protein MW range: 25-500kDa). For semi-dry blotting, proteins were blotted for 90min at 45mA in 1x Tris-glycine buffer containing 10% methanol. For tank blotting, proteins were blotted at distinct conditions depending on the protein MW. PVDF membranes were cut into three strips covering the gel from ~30-60kDa, ~70-190kDa and ~200-500kDa, respectively. Low MW proteins were blotted for 30min in 1x Tris-glycine blotting buffer #1. Proteins of middle MW were blotted for 30min in 1x Tris-glycine blotting buffer #2. High MW proteins were blotted for 90min in 1x Tris-glycine blotting buffer #3, the buffer was replaced after 45min of blotting time. For all conditions, used blotting buffers were pre-cooled at -20°C. Buffers are listed in Table 10. Blotting was performed at 4°C, tank blot chambers were cooled with ice pads. Electric current was constant at 550mA.

3.8.7 Detection of specific protein bands

Membranes were incubated for 90min in either BSA or MP blocking buffer (Table 10) at room temperature. Primary antibodies were diluted in blocking buffer according to

previously validated concentrations; a list of used antibodies is provided in Table 11. Membranes were incubated with primary antibodies with gentle agitation overnight at 4°C. Afterwards, membranes were washed three times in 1xPBS-T for 10min each. Membranes were incubated with horseradish peroxidase-coupled secondary antibodies diluted in blocking buffer for 90min at room temperature. Membranes were washed (3x in 1xPBS-T, 10min each) and then incubated with chemiluminescent substrate for 1min (Table 9). To re-probe Western blots, PVDF membranes were incubated in stripping buffer (Table 9) for 45min at 37°C to remove primary and secondary antibodies. Afterwards, membranes were washed (3x 10min, 1xPBS-T) and used again for protein detection as described above. Membranes were either developed on x-ray films or by using a Peqlab Fusion Solo system (Table 12 in appendix). For semi-quantitative analysis, relative band intensities for the 100kDa synpo band and the 300kDa IP_3R band were measured by applying the Gel Analyzer plugin in Fiji (ImageJ; see Table 13 in appendix). Synpo protein was normalized to the internal loading control (actin) with Excel (Microsoft, see Table 13 in appendix). Normalized synpo protein amount at P10 was set to 1 serving as reference for older age groups. Mean values for relative protein levels were built for n=1 animal between individual values of three technical replicates.

4 Results

4.1 Maturation of the cisternal organelle and AIS during visual cortex development

4.1.1 Dynamic regulation of synpo and CO in AIS during development

Synpo expression has been shown to be developmentally regulated in the hippocampus (Czarnecki et al. 2005). The role of synpo and the SA in synaptic plasticity has been further reported by several studies (reviewed in Vlachos 2012). The CO is a putative structural correlate of the SA in the AIS of hippocampal and cortical neurons (Peters et al. 1968; Kosaka 1980; Spacek 1985; Benedeczky et al. 1994). Therefore, it is feasible to hypothesize that synpo/CO expression in AIS of visual cortex neurons is regulated by neuronal activity and might even contribute to AIS plasticity. The current thesis investigates the development of synpo expression and CO maturation in AIS as well as the effect of synpo/CO on AIS structural maturation during visual cortex development.

4.1.1.1 Validation of antibodies for analysis of synpo/CO and AIS development

For CO detection in visual cortex neurons, the most suitable antibody for immunofluorescence was determined by comparing synpo antibodies derived from different species in wildtype and synpo KO mice (Table 4, Figure 8). All tested antibodies showed specific and reproducible labeling of SA and CO in wildtype mice (Figure 8A-D). Signals were consistently absent in synpo KO mice (Figure 8E-H). The polyclonal rabbit antibody produced a weak unspecific signal in somata of pyramidal neurons in the visual cortex of synpo KO mice (Figure 8G) and was therefore omitted from the study. The most reproducible and robust immunofluorescence signals were produced by the polyclonal guinea pig antibody (Figure 8A). Therefore, this antibody was selected for all subsequent immunostainings of synpo/CO.
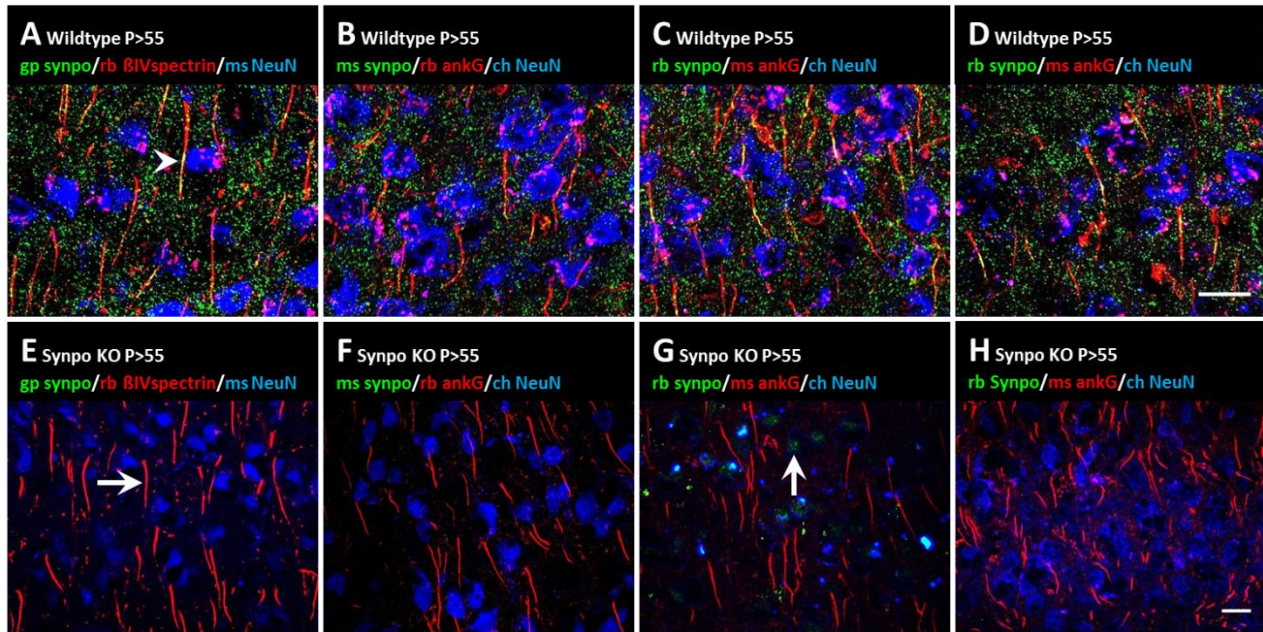
Figure 8: Synpo/CO expression in cortical AIS is verified by different markers.
(A-D) Synpo/CO expression in AIS (arrowhead in **A**) of the visual cortex was stained using various antibodies directed against different epitopes of synpo protein structure. **(E-H)** Synpo immunostaining was absent in synpo KO mice. AIS labeling was verified by two different markers (ankG and ßIV-spectrin, arrow in E). gp anti synpo (green), rb anti ßIV-spectrin (red) and ms anti NeuN (blue) in layer II/III neurons in P>55 wildtype animals **(A)** and in P>55 synpo KO animals **(E).** ms anti synpo (green), rb anti ankG (red) and ch anti NeuN (blue) in wildtype **(B)** and synpo KO mice **(F).** rb anti synpo (green), ms anti ankG (red) and ch anti NeuN (blue) in wildtype **(C)** and synpo KO mice **(G).** rb anti synpo, SE-19 (green), ms anti ankG (red) and ch anti NeuN (blue) in wildtype **(D)** and synpo KO mice **(H).** Scale bar in D for A-D, scale bar in H for E-H = 20 μm.

4.1.1.2 Development of synpo and CO expression in AIS during development

The expression of synpo/CO in AIS of layer II/III and V pyramidal neurons was investigated during primary visual cortex (V1) development in mice. Synpo expression was initially detected at P7 (Figure 9A). Small synpo-positive clusters at this age were not localized in AIS and were most likely restricted to the SA of dendritic spines. In AIS, initial expression of synpo was observed at P10 with highest expression at P15 (Figure 9B). Expression of synpo/CO reached a plateau in adult animals (P>55) (Figure 9C). Throughout V1 development, only a subset of neurons expressed synpo/CO in their AIS. Therefore, the percentage of synpo/CO-expressing AIS in layer II/III and V was measured from P10 until adulthood. The lowest percentage of synpo/CO-expressing AIS was found at P10. At P15, the percentage of synpo/CO-expressing AIS was highest in both layers II/III (48.2±3.8%, Figure 9D, Table 16 in appendix) and layer V (39.1±3.7%, Figure 9E, Table 16 in appendix). The percentage of synpo/CO-expressing AIS then stabilized from P35 in layer II/III

(30.5±1.2%, Figure 9D, Table 16 in appendix) and from P21 in layer V (33.1±4.7%, Figure 9E, Table 16 in appendix) until adulthood (P>55). Of note, the developmental peak in the percentage of synpo/CO-expressing AIS around P15 coincides with eye-opening of mice that occurs between P13-14 (C57BL/6JRj strain). This indicates an activity-regulated expression of synpo/CO in V1 in both layers II/III and V.
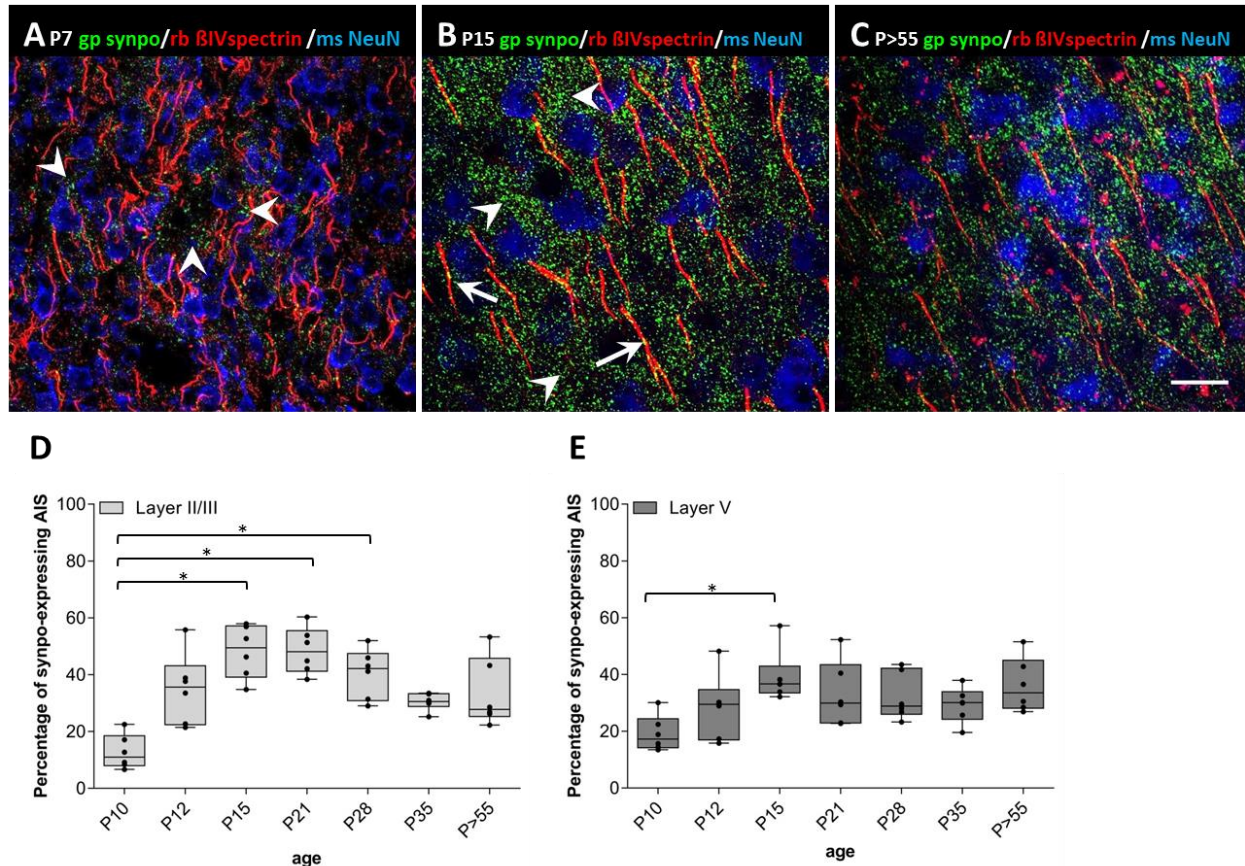
Figure 9: Development of synpo/CO expression in the visual cortex.
Synpo/CO expression in cortical AIS varied during development. Representative immunostainings of synpo (green), ßIV-spectrin (red) and NeuN (blue) in layer II/III neurons in P7, P15 and P>55 wildtype animals.
(A) At P7, synpo was mostly absent from AIS (arrowheads) and was predominantly located at dendritic spines. **(B)** The most abundant synpo expression was observed at P15 in AIS (arrows) and in spines (arrowheads). **(C)** Synpo expression was maintained throughout further developpment until adulthood. Scale bar in E for A-E =10μm. **(D)-(E)** Only a subpopulation of AIS contained synpo/CO. Initial synpo expression in AIS appeared at P10. Percentage of synpo/CO-expressing AIS increased during postnatal development until a maximum at P15. Subsequently, percentage of synpo/CO-containing AIS decreased again from P21/28, then stabilized at P28, persisting throughout adulthood (>P55). Similar observations were made for layer II/III **(D)** and layer V **(E)** neurons, with layer V showing overall less AIS expressing synpo/CO until P35. Boxes extend from the 25th to 75th percentiles. Horizontal lines inside the boxes are plotted at the median. Whisker bars indicate minimum and maximum data points. Dots represent individual data points. n=6 animals, a minimum of 100 AIS per age, animal and layer. Kruskal-Wallis one-way analysis with Dunn's post test. *p≤0.05, S.E.M..

4.1.1.3 Activity-regulated expression of synpo/CO during development

As detailed above, it was hypothesized that synpo/CO expression is regulated by neuronal activity during visual cortex development. To test this hypothesis, the developmental expression of synpo/CO was investigated in AIS of layer II/III and layer V of pyramidal neurons in V1. Number and size of synpo-positive clusters in AIS were quantified for different age groups, starting at P10 (Figure 10) as well as in visually deprived animals (Figure 11). At P10 and P12, the number of synpo/CO clusters per AIS was small (1.47 ± 0.04 for layer II/III, 1.84 ± 0.04 for layer V), but steadily increased during further development (Figure 10A and B, Table 16 in appendix). Between P10 and P15, the number of synpo/CO clusters significantly increased. This timeframe coincides with eye-opening and the first occurrence of directed visual stimuli. During further postnatal development, AIS of layer II/III pyramidal neurons displayed a stable number of synpo/CO clusters, which was maintained until adulthood (Figure 10A and C, Table 16 in appendix). Layer V neurons showed a slight decrease in number of synpo/CO clusters throughout adult stages (Figure 10B, Table 16 in appendix). Numbers of synpo/CO clusters per AIS were significantly correlated to age of the animal only in layer II/III and to AIS length in both, layer II/III and layer V (see appendix Table 24). Sizes of synpo clusters at P10 were $0.49\pm0.02\mu m^2$ in layer II/III and $0.46\pm0.02\mu m^2$ in layer V. Contrary to cluster number, the size of synpo/CO clusters in AIS of V1 neurons did not display significant differences during development (Figure 10D-F, Table 23 in appendix), but showed a weak significant correlation to age of the animal in layer II/III (see appendix Table 35). In contrast, synpo/CO cluster sizes were not significantly correlated to AIS length (see appendix Table 35). However, synpo/CO cluster sizes were significantly and negatively correlated to number of synpo/CO clusters per AIS in layer II/III, whereas a significant and positive correlation was found in layer V neurons (see appendix Table 35).
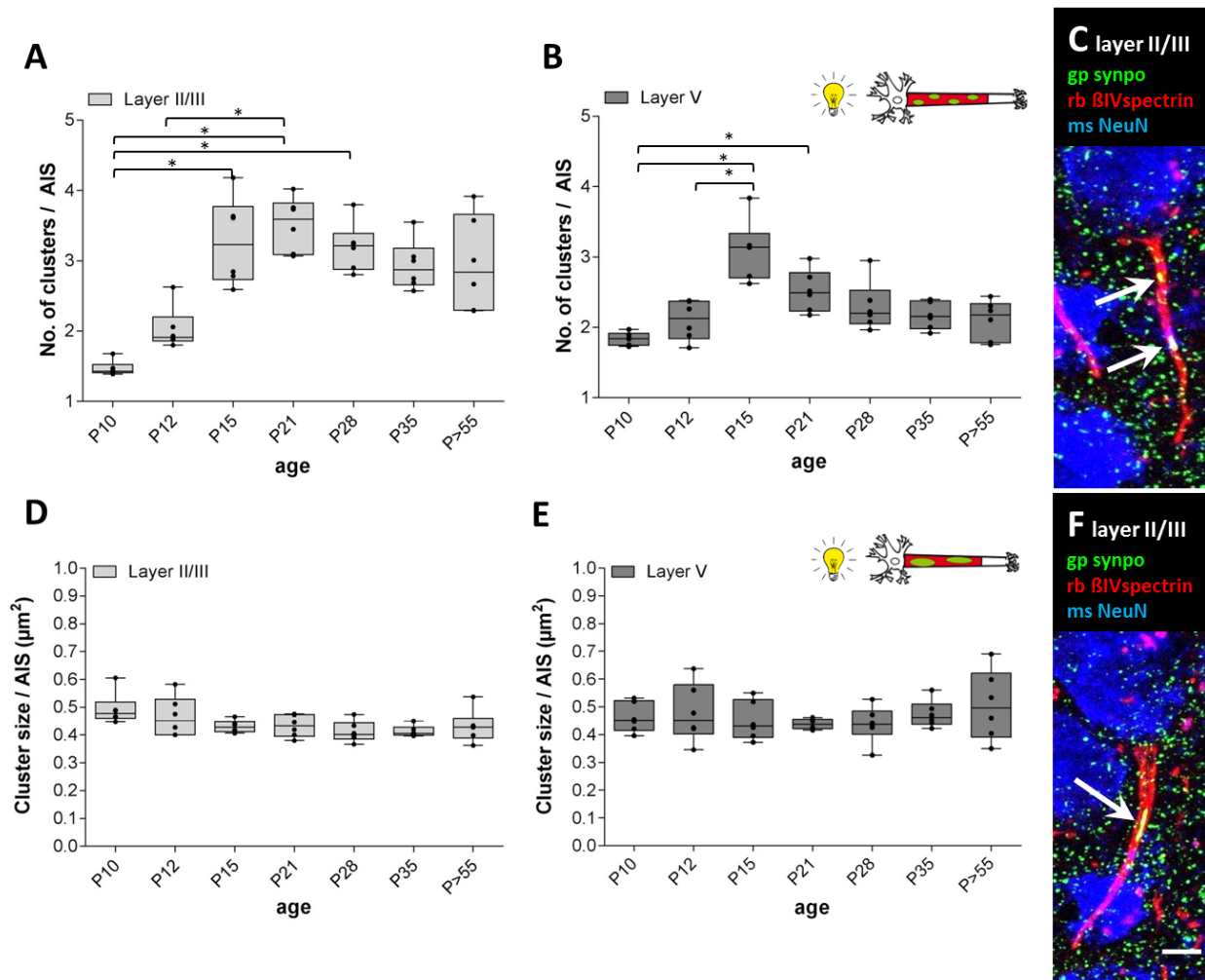
Figure 10: Changes of synpo/CO cluster number and size in AIS during visual cortex development.
(A)-(B) Number of synpo/CO clusters per AIS in layer II/III **(A)** and V **(B)** indicating activity-regulated changes during visual cortex development. Synpo expression in AIS was first observed at P10 with lowest cluster numbers. Numbers significantly increased during further postnatal development with highest values at P15/P21 in layer II/III as well as at P15 in layer V. Subsequently, synpo/CO cluster numbers stayed stable in layer II/III and V persisting throughout adulthood. **(C)** Immunostaining of synpo (green), ßIV-spectrin (red) and NeuN (blue) in layer II/III neurons of wildtype animals**.** Representative synpo/CO expression in AIS showing two synpo/CO clusters (arrows). **(D)-(E)** Size of synpo clusters in AIS of neurons in layer II/III **(D)** and V **(E)** showed no significant changes during development. Synpo/CO clusters in AIS of layer V neurons were larger than in AIS of layer II/III neurons. Boxes extend from the 25th to 75th percentiles. Horizontal lines inside the boxes are plotted at the median. Whisker bars indicate minimum and maximum data points. Dots represent individual data points. n=6 animals, a minimum of 100 AIS per age, animal and layer. Kruskal-Wallis one-way analysis with Dunn's post test. *p≤0.05, S.E.M.. **(F)** Representative synpo/CO expression (synpo, green) in AIS (ßIV-spectrin, red) indicating distinct sizes (compare to **C**) of individual synpo/CO clusters of layer II/III neurons (arrow)**.** Scale bar in F for C and F=10µm.

4.1.1.4 Activity-dependent remodeling of synpo/CO after visual deprivation

AS shown in the previous section, number of synpo/CO clusters in the AIS significantly increased at P15 after eye-opening, which supports the hypothesis that the developmental regulation of synpo/CO is activity-dependent. To further test this hypothesis, percentage of synpo/CO-expressing AIS in V1 as well as number and size synpo/CO clusters in the AIS were analyzed by using a visual deprivation model. Mice were kept in complete darkness from birth until P21, P28, and P35, respectively (Figure 11). For rescue conditions, mice were dark-reared until P28 and then exposed to normal dark/light cycles until P35. Visual deprivation of mice until P21 led to a significant decrease in the percentage of synpo/CO-expressing AIS in layer II/III when compared to P21 controls (Figure 11A, Table 16 and 26 in appendix). No significant differences were found in P28 dark-reared mice compared to P28 controls in both analyzed layers (Figure 11A and B, Table 26 in appendix). However, the P28 rescue condition showed a significant decrease in percentage of synpo/CO-expressing AIS in layer II/III and layer V when compared to P28 dark-reared mice (Figure 11A and B, Table 16 and 26 in appendix). Furthermore, visually deprived animals displayed significant increase in the average number of synpo/CO clusters per AIS only at P21 in layer V when compared to control animals (Figure 11C-E, Table 16 and 22 in appendix). Number of clusters showed indeed a significant correlation to the applied condition (control/dark) (see appendix Table 35). More strikingly, visual deprivation led to a significant increase in synpo/CO cluster size in all conditions in layer II/III and V compared to controls (Figure 11F-H, Table 16 and 24). For P28, cluster sizes increased from $0.41\pm0.02\mu m^2$ to $0.54\pm0.02\mu m^2$ in layer II/III and from $0.44\pm0.03\mu m^2$ to $0.54\pm0.02\mu m^2$ in layer V (Table 16 in appendix). Cluster sizes were also significantly correlated to the applied condition (see Table 35 in appendix). However, the rescue condition did not result in significant differences of neither number nor size of synpo/CO clusters compared to P28 or P35 deprived animals. In summary, synpo/CO clusters show significant activity-dependent plasticity in size already at the beginning of the CP at P21 that lasts until P28, the peak of the CP of visual cortex plasticity.
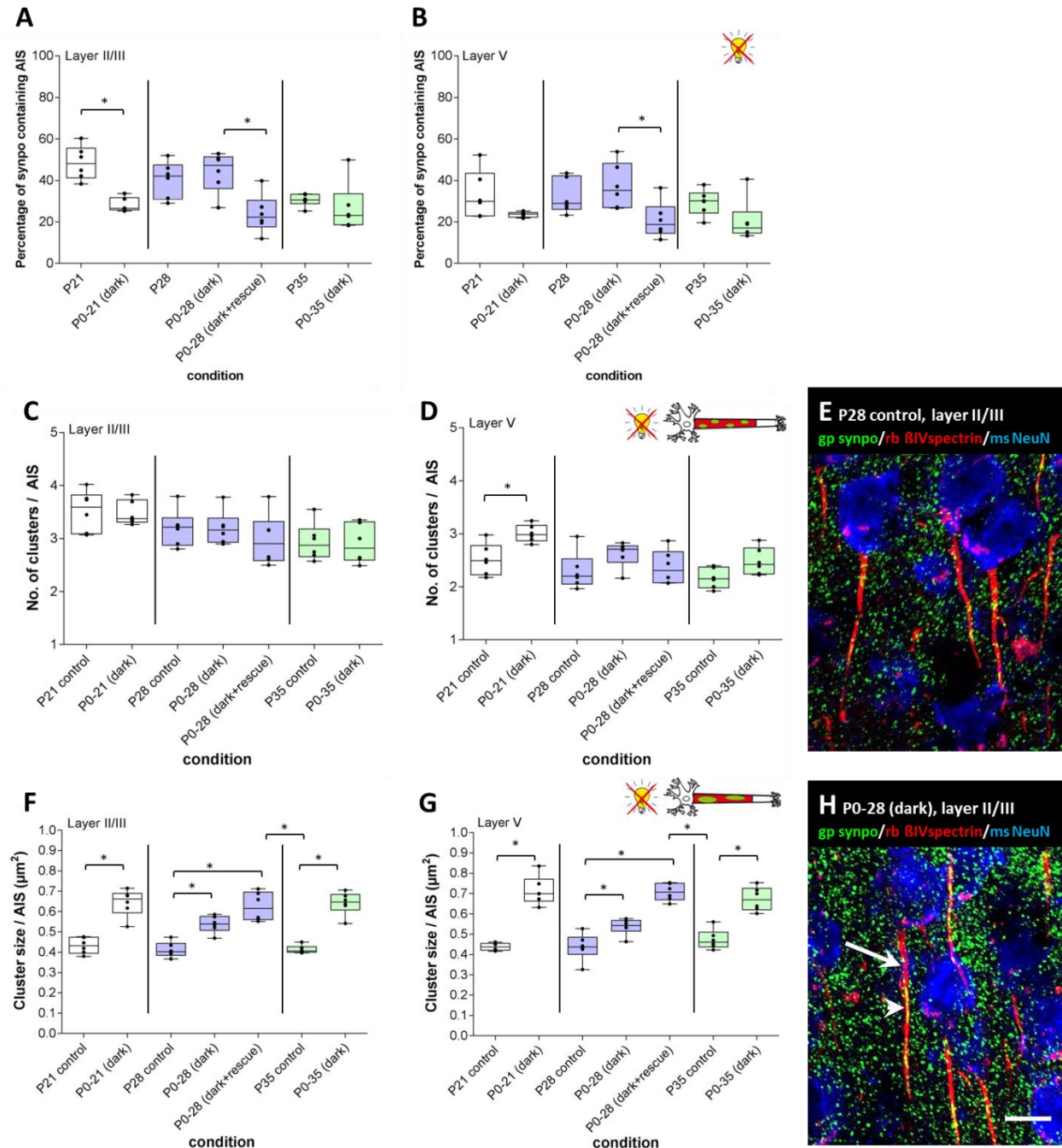
Figure 11: Changes of synpo/CO cluster number and size in AIS after visual deprivation.
(A)-(B) Dark-rearing of mice until P21 led to a significant decrease of percentage of synpo/CO-expressing AIS in layer II/III **(A)**, but not in layer V **(B)**. Visual deprivation did not affect percentage of synpo-expressing AIS in older mice. **(C)-(D)** Dark-rearing of mice from P0-21, P0-28 and P0-35 as well as the P0-28 rescue group (dark-rearing until P28, 1 week light exposure until P35) did not exhibit significant changes in number of synpo/CO clusters in AIS of layer II/III **(C),** but significantly increased in P21 dark-reared animals in layer V **(D)** when compared to controls. **(E)** Synpo/CO expression in AIS of layer II/III in P28 control wildtype animals, as indicated by immunostaining of synpo (green), ßIV-spectrin (red) and NeuN (blue). **(F)-(G)** Visual deprivation for 3, 4 and 5 weeks (P0-21, P0-28 and P0-35) resulted in significant activity-dependent increases

in synpo/CO cluster sizes in AIS of layer II/III **(F)** and V **(G)**. Synpo/CO cluster size increase was highest in P35 animals, which was not reversible in the rescue group. Boxes extend from the 25th to 75th percentiles. Horizontal lines inside the boxes are plotted at the median. Whisker bars indicate minimum and maximum data points. Dots represent individual data points. n=6 animals, a minimum of 100 AIS per age, animal and layer. Wilcoxon rank-sum test and Kruskal-Wallis one-way analysis with Dunn's post test. *p≤0.05, S.E.M.. **(H)** Synpo/CO expression (synpo, green) in AIS (ßIV-spectrin, red) of layer II/III in P28 dark-reared wildtype animals showed an increase in synpo/CO cluster sizes (arrowhead) and AIS length (arrow). Scale bar in H for E and H=10μm.

Vlachos and colleagues have shown that synpo and the SA undergo activity-dependent remodeling after loss of synaptic input in hippocampal neurons (Vlachos et al. 2013). The authors showed that synpo/SA undergoes a significant increase in cluster size and stability as well as stack number in dentate granule cells after entorhinal denervation. This was suggested to be part of a negative feedback mechanism involved in homeostatic plasticity. Likewise, the loss of visually driven synaptic input induced by visual deprivation in the current thesis could also lead to an increase of synpo expression in the SA. To test this, total synpo immunoreactive positive signals (IR+) were quantified in visually deprived mice (Figure 12). Synpo IR+ signals were analyzed in layer IV of V1, which is the major input layer for visual information from the dorsolateral geniculate nucleus (dLGN). Dark-rearing of mice until P28 resulted in a significant increase in number of synpo IR+ signals (Figure 12A, D and E; Table 18 and 37 in appendix), mean fluorescence intensity of synpo IR+ signals (Figure 12B; Table 18 and 37 in appendix) as well as total area of synpo IR+ signals (Figure 12C; Table 18 and 37 in appendix) in layer IV as compared to P28 control animals. It has to be considered that total synpo IR+ signals were measured, which contain signals for both, SAs and COs. However, these results might indicate that besides synpo/CO, also synpo/SA can undergo activity-dependent remodeling in layer IV visual cortex neurons after visual deprivation.
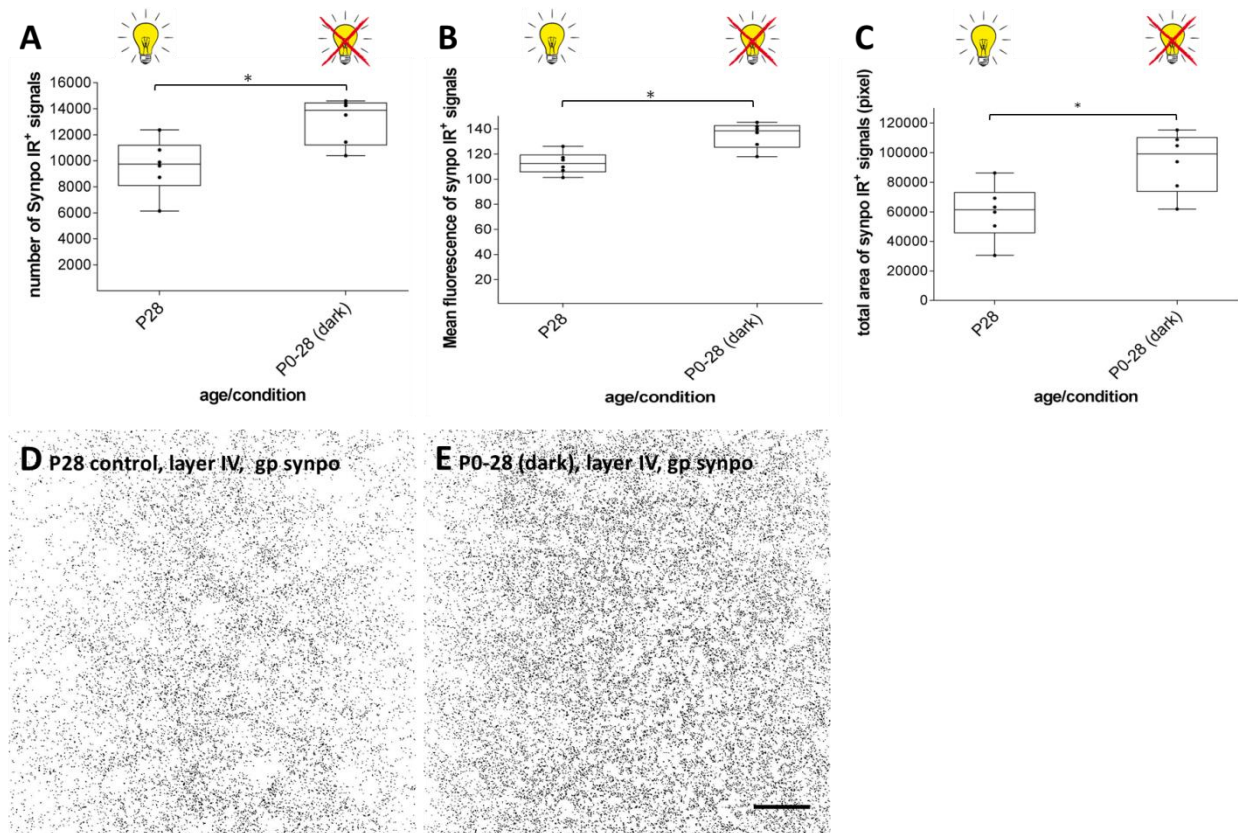
Figure 12: Total changes of synpo immunosignals in visual cortex layer IV after visual deprivation.
Dark-rearing of mice until P28 led to a significant increase in number of synpo immunoreactive positive (IR+)
signals **(A)**, in fluorescence mean intensity values of synpo IR+ signals **(B)**, and in total area of synpo IR+
signals **(C)** as compared to P28 control. Boxes extend from the 25th to 75th percentiles. Horizontal lines inside
the boxes are plotted at the median. Whisker bars indicate minimum and maximum data points. Dots
represent individual data points. n=6 animals. 6 analyzed image sections per age and condition. Wilcoxon
rank-sum test. *p≤0.05, S.E.M.. **(D)** Representative inverted image of synpo IR+ signals in layer IV of V1 in P28
control mice. **(E)** Representative inverted image of synpo IR+ signals in layer IV of V1 in P28 dark reared mice
(P0-28 (dark)). Scale bar in E for D and E=30μm.

As stated above, synpo/CO in AIS of visual cortex neurons undergo a significant increase in
cluster numbers during eye-opening and in cluster sizes after visual deprivation. Does this
activity-dependent remodeling of synpo/CO also correspond to variation of protein levels
of synpo in the visual cortex? And additionally, are protein levels of CO-associated proteins
altered after visual deprivation?

In order to answer this question, protein levels of synpo were analyzed by Western blot of
visual cortex lysates from mice of ages ranging from P7-P35 as well as in dark-reared mice
and P35 synpo KO mice (Figure 13). Furthermore, protein levels of the Ca^{2+}-sensitive IP_3
receptor (IP_3R), which is associated to neuronal ER (Berridge 1998; Augustine et al. 2003)

as well as synpo/CO (Sanchez-Ponce et al. 2011; King et al. 2014; Anton-Fernandez et al. 2015) were investigated after visual deprivation. Representative immunoblot bands are displayed in Figure 13A. Since synpo expression was first detected at P7 in the visual cortex (Figure 9A), ages younger than P7 were not analyzed. Both, synpo and IP$_3$R protein were detected with low levels at P7 (Figure 13A). Synpo was initially found to be expressed in AIS at P10 (Figure 9B), thus P10 was used as reference to quantify protein amounts for synpo and IP$_3$R during development and after visual deprivation. Protein levels of synpo steadily and significantly increased during postnatal development from P10 until P35 (Figure 13A and B, Table 17 and 38 in appendix). Moreover, synpo protein levels showed a slight, but insignificant increase after visual deprivation until P35. Synpo was not detected in visual cortex protein lysates of synpo KO mice. Similar to synpo protein expression, IP$_3$R protein levels displayed a continuous significant increase during development from P10 until P35 (Figure 13A and C, Table 17 and 38 in appendix). In contrast to synpo protein levels, IP$_3$R amounts were decreased after visual deprivation until P28 and P35, however, this decrease was only significant at P35 when compared to controls. IP$_3$R protein levels were also significantly reduced in P35 synpo KO mice as compared to P35 wildtype animals (Figure 13C, Table 17 and 38 in appendix).
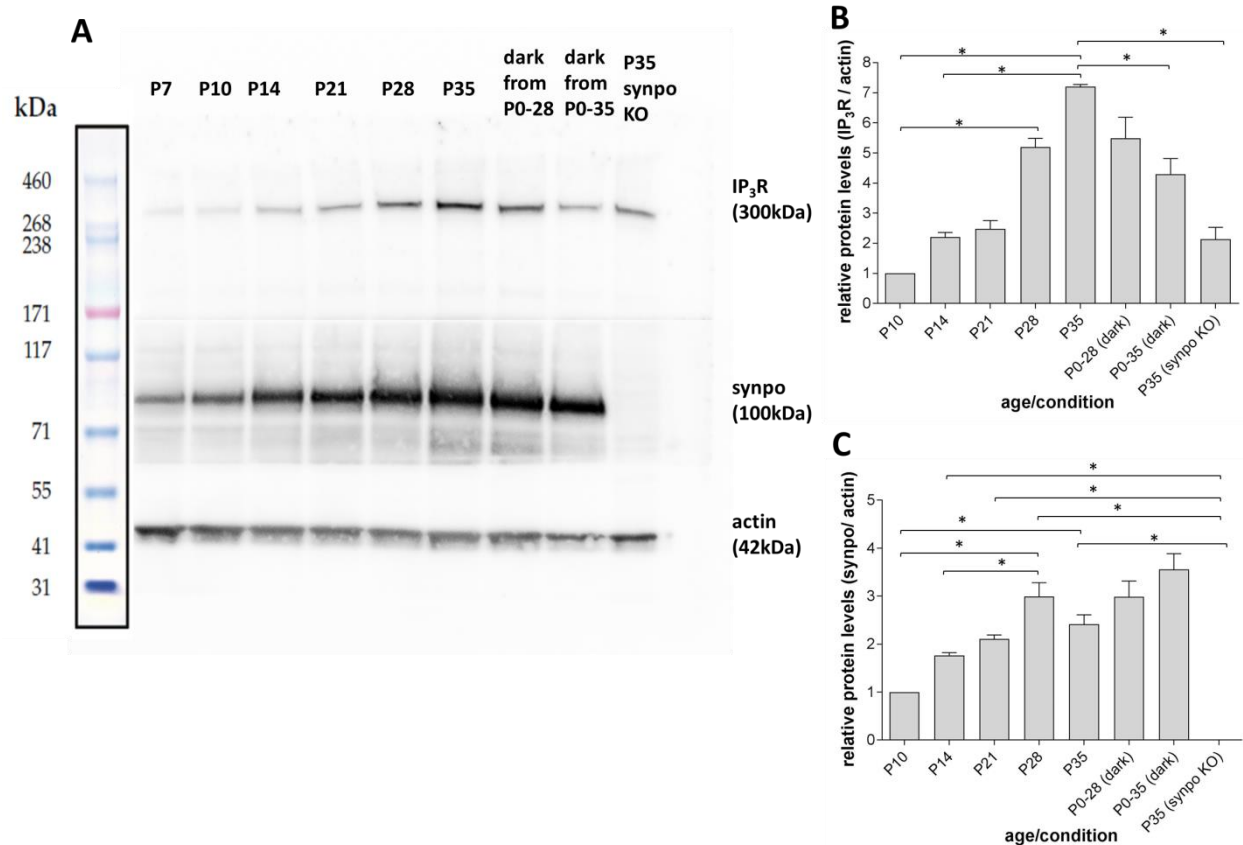
Figure 13: Synpo and IP$_3$ receptor protein expression during visual cortex development of wildtype mice and in synpo KO mice.
(A) Representative immunoblot bands for IP$_3$ receptor (IP$_3$R), synpo and actin in total visual cortex samples from P7-P35, from P28 and P35 dark-reared mice (dark from P0-28/P0-35) as well as from P35 synpo KO mice. Western blot showed antibody-specific protein bands of approximately 300kDa for IP$_3$R, 100kDa for synpo and 42 kDa for actin. Quantification of IP$_3$R **(B)** and synpo **(C)** expression at various ages during visual cortex development, in dark-reared mice and in synpo KO mice. Synpo and IP$_3$R protein was normalized to the internal loading control (actin). Protein levels of synpo and IP$_3$R for each age or condition were expressed relatively to normalized synpo and IP$_3$R amount at P10, respectively. Error bars=S.E.M.. n=2 animals. Mean values from three technical replicates.

4.1.2 Activity-dependent structural maturation of synpo/CO-expressing AIS

The CO is a putative Ca^{2+}-storing organelle in AIS of principal neurons and might be implied in fine-tuning of neuronal excitability (see section 1.3: The cisternal organelle). In this context, it was tempting to speculate that the CO may even contribute to structural AIS plasticity in V1 (Gutzmann et al. 2014). Therefore, structural length maturation in the subset of synpo/CO-expressing AIS was investigated. From P10 until adulthood, length of synpo/CO-expressing AIS in layer II/III and V of V1 was measured (Figure 14A and B). It

was found that synpo/CO-expressing AIS undergo a different morphological maturation than previously described for the entire AIS population in V1 (Figure 3 in Introduction; Gutzmann et al. 2014). At P10, synpo/CO-expressing AIS showed a length of 29.8±0.7µm and 26.3±0.5µm in layer II/III and V, respectively (Figure 14A and B, Table 16 in appendix). These values steadily decreased at younger ages and stayed stable at older ages during further postnatal development. In direct comparison with the tri-phasic length maturation of the entire AIS population (Gutzmann et al. 2014; also see section 1.2: Plasticity of the axon initial segment, Figure 3), the subset of synpo/CO-expressing AIS specifically lacks phase 1 (length increase until P10/15) and phase 2 (length decrease at P28). Synpo/CO-expressing AIS were also shorter compared to the entire AIS population in layer II/III and V in V1 (37.6±1.6 µm, layers II/III for P10-15; from Gutzmann et al. 2014). This implicates that synpo/CO-expressing AIS represent a less dynamic and shorter subset of AIS in V1.

It was further examined whether length maturation of synpo/CO-expressing AIS is dependent on visual activity by investigating AIS length maturation in dark-reared mice.

Each visual deprivation condition (P0-21, P0-28 and P0-35) displayed a significant increase in length of synpo/CO-expressing AIS in both layer II/III and V as compared to control conditions (Figure 14C-F, Table 16 and 28 in appendix). Rescue condition (dark-rearing until P28, light until P35) did not reverse such AIS lengthening. Using a model for linear multiple regression analysis, it was found that age of the animal, applied condition (control/dark) and cortical layer (II/III and V) all contribute in a significant manner to length of synpo/CO-expressing AIS (see Table 36 in appendix). In summary, these results indicate that synpo/CO-expressing AIS in V1 undergo activity-dependent maturation. However, visual deprivation in animals older than P28 did not lead to a higher degree of AIS length increase, neither in P35 mice (P0-35) nor in the rescue condition (P0-28 rescue) (Figure 14D and E, Table 16 in appendix). This suggests that these activity-dependent changes can only occur until P28. Interestingly, dark-rearing for only one week after eye-opening until P21 (P0-21) additionally resulted in significant increases of AIS length in layer II/III and V as compared to P21 control conditions (Figure 14D and E, Table 16 and 28 in appendix).
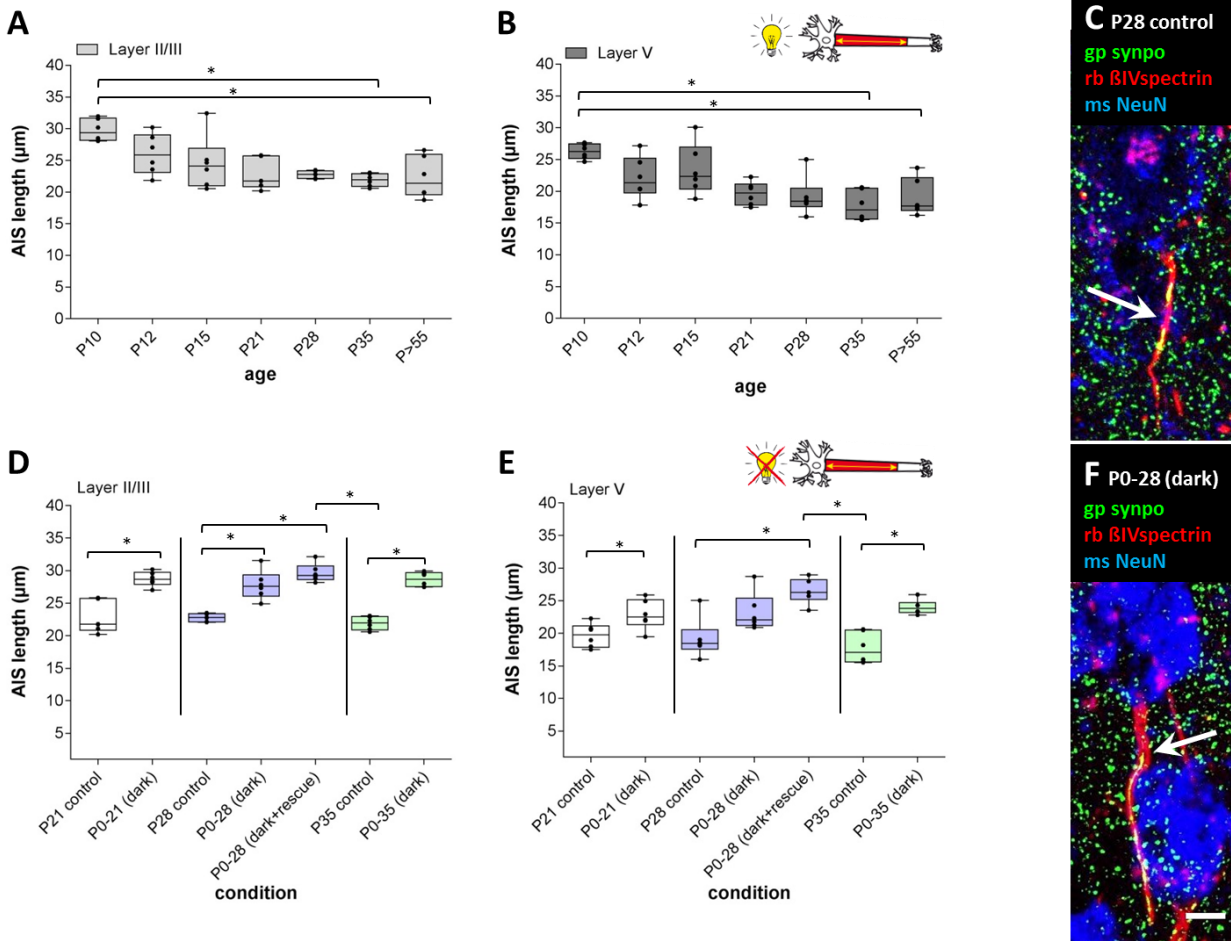
Figure 14: Maturation and elongation of synpo/CO-expressing AIS during visual cortex development and after visual deprivation.

(A)-(B) AIS expressing synpo/CO did not undergo dynamic length maturation in layer II/III and V during development. Length of synpo/CO-expressing AIS was increased until a maximum at P10, shortly before eye-opening between P13-14, and continuously decreased during further postnatal development, showing significant changes only at P35 and P>55 in both layers II/III **(A)** and layer V **(B)**. **(C)** Immunostaining of synpo (green), ßIV-spectrin (red) and NeuN (blue) in layer II/III neurons of P28 control wildtype animals. Representative image of control neuron with short AIS (arrow). **(D)-(E)** Mice were visually deprived from P0-21, P0-28 and P0-35. All conditions resulted in a significant length increase of synpo/CO-expressing AIS in layer II/III as compared to controls, respectively **(D)**. Layer V AIS showed a length increase only in the P0-21 and P0-35 deprived groups **(E)**. Rescue conditions (dark-rearing until P28, followed by light exposure for 1 week until P35) did not reverse activity-dependent AIS length increase. Boxes extend from the 25th to 75th percentiles. Horizontal lines inside the boxes are plotted at the median. Whisker bars indicate minimum and maximum data points. Dots represent individual data points. n=6 animals, a minimum of 100 AIS per age, animal and layer. Wilcoxon rank-sum test and Kruskal-Wallis one-way analysis with Dunn's post test. *p≤0.05, S.E.M.. **(F)** Immunostaining of synpo (green), ßIV-spectrin (red) and NeuN (blue) in layer II/III neurons of P28 dark-reared wildtype animals. Representative image of neuron with long AIS (arrow) after visual deprivation in a dark-deprived animal. Scale bar in F for C and F=10μm.

To investigate the distribution of AIS length during development and after visual deprivation, size frequency histograms of AIS length of layer II/III (Figure 15) and layer V (Figure 16) neurons were analyzed. This analysis highlighted that longer juvenile synpo/CO-expressing AIS at P10 (Figure 15A, 16A) as well as at P12 and P15 (Figure 15B and C, 16B and C) were distributed significantly wider and in a more heterogeneous manner when compared to more adult stages at P21, P28 and P35 (Figure 15D-F, 16D-F; Table 29 in appendix). At adult stages (P>55), AIS length distribution was more homogenous and narrower, which was maintained throughout adulthood (Figure 15G, 16G). After visual deprivation from P0-21, P0-28 and P0-35, respectively, as well as for the P28 rescue condition, the heterogeneous length distribution of synpo/CO-expressing AIS, which was also observed in juvenile AIS, was maintained in both layers significantly shifting to higher AIS length values as compared to controls (Figure 15H-K, 16H-K; Table 30 in appendix). Therefore, visual deprivation led to an AIS length distribution similar to those in young animals and thus, prevented AIS structural maturation. Layer V AIS (Figure 16) showed overall length distribution that was shifted to shorter AIS when compared to layer II/III AIS (Figure 15). Furthermore, P28 dark-reared animals displayed a peak with high numbers of AIS in layer II/III showing length of ~30μm (Figure 15I). No significantly different length distributions were observed between P35 dark-reared animals and the P28 rescue condition in layer II/III AIS (Figure 15J and K; see insert Figure 15; Table 30 in appendix), however, AIS length distribution of these conditions was significantly different in layer V neurons (Figure 16J and K, see insert Figure 16; Table 30 in appendix).

Layer II/III:
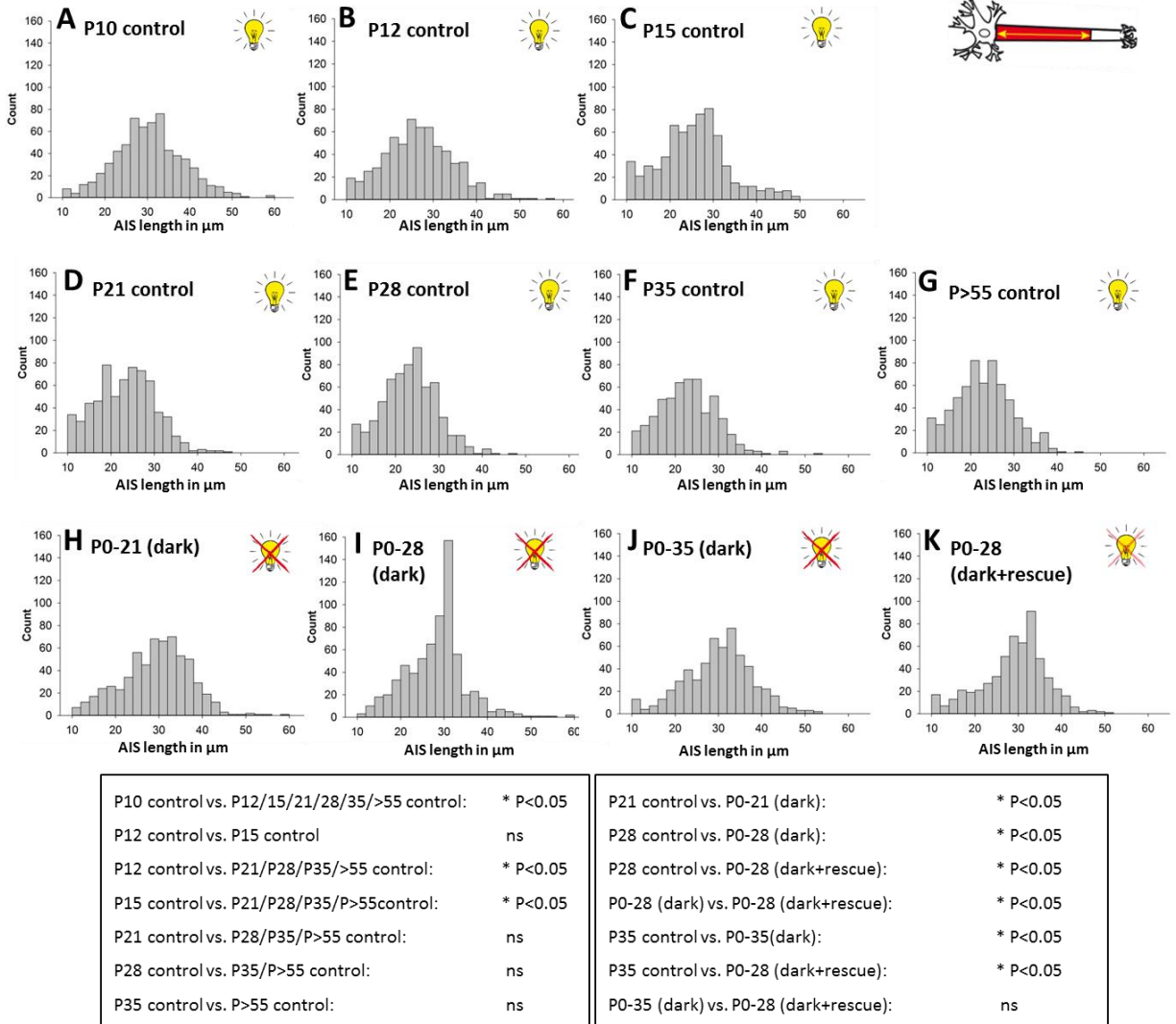
Figure 15: Length distribution of layer II/III synpo/CO-expressing AIS during visual cortex development and after visual deprivation.

(A-K) Size frequency histograms for layer II/III AIS length of various age groups under control and visual deprivation conditions. Wide distribution of AIS length was observed at the peak of juvenile AIS length increase at P10 **(A)** and P12 **(B)** as well as after eye-opening (P13-14) at P15 **(C).** AIS length distribution became significantly narrower during postnatal development at P21 **(D)** with narrowest distributions at P28 **(E)** and P35 **(F)**. This AIS length distribution was maintained throughout adulthood (P>55, **G**). Under visual deprivation for 3 weeks **(H)**, 4 weeks **(I)**, 5 weeks **(J)**, and after rescue (dark-rearing until P28, renewed light exposure until P35, **K**), mature AIS had a significantly broader length distribution as control conditions, which were comparable to the developmental peak at P10 as shown in **A**. P0-28 deprived animals show a high number of AIS with increased length of ~30 μm **(I)**. No significant differences were found between P35 dark-reared animals **(J)** and the P28 rescue condition (**K**, also see insert). n=6 animals, a minimum of 100 AIS per age and animal. Wilcoxon rank-sum test and Kruskal-Wallis one-way analysis with Dunn's post test. *p≤0.05, results in insert.

Layer V:
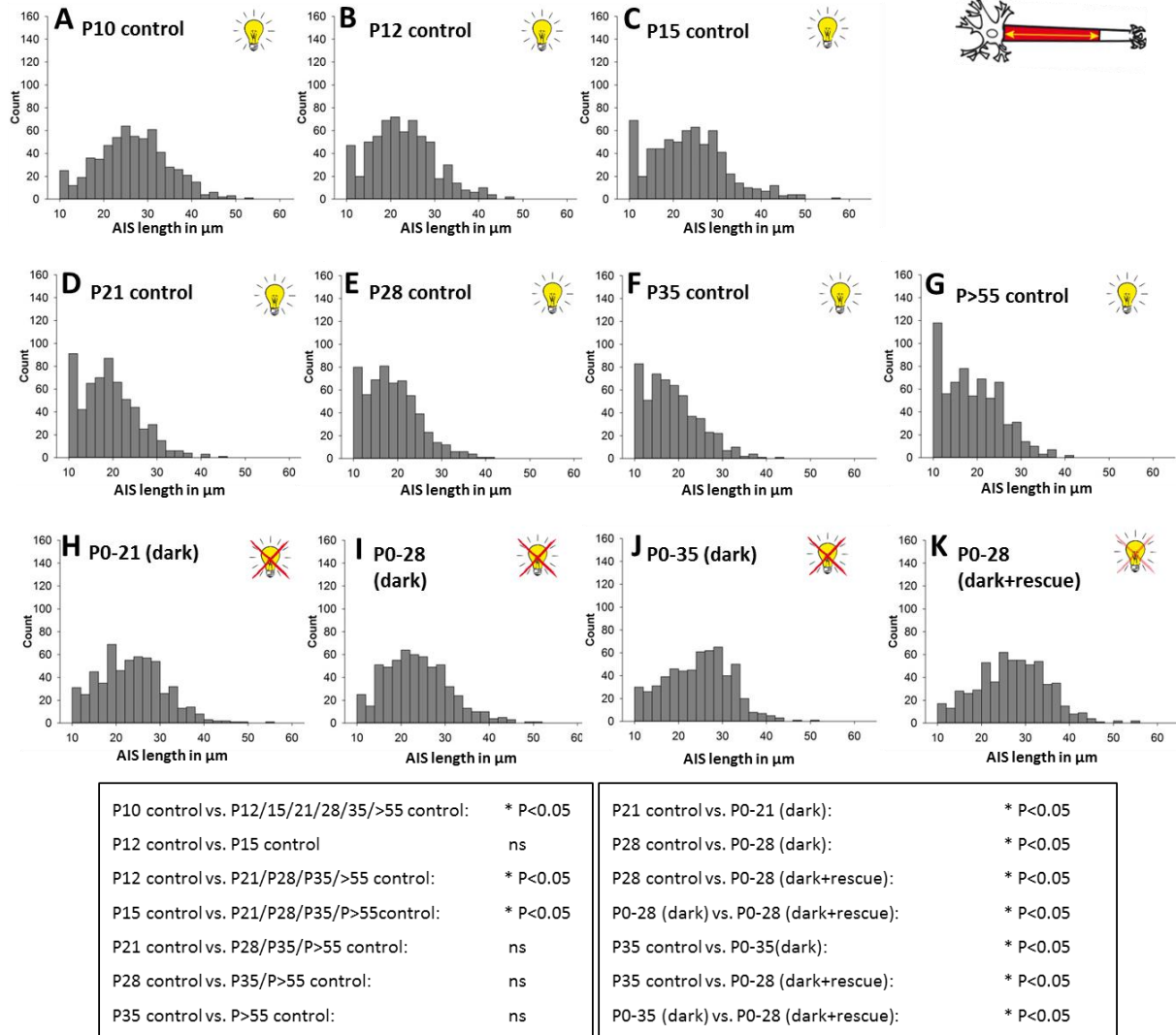
Figure 16: Length distribution of layer V synpo/CO-expressing AIS during visual cortex development and after visual deprivation.

(A-K) Size frequency histograms for layer V AIS length of various age groups under control and visual deprivation conditions. Wide distribution of AIS length was observed at the peak of juvenile AIS length increase at P10 **(A)** and P12 **(B)** as well as after eye-opening (P13-14) at P15 **(C).** AIS length distribution became significantly narrower and more homogenous during postnatal development at P21 **(D)** when AIS shortened. This distribution stayed stable throughout further postnatal development from P28 **(E)** until P35 **(F)** and was maintained into adulthood (P>55, **G**). Under visual deprivation for 3 weeks **(H)**, 4 weeks **(I)**, 5 weeks **(J)**, and after rescue (dark-rearing until P28, renewed light exposure until P35, **K**), mature AIS had a significantly broader length distribution as control conditions, which were comparable to juvenile AIS at P10 and P12 as shown in **A** and **B**. n=6 animals, a minimum of 100 AIS per age and animal. Wilcoxon rank-sum test and Kruskal-Wallis one-way analysis with Dunn's post test. *p≤0.05, results in insert.

.

4.1.3   Activity-dependent structural maturation of AIS in synpo knockout mice

As detailed above, synpo/CO-expressing AIS were restricted to a neuronal subpopulation of cortical neurons in V1 that displayed more static AIS structure as compared to the entire AIS population in V1. Therefore, synpo/CO-expressing AIS might be less sensitive to changes in visually driven synaptic input. Consequently, it was aimed at further elucidating the potential role of synpo/CO in AIS length maturation by studying synpo KO mice during visual cortex development (Figure 17A-C) and after visual deprivation (Figure 17D-F). It was found that during V1 development, AIS length significantly increased in layer II/III and V from younger ages at P1 and P7 to P10/15 during eye-opening (Figure 17A and B, Table 16 and Table 33 in appendix). During further postnatal development, length constantly and significantly decreased from P21 until adulthood (P>55, Figure 17A-C, Table 16 and Table 33 in appendix). Strikingly, phase 2 and thus the sharp AIS length decrease at P28 observed in wildtype mice (Gutzmann et al., 2014; also see Figure 3 in Introduction) was absent. Therefore, tri-phasic AIS structural maturation in synpo KO mice was impaired as compared to that in wildtype mice.

Dark-rearing of synpo KO mice for 3 weeks (P0-21) and 4 weeks (P0-28) led to an interesting finding. AIS length, in particular of layer II/III, significantly decreased after visual deprivation for both conditions (Figure 17D and F, Table 16 and Table 34 in appendix), whereas layer V AIS length changed significantly in P28 and P35 dark-reared animals (Figure 17E, Table 16 and Table 34 in appendix). This AIS length shortening was not reversible in the rescue condition. Applying a model for linear multiple regression analysis revealed that age of the animal, applied condition (control/dark), and cortex layer (II/III and V) all significantly contributed to AIS length (see Table 36 in appendix).
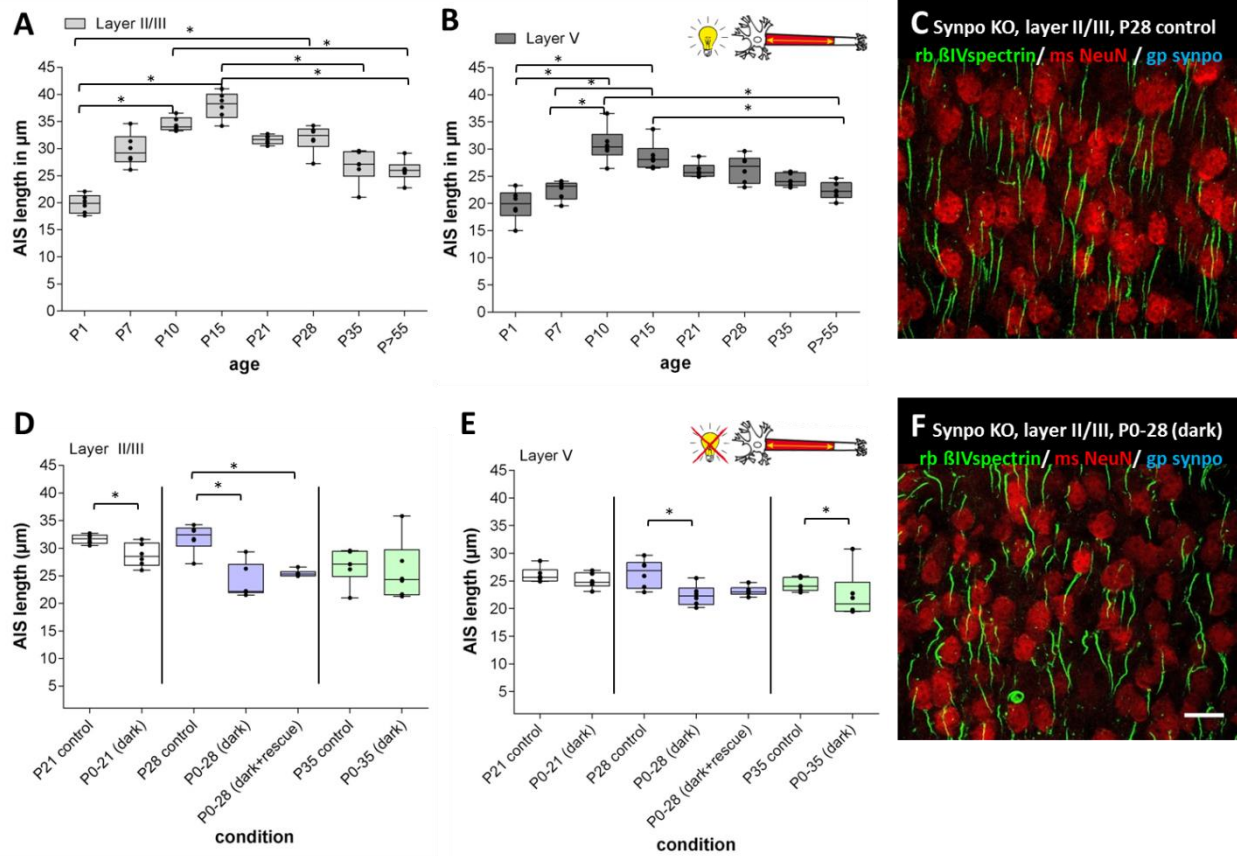
Figure 17: AIS length changes in synpo knockout mice during visual cortex development and after visual deprivation.

(A) AIS of layer II/III and V neurons in the visual cortex of synpo KO mice were shortest at P1 and underwent length increase during further postnatal development until a maximum from P10-P15 during eye-opening. Afterwards, a continuous and significant AIS length shortening occurred in layer II/III **(A)** and layer V **(B)**, which stabilized during adulthood. Layer V neurons showed overall shorter AIS length. **(C)** AIS of layer II/III in synpo KO mice of P28 control condition, immunolabeled against ßIV-spectrin (green), NeuN (red) and synpo (blue). **(D and E)** Mice were dark-reared until P21, P28 and P35. Visual deprivation led to a decrease in length in layer II/III of P21 and P28 **(D)** and layer V of P28 and P35 animals **(E)** as compared to controls. This AIS length decrease was irreversible since P28 rescue groups did not show a re-increase of AIS length. Boxes extend from the 25th to 75th percentiles. Horizontal lines inside the boxes are plotted at the median. Whisker bars indicate minimum and maximum data points. Dots represent individual data points. n=6 animals, a minimum of 100 AIS per age and animal. Wilcoxon rank-sum test and Kruskal-Wallis one-way analysis with Dunn's post test. *p≤0.05, S.E.M.. **(F)** Representative image of AIS (ßIV-spectrin, green) in layer II/III in synpo KO mice after visual deprivation until P28, displaying a decrease in AIS length in P28 dark-reared mice when compared to P28 control **(C)**. Scale bar in F for C and F=20μm.

Length frequency histograms of AIS in synpo KO mice in layer II/III (Figure 18) and layer V (Figure 19) showed that AIS at early postnatal ages at P1 had a significantly narrower length scatter shifted to shorter length as compared to older ages, which was subject to shortened AIS length values at this time point (Figure 18A, 19A; Table 33 in appendix). AIS

length distribution became significantly wider and more heterogeneous during further postnatal development at P7 in both layers (Figure 18B, 19B; Table 33 in appendix), yet, layer V AIS displayed a more homogenous pattern at P7 as compared to layer II/III AIS, which was also not significantly different to AIS length distribution at adult stages in layer V (compare to P>55, Figure 19H). Juvenile AIS at P7, P10 and P15 in layer II/III (Figure 18B-D) as well as at P10 and P15 in layer V (Figure 19C and D) had a significantly more heterogeneous distribution than AIS at adult stages (Figure 18H, 19H; Table 33 in appendix). However, AIS length distribution especially in older synpo KO animals from P21-35 was different as compared to wildtype animals (Figure 15D-F, 16D-F) and displayed a wider distribution with a higher frequency of AIS with 30-40μm in length in layer II/III (Figure 18E-G) and with 20-30μm in length in layer V (Figure 19E-GH). In the context of this result, it is important to consider that AIS of V1 in synpo KO mice are longer than synpo/CO-expressing AIS as well as the entire AIS population of V1 in wildtype animals (Figure 3 in Introduction; Gutzmann et al. 2014) at most ages. AIS length distribution was stable throughout further development after P35 persisting into adulthood (P>55, Figure 18H, 19H).

Dark-rearing of synpo KO mice from P0-21, P0-28 and P0-35, respectively, resulted in AIS length shortening and altered AIS length frequency histograms in layer II/III (Figure 18I-K) and layer V (Figure 19I-K). This also applied to the P28 rescue condition (Figure 18L, 19L). AIS length distribution in dark-reared synpo KO mice was significantly shifted to smaller values for all conditions when compared to controls (Table 34 in appendix), though AIS length shortening was only significant in P21 and P28 dark-reared mice in layer II/III (Figure 17D) as well as in P28 and P35 dark-reared mice in layer V (Figure 17E). However, length distribution in visually deprived mice was not more heterogeneous and wider than in dark-reared wildtype animals (Figure 15, 16). Strikingly, AIS length of P28 deprived animals in layer II/III (Figure 18J) showed a more pronounced wide and heterogeneous distribution that was significantly different to P28 control animals (Figure 18F; Table 34 in appendix). This distribution was shifted to smaller length values and was therefore related to the pronounced AIS length shortening in 4 week dark-reared mice. Distribution of AIS length in the rescue condition in both layers (Figure 18L, 19L) highlighted a significantly

different pattern to that in P28 visually deprived animals (Figure 18J, 19J), but not to P35 dark-reared animals (Figure 18K, 19K; see insert Figure 18 and 19; Table 34 in appendix).
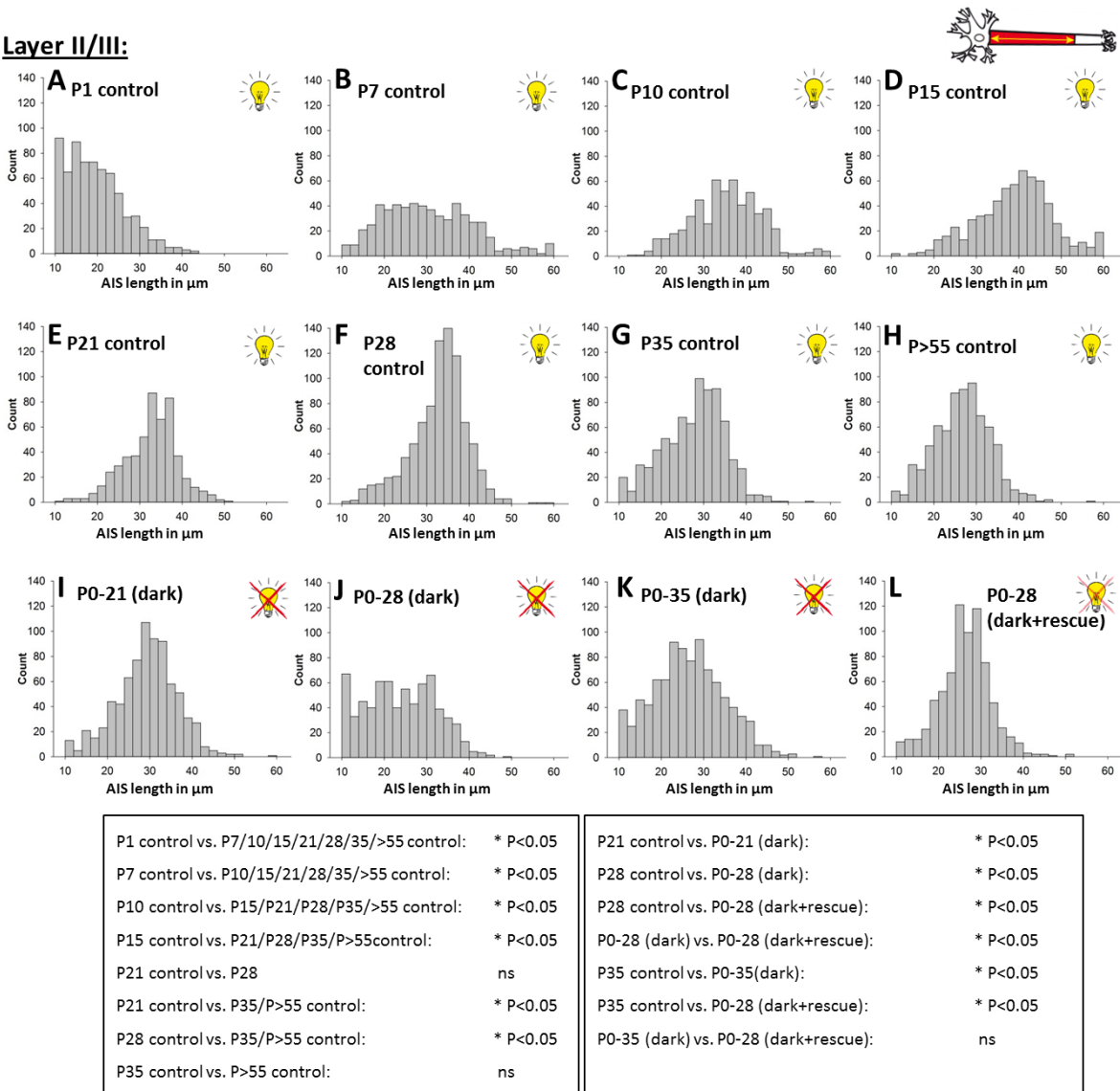
Figure 18: AIS length distribution in layer II/III of synpo KO mice during visual cortex development and after visual deprivation.
(A-L) Size frequency histograms for layer II/III AIS length in synpo KO mice of various age groups under control and visual deprivation conditions. **(A)** At early postnatal ages, AIS length distribution was narrow and shifted to shorter length. **(B-D)** Length distribution of juvenile AIS was widest from P7-P15 during eye-opening and became significantly narrower during further postnatal development and critical periods from P21-P35 **(F-G)**, and stabilized during adulthood **(H)**. Visual deprivation for 3 weeks **(I)** and 5 weeks **(K)**, and rescue (dark rearing until P28, light exposure until P35, **L**) did not lead to an altered AIS length distribution in regard to heterogeneity, but to a significantly displaced distribution to shorter AIS length values. Dark-rearing until P28 **(J)** led to a significantly wider and more heterogeneous distribution as compared to P28 control **(F)**. No significantly different distributions were observed between P35 dark-reared animals **(K)** and the P28 rescue condition (**L;** also see insert). Wilcoxon rank-sum test and Kruskal-Wallis one-way analysis with Dunn's post test. *p≤0.05, results in insert. n=6 animals, a minimum of 100 AIS per age and animal.

Figure 19: AIS length distribution in layer V of synpo knockout mice during visual cortex development and after visual deprivation.
(A-L) Size frequency histograms for layer V AIS length in synpo KO mice of various age groups under control and visual deprivation conditions. **(A)** At early postnatal ages, AIS length distribution was narrow and shifted to shorter length, but became wider starting at P7 **(B)**. **(C-D)** Length distribution of juvenile AIS was widest from P10-P15 during eye-opening and became significantly narrower during further postnatal development and critical periods from P21-P35 **(F-G)**, and stabilized during adulthood **(H)**. Visual deprivation for 3 weeks **(I)**, 4 weeks **(J)** and 5 weeks **(K)**, and rescue (dark rearing until P28, light exposure until P35, **L**) did not lead to an altered AIS length distribution in regard to heterogeneity, but to a significantly displaced distribution to shorter AIS length values. No significantly different distributions were observed between P35 dark-reared animals **(K)** and the P28 rescue condition (**L;** also see insert). Wilcoxon rank-sum test and Kruskal-Wallis one-way analysis with Dunn's post test. *p≤0.05, results in insert. n=6 animals, a minimum of 100 AIS per age and animal.

4.1.3.1 Characterization of CO-associated protein expression in AIS of synpo KO mice

The present thesis shows that lack of synpo expression impairs the structural maturation of AIS during visual cortex development and after visual deprivation. The mechanisms how synpo could affect developmental AIS maturation might be manifold. Lack of synpo leads to the loss of the CO in AIS of principal neurons (Bas Orth et al. 2007), though it is unknown whether lack of synpo alters the expression of CO-associated proteins in the AIS as well. Therefore, synpo KO mice were examined with respect to the expression and localization of α-actinin and $K_V2.1$ in AIS of visual cortex neurons (Figure 20). The actin-binding protein α-actinin is co-localized with synpo in the CO in AIS of hippocampal and cortical neurons (Sanchez-Ponce et al. 2012). Furthermore, the $K_V2.1$ channel is closely clustered with synpo/CO in AIS of principal cells in the cortex and hippocampus (King et al. 2014). As illustrated in Figure 20, the expression of α-actinin in the visual cortex of wildtype mice was comparable to synpo expression and displayed overlapping immunopositive α-actinin and synpo clusters in both, AIS and dendritic spines (Figure 20A and B). In contrast, α-actinin immunofluorescence signals were strongly different in synpo KO mice (Figure 20C). α-actinin did not show specific clustering in AIS or dendritic spines of cortical neurons. Instead, α-actinin was distributed within the cortex showing weak and diffuse immunofluorescence signals in cell bodies. By comparison, the expression of $K_V2.1$ was similar in wildtype and synpo KO visual cortex (Figure 20D and E). $K_V2.1$ was highly enriched in somatodendritic regions of cortical neurons. Additionally, striking immunosignals of clustered $K_V2.1$ were found in AIS of wildtype mice (Figure 20D and D*). $K_V2.1$ clustering at the AIS was indeed observed in synpo KO mice, though it was less conspicuous and apparently reduced in immunointensity (Figure 20E and E*). It therefore appears that synpo is essential for the recruitment of CO-associated proteins to the AIS such as α-actinin and $K_V2.1$.
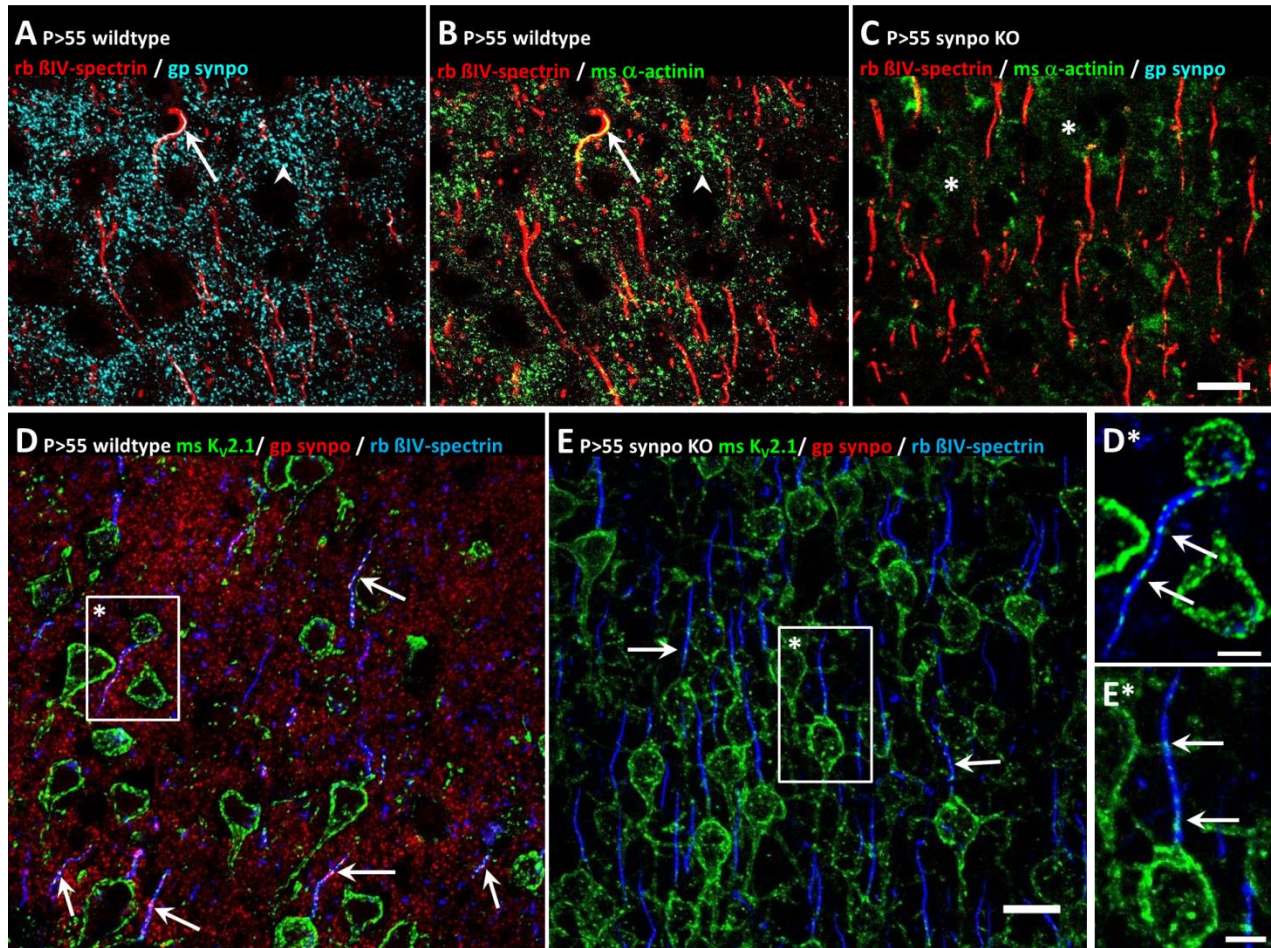
Figure 20: Expression of α-actinin and K$_V$2.1 in the visual cortex of wildtype and synpo KO mice.
(A)-(C) Immunostaining of AIS marker ßIV-spectrin (red), α-actinin (green) and synpo (cyan) in the visual cortex of adult (P>55) wildtype and synpo KO mice. **(A)-(B)** In wildtype mice, synpo **(A)** and α-actinin **(B)** were co-expressed in AIS (arrows) and dendritic spines (arrowheads). **(C)** In KO mice, synpo signals were absent, α-actinin was not clustered in AIS or dendritic spines, but diffusely distributed within the cortex (asterisks). **(D)-(E)** Immunostaining of K$_V$2.1 channel (green), synpo (red) and ßIV-spectrin (blue) in wildtype and synpo KO mice. K$_V$2.1 was clustered at somatodendritic regions in both wildtype **(D)** and KO mice **(E)**. In wildtype mice, several AIS with high degree of K$_V$2.1 clustering were found (**D**, arrows). In synpo KO mice, K$_V$2.1 clustering at the AIS was reduced (**E**, arrows). **(D*)** Higher magnification of box (*) in **D**. To provide a better visualization of K$_V$2.1 expression, only ßIV-spectrin and K$_V$2.1 signals are shown. **(E*)** Higher magnification of box (*) in **E**. Arrows in **D*** and **E*** indicate K$_V$2.1 clustering at the AIS. Scale bars in C for A-c and in E for D-E = 15μm **(A-E)** and 5μm (**D** and **E**).

4.1.4 Summarizing results

In summary, synpo/CO undergoes an activity-dependent expression during development as indicated by increasing synpo/CO cluster numbers during eye-opening around P15 and increasing synpo/CO cluster sizes after visual deprivation. Furthermore, synpo/CO-expressing AIS represent a more mature subpopulation in V1 that show less dynamic length changes during CPs and are also shorter than the entire AIS population in V1. However, synpo/CO-expression does not completely prevent this population's ability to undergo activity-regulated plasticity as indicated by AIS lengthening after visual deprivation (Figure 21A). On the other hand, lack of synpo expression impairs AIS structural maturation during development, as indicated by the absence of phase 2 (sharp length decrease at P28) of AIS tri-phasic length maturation. Moreover, loss of visually-driven synaptic input induces AIS plasticity, which is impaired by lack of synpo as indicated by the absence of a typical AIS length increase after visual deprivation (Figure 21B).
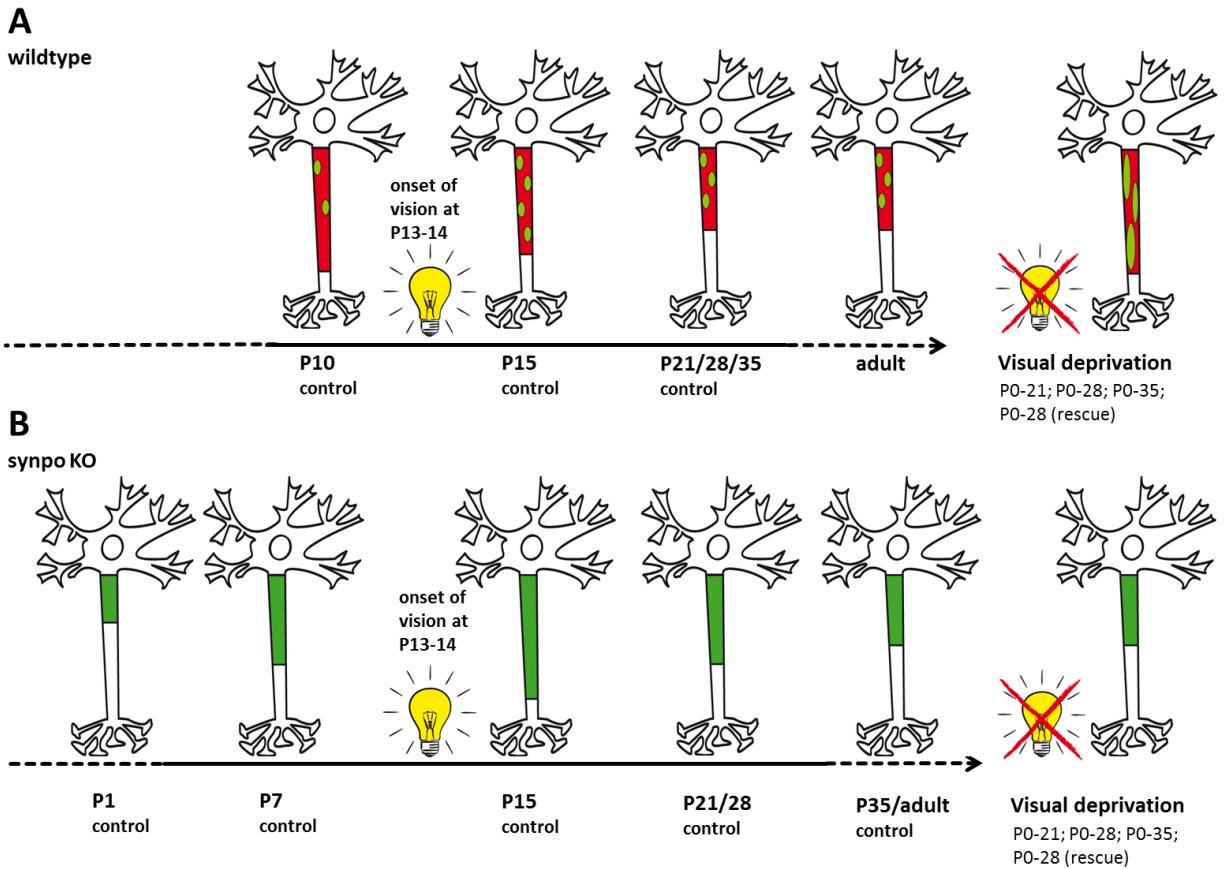
Figure 21: Summary of activity-dependent synpo/CO-expression and role of synpo/CO in AIS structural maturation during visual cortex development.
(A) In AIS of wildtype visual cortex neurons, synpo/CO expression begins at P10. During eye opening between P13-14 when first visual input occurs, synpo/CO cluster numbers increase and reach a maximum at P15. After eye-opening and during further development, synpo/CO expression stabilizes, persisting throughout adulthood. Visual deprivation for 3 weeks (P0-21), 4 weeks (P0-28) and 5 weeks (P0-35) leads to synpo/CO cluster size increase and prevents developmental AIS shortening and maturation. Both, AIS and synpo/CO remodeling were irreversible in P28 mice with renewed light exposure for 1 week until P35 (P0-28 (rescue)).
(B) AIS length maturation in visual cortex neurons of synpo KO mice. During the early postnatal period, AIS are short at P1 and steadily increase in length until a maximum is reached at P15. Eye-opening occurs between P13-14. After eye-opening, AIS length continuously decreases during further development and stabilize throughout adulthood. Visual deprivation for 3 weeks (P0-21) and 4 weeks (P0-28) leads to AIS length shortening. Dark-rearing for 5 weeks (P0-35) do not alter length of AIS when compared to controls. AIS shortening was irreversible in the P28 rescue condition.

4.2 Maturation of the CO in AIS during retinal development

4.2.1 Dynamic regulation of synpo and CO in retinal AIS during development

In the current thesis, the activity-dependent expression of synpo/CO in AIS of the murine visual cortex was demonstrated. The retina, as a part of the visual system, transmits visual information to the visual cortex. So far, the expression of synpo/CO in retinal AIS has not been studied. Accordingly, the existence of a CO-like organelle in retinal AIS remains elusive. In order to reveal a putative synpo/CO expression in retinal AIS, retinae of mice and rats were analyzed during embryonic and postnatal development. Specifically, the present thesis aimed to investigate synpo expression and CO maturation in AIS of RGCs during visual system development and after visual deprivation.

4.2.1.1 mRNA expression of synpo during development

To examine synpo expression in rodent retinae, mRNA expression of synpo was analyzed in retinal tissue from mice for different time-points during embryonic and postnatal development. Various primer pairs specific for synpo gene and for the house-keeping gene hypoxanthine phosphoribosyltransferase 1 (HPRT1) were designed and synthesized. Primer pair criteria met certain characteristics to ensure specific and reproducible mRNA quantification via qPCR (see 3.7 in Material and Methods). Designed primer pairs are described in Table 8 (Material and Methods). All primer pairs were tested in regard to T_m, DNA amplification and DNA reaction side products prior to using them for mRNA quantification by qPCR. Representative agarose gel electrophoresis results for tested primer pairs are shown in Figure 22. For qPCR application, primer pairs synpoAB#1 and HPRT1#1 were chosen on the basis of the following characteristics: First, synpoAB#1 specifically targets both transcript variants A and B of synpo gene, thus excluding possible age-dependent differences in mRNA expression as a result of distinct transcript variant expression, which may occur during development. Second, both synpoAB#1 primer pairs and HPRT1#1 primer pairs produced clear and robust DNA products of predicted size at the same T_m of 60°C (Figure 22B and F). Consequently, these primer pairs were capable of application to same qPCR conditions enabling both, normalization and quantification of synpo mRNA.
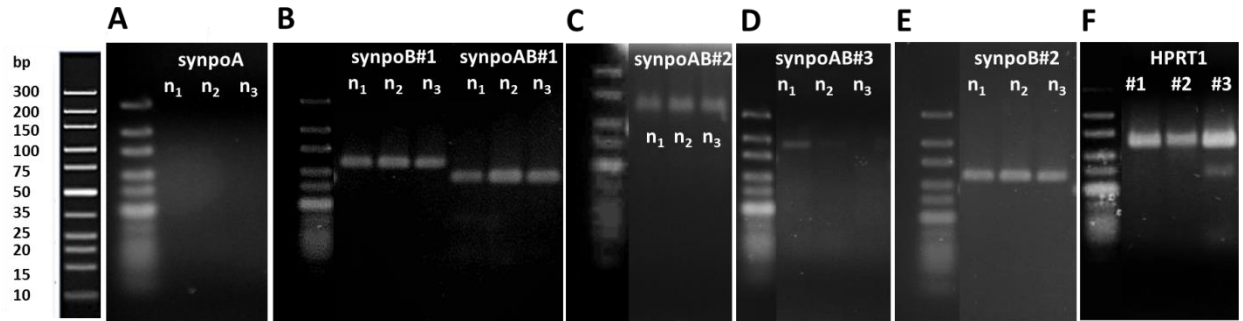
Figure 22: Validation of primer pairs used for qPCR.
Primer pairs targeting synpo and HPRT1 were tested in regard to T_m, DNA amplification and DNA reaction side products prior to using them for qPCR. DNA ladder is shown on the left. Three different cDNA samples produced from different murine tissues were used as templates for various synpo primer pairs: E14.5 brain (n_1), P1 retina (n_2) and P3 retina (n_3). For HPRT1 primer pairs, only E14.5 brain cDNA was used as template. Used primer pairs target genes of distinct transcript variants of synpo: A (synpoA), B (synpoB#1, synpoB#2; two different primer pairs), A and B (synpoAB#1, synpoAB#2, synpoAB#3; three different primer pairs). Three different primer pairs targeting the house-keeping gene HPRT1 were used (HPRT1#1, HPRT1#2, HPRT1#3). **(A)** PCR with synpoA primers did not result in amplified DNA product. Predicted DNA bands of 183bp were not detected. **(B)** PCR with synpoB#1 and synpoAB#1 primers resulted in amplified DNA products of 131bp and 86bp, respectively. **(C)** PCR with synpoAB#2 primers resulted in DNA bands with size of 149bp. **(D)** PCR with synpoAB#3 primers resulted in weak DNA bands with size of 185bp for E14.5 brain cDNA. **(E)** PCR with synpoB#2 primers resulted in amplified DNA products of 111bp. **(F)** PCR with three different HPRT1 primers resulted in PCR bands of 132bp (HPRT1#1), 132bp (HPRT1#2) and 129bp (HPRT1#3). HPRT1#3 primers produced an additional unspecific DNA product after PCR.

Relative synpo mRNA levels were quantified in retinal samples of mice for various time points ranging from E16.5 until P>55. Relative synpo mRNA amounts were normalized against HPRT1. Synpo mRNA levels at E16.5 were set to 1 and served as reference for older age groups. Individual values for qPCR measurement are found in Table 20 (appendix). As illustrated in Figure 23, relative mRNA levels of synpo varied during retinal development in mice. Shortly after birth at P1, mRNA levels increased to approximately 2.5 fold of mRNA levels at E16.5. During further postnatal development, synpo mRNA levels decreased again from P3 until P7 to similar levels observed at E16.5. During eye-opening at P14, synpo mRNA levels were again increased similar to those levels observed at P1. Afterwards, mRNA levels steadily decreased during further late postnatal development from P21 until P28. In adulthood (P>55), synpo mRNA reached lowest observed levels, which were significantly different to synpo mRNA levels at P1 and P14 (Table 41 in appendix). These results demonstrate a previously undescribed mRNA expression of synpo in the murine

retina. Furthermore, these data indicate a developmental-regulated expression of synpo mRNA in the murine retina.
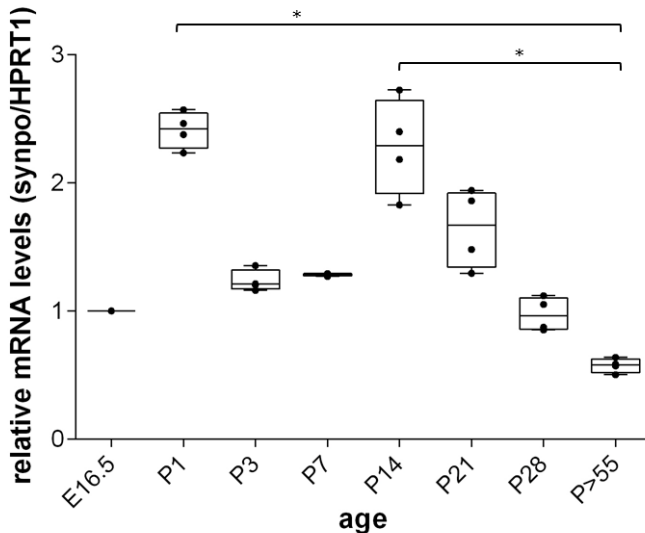
Figure 23: Relative synpo mRNA expression during retinal development of mice.
Normalized synpo mRNA levels at E16.5 were set to 1 serving as a reference for older age groups. Synpo mRNA levels increased after birth at P1 and decreased again throughout further postnatal development from P3 until P7. During eye-opening at P14, synpo mRNA levels re-increased to comparable levels observed at P1. During later postnatal development, synpo mRNA steadily decreased reaching lowest levels in adulthood (P>55). The sharp synpo mRNA increase was only significantly different to mRNA levels at adult stages (P>55). Boxes extend from the 25th to 75th percentiles. Horizontal lines inside the boxes are plotted at the median. Whisker bars indicate minimum and maximum data points. Dots represent individual data points. n=4 animals. Kruskal-Wallis one-way analysis with Dunn's post test. *p ≤ 0.05, S.E.M..

4.2.1.2 Synpo expression in retinal AIS during development

In addition to synpo mRNA, protein expression of synpo was also examined in the murine retina. First, Western blot was performed to analyze whether synpo protein is expressed in the adult mouse retina. It was found that, antibody-specific synpo protein bands of approximately 100kDa were detected in adult retinae (Figure 24). Synpo protein levels of adult (P>55) mouse retinae were considerably lower than those of P21 and adult (P>55) visual cortex. Synpo protein levels in retinae at younger ages (E16.5, P1, P3, P7, P14 and P21) were not detectable (Figure 24). It has to be noted that an additional weaker synpo protein band of approximately 70kDa emerged. These additional bands are most likely corresponding to degradation or denaturation of synpo protein. Furthermore, a strong

unspecific protein band >250kDa was additionally detected in adult visual cortex lysates, which might be related to the formation of protein multimers.
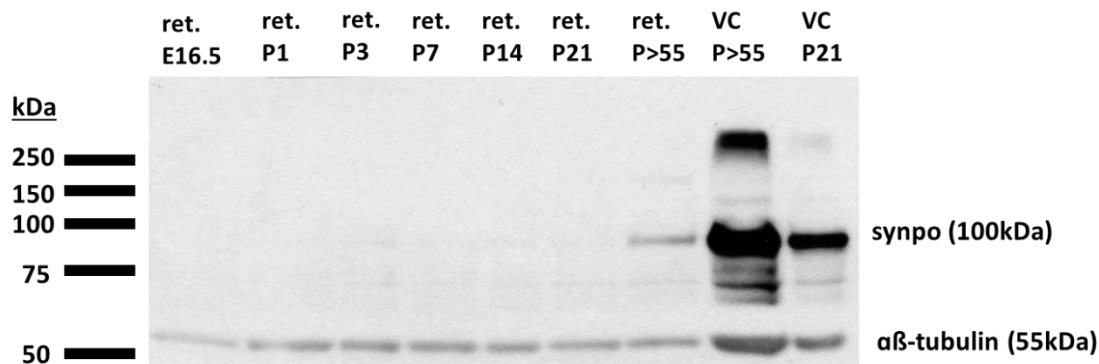
Figure 24: Detection of synpo protein during murine retinal development by Western blot.
Representative immunoblot bands of synpo in mouse retina (ret.) at various time points ranging from E16.5 until P>55. Synpo protein bands in Western blot indicate marginal synpo protein concentration in the adult (P>55) retina when compared to amounts in mouse visual cortex (VC) at P21 or in adulthood (P>55). Synpo proteins were not detected in retina protein lysates from mice of younger ages (E16.5-P21). 100kDa: Antibody-specific synpo lanes in SDS-PAGE/Western Blot. 55kDa: Antibody-specific αß-tubulin lanes in SDS-PAGE/Western Blot. n=2 animals.

To further investigate the expression and specific localization of synpo in the retina, immunofluorescence of sagittal retina sections was performed for various time points during murine retinal development (Figure 25). During embryonic development at E16.5, synpo was diffusely expressed within the ganglion cell layer (GCL) (Figure 25A). This diffuse expression was likely corresponding to migrating somata of RGCs and was largely maintained until P1 (Figure 25B). However, during further early postnatal development beginning at P7, synpo expression became more concentrated towards the nerve fiber layer (NFL) (Figure 25C). At later postnatal ages from P14 until P28, synpo immunosignals in somata of RGCs was even more pronounced (Figure 25D-F). In adulthood (P>55), synpo expression was additionally found in the NFL (Figure 25G-I), whereas co-expression of synpo with both AIS markers ankG and ßIV-spectrin could not be detected (Figure 25H and I). Since immunofluorescence quality is highly dependent on staining conditions, used standard immunofluorescence protocols were adapted. For this purpose, fixation time and concentrations were optimized. Instead of an overnight fixation of retinae in 1%PFA, a minimal postfix in 4%PFA for 10min was applied. This modification resulted in improved

immunofluorescence signals of synpo and AIS markers in sagittal retina sections due to a better signal-to-noise ratio and minimal unspecific background staining as well as reduced autofluorescence (Figure 26). Again, AIS were labeled using markers for ankG (Figure 26A-B) and ßIV-spectrin (Figure 26C-D). Single AIS were detectable that were located in the NFL and also in deeper retinal layers. The latter might represent AIS-like processes of axonless, spiking AII amacrine cells (Wu et al. 2011). Synpo positive immunosignals were found in AIS of RGCs in the NFL and also in deeper layers. Synpo expression was also observed in somata of RGCs. Furthermore, synpo signals were additionally found located at sites within the retina that were in a different optical plane than AIS and RGC somata (Figure 26C, arrowheads), which might be a result of unspecific immunofluorescence signals produced by the primary synpo antibody.
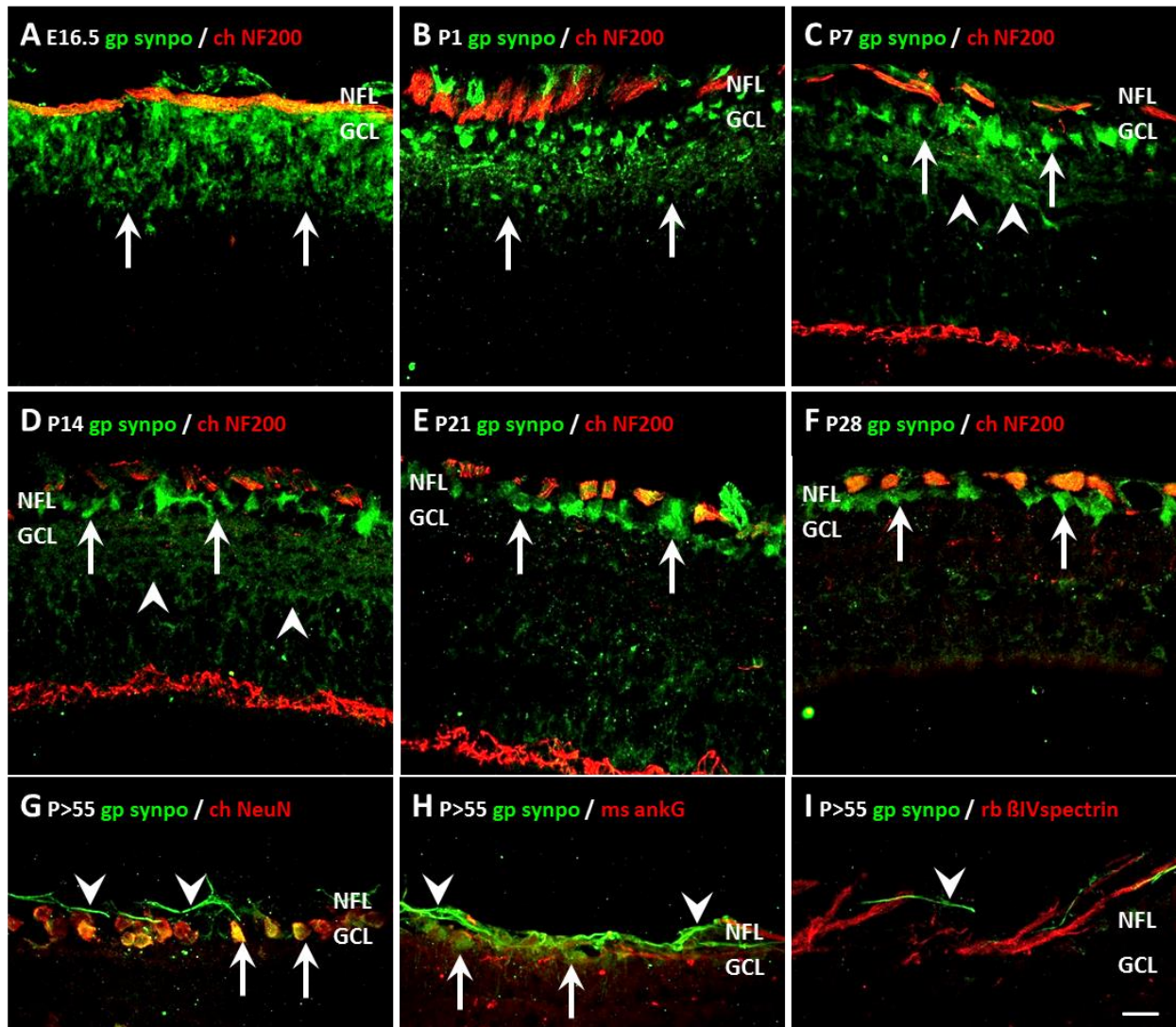
Figure 25: Expression of synpo in mouse sagittal retina sections during development.
(A)-(F) Immunofluorescence of retina sections during development using antibodies against synpo (green) and the 200kDa isoform of neurofilament (NF200, red). **(A)** At E16.5, synpo was initially and probably located to somata of RGCs in the GCL with a diffuse distribution within the GCL (arrows). This distribution was maintained until P1 **(B)**. During further retinal development from P7 **(C)** until P14 **(D)**, P21 **(E)** and P28 **(F)**, synpo localization changed and became more concentrated within the GCL (arrows). Weak synpo-positive signals were additionally present in deeper retinal layers (arrowheads). **(G)-(I)** Immunofluoresence of adult (P>55) mouse retina using antibodies against synpo (green), neuronal nuclei (NeuN, red), ankyrinG (ankG, red), and ßIV-spectrin (red). In adulthood (P>55), synpo was located in somata of RGCs in the GCL (**G**; arrows) and also appeared in the NFL (**G, H** and **I**; arrowheads). Synpo showed no co-localization with ankG **(H)** and ßIV-spectrin **(I)**. Scale bar in I for A-I=20μm.
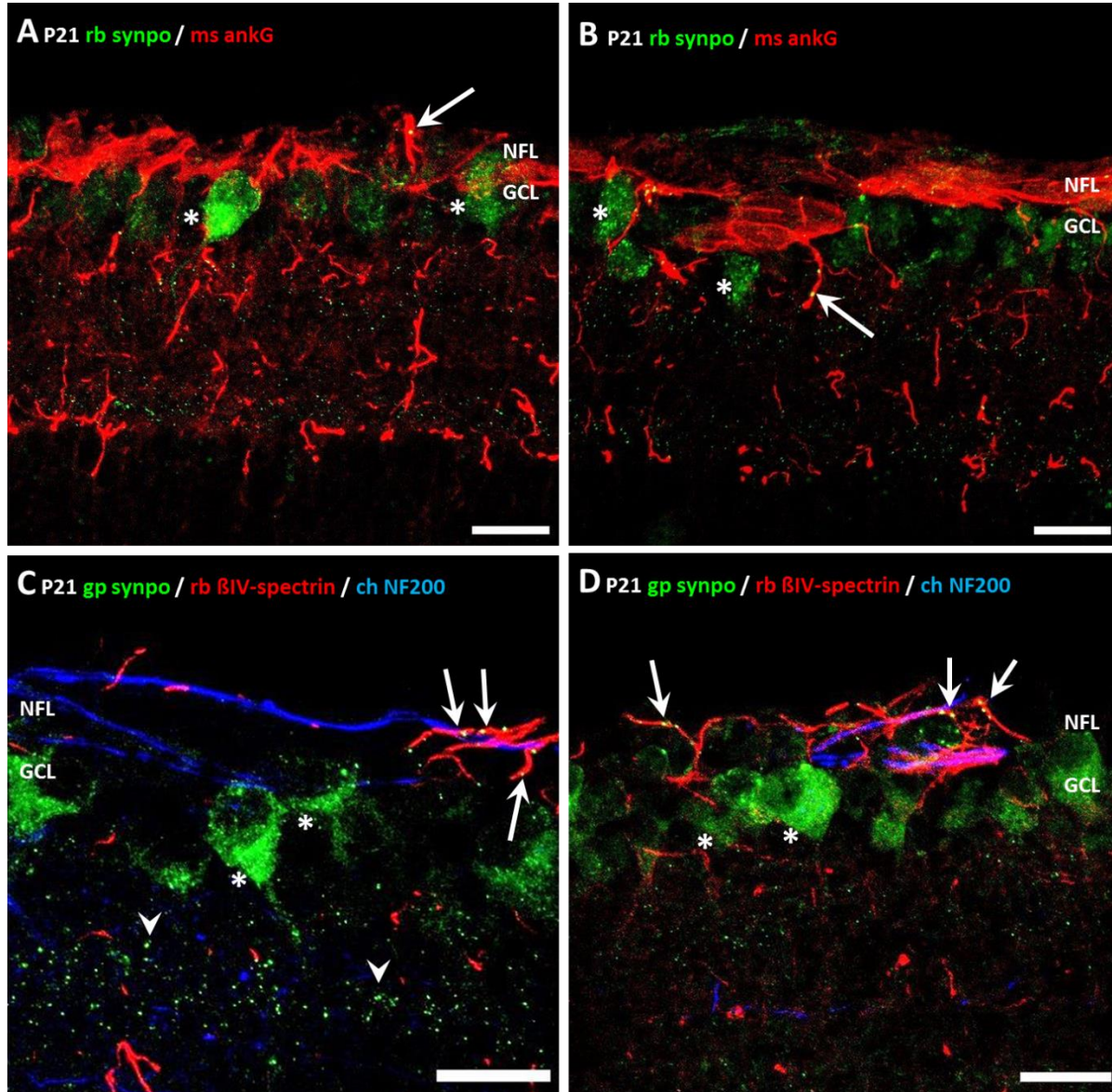
Figure 26: Detection of synpo in AIS in mouse sagittal retinal sections after optimizing immunofluorescence conditions.

(A)-(D) Immunofluorescence of retina sections from P21 mice using antibodies against synpo (green) and the AIS marker ankG (red) **(A, B)** as well as against synpo (green), ßIV-spectrin (red), and the 200kDa isoform of neurofilament (NF200, blue) **(C, D)**. After changing duration (10min instead of overnight) and concentration (4%PFA instead of 1%PFA) of fixation, detection of AIS and synpo-positive signals was improved. Several AIS in the NFL and also in deeper retinal layers could be detected that express synpo (**A-D**, arrows). Synpo immunostaining was also present in somata of RGCs in the GCL (**A-D**, asterisks). Additional punctate synpo signals were found at structures negative for AIS labeling (**C**, arrowheads). Scale bars=20µm.

The expression and localization of synpo in AIS of RGCs was further investigated in more detail by performing whole mount retinal immunostaining modified after previously approved protocols (Sawamiphak et al. 2010). First, it was tested whether using antibodies against ankG and ßIV-spectrin both enable the immunolabeling of AIS in a uniform manner (Figure 27). Both markers produced robust and reproducible AIS signals, and were therefore used for further developmental studies. Moreover, whole mount retinal staining enabled the detection of various synpo-expressing AIS in whole mount samples of adult mice and rats (Figure 28). Synpo expression was not observed in distal axons. Furthermore, synpo clusters in retinal AIS were also reminiscent of synpo/CO clusters found in AIS of pyramidal cells. Taken together, these data show a previously unknown synpo localization to AIS of the rodent retina.
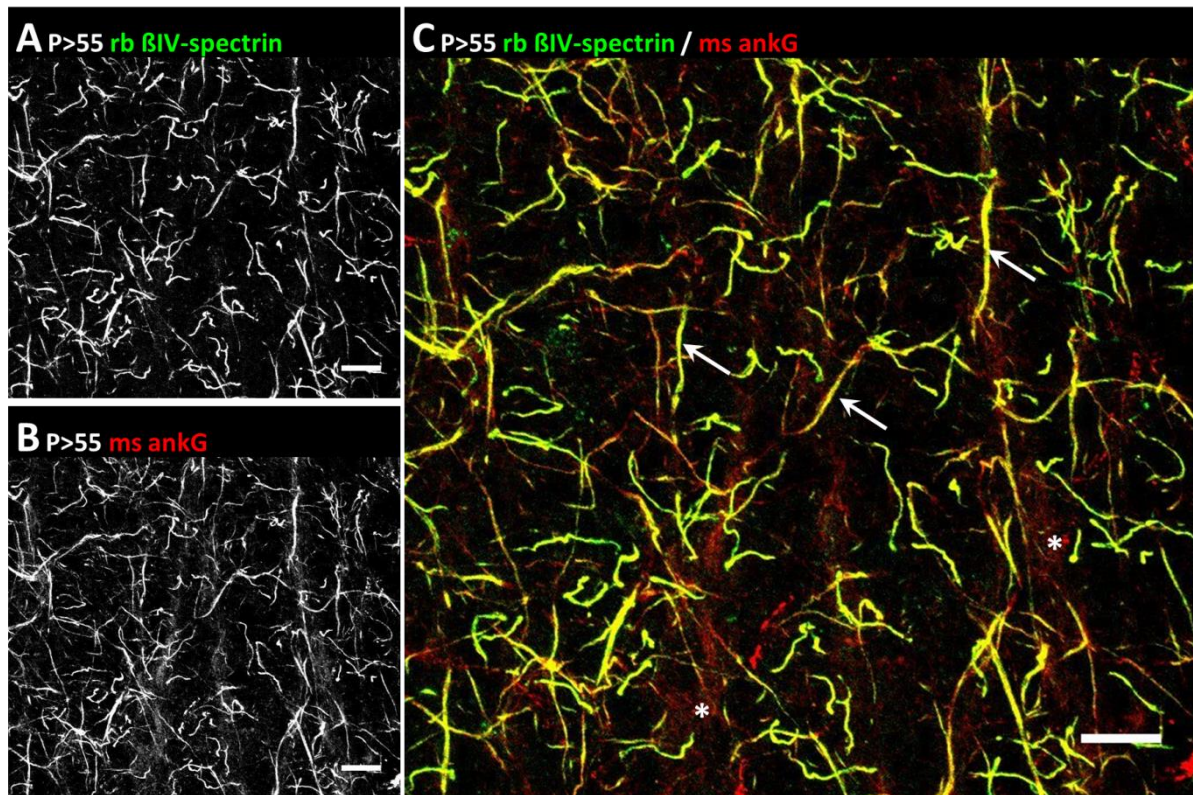
Figure 27: Immunolabeling of AIS of RGCs in whole mount retinae by different AIS markers.
(A)-(C) Immunofluorescence of whole mount retina from adult (P>55) mice using antibodies against ßIV-spectrin (green) and ankG (red). Immunosignals for ßIV-spectrin **(A)** and ankG **(B)** uniformly labeled AIS of RGCs in whole mount retina tissue (arrows). AnkG immunostaining was additionally detected in retinal nerve fibers forming the optic nerve (**B, C**; asterisks). ßIV-spectrin and ankG fluorescence were merged in **C**. Scale bars=15µm.
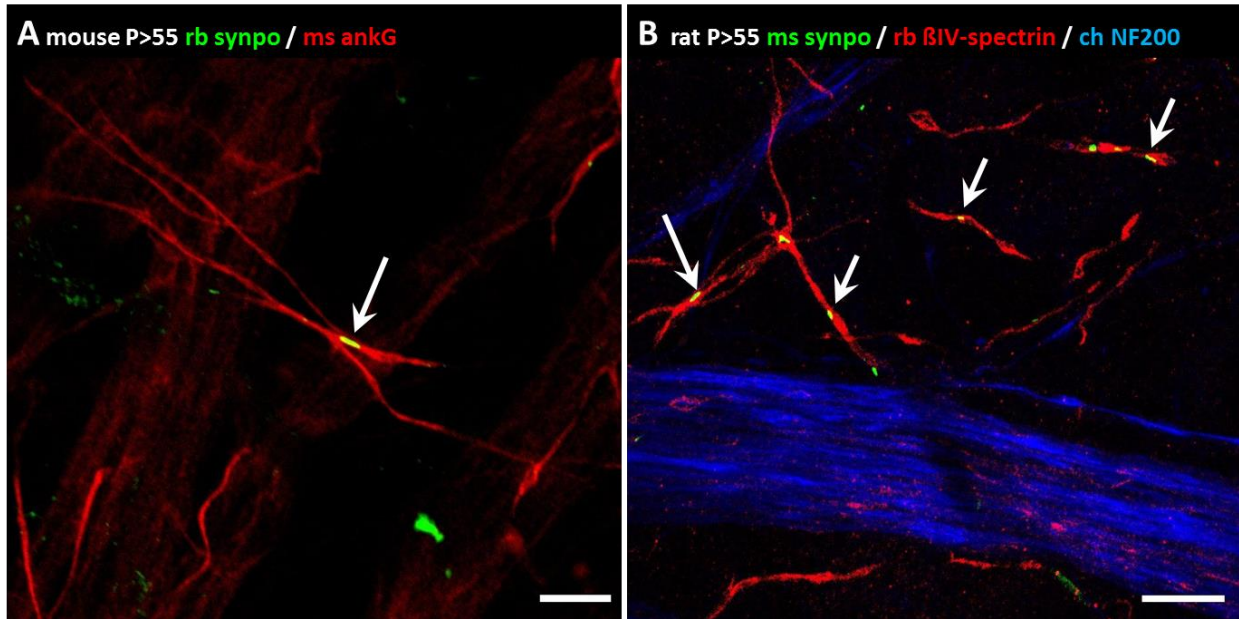
Figure 28: Synpo expression in AIS revealed by retina whole mount staining in adult mice and rats.
(A) Immunofluorescence of whole mount retina from adult (P>55) mice using antibodies against synpo (green) and ankG (red). **(B)** Immunofluorescence of whole mount retinae from adult (P>55) rats using antibodies against synpo (green), ßIV-spectrin (red), and the 200kDa isoform of neurofilament (NF200, blue). Synpo expression was found in AIS of RGCs in both, adult mice and rats (**A, B**; arrows). Scale bars=10μm.

4.2.1.3   Activity-regulated expression of synpo in retinal AIS during development

The current thesis shows that synpo/CO expression is regulated in an activity-dependent manner during visual cortex development (see section: 4.1.1.4), but so far, the developmental and putative activity-regulated expression pattern of synpo/CO in the retina is not known. Therefore, it was further aimed at analyzing synpo expression in RGCs during retinal development. Whole mount retinal staining was applied to label synpo, the AIS markers ankG or ßIV-spectrin as well as the neurofilament marker NF200 for different time points during development (Figure 29). It was observed that RGCs at early postnatal ages (P3) do not express synpo in their respective AIS (Figure 29A). Onset of synpo expression in retinal AIS was found at P8 (Figure 29B). During further postnatal development from P10 until P35, expression of synpo in retinal AIS was maintained (Figure 29C-F). However, it appeared that a higher percentage of synpo-expressing AIS were present at late postnatal stages in retinae from mice older than P15. This time-frame coincide with the eye-opening in mice of the analyzed C57BL6 strain, which occurs around P13-14. It could therefore be

assumed that synpo expression might also be activity-regulated in AIS during retinal development, similar to the observations for visual cortex development as outlined above. For this purpose, the expression of synpo was quantified during murine retinal development from P10 until P>55 (Figure 30). Due to the often observed branching of individual AIS of RGCs as well as their and close localization to each other, it was impossible to quantify for length or percentage for synpo-expressing AIS (Figure 27). However, percentage of synpo-expressing AIS was qualitatively estimated to approximately a maximum of 10% during retinal development. For quantitative studies, expression of synpo in AIS was analyzed in regard to synpo cluster number and sizes. For this purpose, single isolated AIS were selected. Synpo expression in AIS of RGCs first emerged at P8 (Figure 29), however, number of synpo-expressing AIS in retinae from mice of this age was low. Consequently, developmental synpo expression in retinal AIS was at first quantified at P10 since a higher number of synpo-expressing AIS was found at this time point. As illustrated in Figure 30, number of synpo clusters per AIS was 1.61±0.05 at P10, (Figure 30A, Table 19 in appendix), which was similar to synpo cluster numbers in AIS of visual cortex AIS at P10 (1.62±0.05 for layer II/III, 1.84±0.04 for layer V; Figure 10A and B, Table 16 in appendix). In contrast to the observed dynamic changes of synpo cluster number in AIS during visual cortex development (see section 4.1.1.3), number of synpo clusters in AIS during retinal development stayed stable and did not display significant changes between the different time points (Figure 30A and B; Table 40 in appendix). Size of synpo clusters was 0.53±0.01μm^2 at P10 (Figure 30C, Table 19 in appendix). In comparison, synpo cluster sizes in visual cortex AIS were 0.49±0.02μm^2 in layer II/III and 0.46±0.02μm^2 in layer V (Figure 10D and E, Table 16 in appendix). Synpo cluster sizes in retinal AIS steadily increased during further postnatal development reaching highest values at P21. Significant changes were only observed between P21 and P28 (Figure 30C and D, Table 39 in appendix). Synpo cluster sizes significantly decreased at this time point from 0.59±0.01μm^2 at P21 to 0.50±0.2μm^2 at P28 (Table 19 in appendix). Afterwards, cluster sizes re-increased throughout further development at P35 and adulthood (P>55), reaching values comparable to those observed at P10 (Figure 30C and D, Table 19 in appendix). Furthermore, sizes of synpo/CO clusters were significantly correlated to synpo/CO cluster numbers per AIS (Table 42 in appendix). Using a model for linear multiple regression analysis, it was found

that age of the animal did not contribute in a significant manner to synpo cluster sizes or cluster numbers in retinal AIS (Table 43 in appendix), although it was observed that synpo cluster sizes significantly decreased during development from P21 to P28 (Figure 30, Table 39 in appendix).
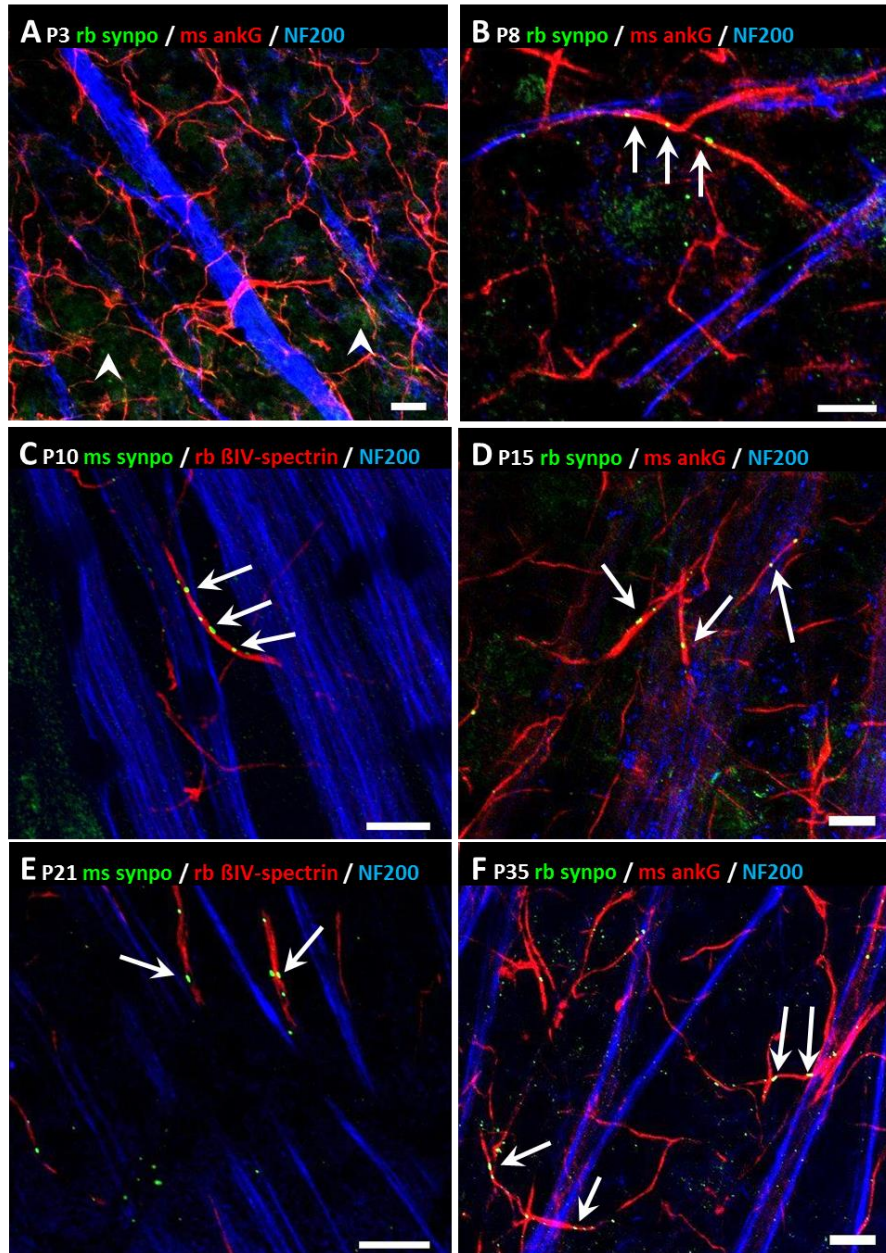
Figure 29: Synpo expression in AIS in whole mount mouse retinae during development.
(A)-(F) Immunofluorescence of whole mount retinae during development using antibodies against synpo (green), ankG or ßIV-spectrin (red), and the 200kDa isoform of neurofilament (NF200, blue). **(A)** Synpo expression at early postnatal stages (P3) was not detected in AIS of RGCs. Only weak signals were found in deeper layers, which likely belonged to somata of RGCs (arrowheads). Synpo expression in AIS of RGCs started at P8 (arrows, **B**) and was maintained throughout further postnatal development at P10 (arrows, **C**), P14 (arrows, **D**), P21 (arrows, **E**), and P35 (arrows, **F**). Scale bars=10µm.
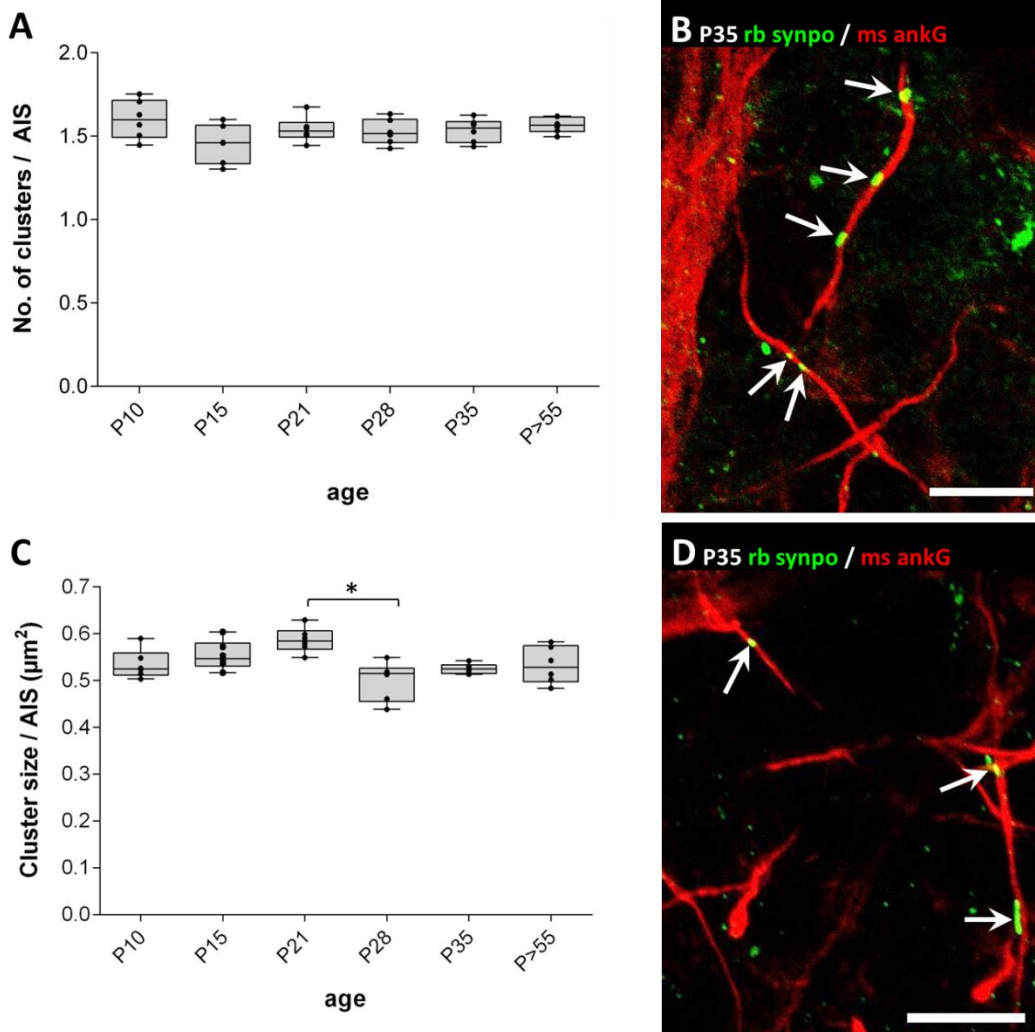
Figure 30: Changes of synpo cluster number and size in AIS during retinal development.
(A) Synpo expression in AIS of RGCs was first observed at P8 and was quantified for various time-points during retinal development starting at P10. Number of synpo clusters in retinal AIS showed no significant changes during development. **(B)** Immunostaining of synpo (green) and ankG (red) in retinal AIS of P35 mice. Representative image of synpo expression in AIS indicating varying numbers of synpo clusters per AIS (arrows). **(C)** Synpo cluster sizes in AIS of RGCs significantly changed during retinal development. From P10 until P21, cluster sizes increased slightly. Between P21 and P28, synpo clusters significantly decreased in their sizes. During further development beginning at P35, synpo cluster sizes stayed stable persisting into adulthood (P>55). Boxes extend from the 25th to 75th percentiles. Horizontal lines inside the boxes are plotted at the median. Whisker bars indicate minimum and maximum data points. Dots represent individual data points. n=6 animals, a minimum of 100 AIS per age and animal. Kruskal-Wallis one-way analysis with Dunn's post test. *p≤0.05, S.E.M.. **(D)** Representative image of synpo expression (green) in retinal AIS (ankG, red), indicating distinct sizes of individual synpo clusters per AIS (arrows)**.** Scale bar=10μm.

4.2.1.4 Activity-dependent expression of synpo in retinal AIS after visual deprivation

The observed onset of synpo expression in AIS of RGCs at P8 coincides with the onset of first visual experience (Krug et al. 2001). Furthermore, the dynamic cluster size changes of synpo in retinal AIS between P21 and P28 accompanies the disappearance of spontaneous activity in the retina of C57BL/6 mice (Demas et al. 2003). Synpo expression was also found to be regulated in an activity-dependent manner in AIS in neurons of the developing visual cortex (Figure 10 and 11). Altogether, these findings led to the assumption that synpo might also be expressed in an activity-dependent manner in AIS of RGCs. To further address this question, retinal AIS of P28 dark-reared mice were analyzed regarding their synpo expression (Figure 31). Visually deprived mice showed a significant increase in the average number of synpo clusters per AIS when compared to P28 control mice (Figure 31A and B; Table 40 in appendix). Cluster numbers increased from 1.53±0.03 to 1.71±0.04 per AIS in average (Table 19). Linear multiple regression analysis demonstrated that synpo cluster numbers in retinal AIS are significantly related to the applied condition (control/dark) (Table 43 in appendix).

Moreover, visual deprivation for four weeks led to a significant increase in synpo cluster size from $0.50\pm0.02\mu m^2$ in P28 controls to $0.58\pm0.01\mu m^2$ in P28 dark-reared animals (Figure 31C and D, Table 19 and 40 in appendix). Using a model for linear multiple regression analysis, it was found that the applied condition (control/dark) contributes in a significant manner to synpo cluster sizes in retinal AIS (Table 43 in appendix).

In summary, synpo clusters in AIS of RGCs show significant plasticity in size during development between P21 and P28 as well as after dark-rearing for four weeks at P28. Number of synpo clusters, however, was static during development, yet showed a significant increase after visual deprivation.
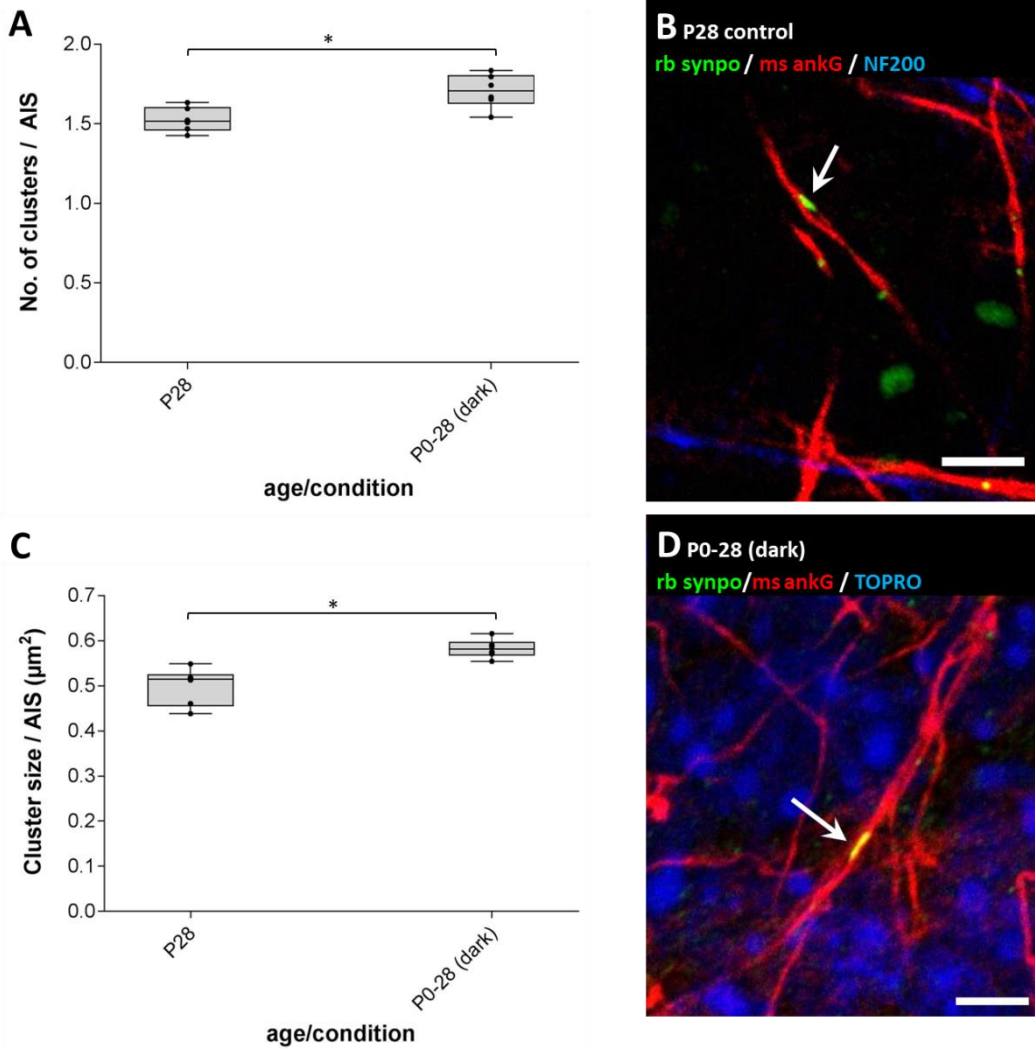
Figure 31: Changes of synpo cluster number and size in retinal AIS after visual deprivation.
(A) Dark-rearing of mice until P28 resulted in significant increase in number of synpo clusters in AIS of RGCs.
(**B**) Synpo expression in retinal AIS in P28 control mice, as indicated by immunostaining of synpo (green), ankG (red), and the 200kDa isoform of neurofilament (NF200, blue). **(C)** Visual deprivation for 4 weeks (P0-28 (dark)) resulted in significant activity-dependent increases in synpo cluster sizes in AIS of retinal neurons. Boxes extend from the 25th to 75th percentiles. Horizontal lines inside the boxes are plotted at the median. Whisker bars indicate minimum and maximum data points. Dots represent individual data points. n=6 animals, a minimum of 100 AIS per age, animal and layer. Wilcoxon rank-sum test. *p≤0.05, S.E.M.. **(D)** Synpo expression (green) in AIS (ankG, red) of RGCs in P28 dark-reared mice showed an increase in synpo cluster sizes. TOPRO (blue) labeled cell nuclei of RGCs. Scale bars=5μm.

4.2.2 Characterization of synpo and CO in retinal ganglion cell AIS

The current thesis provides the first evidence that besides neurons of the visual cortex, also retinal neurons express synpo and a putative CO in their AIS. Moreover, synpo expression in retinal AIS is regulated in an activity-dependent manner during development as indicated by a dynamic remodeling of synpo clusters in AIS after visual deprivation. So far, it is unknown whether AIS of RGCs also contain a CO. To test whether synpo might be associated with COs in AIS of RGCs, retinae of transgenic synpo-overexpressing mice were analyzed. Furthermore, whole mount staining of rat retinae was performed to investigate the co-expression of synpo with distinct CO-associated proteins. In addition, super resolution microscopy was applied to resolve the localization of synpo in AIS of RGCs.

4.2.2.1 Synpo/CO expression in transgenic synpo-overexpressing mice

A previous study has shown that lack of synpo expression leads to an absence of the CO in hippocampal neurons (Bas Orth et al. 2007). Furthermore, overexpression of synpo tagged to GFP or CFP results in strongly elongated synpo signals in the AIS extending into large areas of the AIS and soma (personal communication; Deller group, Clinical Neuroanatomy, Goethe-University Frankfurt, Germany). Synpo overexpression also markedly increases CO stack size as revealed by electron microscopy (unpublished data; Deller group, Clinical Neuroanatomy, Goethe-University Frankfurt, Germany). These data indicate that synpo is an essential component of the CO and that the degree of synpo expression modulates the CO at the ultrastructural level. To test whether synpo overexpression also modifies the expression pattern of synpo in AIS of RGCs, transgenic mice overexpressing synpo were processed. Five different transcript variants of transgenic synpo were investigated: GFP-synpo A, GFP-synpo E, GFP-synpo F, CFP-synpo D and CFP-synpo G (Figure 32; also see Section 3.1 in Material and Methods). Neither endogenous synpo nor fluorescent proteins GFP and CFP were labeled by antibodies; only original GFP-synpo and CFP-synpo fluorescence signals were examined. Mice of all transcript variants showed pronounced synpo-GFP or synpo-CFP signals in AIS of retinal neurons (Figure 32A-E, arrows). The expression of GFP-tagged synpo was higher than that of CFP-tagged synpo as indicated by GFP signals that were strongly elongated and also exhibiting artifacts. Furthermore,

expression of synpo-GFP was highly different to the endogenous synpo expression pattern in wildtype mice. Generally, the expression of transgenic synpo within individual AIS was highly variable. Various AIS contained strongly elongated synpo-clusters, whereas other AIS expressed various smaller synpo clusters similar to those in wildtype animals (Figure 28). Furthermore, a number of CFP and GFP signals were found located to structures within the retina that were not positive for AIS labeling (Figure 32A-E, arrowheads). These signals might be related to the previously observed synpo positive immunosignals in somata of RGCs (Figure 25). Taken together, these results lead to the assumption that synpo could also be an essential part of the CO in AIS of the retina, and that synpo expression might modify CO size and structure in AIS of RGCs. However, the CO structure and size can only be analyzed on the ultrastructural level applying electron microscopy, which will be of interest for future studies about synpo/CO expression in retinal AIS. Nevertheless, using fluorescent protein-tagged synpo-overexpressing mice will be an advantageous tool to further examine the dynamics of synpo/CO in living cell cultures or organotypic slice cultures prepared from retinae and visual cortices.
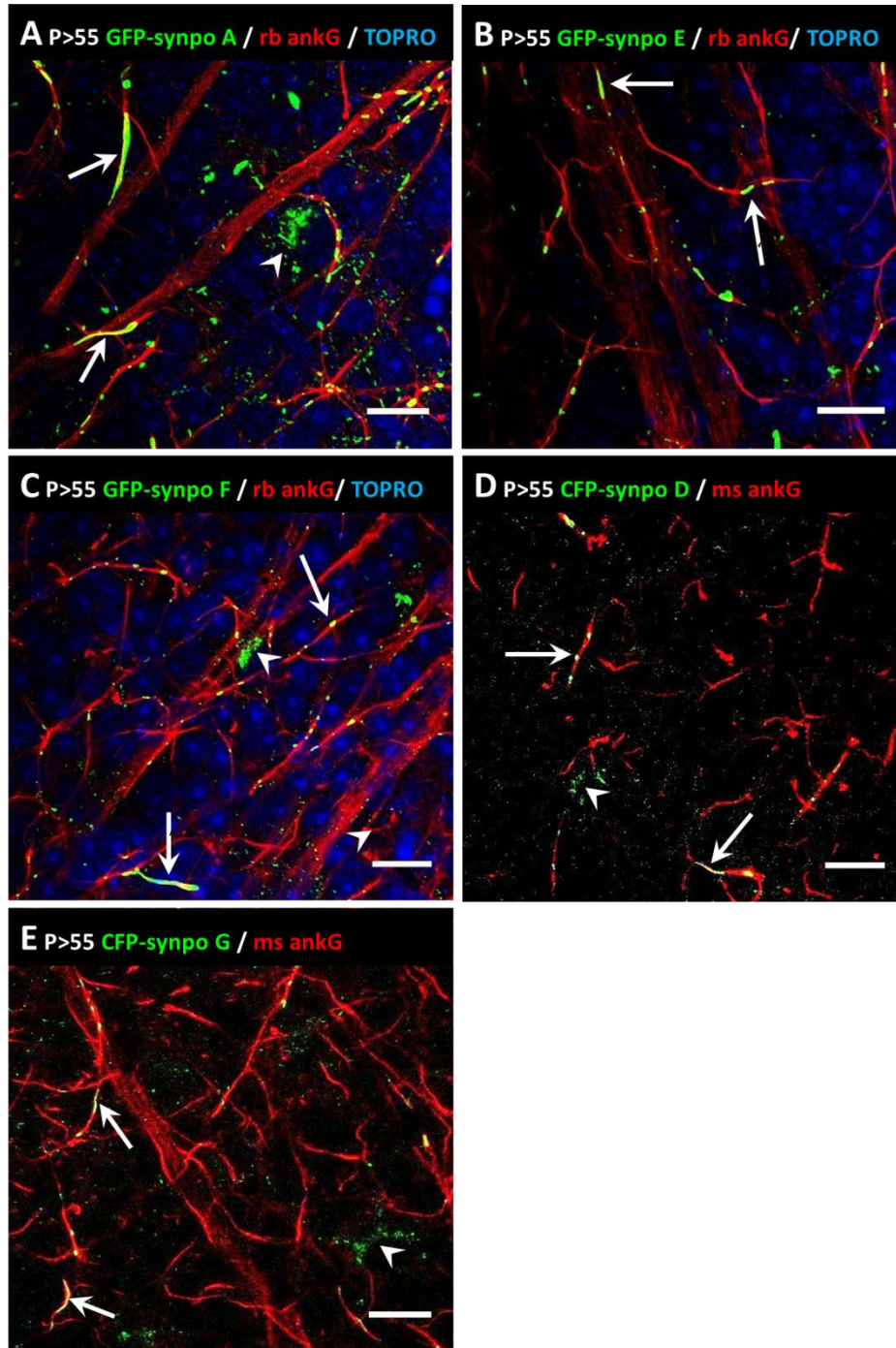
Figure 32: Expression of GFP- and CFP-tagged synpo in AIS of transgenic synpo-overexpressing mice.
(A)-(C) Confocal scans of immunostained whole mount retina of adult (P>55) transgenic synpo GFP- or -CFP-tagged overexpressing mice using antibodies against the AIS marker ankG (red). Cell nuclei were stained with TOPRO (blue). Three transcript variants of GFP-tagged synpo were expressed in mice: GFP-synpo A **(A)**, GFP-synpo F **(B)** and GFP-synpo E **(C).** Two transcript variants of synpo CFP-tagged overexpressing mice were used: CFP-synpo D **(D)** and CFP-synpo G **(E)**. All GFP and CFP variants showed strong transgenic synpo expression in retinal AIS (arrows) as well as within the retina (arrowheads). Expression of GFP-tagged synpo **(A-C)** was overall stronger than expression of CFP-tagged synpo **(D-E)**. Scale bars=15µm.

4.2.2.2 Co-expression of synpo with Ca^{2+}-dependent and CO-associated proteins in retinal AIS

To investigate the putative association with synpo and the CO in retinal AIS, whole mount staining of rat retinae was performed using antibodies against distinct Ca^{2+}-dependent proteins, which were previously found to be co-expressed with synpo/CO in AIS of cortical and hippocampal neurons (Benedeczky et al. 1994; Sanchez-Ponce et al. 2011; King et al. 2014; Anton-Fernandez et al. 2015). Antibodies against the CO-associated proteins SERCA, ryanodine receptor (RyR) and IP$_3$ receptor (IP$_3$R) were used in combination with antibodies against synpo and the AIS marker ßIV-spectrin. It was found that synpo is indeed co-expressed with all tested CO-associated proteins in AIS of RGCs in adult rats (Figure 33, 34 and 35). These results suggest that AIS of RGCs express synpo-associated COs that contain proteins involved in local Ca^{2+}-signalling. Thus, the function of COs in retinal AIS might comply with the Ca^{2+}-sequestering and storing function of the CO previously postulated for AIS of principal cortical neurons (Maggio and Vlachos 2014).
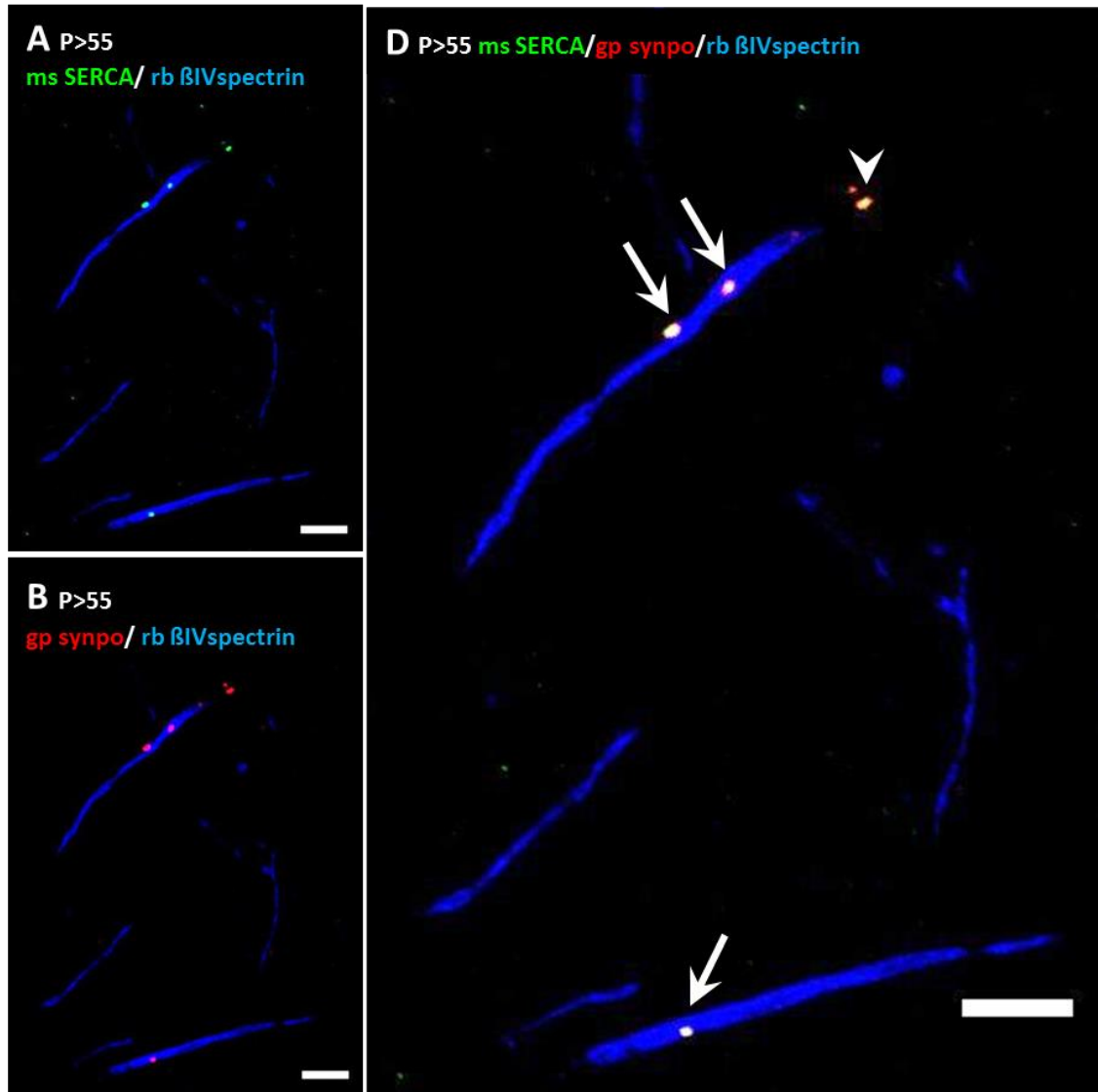
Figure 33: Co-expression of synpo and SERCA type 2 ATPase in retinal AIS of rats.
(A)-(D) Immunofluorescence of whole mount retina of adult (P>55) rats using antibodies against SERCA type2 ATPase (SERCA, green), synpo (red) and the AIS marker ßIV-spectrin (blue). **(A)** Immunofluorescence signals for SERCA. **(C)** Immunofluorescence signals for synpo. **(D)** Merged image of SERCA, synpo and ßIV-spectrin immunosignals. Synpo and SERCA were co-expressed in retinal AIS of adult rats (arrows). A cluster positive for SERCA and synpo that is located outside of the imaged layer was detected as well. Scale bars=5µm.
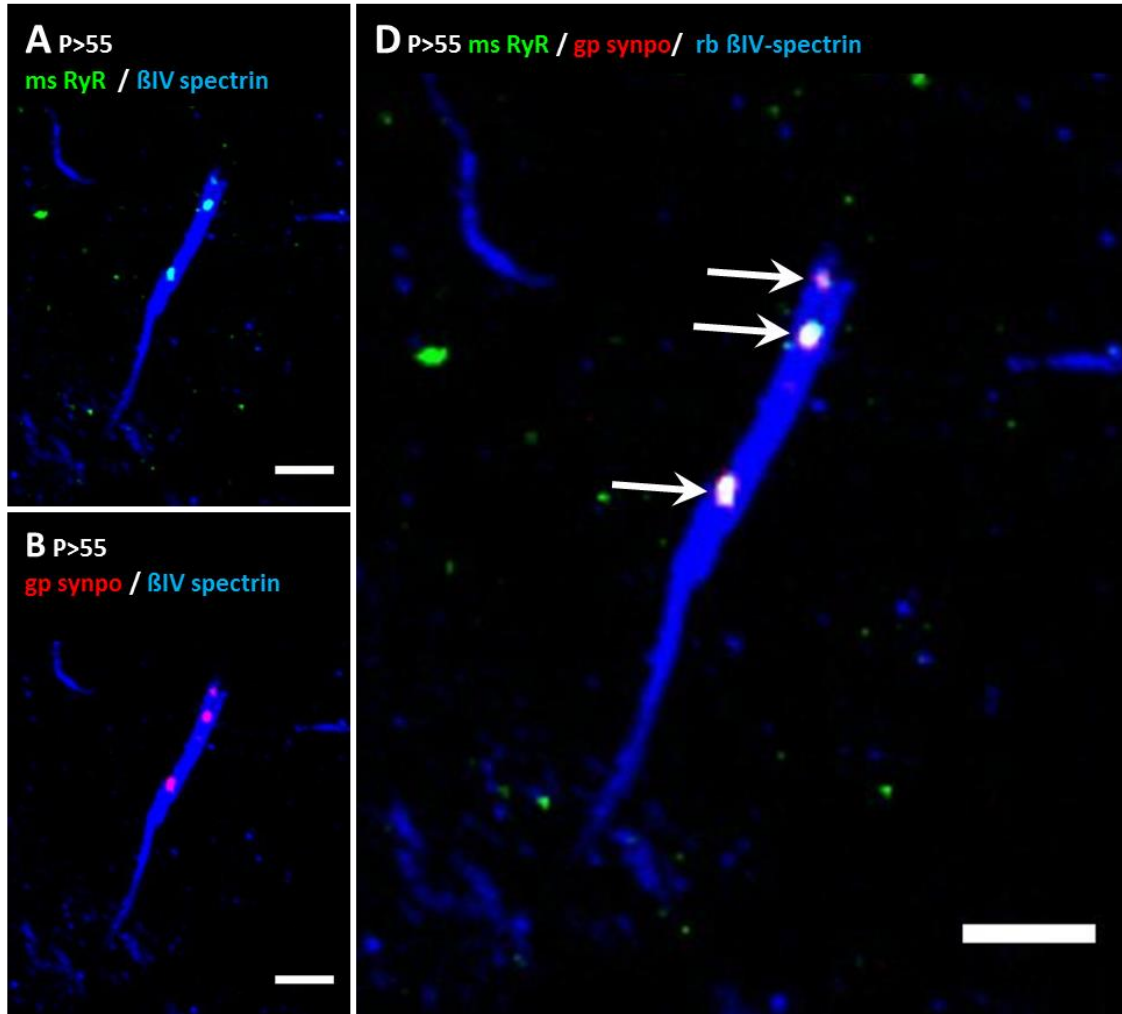
Figure 34: Co-expression of synpo and RyR in retinal AIS of rats.
(A)-(D) Immunofluorescence of whole mount retina of adult rats (P>55) using antibodies against ryanodine receptor (RyR, green), synpo (red) and the AIS marker ßIV-spectrin (blue). **(A)** Immunofluorescence signals for RyR. **(C)** Immunofluorescence signals for synpo. **(D)** Merged image of RyR, synpo and ßIV-spectrin immunosignals. Synpo and RyR were co-expressed in retinal AIS of adult rats (arrows). Scale bars=5µm.
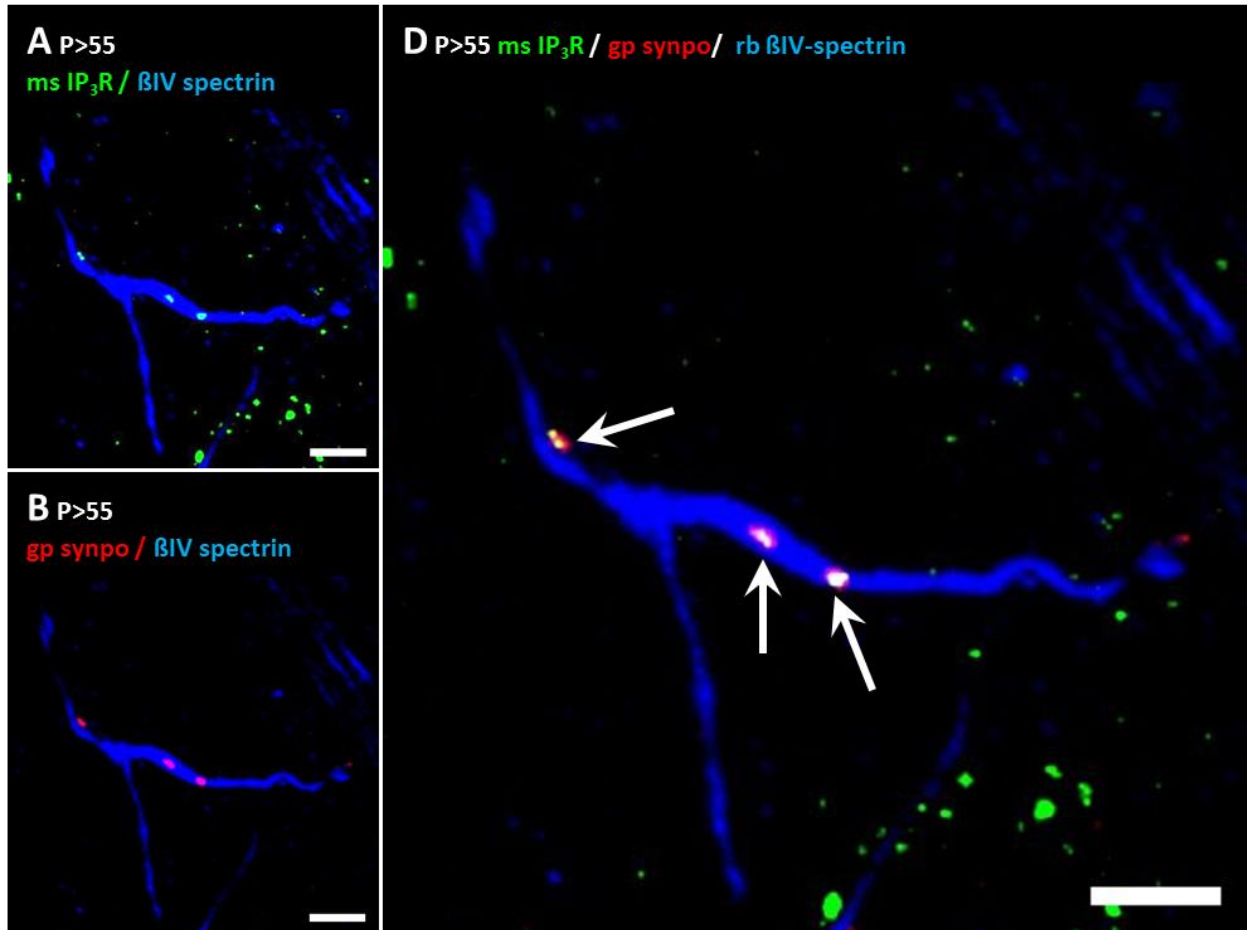
Figure 35: Co-expression of synpo and IP₃ receptor in retinal AIS of rats.
(A)-(D) Immunofluorescence of whole mount retina of adult rats (P>55) using antibodies against IP₃ receptor (IP₃R, green), synpo (red) and the AIS marker ßIV-spectrin (blue). **(A)** Immunofluorescence signals for IP₃R. **(C)** Immunofluorescence signals for synpo. **(D)** Merged image of IP₃R, synpo and ßIV-spectrin positive immunosignals. Synpo and IP₃R were co-expressed in retinal AIS of adult rats (arrows). Scale bars=5µm.

4.2.2.3 Super resolution microscopy of synpo/CO in AIS of RGCs

A recent study in cortical and hippocampal neurons has shown that synpo is located at gaps within the AIS where ankG expression is deficient (King et al. 2014). These gaps in the AIS scaffold are thought to be structural domains where GABAergic synapses of ChC contact the AIS and where K_V channels and COs are enriched (Figure 5 in Introduction; King et al. 2014). To investigate whether synpo localization in retinal AIS is also associated with these gaps, super resolution microscopy of whole mount immunostained retinae was applied. Structured illumination microscopy (SIM) was used to gain a two-fold improved resolution of 3D-scans (Figure 36- 40). Single molecule localization microscopy (SMLM) was applied to

resolve synpo and AIS structure within the 25nm range (Figure 41-43). The AIS scaffold was labeled by using antibodies against ankG and ßIV-spectrin. Since high immunofluorescence signals are required for applying super resolution microscopy, only ßIV-spectrin labeling was used, which was enhanced as compared to ankG labeling. As illustrated in Figure 36-40, applying SIM imaging of retinal AIS expressing synpo enabled the visualization of putative gaps in the ßIV-spectrin scaffold where synpo clusters were located. Hence, a two-fold improved microscopy resolution is sufficient to detect the above described structures within the scaffold in AIS of RGCs *in vivo*. Applying SMLM indeed resulted in the detection of synpo localization to gaps in the AIS scaffold (Figure 41-43A-C). Moreover, resolution was strongly enhanced, allowing the generation of 3D fluorescence histograms for synpo and AIS immunolabeling (Figure 41-43D-F). 3D visualization of both synpo and ßIV-spectrin immunosignals at a super-resolved level revealed that the majority of synpo immunofluorescence of the imaged cluster along the AIS was located inside a gap of the ßIV-spectrin immunosignal. Accordingly, synpo and ßIV-spectrin signals seemed to exclude each other and therefore contributing to the emergence of structural gap domains, previously observed by applying SIM in principal neurons *in vivo* (King et al. 2014). An additional observation by applying super resolution microscopy was a periodic distribution of the AIS scaffolding protein ßIV-spectrin extending from the axonal surface towards the inner cytoskeleton within the AIS (Figure 41-43C).

Taken together, the detection of synpo localization to gaps in the AIS scaffold (Figure 36-43) further indicates the similarity of synpo expression in AIS of RGCs to that in AIS of pyramidal cells. This supposes that retinal AIS contain a CO and that these COs are associated to synpo.
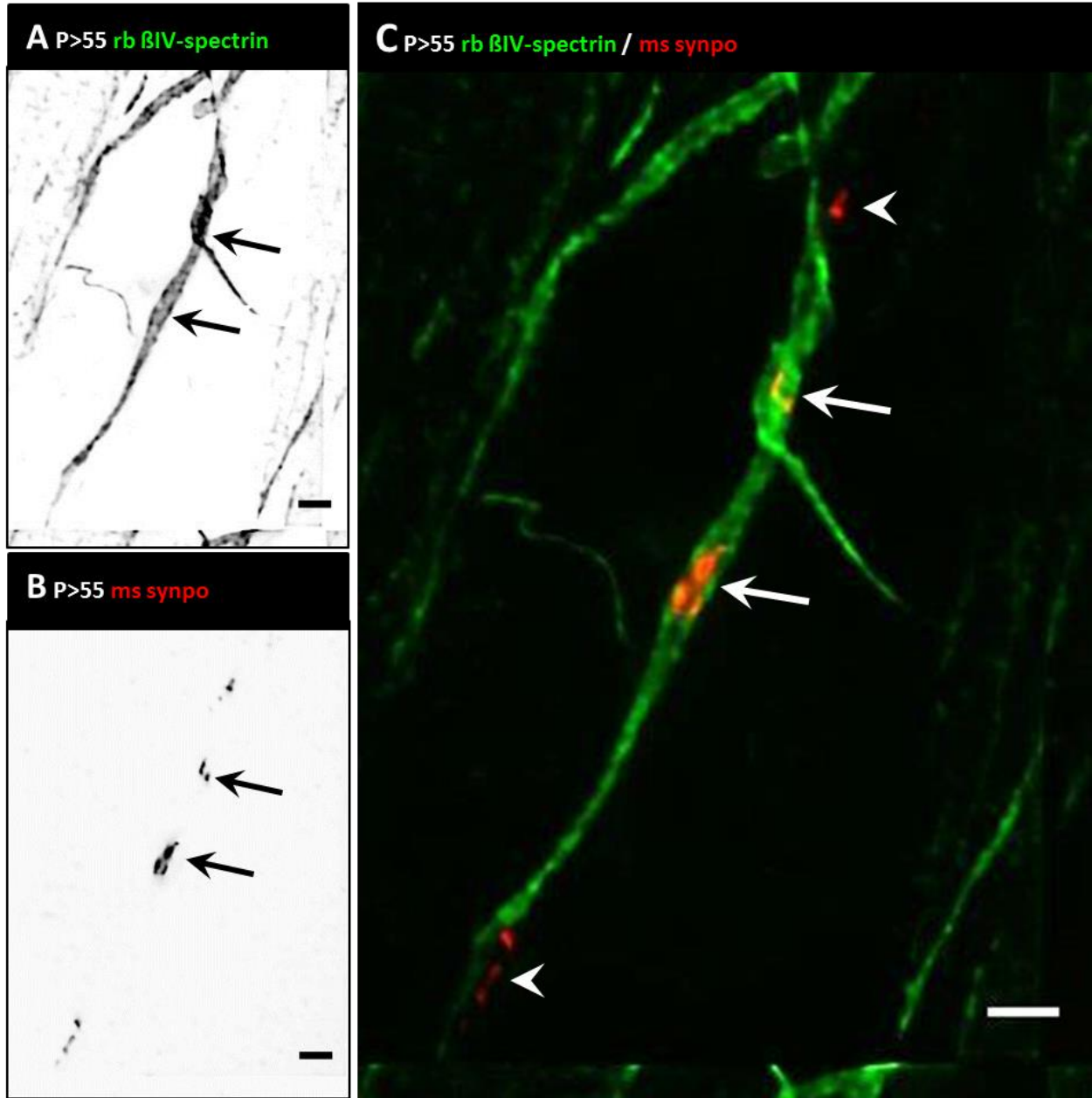
Figure 36: Structured illumination microscopy (SIM) scan of synpo-expressing AIS in rat retina.
(A)-(C) 3D-SIM image of immunolabeled whole mount retina of adult rats (P>55) using antibodies against
ßIV-spectrin (green) and synpo (red). **(A)** 3D-SIM image of AIS marker ßIV-spectrin. **(B)** 3D-SIM image of
synpo (red) in AIS. **(D)** Merged 3D-SIM image for ßIV-spectrin and synpo. Synpo was localized to sites in the
AIS where ßIV-spectrin immunosignals were absent (arrows). Synpo clusters were also found at the AIS
where ßIV-spectrin immunolabeling was low (arrowhead in **C**). Scale bars=1μm.
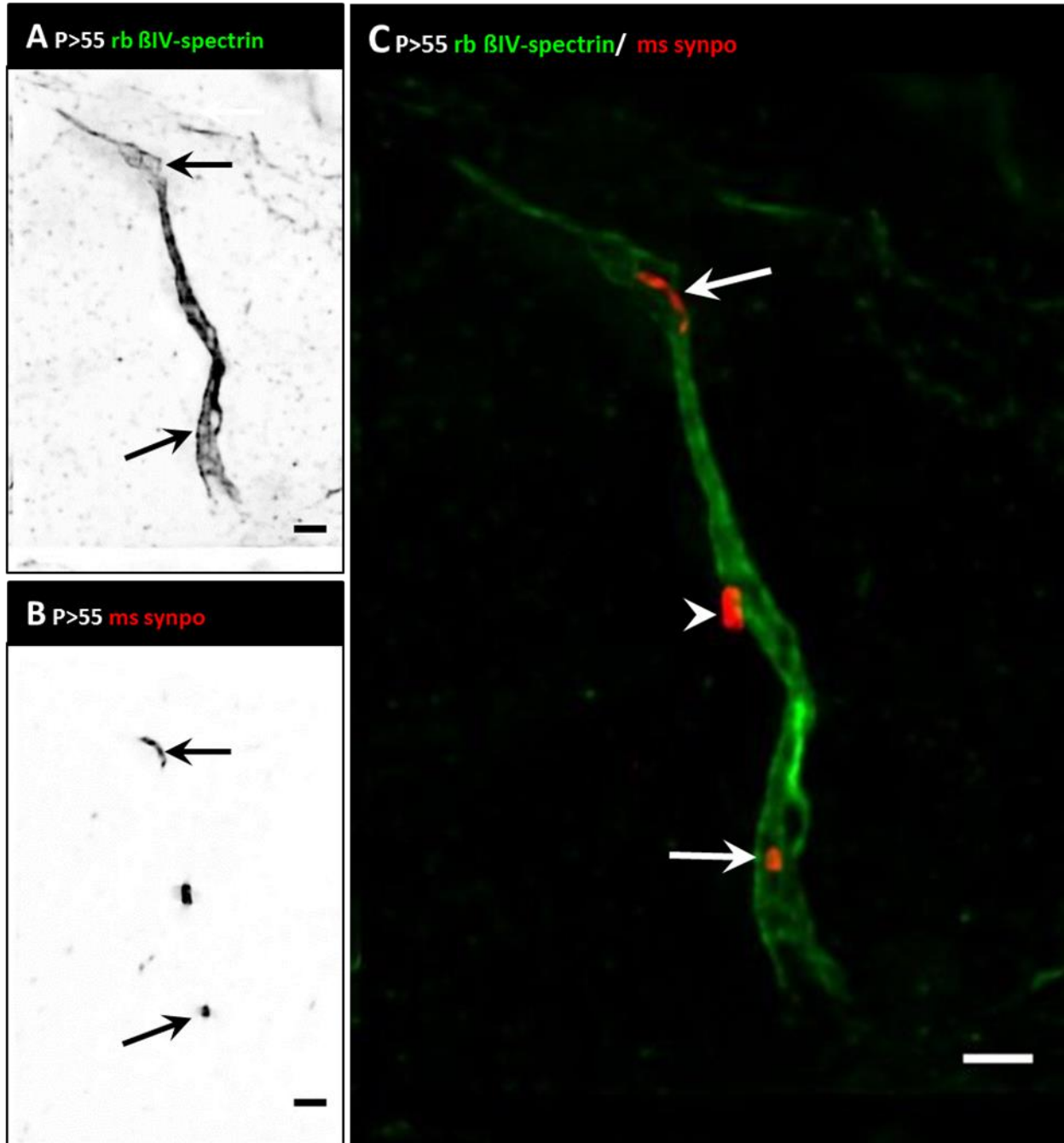
Figure 37: Structured illumination microscopy (SIM) scan of synpo-expressing AIS in rat retina.
(A)-(C) 3D-SIM image of immunolabeled whole mount retina of adult rats (P>55) using antibodies against ßIV-spectrin (green) and synpo (red). **(A)** 3D-SIM image of AIS marker ßIV-spectrin. **(B)** 3D-SIM image of synpo (red) in AIS. **(D)** Merged 3D-SIM image for ßIV-spectrin and synpo. Synpo was localized to sites in the AIS where ßIV-spectrin immunosignals were absent (arrows). Synpo clusters were also found at the AIS where ßIV-spectrin immunolabeling was low (arrowhead in **C**). Scale bars=1µm.
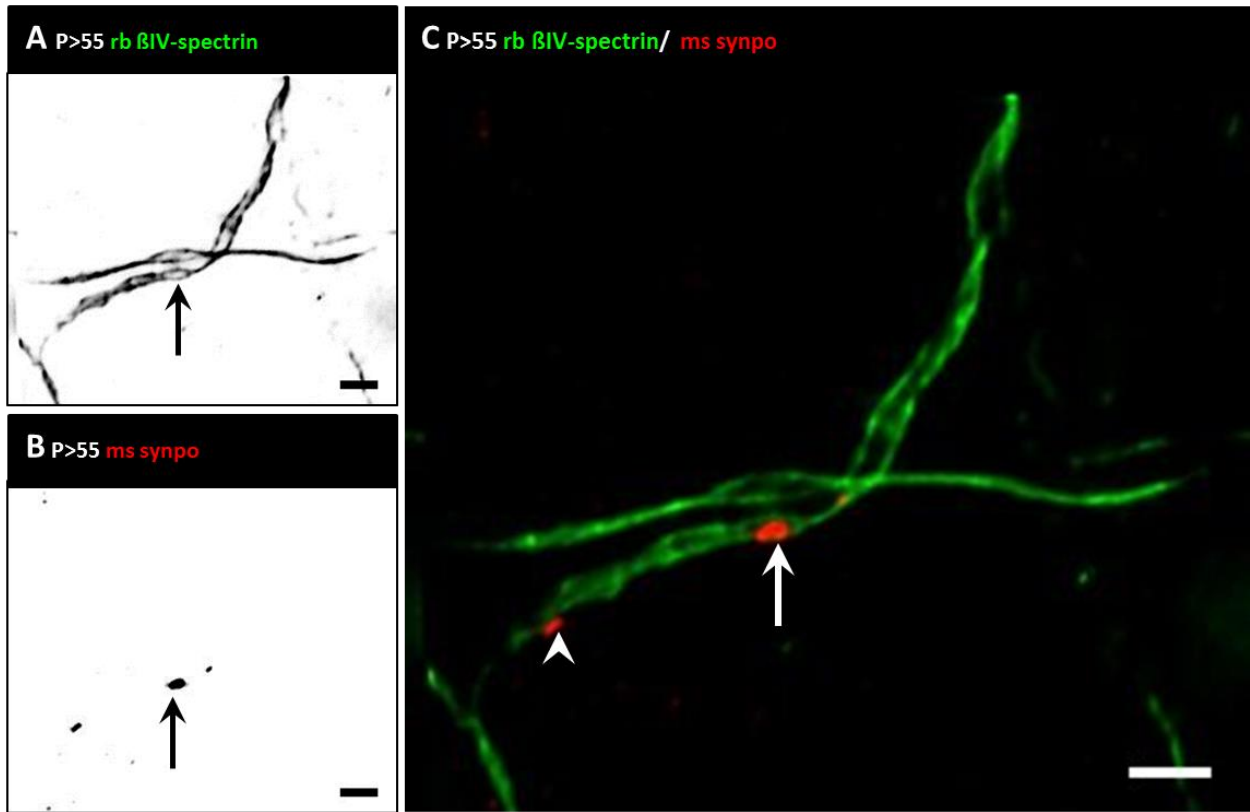
Figure 38: Structured illumination microscopy (SIM) scan of synpo-expressing AIS in rat retina.
(A)-(C) 3D-SIM image of immunolabeled whole mount retina of adult rats (P>55) using antibodies against ßIV-spectrin (green) and synpo (red). **(A)** 3D-SIM image of AIS marker ßIV-spectrin. **(B)** 3D-SIM image of synpo (red) in AIS. **(D)** Merged 3D-SIM image for ßIV-spectrin and synpo. Synpo was localized to sites in the AIS where ßIV-spectrin immunosignals were absent (arrows). Synpo clusters were also found at the AIS where ßIV-spectrin immunolabeling was low (arrowhead in **C**). Scale bars=1μm.
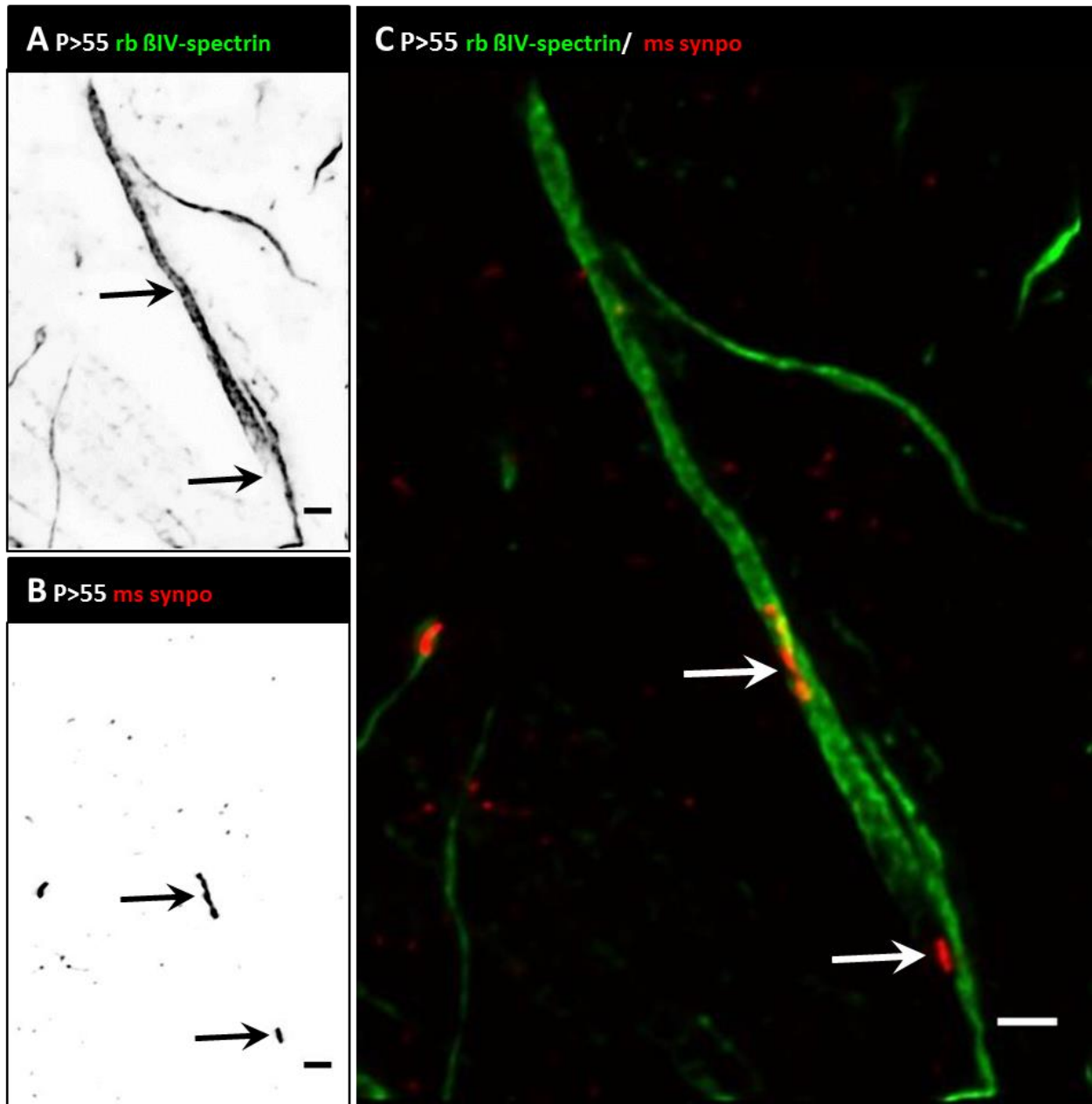
Figure 39: Structured illumination microscopy (SIM) scan of synpo-expressing AIS in rat retina.
(A)-(C) 3D-SIM image of immunolabeled whole mount retina of adult rats (P>55) using antibodies against ßIV-spectrin (green) and synpo (red). **(A)** 3D-SIM image of AIS marker ßIV-spectrin. **(B)** 3D-SIM image of synpo (red) in AIS. **(D)** Merged 3D-SIM image for ßIV-spectrin and synpo. Synpo was localized to sites in the AIS where ßIV-spectrin immunosignals were absent (arrows). Scale bars=1µm.
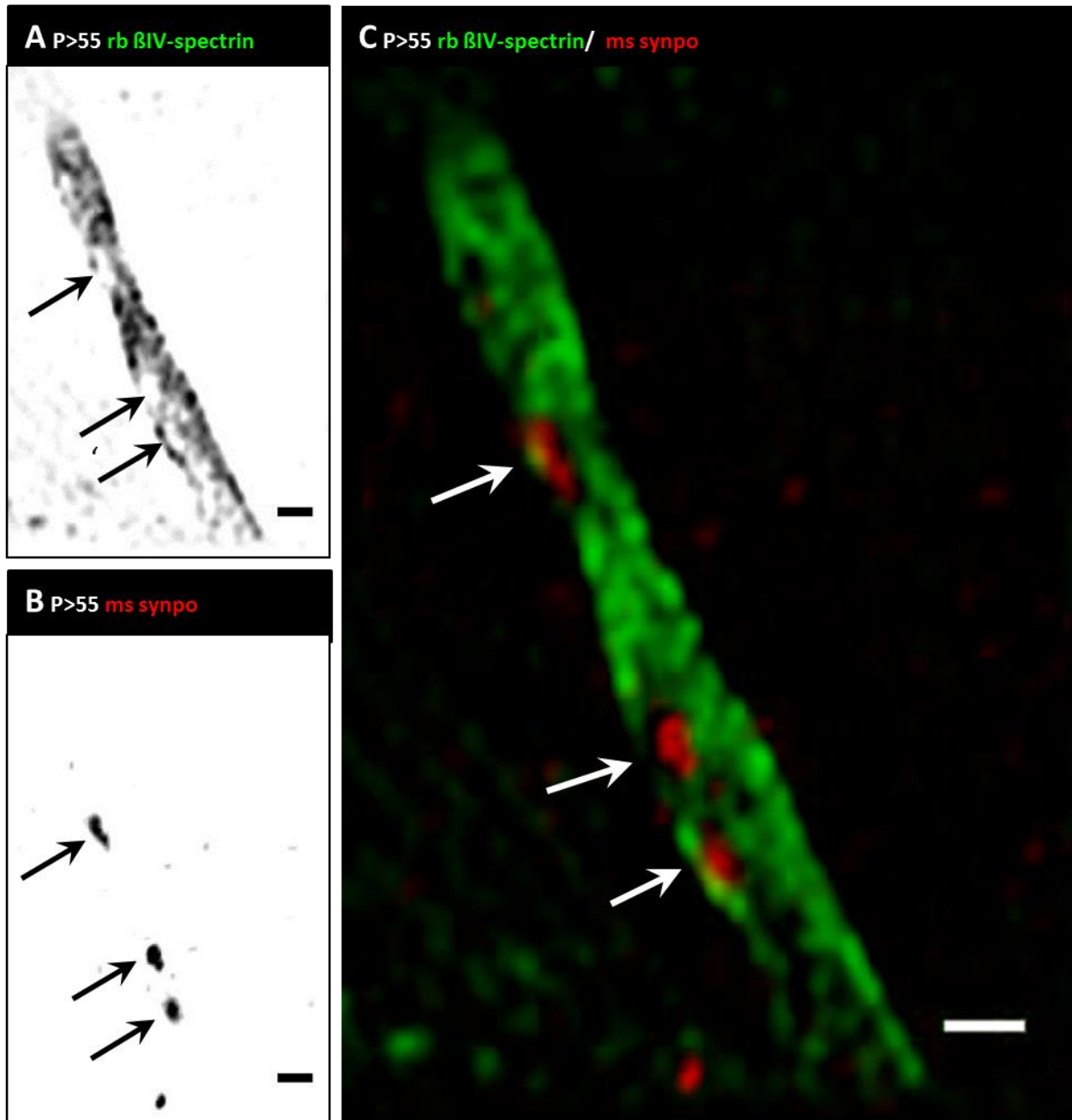
Figure 40: Structured illumination microscopy (SIM) scan of synpo-expressing AIS in rat retina.
(A)-(C) 3D-SIM image of immunolabeled whole mount retina of adult rats (P>55) using antibodies against ßIV-spectrin (green) and synpo (red). **(A)** 3D-SIM image of AIS marker ßIV-spectrin. **(B)** 3D-SIM image of synpo (red) in AIS. **(D)** Merged 3D-SIM image for ßIV-spectrin and synpo. Synpo was located to sites in the AIS where ßIV-spectrin immunosignals were absent (arrows). Scale bars=1µm.
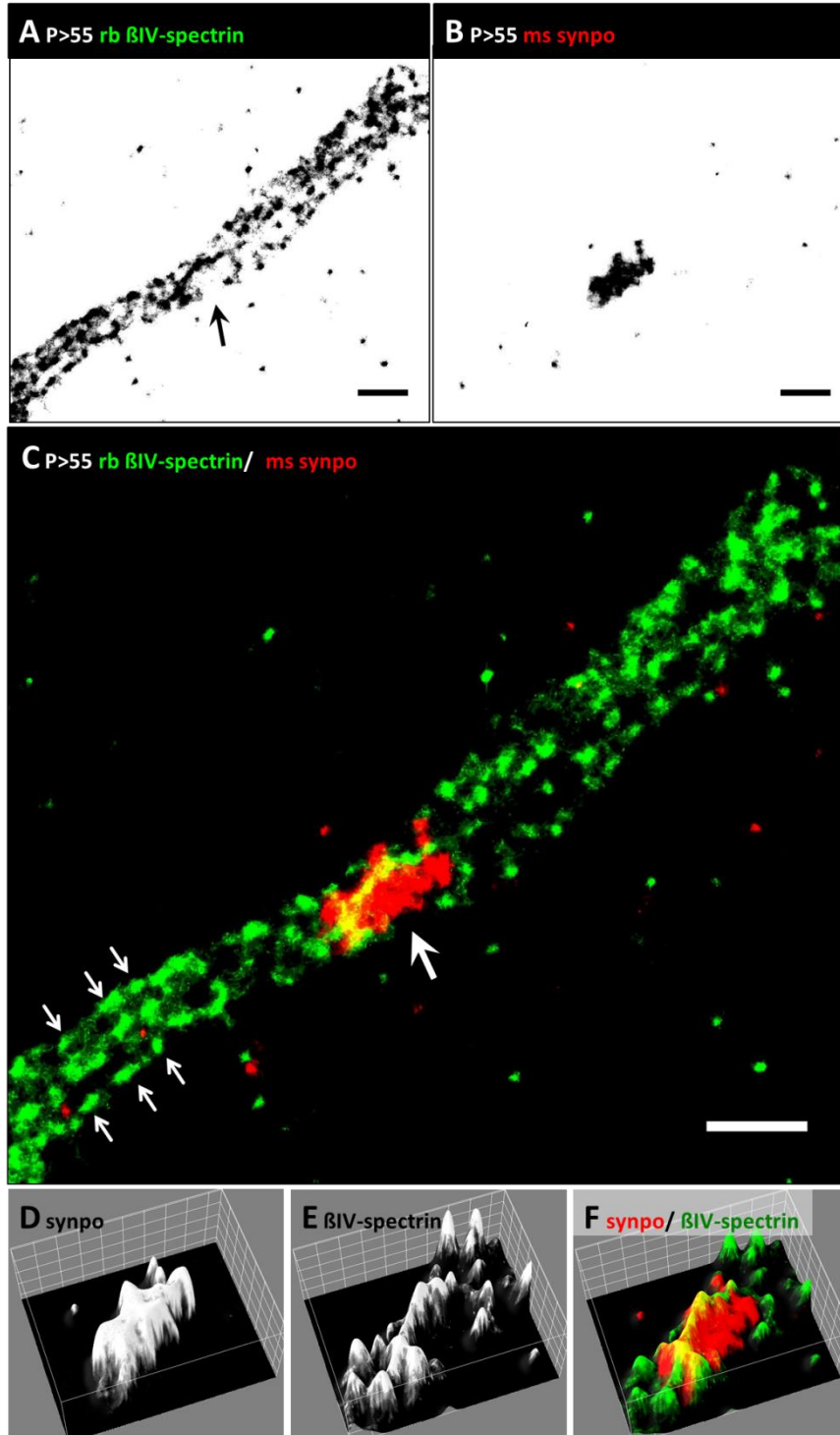
Figure 41: Single molecule localization microscopy (SMLM) scan of synpo-expressing AIS in rat retina.
(A)-(C) 2D-SMLM images of immunolabeled whole mount retina of adult rats (P>55) using antibodies against ßIV-spectrin (green) and synpo (red). **(A)** 2D-SMLM image of AIS marker ßIV-spectrin. **(B)** 2D-SMLM image of synpo (red) inside the AIS. **(C)** Merged 2D-SMLM image for ßIV-spectrin and synpo. Synpo was located to sites in the AIS where ßIV-spectrin immunosignals were absent (arrow). ßIV-spectrin was periodically distributed from the axonal surface towards the inner cytoskeleton within the AIS (small arrows). **(D)-(F)** 3D histograms (gray scale fluorescence signals) across the width of an AIS with a synpo cluster **(D)** underneath the ßIV-spectrin scaffold **(E)**, showing reciprocal exclusion of the signals in the merged image **(F).** Scale bars= 1μm.

Figure 42: Single molecule localization microscopy (SMLM) scan of synpo-expressing AIS in rat retina.
(A)-(C) 2D-SMLM images of immunolabeled whole mount retina of adult rats (P>55) using antibodies against ßIV-spectrin (green) and synpo (red). **(A)** 2D-SMLM image of AIS marker ßIV-spectrin. **(B)** 2D-SMLM image of synpo (red) inside the AIS. **(C)** Merged 2D-SMLM image for ßIV-spectrin and synpo. Synpo was located to sites in the AIS where ßIV-spectrin immunosignals were absent (arrow). ßIV-spectrin was periodically distributed from the axonal surface towards the inner cytoskeleton within the AIS (small arrows). **(D)-(F)** 3D histograms (gray scale fluorescence signals) across the width of an AIS with a synpo cluster **(D)** underneath the ßIV-spectrin scaffold **(E)**, showing reciprocal exclusion of the signals in the merged image. Synpo cluster is closely located to the axonal membrane **(F).** Scale bars= 500nm.
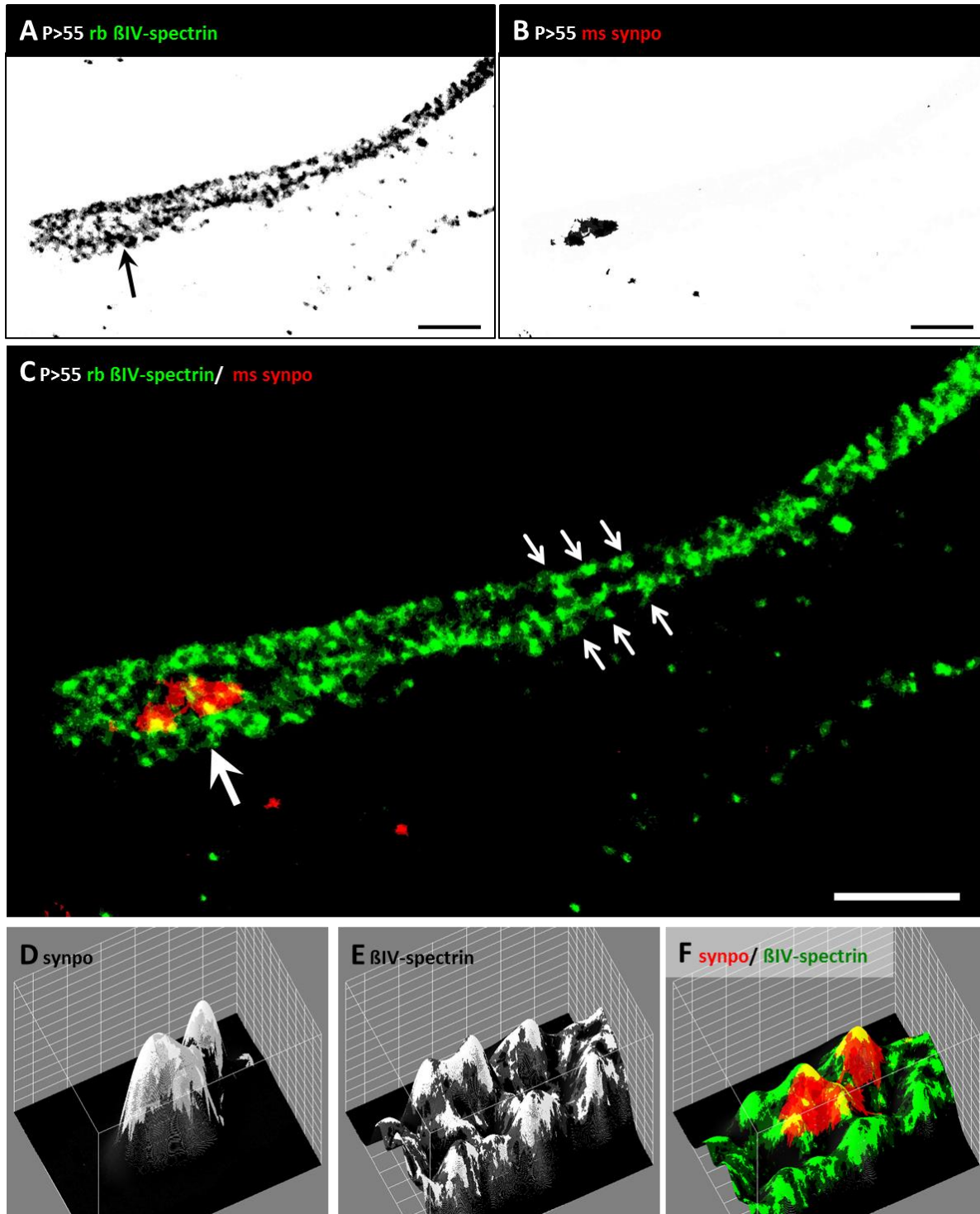
Figure 43: Single molecule localization microscopy (SMLM) scan of synpo-expressing AIS in rat retina.
(A)-(C) 2D-SMLM images of immunolabeled whole mount retina of adult rats (P>55) using antibodies against ßIV-spectrin (green) and synpo (red). **(A)** 2D-SMLM image of AIS marker ßIV-spectrin. **(B)** 2D-SMLM image of synpo (red) inside the AIS. **(C)** Merged 2D-SMLM image for ßIV-spectrin and synpo. Synpo was located to sites in the AIS where ßIV-spectrin immunosignals were absent (arrow). ßIV-spectrin was periodically distributed from the axonal surface towards the inner cytoskeleton within the AIS (small arrows). **(D)-(F)** 3D histograms (gray scale fluorescence signals) across the width of an AIS with a synpo cluster **(D)** underneath the ßIV-spectrin scaffold **(E)**, showing reciprocal exclusion of the signals in the merged image **(F).** Scale bars= 2μm.

5 Discussion

5.1 Maturation of the cisternal organelle and AIS during visual cortex development

So far, the role of synpo and the CO in AIS of principal neurons in the visual cortex is still largely unknown. The aim of this thesis was to investigate the developmental and putative activity-dependent expression of synpo/CO. Furthermore, the effect of synpo/CO on AIS structural maturation during murine visual cortex development and on AIS structural plasticity after visual deprivation was explored. The present thesis documents that only a subpopulation of AIS in the visual cortex contains synpo/CO with a maximum of approximately 50% of the entire population of visual cortex AIS. It is further demonstrated that expression of synpo/CO in the AIS is regulated in an activity-dependent manner during development. Moreover, synpo/CO plays an important role in the developmental maturation of cortical AIS and might have a potential role in AIS plasticity in the visual cortex (for summary see Figure 20).

5.1.1 Activity-regulated expression of synpo/CO

During murine visual cortex development, it was found that synpo is initially expressed in AIS of layer II/III and V pyramidal neurons at P10. Highest expression was observed around P15 as indicated by high percentage of synpo/CO-expressing AIS and increased synpo/CO cluster numbers in the AIS. Mice of the used C57BL/6 strain open their eyes around P13-14. Moreover, vision in mice begins prior to the naturally occurring eye-opening already around P11 (Krug et al. 2001). Thus, the timeframe of the onset of synpo/CO expression as well as the increased expression coincides with the first occurrence of directed visual stimuli, which may indicate an activity-dependent expression of synpo/CO. Likewise, an activity-regulated expression of synpo and the SA was demonstrated during murine hippocampus development (Czarnecki et al. 2005). The authors showed that synpo expression is developmentally regulated following the sequence of hippocampal principal neuron differentiation as well as of dendritic spine formation and maturation. Similar to the function of synpo and the spine apparatus (SA) in Ca^{2+} signaling in dendritic spines (Korkotian and Segal 2011; Korkotian et al. 2014; Grigoryan and Segal 2015), synpo/CO

was also suggested to play a role in modifying neuronal Ca^{2+} signaling in the AIS (Maggio and Vlachos 2014). The observed dynamic expression of synpo/CO in the present thesis might coincide with dynamically regulated Ca^{2+} currents during development. For example, developmental changes in the laminar distribution of extracellular Ca^{2+} in the visual cortex of cats suggested that experience-dependent modifications are triggered by Ca^{2+} influx (Bode-Greuel and Singer 1991). In rat visual cortex, a developmental switch from low-voltage-activated Ca^{2+} currents to high-voltage-activated Ca^{2+} currents occurred around P12 (Tarasenko et al. 1998). Interestingly, high-voltage-activated Ca^{2+} currents were found to contribute to AP hyperpolarization (Umemiya and Berger 1994). As discussed below, synpo/CO might play a functional role for such AP regulation. The putative activity-dependent expression of synpo/CO during murine visual system development was further investigated in the present thesis.

5.1.2 The role of synpo/CO in AIS structural maturation during development

Recent developmental studies of the entire population of AIS in the murine visual cortex demonstrated an activity-dependent tri-phasic structural length maturation: AIS were longest during eye-opening (phase 1), substantially shortened around the peak of the CP at P28 (phase 2), and re-elongated with CP closure at P35 (phase 3). After CP closure, AIS became mature throughout adulthood as indicated by constant length and homogenous length distribution (Gutzmann et al. 2014). By comparison, the present study demonstrates the absence of AIS shortening occurring during phase 2 of AIS length maturation in the subset of synpo/CO-expressing AIS, although their length development is significantly correlated to the developmental stage. Taken together, synpo/CO-containing AIS are less dynamic in their length maturation compared to the entirety of visual cortex AIS. In general, AIS length changes have the capability to modulate and fine-tune neuronal excitability. Current models reveal that neuronal excitability is enhanced when AIS are elongated, whereas short AIS reflect a lowered excitability (Adachi et al. 2015; Gulledge and Bravo 2016). As shown in the current thesis, synpo/CO-containing AIS are shorter and might therefore be preferentially part of a neuronal subpopulation with lowered excitability or

more stable AIS length despite changes in network activity that occur during visual cortex development (Hensch 2005a).

The CO exhibits several structural and putative functional features similar to those of the SA (Peters et al. 1968; Kosaka 1980; Spacek 1985; Benedeczky et al. 1994). Synpo expression, in particular, is essential for the formation of both organelles (Deller et al. 2003; Bas Orth et al. 2007). Reminiscent of the presence of the SA in the neck of mature mushroom-type spines present only in the adult rodent brain (Spacek 1985; Spacek and Harris 1997), synpo/CO might be predominantly expressed in a subpopulation of mature AIS. As described above, structural mature AIS characterized by constant length with homogenous distribution were established after the closing of the CP at P35. In comparison, immature AIS (prior to P15) were long and showed a more heterogeneous length distribution during early development (Gutzmann et al. 2014). In the current thesis, size frequency histograms of AIS length at young ages (P10-12) revealed that immature synpo/CO-expressing AIS have a similar heterogeneous length distribution. Strikingly starting at P15, synpo/CO-expressing AIS become more mature as indicated by a more homogenous length distribution as compared to the entire AIS population. Therefore, synpo/CO-expressing AIS might indeed represent a subpopulation with a higher degree of structural maturity.

If the presence of synpo/CO promotes AIS structural maturation, which effect would the lack of synpo/CO have on AIS maturation? In order to address this question, AIS length maturation was investigated in synpo KO mice. Interestingly, it was observed that lack of synpo/CO leads to an impairment of AIS structural length maturation during visual development. This was most notable during the peak of the CP at P28. AIS maturation is indeed dynamic during development, but at P28, AIS shortening is absent in synpo KO mice. In contrast, this phase was strikingly present in wildtype mice (Gutzmann et al. 2014). AIS length distributions in synpo KO mice display heterogeneous length distributions of adult animals, which are comparable to juvenile AIS in wildtype mice, implying that the lack of synpo impairs AIS structural maturation during postnatal development. This suggests that synpo/CO might be a regulating factor during AIS maturation, which could depend on the state of excitability of the neuron.

The mechanisms how synpo/CO might contribute to a faster AIS structural length maturation during development are still unknown, but are most likely linked to the Ca^{2+}

storing and sequestering function of the CO. In general, the neuronal ER network acts as a Ca^{2+} reservoir modulating neuronal Ca^{2+} signals (Simpson et al. 1995). Specifically, the ER and CO have been suggested to play an active role in neuronal Ca^{2+} signaling through the activation of transmembrane Ca^{2+}-sensitive receptors and pumps (Berridge 1998). Synpo/CO is associated with the sarco/endoplasmic reticulum Ca^{2+} ATPase (SERCA) type 1 Ca^{2+} pump, the inositol 1,4,5-trisphosphate (IP_3) receptor Ca^{2+} channel (IP_3R), and the ryanodine receptor (RyR) (Benedeczky et al. 1994; Sanchez-Ponce et al. 2011; King et al. 2014; Anton-Fernandez et al. 2015). These channels have the potential to be rapidly activated by Ca^{2+} that enters the AIS during AP firing (Bender and Trussell 2012). Intracellular Ca^{2+} storage loading through e.g. SERCA increases the sensitivity of RyRs and IP_3Rs and consequently, might amplify local cytosolic Ca^{2+} transients through Ca^{2+}-induced Ca^{2+} release (CICR) (Berridge 1998). To replenish local stores, trains of APs have to be initiated and as a result, this neuronal activity can be "memorized" by higher Ca^{2+} content in Ca^{2+}-storing organelles. In this regard, the CO could possibly be linked to the "neuron-within-a-neuron concept" postulated by Berridge in 1998. In the framework of this concept, trains of APs and subsequent CICR can lead to slow afterhyperpolarization (sAHP) induction through interaction with K_V channels. This eventually causes a negative membrane potential and increased membrane conductance, thereby modulating neuronal activity (reviewed in Hille 1986; Berridge 1998). As a result, neurons with previous enhanced firing rates become less excitable. One possible candidate for such a link between sAHP induced by Ca^{2+} signaling through the CO is the $K_V2.1$ channel. Indeed, $K_V2.1$ is localized near the CO (King et al. 2014) and several studies suggested a role for $K_V2.1$ in Ca^{2+} signaling (Du et al. 2000; 2004; Misonou et al. 2005; Park et al. 2006; Schulien et al. 2016). Expanding on this hypothesis, the effect of the Ca^{2+} storage function of the CO on triggering sAHP might enable neurons with synpo/CO-expressing AIS to "memorize" previous neuronal activity. As a result, those neurons might adapt their AIS length and thus, excitability in a less sensitive degree in response to alterations in neuronal network activity, e.g. during eye-opening or CPs. This in turn could keep neuronal excitability at more steady levels, which would lead to more homogenous and shorter AIS length in synpo/CO-expressing neurons.

5.1.3   The role of synpo/CO in AIS structural plasticity after visual deprivation

The present thesis demonstrates that structural maturation of synpo/CO is regulated in an activity-dependent manner during visual cortex development. Furthermore, this regulation correlates with AIS length maturation as indicated by the presence of a population of synpo/CO-expressing AIS that are homogenous and more mature in length. To further examine whether synpo/CO modulates AIS length maturation in dependence of visually driven synaptic input, dark-rearing experiments in wildtype mice were conducted. Visual deprivation from birth until P21, P28 and P35 leads to an increased length of synpo/CO-expressing AIS. These lengths were similar to those observed in immature AIS at P10-P12. This implicates that visual deprivation prevents the developmental AIS shortening during late postnatal development as it normally occurs under control conditions for the entire population of visual cortex AIS (Gutzmann et al. 2014). In conclusion, the presence of synpo/CO in the AIS leads indeed to a faster morphological maturation of the AIS. Despite its earlier maturation, the presence of synpo/CO does not completely prevent this population's ability to undergo activity-dependent plasticity as demonstrated by the observed AIS lengthening after visual deprivation. Remarkably, it was found that such modification of length maturation of synpo/CO-expressing AIS is only possible until the peak of the CP at P28, a time-point with high sensitivity to sensory input imbalances (Hooks and Chen 2007). A subsequent prolonged deprivation or rescue by additional exposure to light for one week does not have a significant impact on AIS length maturation.

An interesting finding in the present thesis was that visual deprivation leads to AIS lengthening along with an expansion of synpo/CO cluster size, highlighting a previously unreported plasticity of this ER-associated organelle. In principal, the ER is a dynamic organelle that constantly undergoes remodeling (Schwarz and Blower 2016). In neurons, dendritic ER is subject to reversible fragmentation and expansion, which is triggered by e.g. Ca^{2+}-dependent NMDA receptor activation (Kucharz et al. 2013). Changes in cell conditions result in long-term changes in structure and function of the ER with simultaneous Ca^{2+} signaling modifications (Sammels et al. 2010). Thus, ER expansion most likely provides an increased capacity of Ca^{2+} storages. Likewise, the observed increase of synpo/CO cluster sizes after visual deprivation probably enhances the AIS-associated Ca^{2+} storage capacity.

This might constitute a compensatory mechanism triggered by loss of visually driven synaptic input. Discussing the potential consequence of such an enhanced Ca^{2+} storage capacity, more APs might need to be generated to fill these Ca^{2+} stores and to trigger CICR. This would consequently delay the induction of sAHP triggered by Ca^{2+}-activated K_V channels and hence increase neuronal activity (Berridge 1998). Taken together, synpo/CO clusters might enlarge and simultaneously, the AIS length increases, together possibly indicating a heightened state of neuronal excitability depending on intrinsic Ca^{2+} regulation in response to loss of visually driven synaptic input.

AIS elongation caused by sensory deprivation was previously shown by studies of the avian *nucleus magnocellularis* (Kuba et al. 2010). The authors additionally observed an accompanying increase in whole-cell Na^+ current, membrane excitability and spontaneous firing. These findings were interpreted as a process reminiscent of homeostatic plasticity. Such AIS plasticity after sensory deprivation has recently been confirmed by several additional studies (reviewed in Adachi et al. 2015), showing that AIS structural plasticity compensates for loss of synaptic input as indicated by AIS lengthening, thereby increasing neuronal excitability. Interestingly, synpo and the SA play a pivotal role for homeostatic synaptic plasticity in the hippocampus (Vlachos et al. 2013). Thus, it seems reasonable to hypothesize that synpo/CO, as a putative structural correlate of the SA, might play a similar role for AIS homeostatic plasticity.

It should be considered that both organelles, the SA and the CO, might interplay to regulate neuronal plasticity. It is unknown whether those neurons that develop SAs in their spines also develop COs in their AIS. It will be an interesting aspect to further analyze the communication of both organelles in one neuron via the neuronal ER. It might be the case that synaptic strengthening through synpo/SA remodeling in turn triggers synpo/CO size increase in the AIS in one single neuron. An example for such a remodeling of synpo/SA is a compensatory increase in synpo cluster size and stability with a concomitant increase of SA stack number in dentate granule cells after loss of synaptic input (Vlachos et al. 2013). Similarly, the visual deprivation paradigm used in the present study results in an enhanced synpo expression in layer IV of V1 as indicated by an increase in number, mean fluorescence as well as total area of synpo positive immunosignals, which are most likely associated to SAs. Accordingly, relative synpo protein levels in total visual cortex protein

lysates displayed a slight increase after visual deprivation. These protein levels, however, correspond to the combined synpo expression in spines and AIS. Visual cortex layer IV receives most visual input from the dorsolateral geniculate nucleus (dLGN), thus suggesting that synpo/SA undergo activity-dependent remodeling after visual deprivation. This could also lead to a homeostatic synaptic strengthening in V1, similarly to that described above for the hippocampus. Layer IV connects vertically to layer II/III, V and VI (Bachatene et al. 2012). It is therefore tempting so speculate that synaptic strengthening in layer IV of V1 might in turn trigger remodeling of synpo/CO in AIS of layer II/III and V as observed in the current study.

In the current thesis, it is also found that synpo-cluster/CO size and thus, CO Ca^{2+}-storing capacity remains constant during V1 development. Synpo/CO cluster sizes only changed after visual deprivation. COs might have the ability to trigger sAHP (Berridge 1998). It is unknown whether constant CO sizes would also result in constant Ca^{2+} thresholds within the CO during V1 development. Ca^{2+} storage loading in the ER is regulated by RyR, IP_3R and SERCA pumps via Ca^{2+} sensitivity for those receptors/pumps (Berridge 1998) or through their expression levels and phosphorylation states (Miyakawa et al. 1999; Ziskoven et al. 2007; Prosser et al. 2010). Is RyR, IP_3R and SERCA activity or their concentration at the CO developmentally regulated and modified after sensory deprivation? Relative protein levels of IP_3R in total visual cortex protein lysates increase during development with highest observed levels at P35. Dark-rearing of mice resulted in a significant decrease of IP_3R levels suggesting that expression of Ca^{2+}-sensitive receptors at internal Ca^{2+}-storing organelles, such as the CO, might be down-regulated by loss of visually driven synaptic input. In turn, this could lead to modified Ca^{2+} loading levels of the CO. On the other hand, Ca^{2+} sensitive proteins such as IP_3R are not exclusively expressed at the CO, but are also located in the membrane of neuronal ER (Augustine et al. 2003). Thus, decreased IP_3R levels after dark-rearing might be additionally correlated to a down regulation of this receptor in the entire ER of the neuron instead of a local down regulation at the CO. Plasticity and function of the CO during visual system development and after sensory deprivation are still a wide field to investigate. Further studies have to be conducted to understand the underlying mechanisms as well as consequences of such activity-driven plasticity.

As discussed above, the current thesis shows that the presence of synpo/CO has an effect on developmental AIS length maturation. Furthermore, dark-rearing of mice leads to synpo/CO cluster increase and to the prevention of length maturation of synpo/CO-expressing AIS during development. To test whether structural AIS plasticity is subject to synpo/CO expression, the visual deprivation paradigm was applied to synpo KO mice. As recently shown, visual deprivation led to the prevention of AIS length maturation in wildtype mice (Gutzmann et al. 2014). Interestingly, here it is demonstrated that this deprivation-induced AIS plasticity is impaired in synpo KO mice. Moreover, in P21 and P28 dark-reared synpo KO mice, a significant AIS length decrease is observed. This implicates that in fact, AIS plasticity is indeed impaired by lack of synpo, especially during CPs of visual cortex plasticity.

How synpo/CO might regulate structural plasticity of the AIS is not known. It should be taken into account, however, that synpo/CO and Ca^{2+} signaling might be involved in the modulation of GABA-A receptors at the AIS (Llano et al. 1991; Benedeczky et al. 1994; King et al. 2014). GABA-A receptors are the postsynaptic target of terminals of Chandelier cells (ChC), which specifically form axo-axonic synapses (AAS) at the AIS. GABA-A receptors can be modulated through Ca^{2+} dependent mechanisms (Saliba et al. 2012; Dacher et al. 2013). Synpo/CO is located in close approximation with AAS (Benedeczky et al. 1994; King et al. 2014) and might therefore have a modulatory effect on GABA-A receptors through Ca^{2+} signaling. In addition, ChC have the potential to be either inhibitory or excitatory, depending on the membrane potential of the postsynaptic neuron (Woodruff et al. 2010), which in turn might be regulated through the above hypothesized $K_V2.1$ and CO function on triggering sAHPs. Taken together, the CO, AAS and $K_V2.1$ channels at the AIS might interact in modifying excitability of the neuron. However, there are still pending questions: How does Ca^{2+} signaling affect the communication between $K_V2.1$ channels, AAS and COs? And what is the nature of AAS (excitatory or inhibitory) at the AIS in regard to Ca^{2+} storage loading and membrane potential? And in turn, does firing or non-firing of AAS lead to increased or decreased Ca^{2+} store loading in the CO? The mechanisms are still a mystery and it remains to be elucidated how this complex interaction might function.

The importance of GABAergic transmission for proper maturation of the visual cortex during CPs has been shown by several studies (reviewed in Hensch 2005b). Sensory

experience is also important for the maturation of GABAergic signaling and synapses in interneurons during visual cortex development and after visual deprivation (Gabbott and Stewart 1987; 1992; Benevento et al. 1995; Keck et al. 2011; Le Magueresse and Monyer 2013). In the visual cortex, rates of spontaneous activity are increased after dark rearing of rats (Benevento et al. 1992).

Based on the previous observation that synpo/CO is closely located to AAS (Benedeczky et al. 1994; King et al. 2014), it is tempting to raise the question whether AAS might be increased in their number at sites of enlarged synpo/CO clusters occurring after visual deprivation in the current study. AAS function, and thus neuronal excitability, might be modulated by this synpo/CO size remodeling. Noticeably, only the size, but not the number of synpo/CO clusters increases after visual deprivation. However, it cannot be excluded that the CO size increase is a result of a fusion of single synpo clusters. It has been shown that dark rearing of mice leads to a selective reduction in the magnitude of GABA response amplitude and GABA-A receptor density only on the soma and proximal dendrites, but not on AIS of pyramidal neurons in visual cortex slices (Katagiri et al. 2007). Furthermore, photo-activation of cultured CA1 pyramidal neurons leads to distal AIS relocation, a mean by which neurons also decrease excitability (Grubb and Burrone 2010a). However, AAS at the AIS do not change their position or number, which was supposed to be optimal for opposing AP generation and thus down-regulating cell excitability (Wefelmeyer et al. 2015). These studies suggest that the adaption of inhibitory or excitatory properties of AAS to external conditions might not occur through structural changes of these synapses, such as number or size at one single AIS. More likely, AAS could be regulated by functional properties at the presynaptic and postsynaptic site (Wang et al. 2016b). It remains to be elucidated whether CO remodeling might modify AAS number and/or activity at the AIS. Here, it is additionally found that dark-rearing for 3 weeks leads to a significant reduction in percentage of synpo/CO-expressing AIS. Prolonged dark-rearing for 4 or 5 weeks however results in similar percentage of synpo/CO-expressing AIS as compared to control animals, suggesting that the percentage of AIS that express synpo/CO is sensitive to visual deprivation only until the beginning of the CP around P21. It would be interesting to test whether the decrease of percentage of synpo/CO-expressing AIS observed in the current also correlates with a decrease of percentage of AAS. Future quantification of AAS after

dark-rearing in V1 are required in order to better understand the interaction between synpo/CO and AAS at the AIS.

It is important to remember that AAS are predominantly found in supragranular layers of the cortex (Peters et al., 1982). As shown in the present study, the CO in AIS of these layers displays smaller cluster sizes, which are located closely to the AIS membrane and may therefore represent small organelles interacting with GABAergic synapses at the AIS. Layer V neurons have more elongated and centered localized synpo/CO clusters extending through large portions of the AIS also designated as "giant saccular organelles" (Sánchez-Ponce et al., 2012; Antón-Fernández, 2015). These giant organelles might therefore predominantly function as Ca^{2+} storages and might not necessarily be closely located to AAS. In the current thesis, synpo/CO size increase is also observed in AIS of layer V neurons after visual deprivation. Activity of layer V neurons might be fine-tuned in a distinctly different way than those in layer II/III, which may be predominantly independent of regulation through AAS. For instance, layer V neurons are expected to be rather limited in their excitability as a function of their large somatodendritic sizes, shorter AIS and AIS starting position (Gulledge and Bravo 2016).

If the presence of synpo/CO in AIS would have an effect on firing properties of the corresponding neuron, which consequence would then the lack of synpo/CO have on neuronal excitability? During cortical development, GABAergic transmission undergoes an overall switch from excitation to inhibition (Druga 2009). Simultaneously, intracellular Ca^{2+} signals increase, which is induced by GABA-A receptor activation probably through Ca_V channels in visual cortex slices at early postnatal ages (P0-2). Afterwards, these signals continuously decrease with further development and become undetectable after P20 (Lin et al. 1994). The development of synpo/CO expression in AIS in the visual cortex might contribute to that switch of GABAergic function. Furthermore, it is conceivable that lack of synpo/CO could probably lead to functional changes of the excitation/inhibition balance in cortical networks during development and after sensory deprivation. In rodents, total GABAergic input into layer II/III pyramidal neurons increases significantly between eye opening and CP closure (Morales et al., 2002). This might in turn lead to the significant AIS shortening at P28 as observed in wildtype mice (Gutzmann et al., 2014). If GABAergic input is affected by the lack of synpo/CO, this might also affect AIS maturation and neuron

excitability, and could be a reason for the absence of the structural AIS shortening during CP. Moreover, lack of synpo/CO might have a major impact on axonal membrane potential properties and neuronal excitability properties based on local Ca^{2+} signaling and interactions with K_V channels at the AIS discussed above. Supporting observations were made in the present thesis, showing that lack of synpo/CO results in a putative reduction of $K_V2.1$ clustering at the AIS. Furthermore, a significant decrease of IP_3R protein levels in total visual cortex lysates of synpo KO mice is found, which is in turn most likely correlated to a reduction in IP_3R clustering at the AIS, dendritic spines and also neuronal ER. In comparison, specific α-actinin immunosignals in AIS and dendritic spines, which are generally observed in wildtype mice (Asanuma et al. 2005; Sanchez-Ponce et al. 2012) are absent in synpo KO mice. α-actinin is directly co-expressed with synpo/CO (Sanchez-Ponce et al. 2012) and thus, it seems reasonable that α-actinin expression and localization to the AIS is affected in a higher degree than that of $K_V2.1$, which is closely located to synpo/CO and not directly co-expressed with synpo or located in the CO. In conclusion, these findings indicate that synpo might have a putative recruitment function for proteins in the AIS, such as α-actinin, K_V channels and IP_3R. Furthermore, the putative function of synpo/CO in GABAergic transmission as well as in modulating neuronal excitability potentially may contribute to AIS structural plasticity. The absence of a putative compensatory length increase after visual deprivation in synpo KO mice in the present study, along with the impaired tri-phasic structural maturation of AIS as indicated by the absence of AIS shortening at P28, might be attributed to synpo/CO. However, any analysis of the CO is necessarily confounded by the SA in dendritic spines, which is additionally absent in synpo KO mice (Deller et al. 2003). Altered developmental AIS structural plasticity through loss of visually driven synaptic input might therefore additionally be impaired by lack of the SA. In conclusion, cortical network activity in synpo KO mice might be influenced by the lack of Ca^{2+} storages in both, axonal and dendritic compartments. In contrast, a previous study utilizing whole-cell-patch-clamp recordings to analyze APs of hippocampal pyramidal cells in synpo KO mice did not find significant differences to APs in littermate controls (Bas Orth et al. 2007). The authors concluded that the CO does not have a critical impact on AP generation in the hippocampus. It will therefore be an interesting aspect to further study whether cortical network activity of synpo KO mice is changed during the CP in V1.

Furthermore, only a subpopulation of neurons in wildtype mice express synpo/CO and it is not known how AIS that naturally do not express a CO would react in this network, since both types are indistinguishable in synpo KO mice. The ones without a CO probably still show homeostatic plasticity as it was observed for the entire AIS population by homeostatic length increase after visual deprivation in V1 of wildtype mice (Gutzmann et al. 2014). This leads to the assumption that CO presence is not crucial for AIS to function properly, but that it may give the neuron an advantage under certain physiological parameters. Taken together, both, synpo-expressing and synpo-lacking neurons might be necessary with their specific characteristics to form a cortical network. More functional aspects have to be investigated to gain further understanding of how synpo and the CO specifically regulate AIS maturation and plasticity during visual cortex development. For example, the differences of electrophysiology properties of single AIS will be interesting to explore in dependence of synpo/CO expression during V1 development wildtype mice. Furthermore, the investigation of maturation of GABAergic transmission during CPs of visual cortex plasticity in synpo KO mice would contribute to address these questions.

In summary, the present thesis shows that a subpopulation of principal neurons in layer II/III and V express synpo/CO. Moreover, synpo/CO is a dynamic structure and its structural maturation is regulated in an activity-dependent manner. This provides the first evidence that structural plasticity can occur for organelles in the AIS in response to sensory deprivation. Synpo/CO has the potential to contribute to AIS plasticity, possibly in compensating loss of visually driven synaptic input.

5.2 Maturation of the cisternal organelle in AIS during retinal development

The present thesis demonstrates a hitherto unknown regulation of synpo/CO expression during murine visual cortex development that depends on visual activity. Visual information is first processed by photoreceptors in the retina. Amacrine and bipolar cells integrate information from photoreceptors and transmit it to retinal ganglion cells (RGCs), which are the major output neurons of the retina. Axons of RGCs form the optic nerve, which transmits visual information to the dLGN and visual cortex (Erskine and Herrera 2014). RGCs axons remain unmyelinated for several millimeters within the retina and become myelinated only after entering the optic nerve at the *lamina cribrosa* (Forrester and Peters 1967; Foster et al. 1982). The AIS of RGCs is proximally located in the unmyelinated part of the axon and is therefore spatially separated from the distal myelinated part (Hildebrand and Waxman 1983; Koontz 1993). The similarity of AIS of RGCs to those of principal neurons has been shown by several studies (Hildebrand and Waxman 1983; Carras et al. 1992; Koontz 1993; Boiko et al. 2003; Van Wart et al. 2007; Zhang et al. 2015). So far, however, the presence of synpo and the CO in AIS of RGCs is completely unknown. The aim of this study was to investigate synpo/CO expression in AIS of the developing murine retina. The precise localization of synpo/CO in retinal AIS was further explored by applying super resolution microscopy. Moreover, it was aimed at investigating the putative activity-dependent expression of synpo/CO in retinal AIS during development and after visual deprivation.

First, synpo mRNA expression was analyzed for various ages during retinal development. It was found that synpo mRNA in the retina is detectable already at embryonic stages. Furthermore, mRNA levels significantly increase shortly after birth at P1 and during eye-opening at P14, indicating a developmentally regulated expression. Synpo protein localization to AIS of RGCs is initially observed at P8. Thus, mRNA expression of synpo precedes synpo protein translation in the retina. A similar observation for synpo mRNA expression was made in the developing murine hippocampus (Czarnecki et al. 2005). The authors found that at P1, first synpo mRNA is exclusively found in somata of CA3 pyramidal neurons. Synpo mRNA expression started four days before onset of synpo protein

expression in dendritic spines. The somatic location was maintained suggesting that synpo mRNA is not transported to dendritic spines or the AIS in principal neurons (Czarnecki et al. 2005). The same might apply for synpo mRNA localization in the developing retina. Early mRNA expression of synpo might be required to ensure a time window in which protein translational modifications and sorting to the retinal AIS will be completed at P8. In contrast, synpo protein expression is additionally found in somata of RGCs beginning at E16.5, which would coincide with an early retinal mRNA expression of synpo. Increased mRNA levels at P1 might accompany the concentration of synpo protein expression within the GCL towards the NFL, which was observed in the present thesis. During embryonic development, newly born RGCs migrate toward the basal side of the retina to form the future GCL (Hinds and Hinds 1974). This could result in the aforementioned change in localization of synpo expression within the developing retina, however, this would not necessarily coincide with an enhanced mRNA expression of genes that are not involved in cell migration, such as synpo. In contrast, RGCs first appear at E11.5 and differentiation lasts until P1 (Byerly and Blackshaw 2009), which potentially results in developmental changes of synpo mRNA at P1. The additional observed peak of synpo mRNA expression during eye-opening at P14 might in turn be triggered by the onset of directed visual input. On the other hand, mRNA was isolated from total retinal tissue. Thus, quantified synpo mRNA represents mRNA levels for the entire retinal cell population during development. Hence, it cannot be excluded that synpo mRNA is additionally expressed in other retinal cell types. The precise synpo mRNA expression and localization within the retina can only be determined by performing *in situ* hybridization or qPCR combined with laser microdissection. Taken together, synpo mRNA expression in the whole retina might indeed be increased shortly after birth and during eye-opening, albeit on a protein level, synpo expression was low during postnatal retinal development and not detectable in Western blot.

To date, the presence of a CO in retinal AIS has not yet been reported. In this thesis, it was found that synpo is co-expressed with typical CO-associated proteins, such as SERCA, RyR and IP_3R in AIS of some RGCs. This strongly suggests that a distinct population of RCGs indeed contain COs in their AIS, which might possibly play a role in local Ca^{2+}-signalling. On

the other hand, only the application of electron microscopy will reveal the presence of a CO in retinal AIS. It will be further interesting to consider whether synpo/CO could have a function in AIS plasticity during retinal development similar to its role for AIS plasiticity during visual cortex development as it was observed in the current thesis. To further adress this question, the developmental expression of synpo/CO was investigated in the retina of mice.

As outlined above, it was observed that synpo is initially expressed at P8 in AIS of RGCs. Number and size of synpo/CO clusters in retinal AIS are stable during eye-opening at P14, thus, it is unlikely that an increased synpo mRNA expression at this age would enhance synpo protein expression in individual AIS. On the other hand, it could be well possible that total number of synpo/CO-expressing AIS is increased at P14. The quantification of percentage and length of individual RGC AIS was not possible in the present thesis due to the technical limitation that these AIS are often branched and closely located with each other. Therefore, only expression of synpo in AIS was analyzed in regard to synpo cluster number and sizes. However, it indeed seemed that percentage of synpo-expressing AIS increases during postnatal development. Estimated by qualitative assessment, marginal percentage at P8 seemed to rapidly increase from P10 until P14, which could coincide with the enhanced synpo mRNA levels during eye-opening. However, highest percentage of synpo/CO-expressing AIS is apparently present in adulthood.

After eye-opening around P14, changes in synpo protein expression were found in single AIS of RGCs as indicated by a significant decrease of synpo/CO cluster sizes from P21 to P28. In contrast, number of synpo clusters did not show significant differences during the entire period of retinal development. What could account for this observed developmental decrease of synpo/CO cluster sizes in retinal AIS? A possible trigger could be spontaneous periodic activity, which is a characteristic feature of the developing retina (reviewed in Firth et al. 2005). RGCs spontaneously fire periodic bursts of APs with accompanying large increases of intracellular Ca^{2+} levels. APs propagate across the developing inner and outer retina as waves triggering neighboring RGCs to fire correlated bursts (Firth et al. 2005). In mice, stage I cholinergic and gap-junction mediated spontaneous retinal activity is initially detected around E16.5 (Bansal et al. 2000; Huberman et al. 2008). Stage II waves approximately begin when mice are born and are driven by acetylcholine release from

starburst amacrine cells (Feller et al. 1996; Zhang and McCall 2012). Shortly before eye-opening from P10-P12, stage III spontaneous retinal waves emerge, which are mediated by glutamate release from bipolar cells and last until eye-opening (reviewed in Huberman et al. 2008). Vision in mice begins around P11 through naturally closed eye lids (Krug et al. 2001). Thus, stage III spontaneous retinal activity co-exists with visually driven activity in dLGN and V1 (Huberman et al. 2008). Around eye-opening, spontaneous retinal activity begins to disappear and is finally absent around P21 (Demas et al. 2003). Altogether, these findings suggest that onset of synpo expression in retinal AIS at P8 might coincide with the appearance of stage III retinal waves as well as with the onset of vision before eye-opening. Further investigations of spontaneous waves in retinae of synpo KO mice would contribute to elucidate a possible correlation between dynamic synpo expression and spontaneous retinal activity. Interestingly, spontaneous retinal activity that occurs prior to the onset of vision drives the development of the visual cortex to a certain degree and promotes development of OD columns in V1 (Crair et al. 1998). However, retinal waves are not sufficient to drive the generation and maturation of single neurons in V1 (reviewed in Ackman and Crair 2014). It will thus be of interest to examine whether retinal waves are abnormal in synpo KO mice, and whether such impaired retinal waves would result in abnormal maturation in V1. So far, it is unknown whether synpo KO mice exhibit developmental malfunctions in the retina or visual cortex, hence, it will be fascinating to investigate a possible impact of lack of synpo/CO on visual information processing.

The observed decrease of synpo clusters in AIS of RGCs from P21 until P28 in the present study might be triggered by early visual experience along with the disappearance of retinal waves around P21 (Demas et al. 2003). In mice, synaptogenesis in the outer plexiform layer and inner plexiform layer begins before eye-opening and persists for several weeks. The density of synapses peaks around P21 (Xu and Tian 2004). From P22 until P27, an increase of spontaneous excitatory and inhibitory postsynaptic currents emerges, which enhances RGC synaptic input more than fourfold (Tian and Copenhagen 2001). This increase of synaptic input also has the potential to change the firing properties of RGCs, which in turn might lead to the observed remodeling of synpo/CO in retinal AIS from P21 to P28. Taken together, synpo/CO expression in AIS of RGCs changes during development and these

alterations coincide with different types of activity-driven processes in the developing retina.

In the present thesis, the activity-dependent regulation of synpo/CO expression was indeed shown for visual cortex development. Therefore, it was hypothesized that synpo/CO might also be expressed in an activity-dependent manner during retinal development. Consequently, synpo/CO expression was further investigated in P28 dark-reared mice. It was found that synpo/CO cluster number and size in AIS of RGCs significantly increase after visual deprivation. Thus, synpo/CO expression is indeed regulated in an activity-dependent manner during retinal development. The effect of visual deprivation on functional maturation of the retina has been well studied (reviewed in Xu and Tian 2004). For example, visual deprivation impeded a developmental surge of spontaneous excitatory and inhibitory synaptic input into RGCs (Tian and Copenhagen 2001). Furthermore, the density of conventional inhibitory synapses between amacrine cells and RGCs that provide inhibitory synaptic input onto RGCs increased after dark-rearing of mice (Fisher 1979).

To date, the effect of visual deprivation on axonal plasticity in RGCs has not been studied. This thesis shows an activity-dependent remodeling of synpo/CO in AIS of RGCs and thus, plasticity for organelles in retinal axons caused by loss of visually driven synaptic input. This is also shown for visual cortex AIS in the current thesis. However, synpo expression in retinal AIS was different to that of visual cortex neurons, where synpo clusters did not undergo developmental changes in sizes. Instead, during visual cortex development, number of synpo clusters changed. Strikingly, dark-rearing led to synpo cluster size increase in both retinal and cortical AIS. An increase in synpo cluster number per AIS after visual deprivation was only observed in retinal AIS and in layer V cortical neurons at P21. This suggests a differentially regulated expression of synpo/CO in retinal versus cortical AIS that might be related to different characteristics of these distinct types of neurons. Altogether, it is assumed that synpo/CO in AIS of RGCs might be the functional and structural correlate to synpo/CO in AIS of pyramidal neurons.

Indeed, also a putative structural correlation of the CO in retinal AIS to the CO in cortical neurons was found in the current thesis since it was demonstrated that CO-associated

proteins are co-expressed with synpo in AIS of RGCs. In principal neurons, synpo/CO was previously shown to localize at gaps in the AIS meshwork where ankG expression was absent (King et al. 2014). Synpo/CO was clustered at these gaps in close approximation to GABAergic AAS. This particular localization was revealed by applying structured illumination microscopy (SIM), which is a high resolution microscopy technique enhancing spatial resolution by factor two (Heintzmann and Cremer 1999; Rossberger et al. 2013a). To elucidate whether synpo/CO in AIS of RGCs shows further structural similarities to synpo/CO in principal neurons, SIM and single molecule localization microscopy (SMLM) was applied in the rodent retina *in vivo.* Interestingly, both super resolution techniques reveal the existence of gaps in the meshwork underneath the AIS plasma membrane in RGCs. These gaps in the AIS are characterized by the absence of immunolabeling for the AIS marker ßIV-spectrin. Furthermore, synpo/CO appeared to be localized to these gaps in the retinal AIS. By applying SMLM, the resolution is improved to the 25nm range (Rossberger et al. 2013b). 3D histograms of fluorescence signals for ßIV-spectrin and synpo/CO reveal that both signals exclude each other, which highlights that synpo/CO is indeed localized to gaps in the AIS scaffold in RGCs. These observations further support the hypothesis that retinal AIS contain a CO, which is likely to be the structural correlate to the CO in AIS of principal neurons. However, these studies are impeded by the scarcity of EM application.

It remains further to be elucidated whether synpo/CO in the retina shares additional structural and functional similarities with synpo/CO in the cortex. Gaps in the AIS scaffold of principal neurons are thought to be sites where COs cluster together with $K_V2.1$ channels in close proximity to GABAergic AAS (King et al. 2014). It was therefore hypothesized that COs interact with K_V channels possibly in modulating GABAergic synapses at the AIS. The localization of COs close to GABAergic boutons at the AIS in principal neurons was reported by early electron microscopy studies (Kosaka 1980; Benedeczky et al. 1994). Further observations suggested that GABA-immunoreactive amacrine cells, which are displaced in the ganglion cell layer, establish synapses onto sites of the soma, axon hillock and the AIS of RGCs (Koontz et al. 1989; Koontz 1993). However, additional evidence for such existence of GABAergic synapses at AIS of RGCs has not been published so far. Furthermore, the presence of a CO or related structures in retinal AIS has also not yet been described. In general, it is well known that RGCs are contacted by inhibitory and excitatory synapses

regulating output of visual information from the retina to the visual cortex (Tian 1995; 2008). These synapses are generally formed between the dendrites of RGCs and the axons of retinal interneurons (Xu and Tian 2004; Hoon et al. 2014), though another study indicated the existence of GABAergic and glycinergic inhibitory synapses at the somatodendric domain of RGCs (Koulen et al. 1996). The formation of synapses between interneurons and the somatodendritic domain of neurons in the brain was well studied for principal neocortical neurons (Tremblay et al. 2016) and for cerebellar Purkinje cells (Barmack and Yakhnitsa 2008). In the visual cortex, neuronal output is modified by excitatory and inhibitory synapses onto the somatodendritic domain as well as onto the AIS (Tremblay et al. 2016). It is quite conceivable that AAS are also clustered at the AIS of RGCs to possibly regulate the back-propagation of APs, neuronal output or the fine-tuning of neuronal excitability, which has been previously postulated for principal neurons (Lewis 2011; Inan and Anderson 2014; Wang et al. 2016b).

An additional interesting observation in the present thesis is that ßIV-spectrin is periodically distributed along the RGC AIS displaying ring-like structures located underneath the plasma membrane. Such submembranous periodic rings were previously observed in dissociated hippocampal neurons and were suggested to be pre-arranged by ßII- and ßIV-spectrin (Zhong et al. 2014; Leterrier et al. 2015). It has been shown that these regularly spaced rings form subsequently after axon specification *in vitro* and have the potential to provide flexible and elastic properties of the axon (Zhong et al. 2014; Jones and Svitkina 2016; Zhang and Rasband 2016). The present thesis demonstrates that in RGCs *in vivo*, AIS-specific scaffolding proteins are also periodically arranged along the axon with a submembranous localization. Further analysis of these findings will include the measurement of distances between these periodic structures. Are periodic rings in AIS of RGCs *in vivo* similarly arranged to those observed in hippocampal neurons *in vitro*? And how is the formation of this pattern established during retinal development? It will be interesting to study whether alterations exist in the periodic arrangement of AIS specific scaffolding proteins during different stages of RGC maturation and also in synpo KO mice. Furthermore, it will be intriguing to address the question whether synpo/CO has an impact

on the periodicity of these rings in AIS by comparing AIS that express synpo/CO with AIS that do not express synpo/CO.

The molecular composition of the AIS in RGCs closely resembles that of principal neurons, in particular in regard to clustering of Na_V channels (Boiko et al. 2003; Van Wart et al. 2007). This was suggested to be important for the generation of sustained spike firing in RGCs (Zhang et al. 2015). No clear evidence could so far be provided for the expression of K_V channels in retinal AIS. However, it was found that $K_V1.2$ channels might be localized at the distal AIS in RGCs, although they were also found in more distal regions of the axon (Van Wart et al. 2007).

In conclusion, the structural and functional characteristics of AIS in RGCs are however so far poorly understood. This thesis reports that RGCs most likely express COs in their AIS, which have structural and possibly functional similarities to COs in principal neurons. The function of the CO is probably associated with Ca^{2+} signaling due to an observed co-expression of synpo with IP_3R, SERCA and RyR in retinal AIS. This Ca^{2+} function has also been previously postulated for the CO in principal neurons (Maggio and Vlachos 2014). It will be of interest to further study the properties of CO and AIS in RGCs. The question arises whether $K_V2.1$ is also clustered at gaps in the AIS scaffold and co-localizes with synpo/CO. Furthermore, the presence of AAS at AIS of RGCs remains to be elucidated, yet, it is tempting to speculate that synpo/CO is localized close to GABAergic synapses at RGC AIS as well. In comparison to the visual cortex, synpo expression in the retina was additionally found in somata of RGCs as well as at sites within the retina that are negative for AIS labeling. It should be taken into consideration that these observed synpo immunosignals might result from unspecific epitope recognition. In contrast, synpo overexpression in CFP and GFP transgenic mice reveal similar fluorescence signals for CFP- or GFP-tagged synpo. Transgenic synpo expression in these mice is located at various sites within the retina that lie in a different optical plane than RGC AIS and could therefore be associated with other structures within the retina, such as cell bodies or even dendritic spines of RGCs (Wong et al. 1992). Thus, the similar observed synpo signals in RGC somata as well as within the retina of wildtype mice are most likely specific and not a result of unspecific immunolabeling.

In summary, it is demonstrated that a small proportion of RGCs express synpo/CO in their AIS. The structure of synpo/CO is dynamically regulated in an activity-dependent manner showing plasticity in response to visual deprivation. Furthermore, synpo/CO in AIS of RGCs shows structural and possibly functional similarities to synpo/CO in cortical AIS. It is therefore proposed that retinal AIS might contain Ca^{2+} storing organelles, which could contribute to AP transduction in RGCs.

6 Acknowledgement

7 Appendix

7.1 Equipment

Table 12: Equipment used in the current thesis

Equipment	Indication / Version / Method	Source
Agarose gel electrophoresis chamber	Horizontal electrophoresis system	Bio-Rad, Hercules, CA, USA
Agarose gel document system	Serial No. 08 200 200	Peqlab, Erlangen, Germany
Brain matrix slicer	1mm coronal adult mouse brain slicer	Zivic Instruments, Pittsburgh, USA
Blotting system	Semidry	NeoLab, Heidelberg, Germany
	Tank	Bio-Rad, Hercules, CA, USA
Confocal microscopes	Digital Eclipse C1 plus - Nikon Laser lines: -Ar laser (488nm/10mW) -G-HeNe laser(543nm/2mW random polarization) -R-HeNe laser (633nm, 5mW) Objectives: -Nikon Plan Apo VC 20x NA 0.75 -Nikon Plan Apo VC 60x NA 1.4 oil immersion	Nikon Instruments Europe, Düsseldorf, Germany
	Leica TCS SP5 Laser lines: -Diode laser (405nm /50mW) -Ar-Laser (458nm/5mW; 476nm/5mW; 488nm/20mW; 514nm20mW) -HeNe (543 nm/1mW, 633 nm /10 mW) Objectives: - 5x/0.15 NA Air; 10x/0.30 NA Air; 20x/0.7 NA Mult. Imm.; 40x/1,3 NA Oil; 63x/1,4 NA Oil	Leica, Wetzlar, Germany
Cryostat	Microm HM 550	Thermo Scientific, Waltham, USA
Power supply	Power pac 250V/ 3.0A/ 300W (for gel electrophoresis)	Peqlab, Erlangen, Germany
	EV231 (for SDS-PAGE / Western blot)	Peqlab, Erlangen, Germany
Forceps	Dumont Assorted Styles -straight Dumont Dumoxel Standard Tip –angled Extra Fine Graefe Forceps -curved	Fine Science Tools, Heidelberg, Germany
Gradient gels	NuPAGE™ Novex™ 3-8% Tris-Acetate Protein Gradient Gels	Thermo Fisher Scientific, Waltham, MA USA
Glass Slides	SuperFrost® slides	Thermo Scientific, Waltham, USA
	Microscope Slides	R. Langenbrinck,

		Emmendingen, Germany
Super resolution microscope	SIM/SMLM combining microscope setup Laser lines: -568 nm: Coherent sapphire 488/568 HP, 200 mW, Coherent, Dieburg, Germany -671 nm: DPSS, VA-I-300-671, 300 mW, Beijing Viasho Technology Co. Ltd, Beijing, PRC Objective: - HCX PL APO 63x/1.4 - 0.6 oil CS, Leica, Wetzlar, Germany Beam splitter: - 568 Di02-R568 Semrock, Rochester, NY - 680 Q680LP Semrock, Rochester, NY Emission filter: - 561 BLP01-561 Semrock, Rochester, NY - 690 LP XF 3104 Omega Optical, Olching, GER - ET610/75m Chroma Technology Corp., Vermont, USA CCD camera: - Sensicam QE, PCO, Kelheim, Germany	Kirchhoff Institute of Physics, Heidelberg University, Germany
Microplate reader	Infinite M200 TECAN reader	Tecan, Männedorf, Switzerland
Nanodrop	NanoDrop® 8-sample spectrometer	Peqlab, Erlangen, Germany
PCR cycler	PCR Mastercycler® pro	Eppendorf, Hamburg, Germany
Power supply	EV231	Consort, Turnhout, Belgium
PVDF membrane	Immobilon®-P, poresize 0.45 µm	Millipore, Billerica, USA
SDS-PAGE chambers	for self-made gels	BioRad, Hercules, USA
	for gradient gels	Peqlab, Erlangen, Germany
Scissors	Vannas Spring Scissors 2.5mm Blades Vannas Spring Scissors 5mm Blades	Fine Science Tools GmbH, Heidelberg, Germany
qPCR cycler	Mx3000P QPCR System	Agilent Technologies, Santa Clara, CA, USA
Western blot membrane document system	Peqlab Fusion Solo Vilber Lourmat	Vilber Lourmat, Eberhardzell, Germany
X-ray film	KODAK X-ray film	Raymed Imaging AG, Düdingen, Switzerland
X-ray film processing	Cawomat 2000 IR processor	Cawo solutions, Düsseldorf, Germany

7.2 Software

Table 13: Software used in the current thesis

Software	Version	Source
EndNote®	X7	Thompson Reuters, New York, USA
Excel Microsoft Office Proffessional Plus 2010	14.0.4760.1000	Microsoft, Redmond, WA, USA
Fusion Capt Advanced Software	416.08a	Peqlab, Erlangen, Germany
i-control microplate reader	3.4.2.0	Tecan, Männedorf, Switzerland
ImageJ	Fiji 1.46h+ plugins	(Schindelin et al. 2012)
GraphPad Prism	7	GraphPad Software, Inc., La Jolla, CA, USA
GraphPad Instat	3	GraphPad Software, Inc., La Jolla, CA, USA
MxPro QPCR Software	4.10	Agilent Technologies, Santa Clara, CA , USA
Nanodrop	2.21	NanoDrop 8000
Photoshop	CS5	Adobe Systems, San Jose, CA, USA
PYME	16.05.24	(Baddeley and Soeller 2014).
Sigma Plot	12.5	Systat Software, Inc., San Jose, CA, USA
Vaa3D	2.7	Dr. Hanchuan Peng, Allen Institute for Brain Science, Seattle, WA, USA

7.3 Self-written macro codes for synpo/CO cluster and AIS length analysis

7.3.1 Macro code in Fiji (ImageJ) for synpo/CO cluster measurement and AIS fluorescence intensity profile acquisition

Table 14: Fiji (ImageJ) macro code for synpo/CO cluster and AIS length analysis.
This macro was developed in Image J macro language enabling to half-automatically select individual AIS expressing synpo/CO, which are analyzed in a second step in regard to intensity profiles of AIS immunofluorescence signals and to synpo/CO cluster number and size per AIS.

```
1   macro "Analysis Action Tool - C333R11ff"
2   {
3   dir2 = getDirectory("Choose Destination Directory-AIS");
4   /* Ask user for folder location to store AIS results*/
5   dir = getDirectory("Choose Destination Directory-CLUSTER");
6   /* Ask user for folder location to store synpo/CO cluster results*/
7   Dialog.create("Name");
8   Dialog.addString("PicLabel","Name");
9   /* Ask user for image name*/
```

```
10 Dialog.show();
11 Bildname= Dialog.getString();
12 rename (Bildname);
13 run("Split Channels");
14 selectWindow(Bildname + " (blue)");
15 close();
16 run("Merge Channels...", "c1=["+Bildname+" (red)] c2=["+Bildname+"
   (green)] create");
17 /* Convert three-colored image (green, red, blue into two-colored images
   (green, red)*/
18 saveAs ("jpeg", dir2 + Bildname);
19 saveAs ("Tiff", dir2 + Bildname);
20 run("ROI Manager...");
21 roiManager("Show All");
22 roiManager("Show All with labels");
23 /* to keep track of marked AIS+COs */
24 Bild = getTitle();
25 y=0;
26 for (x=1; x==1; y++) {
27 setTool("polyline");
28 waitForUser("select AIS + CO ");
29 roiManager("Add");
30 x = getBoolean("select more?");
31 if (x!=1){
32 z = getBoolean("sure? ...select more?");
33 if(z!=1)
34 waitForUser("Ok, go on with Analysis!");
35 else
36 x=1;}
37 /* User marks all AIS with COs seen in the image with an overlapping
   line */
38 }
39 roiManager("Save", dir2 +"ROI.zip");
40 /* to keep track of marked AIS+COs */
41 time = getTime();
42 for (i=0; i< y; i++) {
43 /* for each marked AIS+CO from Roi manager */
44 selectWindow(Bild);
45 roiManager("Select", i);
```

```
46 run("Straighten...", "line=20");
47 /* straighten marked AIS */
48 Bild2 = getTitle();
49 run("Set... ", "zoom=800 x=137 y=10");
50 setTool("line");
51 waitForUser("mark AIS!");
52 /* User draws overlapping line through all straightened AIS */
53 run("Color Profiler");
54 /* pixel versus intensity diagram */
55 selectWindow("Plot Values");
56 saveAs("Text", dir2 +"-"+time+"-"+i+".xls");
57 /* converts diagram to excel file, save */
58 print("Value stored: " + i); close();
59 setTool("polygon");
60 waitForUser("border CO!");
61 /* User borders the CO in the AIS */
62 run("Clear Outside");
63 run("Color Threshold...");
64 waitForUser("Set Threshold!");
65 /* User adjusts threshold for CO cluster measuring*/
66 selectWindow(Bild2);
67 run("Analyze Particles...", "size=5-Infinity circularity=0.00-1.00
   show=Outlines display summarize");
68 /* CO clusters are measured in number and size (see options "set
   measurements...")*/
69 saveAs("Jpeg", dir +"Cluster" +i); close();
70 /* saves image of measured CO clusters */
71 selectWindow(Bild2); close();
72 selectWindow("Plot Values");
73 run("Close");
74 }
75 selectWindow("Results");
76 saveAs("Text", dir +"ClusterResults"+i+".xls");
77 selectWindow("Summary");
78 saveAs("Text", dir +"ClusterSummary"+i+".xls");
79 /* converts measurement to excel file, save */
80 }
```

7.3.2 Macro code in Excel Visual Basic for Applications (VBA, Microsoft) for AIS length calculation

Table 15: VBA (Excel) macro code for AIS length calculation.
This macro was developed in VBA (Excel) language enabling to half-automatically calculate AIS length out of plotted intensity profiles of AIS immunofluorescence signals that were saved as Excel files.

```vba
1   Sub AIS_length_calculation()
2   Dim Pfad, Dateiname
3   Workbooks.Add
4   ActiveWorkbook.SaveAs Filename:= _ "X:\AISlengthCalculation\WT\Results",
    FileFormat:= _ xlNormal, Password:="", WriteResPassword:="",
    ReadOnlyRecommended:=False _ ,CreateBackup:=False
5   'creates main Excel file "Results.xls" in selected path under "Pfad";
    X:= volume's drive letter
6   Pfad = "X:\AISlengthCalculation\WT\"
7   Workbooks.Open Pfad & "Results.xls"
8   'opens main Excel file; X: = volume's drive letter
9   Pfad = "X:\AISlengthCalculation\WT\P10\M1\001a\"
10  Dateiname = Dir(Pfad & "*.xls")
11  'path of folder of saved Excels files (by Fiji) for each plotted AIS;
    X:= volume's drive letter
12  Buchstabe = "A"
13  Nummer = 1
14  'defines starting position (column&row) in main Excel file
    "Results.xls"; AIS length are written in that row consecutively for each
    analyzed AIS Excel file
15  Do While Dateiname <> ""
16  Workbooks.Open Pfad & Dateiname
17  'runs through all AIS Excel files in the selected path of folder
18  Range("E4").Select
19  ActiveCell.FormulaR1C1 = "Max ßIV-spectrin"
20  Range("F4").Select
21  ActiveCell.FormulaR1C1 = "=MAX(C[-4])"
22  'determines the maximum intensity value of AIS staining
23  Range("E6").Select
24  ActiveCell.FormulaR1C1 = "Threshold ßIV-spectrin"
25  Range("F6").Select
26  ActiveCell.FormulaR1C1 = "=R[-2]C*0.1"
27  'threshold of intensity value is set to 10% of maximum intensity value
```

```
       of AIS staining
28  Range("E9").Select
29  ActiveCell.FormulaR1C1 = "AIS start"
30  Range("F9").Select
31  Selection.FormulaArray = _ "=MIN(IF((R[-7]C[-4]:R[491]C[-4])*(R[-7]C[-
    4]:R[491]C[-4]>R[-3]C),R[-7]C[-5]:R[491]C[-5]))"
32  'first intensity value higher than threshold is searched top-down;
    corresponding  pixel is AIS start
33  Range("E10").Select
34  ActiveCell.FormulaR1C1 = "AIS end"
35  Range("F10").Select
36  Selection.FormulaArray = _ "=MAX(IF((R[-8]C[-4]:R[490]C[-4])*(R[-8]C[-
    4]:R[490]C[-4]>R[-4]C),R[-8]C[-5]:R[490]C[-5]))"
37  'first intensity higher than threshold is searched bottom-up;
    corresponding  pixel is AIS end
38  Range("E12").Select
39  ActiveCell.FormulaR1C1 = "AIS Length"
40  Range("F12").Select
41  ActiveCell.FormulaR1C1 = "=R[-2]C-R[-3]C"
42  'subtraction of pixel-value(AIS-start)from pixel-value(AIS-end) results
    in AIS length (in pixel)
43  Range("E13").Select
44  ActiveCell.FormulaR1C1 = "in µm"
45  Range("F13").Select
46  ActiveCell.FormulaR1C1 = "=R[-1]C*0.21"
47  'AIS length (in pixel) is converted into AIS length (in µm) according to
    microscope resolution (0.21 µm/pixel)
48  Wert = Range("F13")
49  Windows("Results.xls").Activate
50  Range(Buchstabe & Nummer) = Wert
51  ActiveWorkbook.Save
52  'AIS length (µm) is described as "Wert" and written into main Excel file
    "Results.xls"
53  Windows("Results.xls").ActivatePrevious
54  ActiveWorkbook.SaveAs Filename:=Pfad & "mod" & Dateiname, _
55  FileFormat:=xlOpenXMLWorkbook, Password:="", WriteResPassword:="", _
56  ReadOnlyRecommended:=False, CreateBackup:=False
57  'modulated AIS Excel files are saved with a new file name
58  ActiveWorkbook.Close False
```

```
59  Nummer = Nummer + 1

60  Dateiname = Dir()

61  Loop

62  End Sub
```

7.4 Individual measured values for synpo/CO and AIS development

7.4.1 Visual cortex development

Table 16: Measured values for AIS percentage, AIS length as well as number and size of synpo clusters in visual cortex development with indication of age of the animal, mouse strain and period of visual deprivation.
Mean values and S.E.M. are built between the six measured mean values (n=6 animals) for each age/condition. Number of analyzed AIS for synpo/CO cluster number and size are equal to those indicated for AIS length in the second row.

	age/ condition	wildtype (control)		wildtype (visual deprivation)	
		values layer II/III *(n of AIS)*	values layer V *(n of AIS)*	values layer II/III *(n of AIS)*	values layer V *(n of AIS)*
AIS percentage in % *(n=6 animals for each age and layer)*	P10	12.79 ± 2.47 *(2435)*	19.18 ± 2.56 *(2282)*	-	-
	P12	35.03 ± 5.14 *(1710)*	28.43 ± 4.76 *(1637)*	-	-
	P15	48.21 ± 3.80 *(1462)*	39.14 ± 3.71 *(1184)*	-	-
	P21	48.19 ± 3.33 *(1314)*	33.05 ± 4.67 *(1395)*	28.17 ± 1.40 *(2076)*	23.54 ± 0.52 *(2059)*
	P28	40.44 ± 3.57 *(1380)*	32.18 ± 3.42 *(1356)*	44.06 ± 4.00 *(1555)*	37.40 ± 4.44 *(1542)*
	P28 Rescue	-	-	23.83 ± 3.82 *(1843)*	20.86 ± 3.60 *(1782)*
	P35	30.50 ± 1.22 *(1326)*	30.00 ± 2.54 *(1113)*	26.90 ± 4.84 *(1601)*	20.44 ± 4.15 *(1871)*
	P>55	33.44 ± 4.94 *(1369)*	36.14 ± 3.91 *(1312)*	-	-
AIS length in μm *(n=6 animals for each age and layer)*	P10	29.76 ± 0.72 *(654)*	26.26 ± 0.49 *(608)*	-	-
	P12	25.99 ± 1.30 *(629)*	22.10 ± 1.37 *(638)*	-	-
	P15	24.58 ± 1.74 *(661)*	23.39 ± 1.65 *(637)*	-	-
	P21	22.71 ± 0.99 *(660)*	19.67 ± 0.75 *(605)*	28.72 ± 0.46 *(621)*	22.87 ± 0.94 *(608)*
	P28	22.77 ± 0.24 *(644)*	19.18 ± 1.25 *(681)*	27.78 ± 0.91 *(675)*	23.21 ± 1.20 *(600)*
	P28 Rescue	-	-	29.63 ± 0.58 *(608)*	26.45 ± 0.77 *(604)*
	P35	21.91 ± 0.41 *(638)*	17.75 ± 0.97 *(608)*	28.64 ± 0.45 *(605)*	24.01 ± 0.46 *(619)*
	P>55	22.30 ± 1.35 *(622)*	19.04 ± 1.20 *(655)*	-	-
Synpo/CO cluster number *(n=6 animals for each age*	P10	1.47 ± 0.04	1.84 ± 0.04	-	-
	P12	2.03 ± 0.12	2.10 ± 0.11	-	-
	P15	3.27 ± 0.26	3.11 ± 0.18	-	-
	P21	3.52 ± 0.16	2.52 ± 0.12	3.48 ± 0.09	3.01 ± 0.07
	P28	3.20 ± 0.14	2.30 ± 0.14	3.20 ± 0.13	2.62 ± 0.10

and layer)	P28 Rescue	-	-	2.98 ± 0.20	2.37 ± 0.13
	P35	2.94 ± 0.14	2.16 ± 0.08	2.90 ± 0.15	2.48 ± 0.11
	P>55	2.96 ± 0.28	2.11 ± 0.12	-	-
Synpo/CO cluster size in µm² *(n=6 animals for each age and layer)*	P10	0.49 ± 0.02	0.46 ± 0.02	-	-
	P12	0.47 ± 0.03	0.48 ± 0.04	-	-
	P15	0.43 ± 0.01	0.45 ± 0.03	-	-
	P21	0.43 ± 0.02	0.44 ± 0.01	0.64 ± 0.03	0.71 ± 0.03
	P28	0.41 ± 0.02	0.44 ± 0.03	0.54 ± 0.02	0.54 ± 0.02
	P28 Rescue	-	-	0.51 ± 0.03	0.71 ± 0.02
	P35	0.41 ± 0.01	0.47 ± 0.02	0.64 ± 0.03	0.67± 0.02
	P>55	0.43 ± 0.02	0.51 ± 0.05	-	-

	age/ condition	synpo KO (control)		synpo KO (visual deprivation)	
		values layer II/III *(n of AIS)*	layer V *(n of AIS)*	values layer II/III *(n of AIS)*	layer V *(n of AIS)*
AIS length in µm *(n=6 animals for each age and layer)*	P1	19.78 ± 0.69 *(688)*	19.73 ± 1.17 *(716)*	-	-
	P7	29.76 ± 1.22 *(606)*	22.48 ± 0.71 *(802)*	-	-
	P10	34.46 ± 0.52 *(606)*	30.82 ± 1.35 *(669)*	-	-
	P15	37.96 ± 1.01 *(645)*	28.65 ± 1.10 *(636)*	-	-
	P21	31.65 ± 0.34 *(610)*	26.06 ± 0.57 *(604)*	28.77 ± 0.87 *(784)*	25.03 ± 0.56 *(744)*
	P28	31.86 ± 1.03 *(876)*	26.35 ± 1.04 *(679)*	23.94 ± 1.30 *(693)*	22.39 ± 0.77 *(749)*
	P28 Rescue	-	-	25.44 ± 0.25 *(742)*	23.17 ± 0.36 *(809)*
	P35	26.73 ± 1.27 *(784)*	24.32 ± 0.48 *(649)*	25.84 ± 2.21 *(936)*	22.38 ± 1.77 *(625)*
	P>55	25.95 ± 0.83 *(726)*	22.37 ± 0.65 *(652)*	-	-

Table 17: Measured values in Western blot for relative synpo and IP$_3$R protein levels during visual cortex development.
Synpo protein levels were relatively quantified to the normalizer gene actin. Relative protein levels at P10 were set to 1 and served as reference for older age groups. Three technical replicates were generated building mean values and S.E.M. for relative protein levels of each age/condition.

	age/	Normalized to E16.5
relative	P10	1.00 ± 0.00
synpo protein levels	P14	1.77 ± 0.05
(n=1 animals for each	P21	2.11 ± 0.08
age and condition)	P28	2.99 ± 0.29
	P35	2.41 ± 0.20
	P0-28 (dark)	2.98 ± 0.33
	P0-35 (dark)	3.56 ± 0.33
	P35 synpo KO	0.00 ± 0.00

	age/	Normalized to E16.5
relative	P10	1.00 ± 0.00
IP$_3$R protein levels	P14	2.21 ± 0.15
(n=1 animals for each	P21	2.48 ± 0.28
age and condition)	P28	5.19 ± 0.29
	P35	7.20 ± 0.08
	P0-28 (dark)	5.48 ± 0.70
	P0-35 (dark)	4.30 ± 0.52
	P35 synpo KO	2.14 ± 0.39

Table 18: Measured values of total synpo expression between P28 control group and P28 visual deprivation group of visual cortex layer IV in wildtype mice.
Mean values and S.E.M. are built between the six measured mean values (n=6 animals) for each age/condition. Mean values are displayed for number of synpo immunoreactive positive (IR$^+$) signals, for fluorescence mean intensity values of synpo IR$^+$ signals, and of total area of synpo IR$^+$ signals.

age/ condition	number of synpo IR$^+$ signals	mean intensity of synpo IR$^+$ signals	total area of synpo IR$^+$ signals (in pixel)
P28	9595 ± 856.9	112.7 ± 3.56	59903 ± 7636
P0-28 (dark)	13103 ± 721.4	134.9 ± 4.19	93710 ± 8364

7.4.2 Retinal development

Table 19: Measured values for number and size of synpo clusters in AIS for retinal development with indication of age of the animal and period of visual deprivation.
Mean values and S.E.M. are built between the six measured mean values (n=6 animals) for each age/condition. Number of analyzed AIS for synpo/CO cluster size are equal to those indicated for synpo/CO cluster number in the first row.

	age/ condition	wildtype (control) values (n of AIS)	wildtype (visual deprivation) values (n of AIS)
Synpo/CO cluster number *(n=6 animals for each age*	P10	1.60 ± 0.05 *(802)*	
	P15	1.45 ± 0.05 *(1033)*	
	P21	1.54 ± 0.03 *(1096)*	
	P28	1.53 ± 0.03 *(1039)*	1.71 ± 0.04 *(1086)*
	P35	1.53 ± 0.03 *(845)*	
	P>55	1.57 ± 0.02 *(1067)*	
Synpo/CO cluster size in μm^2 *(n=6 animals for each age*	P10	0.53 ± 0.01	
	P15	0.55 ± 0.01	
	P21	0.59 ± 0.01	
	P28	0.50 ± 0.01	0.58 ± 0.01
	P35	0.53 ± 0.01	
	P>55	0.53 ± 0.02	

Table 20: Measured values in qPCR for relative synpo mRNA levels during retinal development.
Synpo mRNA levels were relatively quantified to the normalizer gene HPRT1. Relative mRNA levels at E16.5 were set to 1 and served as reference for older age groups. Mean values and S.E.M. are built between the four measured mean values (n=4 animals) for each age.

	age/	Normalized to E16.5
relative synpo mRNA levels *(n=4 animals for each age)*	E16.5	1.00 ± 0.00
	P1	2.41 ± 0.07
	P3	1.23 ± 0.04
	P7	1.28 ± 0.01
	P14	2.28 ± 0.19
	P21	1.64 ± 0.15
	P28	0.97 ± 0.07
	P>55	0.58 ± 0.03

Appendix
138

7.5 Individual results of statistical comparisons

7.5.1 Visual cortex development

Table 21: Results of statistical comparisons of synpo/CO-cluster numbers per AIS between control groups during visual cortex development in wildtype mice.
P values of applied Kruskal-Wallis one-way analysis with Dunn's post test are displayed for synpo/CO-cluster number comparisons between ages (green fields) within layer II/III (white fields) and layer V (grey fields), respectively. Each age group was additionally tested for cluster number differences between layer II/III and layer V (p values in green fields). Significant differences are marked in red. Confidence level: p=0.05.

			layer II/III				
P10 0.0022	>0.999	0.0095	0.0004	0.0073	0.1646	0.0997
>0.999	**P12** 0.6991	0.2167	0.0175	0.1764	>0.999	>0.999
0.0001	0.0431	**P15** 0.7879	>0.999	>0.999	>0.999	>0.999
0.0190	>0.999	>0.999	**P21** 0.0022	>0.999	>0.999	>0.999
0.5663	>0.999	0.4163	>0.999	**P28** 0.0087	>0.999	>0.999
>0.999	>0.999	0.1239	>0.999	>0.999	**P35** 0.0022	>0.999
>0.999	>0.999	0.0504	>0.999	>0.999	>0.999	**P>55** 0.0260

Table 22: Results of statistical comparisons of synpo/CO-cluster numbers per AIS between control groups and visual deprivation groups of wildtype mice.

P values of applied Wilcoxon rank-sum test and Kruskal-Wallis one-way analysis with Dunn's post test are displayed for synpo/CO-cluster number comparisons between control (C, green fields) and visual deprivation groups (D: dark, R:rescue; green fields) within layer II/III (white fields) and layer V (grey fields), respectively. Each age/condition was additionally tested for cluster number differences between layer II/III and layer V (p values in green fields). Significant differences are marked in red. Confidence level: p=0.05.

	layer II/III						
	P21C 0.0022	0.8182	———	———	———	———	———
	0.0152	**P0-21D** 0.0260	———	———	———	———	———
layer V	———	———	**P28C** 0.0087	>0.999	0.5293	———	———
	———	———	0.4329	**P0-28D** 0.0022	0.8385	———	———
	———	———	>0.999	0.5831	**P0-28R** 0.0260	>0.999	>0.999
	———	———	———	———	0.6408	**P35C** 0.0022	>0.999
	———	———	———	———	>0.999	0.0916	**P0-35D** 0.0649

Table 23: Results of statistical comparisons of synpo/CO-cluster sizes per AIS between control groups during visual cortex development in wildtype mice.

P values of applied Kruskal-Wallis one-way analysis with Dunn's post test are displayed for synpo/CO-cluster size comparisons between ages (green fields) within layer II/III (white fields) and layer V (grey fields), respectively. Each age group was additionally tested for cluster size differences between layer II/III and layer V (p values in green fields). Significant differences are marked in red. Confidence level: p=0.05.

	layer II/III						
P10 0.3939	>0.999	>0.999	>0.999	0.0798	0.1073	0.5664	
>0.999	**P12** 0.9372	>0.999	>0.999	>0.999	>0.999	>0.999	
>0.999	>0.999	**P15** >0.999	>0.999	>0.999	>0.999	>0.999	
>0.999	>0.999	>0.999	**P21** 0.8182	>0.999	>0.999	>0.999	
>0.999	>0.999	>0.999	>0.999	**P28** 0.3939	>0.999	>0.999	
>0.999	>0.999	>0.999	>0.999	>0.999	**P35** 0.0087	>0.999	
>0.999	>0.999	>0.999	>0.999	>0.999	>0.999	**P>55** 0.3939	

(row header: layer V)

Table 24: Results of statistical comparisons of synpo/CO-cluster sizes per AIS between control groups and visual deprivation groups of wildtype mice.

P values of applied Wilcoxon rank-sum test and Kruskal-Wallis one-way analysis with Dunn's post test are displayed for synpo/CO-cluster size comparisons between control (C, green fields) and visual deprivation groups (D: dark, R:rescue; green fields) within layer II/III (white fields) and layer V (grey fields), respectively. Each age/condition was additionally tested for cluster size differences between layer II/III and layer V (p values in green fields). Significant differences are marked in red. Confidence level: p=0.05.

			layer II/III				
layer V	**P21C** 0.8182	0.0022	———	———	———	———	———
	0.0022	**P0-21D** 0.1797	———	———	———	———	———
	———	———	**P28C** 0.3939	0.0305	0.0004	———	———
	———	———	0.0836	**P0-28D** >0.999	0.1764	———	———
	———	———	0.0002	0.0399	**P0-28R** 0.0931	0.0035	>0.999
	———	———	———	———	0.0029	**P35C** 0.0022	0.0035
	———	———	———	———	>0.999	0.0029	**P0-35D** 0.5887

Table 25: Results of statistical comparisons of percentage of synpo/CO-expressing AIS between control groups during visual cortex development in wildtype mice.

P values of applied Kruskal-Wallis one-way analysis with Dunn's post test are displayed for synpo/CO-expressing AIS percentage comparisons between ages (green fields) within layer II/III (white fields) and layer V (grey fields), respectively. Each age group was additionally tested for synpo/CO-expressing AIS percentage differences between layer II/III and layer V (p values in green fields). Significant differences are marked in red. Confidence level: p=0.05.

		layer II/III					
	P10 0.1320	0.3910	0.0008	0.0009	0.0398	>0.999	0.8534
	>0.999	**P12** 0.3095	>0.999	>0.999	>0.999	>0.999	>0.999
	0.0067	0.9552	**P15** 0.1320	>0.999	>0.999	0.3669	0.8061
layer V	0.5016	>0.999	>0.999	**P21** 0.0411	>0.999	0.3910	0.8534
	0.7180	>0.999	>0.999	>0.999	**P28** 0.1320	>0.999	>0.999
	>0.999	>0.999	>0.999	>0.999	>0.999	**P35** 0.8182	>0.999
	0.0926	>0.999	>0.999	>0.999	>0.999	>0.999	**P>55** 0.5887

Table 26: Results of statistical comparisons of percentage of synpo/CO-expressing AIS between control groups and visual deprivation groups of wildtype mice.

P values of applied Wilcoxon rank-sum test and Kruskal-Wallis one-way analysis with Dunn's post test are displayed for synpo/CO-expressing AIS percentage comparisons between control (C, green fields) and visual deprivation groups (D: dark, R:rescue; green fields) within layer II/III (white fields) and layer V (grey fields), respectively. Each age/condition was additionally tested for synpo/CO-expressing AIS percentage differences between layer II/III and layer V (p values in green fields). Significant differences are marked in red. Confidence level: p=0.05.

	layer II/III						
	P21C 0.0411	0.0022	———	———	———	———	———
	0.1320	**P0-21D** 0.0022	———	———	———	———	———
	———	———	**P28C** 0.1320	>0.999	0.0602	———	———
layer V	———	———	>0.999	**P0-28D** 0.3939	0.0206	———	———
	———	———	0.1547	0.0283	**P0-28R** 0.5887	0.1980	>0.999
	———	———	———	———	0.2810	**P35C** 0.8182	0.2507
	———	———	———	———	>0.999	0.1197	**P0-35D** 0.1797

Table 27: Results of statistical comparisons of AIS length between control groups during visual cortex development in wildtype mice.

P values of applied Kruskal-Wallis one-way analysis with Dunn's post test are displayed for AIS length comparisons between ages (green fields) within layer II/III (white fields) and layer V (grey fields), respectively. Each age group was additionally tested for AIS length differences between layer II/III and layer V (p values in green fields). Significant differences are marked in red. Confidence level: p=0.05.

		layer II/III					
layer V	**P10** 0.0022	>0.999	0.7180	0.0504	0.1430	0.0148	0.0267
	>0.999	**P12** 0.0931	>0.999	>0.999	>0.999	0.5664	0.8534
	>0.999	>0.999	**P15** 0.6991	>0.999	>0.999	>0.999	>0.999
	0.1534	>0.999	>0.999	**P21** 0.0649	>0.999	>0.999	>0.999
	0.0589	>0.999	>0.999	>0.999	**P28** 0.0649	>0.999	>0.999
	0.0038	0.9552	0.1646	>0.999	>0.999	**P35** 0.0043	>0.999
	0.0245	>0.999	0.6384	>0.999	>0.999	>0.999	**P>55** 0.0931

Table 28: Results of statistical comparisons of AIS length between control groups and visual deprivation groups of wildtype mice.

P values of applied Wilcoxon rank-sum test and Kruskal-Wallis one-way analysis with Dunn's post test are displayed for AIS length comparisons between control (C, green fields) and visual deprivation groups (D: dark, R:rescue; green fields) within layer II/III (white fields) and layer V (grey fields), respectively. Each age/condition was additionally tested for AIS length differences between layer II/III and layer V (p values in green fields). Significant differences are marked in red. Confidence level: p=0.05.

	layer II/III						
	P21C 0.0649	0.0022	———	———	———	———	———
	0.0411	**P0-21D** 0.0022	———	———	———	———	———
	———	———	**P28C** 0.0649	0.0494	0.0011	———	———
layer V	———	———	0.2810	**P0-28D** 0.0411	0.5831	———	
	———	———	0.0043	0.3900	**P0-28R** 0.0087	0.0029	>0.999
	———	———	———	———	0.0007	**P35C** 0.0043	0.0331
	———	———	———	———	0.3900	0.0916	**P0-35D** 0.0022

Table 29: Results of statistical comparisons of AIS length distribution between control groups during visual cortex development in wildtype mice.
P values of applied Kruskal-Wallis one-way analysis with Dunn's post test are displayed for AIS length distribution comparisons between ages (green fields) within layer II/III (white fields) and layer V (grey fields), respectively. Each age group was additionally tested for AIS length distribution differences between layer II/III and layer V (p values in green fields). Significant differences are marked in red. Confidence level: p=0.05.

	layer II/III						
	P10 <0.0001	<0.0001	<0.0001	<0.0001	<0.0001	<0.0001	<0.0001
	<0.0001	**P12** <0.0001	0.4122	<0.0001	<0.0001	<0.0001	<0.0001
	<0.0001	>0.999	**P15** <0.0001	<0.0001	<0.0001	<0.0001	<0.0001
layer V	<0.0001	<0.0001	<0.0001	**P21** <0.0001	>0.999	>0.999	>0.999
	<0.0001	<0.0001	<0.0001	>0.999	**P28** <0.0001	>0.999	>0.999
	<0.0001	<0.0001	<0.0001	>0.999	>0.999	**P35** <0.0001	>0.999
	<0.0001	<0.0001	<0.0001	>0.999	>0.999	>0.999	**P>55** <0.0001

Table 30: Results of statistical comparisons of AIS length distribution between control groups and visual deprivation groups of wildtype mice.

P values of applied Wilcoxon rank-sum test and Kruskal-Wallis one-way analysis with Dunn's post test are displayed for AIS length distribution between control (C, green fields) and visual deprivation groups (D: dark, R:rescue; green fields) within layer II/III (white fields) and layer V (grey fields), respectively. Each age/condition was additionally tested for AIS length distribution differences between layer II/III and layer V (p values in green fields). Significant differences are marked in red. Confidence level: p=0.05.

	layer II/III						
	P21C <0.0001	<0.0001	———	———	———	———	———
	<0.0001	**P0-21D** <0.0001	———	———	———	———	———
layer V	———	———	**P28C** <0.0001	<0.0001	<0.0001	———	———
	———	———	<0.0001	**P0-28D** <0.0001	<0.0001	———	———
	———	———	<0.0001	<0.0001	**P0-28R** <0.0001	<0.0001	0.2838
	———	———	———	———	<0.0001	**P35C** <0.0001	<0.0001
	———	———	———	———	<0.0001	<0.0001	**P0-35D** <0.0001

Table 31: Results of statistical comparisons of AIS length between control groups during visual cortex development in synpo KO mice.

P values of applied Kruskal-Wallis one-way analysis with Dunn's post test are displayed for AIS length comparisons between ages (green fields) within layer II/III (white fields) and layer V (grey fields), respectively. Each age group was additionally tested for AIS length distribution differences between layer II/III and layer V (p values in green fields). Significant differences are marked in red. Confidence level: p=0.05.

		layer II/III						
layer V	**P1** 0.9372	0.4436	0.0004	<0.0001	0.0730	>0.999	0.0292	>0.999
	>0.999	**P7** 0.0022	>0.999	0.2326	>0.999	>0.999	>0.999	>0.999
	0.0001	0.0080	**P10** 0.0411	>0.999	>0.999	>0.999	0.1090	0.0272
	0.0012	0.0483	>0.999	**P15** 0.0022	>0.999	>0.999	0.0093	0.0018
	0.0836	>0.999	>0.999	>0.999	**P21** 0.0022	>0.999	>0.999	>0.999
	0.0836	>0.999	>0.999	>0.999	>0.999	**P28** 0.0152	>0.999	>0.999
	>0.999	>0.999	0.2326	0.8959	>0.999	>0.999	**P35** 0.0649	0.7267
	>0.999	>0.999	0.0049	0.0314	0.8959	0.8959	>0.999	**P>55** 0.0087

Table 32: Results of statistical comparisons of AIS length between control groups and visual deprivation groups of synpo KO mice.

P values of applied Wilcoxon rank-sum test and Kruskal-Wallis one-way analysis with Dunn's post test are displayed for AIS length comparisons between control (C, green fields) and visual deprivation groups (D: dark, R:rescue; green fields) within layer II/III (white fields) and layer V (grey fields), respectively. Each age/condition was additionally tested for AIS length differences between layer II/III and layer V (p values in green fields). Significant differences are marked in red. Confidence level: p=0.05.

	layer II/III						
P21C 0.0022	0.0260	———	———	———	———	———
0.1797	**P0-21D** 0.0087	———	———	———	———	———
———	———	**P28C** 0.0152	0.0043	0.0386	———	———
———	———	0.0148	**P0-28D** 0.4848	>0.999	———	———
———	———	0.1752	>0.999	**P0-28R** 0.0022	0.8385	>0.999
———	———	———	———	0.6408	**P35C** 0.0649	0.5293
———	———	———	———	0.6408	0.0386	**P0-35D** 0.1797

(layer V — row label along left side)

Table 33: Results of statistical comparisons of AIS length distribution between control groups during visual cortex development in synpo KO mice.

P values of applied Kruskal-Wallis one-way analysis with Dunn's post test are displayed for AIS length distribution comparisons between ages (green fields) within layer II/III (white fields) and layer V (grey fields), respectively. Each age group was additionally tested for AIS length distribution differences between layer II/III and layer V (p values in green fields). Significant differences are marked in red. Confidence level: p=0.05.

				layer II/III					
layer V	**P1** 0.0886	<0.0001	<0.0001	<0.0001	<0.0001	<0.0001	<0.0001	<0.0001
	<0.0001	**P7** <0.0001	<0.0001	<0.0001	<0.0001	<0.0001	<0.0001	<0.0001
	<0.0001	<0.0001	**P10** <0.0001	<0.0001	0.0008	0.0017	<0.0001	<0.0001
	<0.0001	<0.0001	0.0008	**P15** <0.0001	<0.0001	<0.0001	<0.0001	<0.0001
	<0.0001	<0.0001	<0.0001	0.0035	**P21** <0.0001	>0.999	<0.0001	<0.0001
	<0.0001	<0.0001	<0.0001	0.0291	>0.999	**P28** <0.0001	<0.0001	<0.0001
	<0.0001	<0.0001	<0.0001	<0.0001	0.0195	0.0007	**P35** <0.0001	0.1454
	<0.0001	>0.999	<0.0001	<0.0001	<0.0001	<0.0001	<0.0001	**P>55** <0.0001

Table 34: Results of statistical comparisons of AIS length distribution between control groups and visual deprivation groups of synpo KO mice.

P values of applied Wilcoxon rank-sum test and Kruskal-Wallis one-way analysis with Dunn's post test are displayed for AIS length distribution comparisons between control (C, green fields) and visual deprivation groups (D: dark, R:rescue; green fields) within layer II/III (white fields) and layer V (grey fields), respectively. Each age/condition was additionally tested for AIS length distribution differences between layer II/III and layer V (p values in green fields). Significant differences are marked in red. Confidence level: p=0.05.

				layer II/III				
layer V	**P21C** <0.0001	<0.0001	_____	_____	_____	_____	_____
	0.0275	**P0-21D** <0.0001	_____	_____	_____	_____	_____
	_____	_____	**P28C** <0.0001	<0.0001	<0.0001	_____	_____
	_____	_____	<0.0001	**P0-28D** 0.6249	0.0005	_____	_____
	_____	_____	<0.0001	0.0008	**P0-28R** <0.0001	<0.0001	>0.9999
	_____	_____	_____	_____	<0.0001	**P35C** <0.0001	<0.0001
	_____	_____	_____	_____	>0.9999	<0.0001	**P0-35D** <0.0001

Table 35: Results of Spearman rank correlation analysis of individual parameters for synpo-expressing AIS in visual cortex.

Parameters for correlation analysis (in green fields) were synpo/CO cluster number, synpo/CO cluster size, length of synpo/CO-expressing AIS, condition (control or visual deprivation) and age of the animal. Correlation was applied for these parameters for layer II/III (white fields) and layer V (grey fields). Results in each field are presented as r/p value. r: Spearman rank coefficient. Significant correlations are marked in red. Confidence level: p=0.05.

			layer II/III		
layer V	**Cluster number**	-0.3361/ <0.0001	0.2264 / <0.0001	0.1582 / <0.0001	0.3308 / <0.0001
	0.3985 / <0.0001	**cluster size**	0.02466 / 0.0504	0.3214 / <0.0001	-0.1422/ <0.0001
	0.2988 / <0.0001	0.01882 / 0.1659	**AIS length**	_____	_____
	0.1607 / <0.0001	0.2407 / <0.0001	_____	**condition**	_____
	0.01575/ 0.3040	0.003563/ 0.8161	_____	_____	**age**

Table 36: Results of multiple linear regression analysis of individual parameters for AIS in visual cortex of wildtype and synpo KO mice.

The applied model for regression was $y = x_1 + x_2 + x_3$. AIS length was set as constant (y, red). Independent x parameters for regression analysis (in green fields) were age (x_1), condition (control or visual deprivation, x_2) and cortex layer (II/III and V, x_3). Regression analysis was applied for these parameters for wildtype mice (white fields) and for synpo KO mice V (grey fields). Results in each field are presented as t-ratio/p value. Significant regressions are marked in red. Confidence level: $p = 0.05$.

synpo KO mice		wildtype mice		
	AIS length (y)	-23.26/ <0.0001	21.93/ <0.0001	-30.64/ <0.0001
-5.13/ <0.0001	**age (x₁)**		———	———
-17.401/ <0.0001	———	**condition (x₂)**		———
-29.408/ <0.0001	———	———	**layer (x₃)**	

Table 37: Results of statistical comparisons of total synpo expression signals between P28 control group and P28 visual deprivation group of visual cortex layer IV in wildtype mice.

P values of applied Wilcoxon rank-sum test are displayed for number of synpo immunoreactive positive (IR[+]) signals (n, left box), for fluorescence mean intensity values of synpo IR[+] signals (I, middle box), and of total area of synpo IR[+] signals (a, right box). Significant differences are marked in red. Confidence level: $p = 0.05$.

n	layer IV	
	P28C	0.0152
		P28D

I	layer IV	
	P28C	0.0043
		P28D

a	layer IV	
	P28C	0.0260
		P28D

Appendix

Table 38: Results of statistical comparisons of relative synpo and IP$_3$R protein levels measured in Western blot between control groups and visual deprivation groups during visual cortex development.

P values of applied Wilcoxon rank-sum test and Kruskal-Wallis one-way analysis with Dunn's post test are displayed for relative protein level comparisons between control (C, green fields), visual deprivation groups (D: dark, R:rescue; green fields) and synpo KO (P35 KO, green field) for synpo (white fields) and IP$_3$R (grey fields), respectively. Significant differences are marked in red. Confidence level: p=0.05.

synpo protein levels							
P10	0.4895	0.1246	0.0072	0.0459	——	——	0.4895
0.1927	**P14**	0.3983	0.0459	0.1917	——	——	0.0260
0.1254	0.8182	**P21**	0.2494	0.6450	——	——	0.0260
0.0058	0.1454	0.2202	**P28C**	0.4895	>0.999	——	0.0007
0.0006	0.0319	0.0554	0.4904	**P35C**	——	0.1000	0.0072
——	——	——	>0.999	——	**P28D**	——	——
——	——	——	——	0.0396	——	**P35D**	——
0.1927	>0.999	0.8182	0.1454	0.0319	——	——	**P35 KO**

(Row/column label: IP$_3$R protein levels)

7.5.2 Retinal development

Table 39: Results of statistical comparisons of synpo/CO cluster size in AIS between control groups as well as between control groups and visual deprivation groups during retinal development.
P values (white fields) of applied Wilcoxon rank-sum test and Kruskal-Wallis one-way analysis with Dunn's post test are displayed for synpo cluster size comparisons between ages (green fields). The P28 age group was additionally tested for synpo/CO cluster size differences compared to P28 visual deprivation group (p value in violet field). Significant differences are marked in red. Confidence level: p=0.05.

retina					
P10	>0.999	0.2979	>0.999	>0.999	>0.999
	P15	>0.999	0.3443	>0.999	>0.999
		P21	0.0061	0.1001	0.1898
			P28 0.0087	>0.999	>0.999
				P35	>0.999
					P>55

Table 40: Results of statistical comparisons of synpo cluster number in AIS between control groups as well as between control groups and visual deprivation groups during retinal development.
P values (white fields) of applied Wilcoxon rank-sum test and Kruskal-Wallis one-way analysis with Dunn's post test are displayed for synpo cluster number comparisons between ages (green fields). The P28 age group was additionally tested for synpo/CO cluster number differences compared to P28 visual deprivation group (p value in violet field). Significant differences are marked in red. Confidence level: p=0.05.

retina					
P10	0.5594	>0.999	>0.999	>0.999	>0.999
	P15	>0.999	>0.999	>0.999	>0.999
		P21	>0.999	>0.999	>0.999
			P28 0.0022	>0.999	>0.999
				P35	>0.999
					P>55

Table 41: Results of statistical comparisons of relative synpo mRNA levels between control groups during retinal development.

P values (white fields) of applied Kruskal-Wallis one-way analysis with Dunn's post test are displayed for synpo mRNA level comparisons between ages (green fields). Significant differences are marked in red. Confidence level: p=0.05.

retina							
E16.5	0.1090	>0.999	>0.999	0.1090	>0.999	>0.999	>0.999
	P1	>0.999	>0.999	>0.999	>0.999	0.1090	0.0049
		P3	>0.999	>0.999	>0.999	>0.999	>0.999
			P7	>0.999	>0.999	>0.999	0.8507
				P14	>0.999	0.1090	0.0049
					P21	>0.999	0.1090
						P28	>0.999
							P>55

Table 42: Results of Spearman rank correlation analysis of individual parameters for synpo-expressing AIS in the retina.

Parameters for correlation analysis were synpo/CO cluster number and synpo/CO cluster size. Results are presented as r/p value. r: Spearman rank coefficient. Significant correlations are marked in red. Confidence level: p=0.05.

retina	
Cluster number	-0.2570/ <0.0001
	cluster size

Table 43: Results of multiple linear regression analysis of individual parameters for synpo/CO-expressing AIS in the retina.

The applied model for regression was $y=x_1+x_2$. Synpo/CO cluster number (n, left box) or synpo/CO cluster size (s, right box) was set as constant (red, y). Independent x parameters for regression analysis were age (x_1) and condition (control or visual deprivation, x_2). Results in each field are presented as t-ratio/P value. Significant regressions are marked in red. Confidence level: p=0.05.

n	retina		
	cluster number (y)	1.626/ 0.104	6.022/ <0.0001
	⎯⎯	**age (x_1)**	⎯⎯
	⎯⎯	⎯⎯	**condition (x_2)**

s	retina		
	cluster size (y)	-0.613/ 0.540	4.190/ <0.0001
	⎯⎯	**age (x_1)**	⎯⎯
	⎯⎯	⎯⎯	**condition (x_2)**

8   References

Ackman JB, Crair MC. 2014. Role of emergent neural activity in visual map development. Current opinion in neurobiology. 24(1):166-175.

Adachi R, Yamada R, Kuba H. 2015. Plasticity of the axonal trigger zone. The Neuroscientist : a review journal bringing neurobiology, neurology and psychiatry. 21(3):255-265.

Ango F, di Cristo G, Higashiyama H, Bennett V, Wu P, Huang ZJ. 2004. Ankyrin-based subcellular gradient of neurofascin, an immunoglobulin family protein, directs gabaergic innervation at purkinje axon initial segment. Cell. 119(2):257-272.

Anton-Fernandez A, Rubio-Garrido P, DeFelipe J, Munoz A. 2015. Selective presence of a giant saccular organelle in the axon initial segment of a subpopulation of layer v pyramidal neurons. Brain structure & function. 220(2):869-884.

Asanuma K, Kim K, Oh J, Giardino L, Chabanis S, Faul C, Reiser J, Mundel P. 2005. Synaptopodin regulates the actin-bundling activity of alpha-actinin in an isoform-specific manner. The Journal of clinical investigation. 115(5):1188-1198.

Augustine GJ, Santamaria F, Tanaka K. 2003. Local calcium signaling in neurons. Neuron. 40(2):331-346.

Baalman KL, Cotton RJ, Rasband SN, Rasband MN. 2013. Blast wave exposure impairs memory and decreases axon initial segment length. Journal of neurotrauma. 30(9):741-751.

Bachatene, Bharmauria, Molotchnikoff. 2012. Adaptation and neuronal network in visual cortex. In: Rouat Ma, editor. Visual cortex - current status and perspectives.

Baddeley, Soeller. 2014. The python microscopy environment. https://bitbucket.org/david_baddeley/python-microscopy: FOM 2014, Abstract 376

Bansal A, Singer JH, Hwang BJ, Xu W, Beaudet A, Feller MB. 2000. Mice lacking specific nicotinic acetylcholine receptor subunits exhibit dramatically altered spontaneous activity patterns and reveal a limited role for retinal waves in forming on and off circuits in the inner retina. The Journal of neuroscience : the official journal of the Society for Neuroscience. 20(20):7672-7681.

Barmack NH, Yakhnitsa V. 2008. Functions of interneurons in mouse cerebellum. The Journal of neuroscience : the official journal of the Society for Neuroscience. 28(5):1140-1152.

Bas Orth C, Schultz C, Muller CM, Frotscher M, Deller T. 2007. Loss of the cisternal organelle in the axon initial segment of cortical neurons in synaptopodin-deficient mice. The Journal of comparative neurology. 504(5):441-449.

Bender KJ, Ford CP, Trussell LO. 2010. Dopaminergic modulation of axon initial segment calcium channels regulates action potential initiation. Neuron. 68(3):500-511.

Bender KJ, Trussell LO. 2009. Axon initial segment ca2+ channels influence action potential generation and timing. Neuron. 61(2):259-271.

Bender KJ, Trussell LO. 2012. The physiology of the axon initial segment. Annual review of neuroscience. 35:249-265.

Benedeczky I, Molnar E, Somogyi P. 1994. The cisternal organelle as a ca(2+)-storing compartment associated with gabaergic synapses in the axon initial segment of hippocampal pyramidal neurones. Experimental brain research. 101(2):216-230.

Benevento LA, Bakkum BW, Cohen RS. 1995. Gamma-aminobutyric acid and somatostatin immunoreactivity in the visual cortex of normal and dark-reared rats. Brain research. 689(2):172-182.

Benevento LA, Bakkum BW, Port JD, Cohen RS. 1992. The effects of dark-rearing on the electrophysiology of the rat visual cortex. Brain research. 572(1-2):198-207.

Benned-Jensen T, Christensen RK, Denti F, Perrier JF, Rasmussen HB, Olesen SP. 2016. Live imaging of kv7.2/7.3 cell surface dynamics at the axon initial segment: High steady-state stability and calpain-

dependent excitotoxic downregulation revealed. The Journal of neuroscience : the official journal of the Society for Neuroscience. 36(7):2261-2266.

Berridge MJ. 1998. Neuronal calcium signaling. Neuron. 21(1):13-26.

Best G. 2014. Development of a structured illumination ophthalmoscope for high resolution imaging of the human eyeground and improvements to structured illumination microscopy [PhD Thesis]. [Heidelberg, Germany]: University of Heidelberg, http://www.ub.uni-heidelberg.de/archiv/17100

Bode-Greuel KM, Singer W. 1991. Developmental changes of calcium currents in the visual cortex of the cat. Experimental brain research. 84(2):311-318.

Boiko T, Van Wart A, Caldwell JH, Levinson SR, Trimmer JS, Matthews G. 2003. Functional specialization of the axon initial segment by isoform-specific sodium channel targeting. The Journal of neuroscience : the official journal of the Society for Neuroscience. 23(6):2306-2313.

Buffington SA, Rasband MN. 2011. The axon initial segment in nervous system disease and injury. The European journal of neuroscience. 34(10):1609-1619.

Buisseret P, Imbert M. 1976. Visual cortical cells: Their developmental properties in normal and dark reared kittens. The Journal of physiology. 255(2):511-525.

Byerly MS, Blackshaw S. 2009. Vertebrate retina and hypothalamus development. Wiley interdisciplinary reviews Systems biology and medicine. 1(3):380-389.

Callaway EM. 1998. Local circuits in primary visual cortex of the macaque monkey. Annual review of neuroscience. 21:47-74.

Callewaert G, Eilers J, Konnerth A. 1996. Axonal calcium entry during fast 'sodium' action potentials in rat cerebellar purkinje neurones. The Journal of physiology. 495 (Pt 3):641-647.

Cang J, Renteria RC, Kaneko M, Liu X, Copenhagen DR, Stryker MP. 2005. Development of precise maps in visual cortex requires patterned spontaneous activity in the retina. Neuron. 48(5):797-809.

Carras PL, Coleman PA, Miller RF. 1992. Site of action potential initiation in amphibian retinal ganglion cells. Journal of neurophysiology. 67(2):292-304.

Cepko CL, Austin CP, Yang X, Alexiades M, Ezzeddine D. 1996. Cell fate determination in the vertebrate retina. Proceedings of the National Academy of Sciences of the United States of America. 93(2):589-595.

Chand AN, Galliano E, Chesters RA, Grubb MS. 2015. A distinct subtype of dopaminergic interneuron displays inverted structural plasticity at the axon initial segment. The Journal of neuroscience : the official journal of the Society for Neuroscience. 35(4):1573-1590.

Chapman B, Stryker MP. 1993. Development of orientation selectivity in ferret visual cortex and effects of deprivation. The Journal of neuroscience : the official journal of the Society for Neuroscience. 13(12):5251-5262.

Chapman B, Stryker MP, Bonhoeffer T. 1996. Development of orientation preference maps in ferret primary visual cortex. The Journal of neuroscience : the official journal of the Society for Neuroscience. 16(20):6443-6453.

Citri A, Malenka RC. 2008. Synaptic plasticity: Multiple forms, functions, and mechanisms. Neuropsychopharmacology : official publication of the American College of Neuropsychopharmacology. 33(1):18-41.

Connor JA, Stevens CF. 1971. Voltage clamp studies of a transient outward membrane current in gastropod neural somata. The Journal of physiology. 213(1):21-30.

Crair MC, Gillespie DC, Stryker MP. 1998. The role of visual experience in the development of columns in cat visual cortex. Science (New York, NY). 279(5350):566-570.

Cruz DA, Lovallo EM, Stockton S, Rasband M, Lewis DA. 2009. Postnatal development of synaptic structure proteins in pyramidal neuron axon initial segments in monkey prefrontal cortex. The Journal of comparative neurology. 514(4):353-367.

Cynader M, Berman N, Hein A. 1976. Recovery of function in cat visual cortex following prolonged deprivation. Experimental brain research. 25(2):139-156.

Czarnecki K, Haas CA, Bas Orth C, Deller T, Frotscher M. 2005. Postnatal development of synaptopodin expression in the rodent hippocampus. The Journal of comparative neurology. 490(2):133-144.

Czyrak A, Czepiel K, Mackowiak M, Chocyk A, Wedzony K. 2003. Serotonin 5-ht1a receptors might control the output of cortical glutamatergic neurons in rat cingulate cortex. Brain research. 989(1):42-51.

Dacher M, Gouty S, Dash S, Cox BM, Nugent FS. 2013. A-kinase anchoring protein-calcineurin signaling in long-term depression of gabaergic synapses. The Journal of neuroscience : the official journal of the Society for Neuroscience. 33(6):2650-2660.

Daw NW, Wyatt HJ. 1976. Kittens reared in a unidirectional environment: Evidence for a critical period. The Journal of physiology. 257(1):155-170.

DeFelipe J, Arellano JI, Gomez A, Azmitia EC, Munoz A. 2001. Pyramidal cell axons show a local specialization for gaba and 5-ht inputs in monkey and human cerebral cortex. The Journal of comparative neurology. 433(1):148-155.

Deller T, Korte M, Chabanis S, Drakew A, Schwegler H, Stefani GG, Zuniga A, Schwarz K, Bonhoeffer T, Zeller R et al. 2003. Synaptopodin-deficient mice lack a spine apparatus and show deficits in synaptic plasticity. Proceedings of the National Academy of Sciences of the United States of America. 100(18):10494-10499.

Deller T, Merten T, Roth SU, Mundel P, Frotscher M. 2000. Actin-associated protein synaptopodin in the rat hippocampal formation: Localization in the spine neck and close association with the spine apparatus of principal neurons. The Journal of comparative neurology. 418(2):164-181.

Demas J, Eglen SJ, Wong RO. 2003. Developmental loss of synchronous spontaneous activity in the mouse retina is independent of visual experience. The Journal of neuroscience : the official journal of the Society for Neuroscience. 23(7):2851-2860.

Des Rosiers MH, Sakurada O, Jehle J, Shinohara M, Kennedy C, Sokoloff L. 1978. Functional plasticity in the immature striate cortex of the monkey shown by the [14c]deoxyglucose method. Science (New York, NY). 200(4340):447-449.

Druga R. 2009. Neocortical inhibitory system. Folia biologica. 55(6):201-217.

Du J, Haak LL, Phillips-Tansey E, Russell JT, McBain CJ. 2000. Frequency-dependent regulation of rat hippocampal somato-dendritic excitability by the k+ channel subunit kv2.1. The Journal of physiology. 522 Pt 1:19-31.

Engelhardt M, Vorwald S, Sobotzik JM, Bennett V, Schultz C. 2013. Ankyrin-b structurally defines terminal microdomains of peripheral somatosensory axons. Brain structure & function. 218(4):1005-1016.

Erskine L, Herrera E. 2014. Connecting the retina to the brain. ASN neuro. 6(6).

Espinosa JS, Stryker MP. 2012. Development and plasticity of the primary visual cortex. Neuron. 75(2):230-249.

Evans MD, Dumitrescu AS, Kruijssen DL, Taylor SE, Grubb MS. 2015. Rapid modulation of axon initial segment length influences repetitive spike firing. Cell reports. 13(6):1233-1245.

Evans MD, Sammons RP, Lebron S, Dumitrescu AS, Watkins TB, Uebele VN, Renger JJ, Grubb MS. 2013. Calcineurin signaling mediates activity-dependent relocation of the axon initial segment. The Journal of neuroscience : the official journal of the Society for Neuroscience. 33(16):6950-6963.

Fagiolini M, Pizzorusso T, Berardi N, Domenici L, Maffei L. 1994. Functional postnatal development of the rat primary visual cortex and the role of visual experience: Dark rearing and monocular deprivation. Vision research. 34(6):709-720.

Farias GG, Guardia CM, Britt DJ, Guo X, Bonifacino JS. 2015. Sorting of dendritic and axonal vesicles at the pre-axonal exclusion zone. Cell reports. 13(6):1221-1232.

Feldheim DA, O'Leary DD. 2010. Visual map development: Bidirectional signaling, bifunctional guidance molecules, and competition. Cold Spring Harbor perspectives in biology. 2(11):a001768.

Feller MB, Wellis DP, Stellwagen D, Werblin FS, Shatz CJ. 1996. Requirement for cholinergic synaptic transmission in the propagation of spontaneous retinal waves. Science (New York, NY). 272(5265):1182-1187.

Firth SI, Wang CT, Feller MB. 2005. Retinal waves: Mechanisms and function in visual system development. Cell calcium. 37(5):425-432.

Fisher LJ. 1979. Development of retinal synaptic arrays in the inner plexiform layer of dark-reared mice. Journal of embryology and experimental morphology. 54:219-227.

Forrester J, Peters A. 1967. Nerve fibres in optic nerve of rat. Nature. 214(5085):245-247.

Foster RE, Connors BW, Waxman SG. 1982. Rat optic nerve: Electrophysiological, pharmacological and anatomical studies during development. Brain research. 255(3):371-386.

Freal A, Fassier C, Le Bras B, Bullier E, De Gois S, Hazan J, Hoogenraad CC, Couraud F. 2016. Cooperative interactions between 480 kda ankyrin-g and eb proteins assemble the axon initial segment. The Journal of neuroscience : the official journal of the Society for Neuroscience. 36(16):4421-4433.

Fried SI, Lasker AC, Desai NJ, Eddington DK, Rizzo JF, 3rd. 2009. Axonal sodium-channel bands shape the response to electric stimulation in retinal ganglion cells. Journal of neurophysiology. 101(4):1972-1987.

Gabbott PL, Stewart MG. 1987. Quantitative morphological effects of dark-rearing and light exposure on the synaptic connectivity of layer 4 in the rat visual cortex (area 17). Experimental brain research. 68(1):103-114.

Galiano MR, Jha S, Ho TS, Zhang C, Ogawa Y, Chang KJ, Stankewich MC, Mohler PJ, Rasband MN. 2012. A distal axonal cytoskeleton forms an intra-axonal boundary that controls axon initial segment assembly. Cell. 149(5):1125-1139.

Gilbert CD, Li W. 2013. Top-down influences on visual processing. Nature reviews Neuroscience. 14(5):350-363.

Godement P, Salaun J, Imbert M. 1984. Prenatal and postnatal development of retinogeniculate and retinocollicular projections in the mouse. The Journal of comparative neurology. 230(4):552-575.

Grigoryan G, Segal M. 2015. Ryanodine-mediated conversion of stp to ltp is lacking in synaptopodin-deficient mice. Brain structure & function. 10.1007/s00429-015-1026-7.

Grubb MS, Burrone J. 2010a. Activity-dependent relocation of the axon initial segment fine-tunes neuronal excitability. Nature. 465(7301):1070-1074.

Grubb MS, Burrone J. 2010b. Building and maintaining the axon initial segment. Current opinion in neurobiology. 20(4):481-488.

Gulledge AT, Bravo JJ. 2016. Neuron morphology influences axon initial segment plasticity. eNeuro. 3(1).

Gutzmann A, Ergul N, Grossmann R, Schultz C, Wahle P, Engelhardt M. 2014. A period of structural plasticity at the axon initial segment in developing visual cortex. Frontiers in neuroanatomy. 8:11.

Hanover JL, Huang ZJ, Tonegawa S, Stryker MP. 1999. Brain-derived neurotrophic factor overexpression induces precocious critical period in mouse visual cortex. The Journal of neuroscience : the official journal of the Society for Neuroscience. 19(22):Rc40.

Hausser M, Stuart G, Racca C, Sakmann B. 1995. Axonal initiation and active dendritic propagation of action potentials in substantia nigra neurons. Neuron. 15(3):637-647.

. Laterally modulated excitation microscopy: Improvement of resolution by using a diffraction grating. 1999.

Hensch TK. 2005a. Critical period mechanisms in developing visual cortex. Current topics in developmental biology. 69:215-237.

Hensch TK. 2005b. Critical period plasticity in local cortical circuits. Nature reviews Neuroscience. 6(11):877-888.

Herde MK, Iremonger KJ, Constantin S, Herbison AE. 2013. Gnrh neurons elaborate a long-range projection with shared axonal and dendritic functions. The Journal of neuroscience : the official journal of the Society for Neuroscience. 33(31):12689-12697.

Hildebrand C, Waxman SG. 1983. Regional node-like membrane specializations in non-myelinated axons of rat retinal nerve fiber layer. Brain research. 258(1):23-32.

Hille B. 1986. Ionic channels: Molecular pores of excitable membranes. Harvey lectures. 82:47-69.

Hinds JW, Hinds PL. 1974. Early ganglion cell differentiation in the mouse retina: An electron microscopic analysis utilizing serial sections. Developmental biology. 37(2):381-416.

Hinman JD, Rasband MN, Carmichael ST. 2013. Remodeling of the axon initial segment after focal cortical and white matter stroke. Stroke; a journal of cerebral circulation. 44(1):182-189.

Holtmaat A, Svoboda K. 2009. Experience-dependent structural synaptic plasticity in the mammalian brain. Nature reviews Neuroscience. 10(9):647-658.

Hooks BM, Chen C. 2007. Critical periods in the visual system: Changing views for a model of experience-dependent plasticity. Neuron. 56(2):312-326.

Hoon M, Okawa H, Della Santina L, Wong RO. 2014. Functional architecture of the retina: Development and disease. Progress in retinal and eye research. 42:44-84.

Horton JC, Hocking DR. 1996. An adult-like pattern of ocular dominance columns in striate cortex of newborn monkeys prior to visual experience. The Journal of neuroscience : the official journal of the Society for Neuroscience. 16(5):1791-1807.

Howard A, Tamas G, Soltesz I. 2005. Lighting the chandelier: New vistas for axo-axonic cells. Trends in neurosciences. 28(6):310-316.

Hu W, Tian C, Li T, Yang M, Hou H, Shu Y. 2009. Distinct contributions of na(v)1.6 and na(v)1.2 in action potential initiation and backpropagation. Nature neuroscience. 12(8):996-1002.

Huang ZJ, Kirkwood A, Pizzorusso T, Porciatti V, Morales B, Bear MF, Maffei L, Tonegawa S. 1999. Bdnf regulates the maturation of inhibition and the critical period of plasticity in mouse visual cortex. Cell. 98(6):739-755.

Hubel DH, Wiesel TN. 1963. Receptive fields of cells in striate cortex of very young, visually inexperienced kittens. Journal of neurophysiology. 26:994-1002.

Hubener M, Bonhoeffer T. 2014. Neuronal plasticity: Beyond the critical period. Cell. 159(4):727-737.

Huberman AD, Feller MB, Chapman B. 2008. Mechanisms underlying development of visual maps and receptive fields. Annual review of neuroscience. 31:479-509.

Inan M, Anderson SA. 2014. The chandelier cell, form and function. Current opinion in neurobiology. 26:142-148.

Jarnot MD, Corbett AM. 1995. High titer antibody to mammalian neuronal sodium channels produces sustained channel block. Brain research. 674(1):159-162.

Jedlicka P, Schwarzacher SW, Winkels R, Kienzler F, Frotscher M, Bramham CR, Schultz C, Bas Orth C, Deller T. 2009. Impairment of in vivo theta-burst long-term potentiation and network excitability in the dentate gyrus of synaptopodin-deficient mice lacking the spine apparatus and the cisternal organelle. Hippocampus. 19(2):130-140.

Jedlicka P, Vlachos A, Schwarzacher SW, Deller T. 2008. A role for the spine apparatus in ltp and spatial learning. Behavioural brain research. 192(1):12-19.

Jenkins PM, Kim N, Jones SL, Tseng WC, Svitkina TM, Yin HH, Bennett V. 2015. Giant ankyrin-g: A critical innovation in vertebrate evolution of fast and integrated neuronal signaling. Proceedings of the National Academy of Sciences of the United States of America. 112(4):957-964.

Jones SL, Korobova F, Svitkina T. 2014. Axon initial segment cytoskeleton comprises a multiprotein submembranous coat containing sparse actin filaments. The Journal of cell biology. 205(1):67-81.

Jones SL, Svitkina TM. 2016. Axon initial segment cytoskeleton: Architecture, development, and role in neuron polarity. Neural plasticity. 2016:6808293.

Kanold PO, Luhmann HJ. 2010. The subplate and early cortical circuits. Annual review of neuroscience. 33:23-48.

Katagiri H, Fagiolini M, Hensch TK. 2007. Optimization of somatic inhibition at critical period onset in mouse visual cortex. Neuron. 53(6):805-812.

Keck T, Scheuss V, Jacobsen RI, Wierenga CJ, Eysel UT, Bonhoeffer T, Hubener M. 2011. Loss of sensory input causes rapid structural changes of inhibitory neurons in adult mouse visual cortex. Neuron. 71(5):869-882.

Kevenaar JT, Hoogenraad CC. 2015. The axonal cytoskeleton: From organization to function. Frontiers in molecular neuroscience. 8:44.

King AN, Manning CF, Trimmer JS. 2014. A unique ion channel clustering domain on the axon initial segment of mammalian neurons. The Journal of comparative neurology. 522(11):2594-2608.

Ko KW, Rasband MN, Meseguer V, Kramer RH, Golding NL. 2016. Serotonin modulates spike probability in the axon initial segment through hcn channels. Nature neuroscience. 19(6):826-834.

Kole MH, Stuart GJ. 2008. Is action potential threshold lowest in the axon? Nature neuroscience. 11(11):1253-1255.

Kole MH, Stuart GJ. 2012. Signal processing in the axon initial segment. Neuron. 73(2):235-247.

Koontz MA. 1993. Gaba-immunoreactive profiles provide synaptic input to the soma, axon hillock, and axon initial segment of ganglion cells in primate retina. Vision research. 33(18):2629-2636.

Koontz MA, Hendrickson AE, Ryan MK. 1989. Gaba-immunoreactive synaptic plexus in the nerve fiber layer of primate retina. Visual neuroscience. 2(1):19-25.

Korkotian E, Frotscher M, Segal M. 2014. Synaptopodin regulates spine plasticity: Mediation by calcium stores. The Journal of neuroscience : the official journal of the Society for Neuroscience. 34(35):11641-11651.

Korkotian E, Segal M. 2011. Synaptopodin regulates release of calcium from stores in dendritic spines of cultured hippocampal neurons. The Journal of physiology. 589(Pt 24):5987-5995.

Kosaka T. 1980. The axon initial segment as a synaptic site: Ultrastructure and synaptology of the initial segment of the pyramidal cell in the rat hippocampus (ca3 region). Journal of neurocytology. 9(6):861-882.

Koulen P, Sassoe-Pognetto M, Grunert U, Wassle H. 1996. Selective clustering of gaba(a) and glycine receptors in the mammalian retina. The Journal of neuroscience : the official journal of the Society for Neuroscience. 16(6):2127-2140.

Kremerskothen J, Plaas C, Kindler S, Frotscher M, Barnekow A. 2005. Synaptopodin, a molecule involved in the formation of the dendritic spine apparatus, is a dual actin/alpha-actinin binding protein. Journal of neurochemistry. 92(3):597-606.

Krug K, Akerman CJ, Thompson ID. 2001. Responses of neurons in neonatal cortex and thalamus to patterned visual stimulation through the naturally closed lids. Journal of neurophysiology. 85(4):1436-1443.

Kuba H. 2007. Cellular and molecular mechanisms of avian auditory coincidence detection. Neuroscience research. 59(4):370-376.

Kuba H, Adachi R, Ohmori H. 2014. Activity-dependent and activity-independent development of the axon initial segment. The Journal of neuroscience : the official journal of the Society for Neuroscience. 34(9):3443-3453.

Kuba H, Ishii TM, Ohmori H. 2006. Axonal site of spike initiation enhances auditory coincidence detection. Nature. 444(7122):1069-1072.

Kuba H, Oichi Y, Ohmori H. 2010. Presynaptic activity regulates na(+) channel distribution at the axon initial segment. Nature. 465(7301):1075-1078.

Kuba H, Yamada R, Ishiguro G, Adachi R. 2015. Redistribution of kv1 and kv7 enhances neuronal excitability during structural axon initial segment plasticity. Nature communications. 6:8815.

Kucharz K, Wieloch T, Toresson H. 2013. Fission and fusion of the neuronal endoplasmic reticulum. Translational stroke research. 4(6):652-662.

Le Magueresse C, Monyer H. 2013. Gabaergic interneurons shape the functional maturation of the cortex. Neuron. 77(3):388-405.

Leterrier C, Dargent B. 2014. No pasaran! Role of the axon initial segment in the regulation of protein transport and the maintenance of axonal identity. Seminars in cell & developmental biology. 27:44-51.

Leterrier C, Potier J, Caillol G, Debarnot C, Rueda Boroni F, Dargent B. 2015. Nanoscale architecture of the axon initial segment reveals an organized and robust scaffold. Cell reports. 13(12):2781-2793.

LeVay S, Wiesel TN, Hubel DH. 1980. The development of ocular dominance columns in normal and visually deprived monkeys. The Journal of comparative neurology. 191(1):1-51.

Lewis DA. 2011. The chandelier neuron in schizophrenia. Developmental neurobiology. 71(1):118-127.

Li Y, Fitzpatrick D, White LE. 2006. The development of direction selectivity in ferret visual cortex requires early visual experience. Nature neuroscience. 9(5):676-681.

Lim ST, Antonucci DE, Scannevin RH, Trimmer JS. 2000. A novel targeting signal for proximal clustering of the kv2.1 k+ channel in hippocampal neurons. Neuron. 25(2):385-397.

Lin MH, Takahashi MP, Takahashi Y, Tsumoto T. 1994. Intracellular calcium increase induced by gaba in visual cortex of fetal and neonatal rats and its disappearance with development. Neuroscience research. 20(1):85-94.

Llano I, Leresche N, Marty A. 1991. Calcium entry increases the sensitivity of cerebellar purkinje cells to applied gaba and decreases inhibitory synaptic currents. Neuron. 6(4):565-574.

Lorincz A, Nusser Z. 2008. Cell-type-dependent molecular composition of the axon initial segment. The Journal of neuroscience : the official journal of the Society for Neuroscience. 28(53):14329-14340.

Maggio N, Vlachos A. 2014. Synaptic plasticity at the interface of health and disease: New insights on the role of endoplasmic reticulum intracellular calcium stores. Neuroscience. 281c:135-146.

Martina M, Vida I, Jonas P. 2000. Distal initiation and active propagation of action potentials in interneuron dendrites. Science (New York, NY). 287(5451):295-300.

Martinello K, Huang Z, Lujan R, Tran B, Watanabe M, Cooper EC, Brown DA, Shah MM. 2015. Cholinergic afferent stimulation induces axonal function plasticity in adult hippocampal granule cells. Neuron. 85(2):346-363.

Medini P. 2014. Experience-dependent plasticity of visual cortical microcircuits. Neuroscience. 278:367-384.

Misonou H, Menegola M, Mohapatra DP, Guy LK, Park KS, Trimmer JS. 2006. Bidirectional activity-dependent regulation of neuronal ion channel phosphorylation. The Journal of neuroscience : the official journal of the Society for Neuroscience. 26(52):13505-13514.

Misonou H, Mohapatra DP, Menegola M, Trimmer JS. 2005. Calcium- and metabolic state-dependent modulation of the voltage-dependent kv2.1 channel regulates neuronal excitability in response to ischemia. The Journal of neuroscience : the official journal of the Society for Neuroscience. 25(48):11184-11193.

Misonou H, Mohapatra DP, Park EW, Leung V, Zhen D, Misonou K, Anderson AE, Trimmer JS. 2004. Regulation of ion channel localization and phosphorylation by neuronal activity. Nature neuroscience. 7(7):711-718.

Miyakawa T, Maeda A, Yamazawa T, Hirose K, Kurosaki T, Iino M. 1999. Encoding of ca2+ signals by differential expression of ip3 receptor subtypes. The EMBO journal. 18(5):1303-1308.

Mohapatra DP, Misonou H, Pan SJ, Held JE, Surmeier DJ, Trimmer JS. 2009. Regulation of intrinsic excitability in hippocampal neurons by activity-dependent modulation of the kv2.1 potassium channel. Channels (Austin, Tex). 3(1):46-56.

Moshiri A, Close J, Reh TA. 2004. Retinal stem cells and regeneration. The International journal of developmental biology. 48(8-9):1003-1014.

Mower GD. 1991. The effect of dark rearing on the time course of the critical period in cat visual cortex. Brain research Developmental brain research. 58(2):151-158.

Muir J, Kittler JT. 2014. Plasticity of gabaa receptor diffusion dynamics at the axon initial segment. Frontiers in cellular neuroscience. 8:151.

Mundel P, Heid HW, Mundel TM, Kruger M, Reiser J, Kriz W. 1997. Synaptopodin: An actin-associated protein in telencephalic dendrites and renal podocytes. The Journal of cell biology. 139(1):193-204.

Naka A, Adesnik H. 2016. Inhibitory circuits in cortical layer 5. Frontiers in neural circuits. 10:35.

Nelson R. 1995. Visual responses of ganglion cells. In: Kolb H, Fernandez E, Nelson R, editors. Webvision: The organization of the retina and visual system. Salt Lake City (UT): University of Utah Health Sciences Center.

Nelson SB, Turrigiano GG. 2008. Strength through diversity. Neuron. 60(3):477-482.

Niell CM, Stryker MP. 2008. Highly selective receptive fields in mouse visual cortex. The Journal of neuroscience : the official journal of the Society for Neuroscience. 28(30):7520-7536.

Nienhaus K, Nienhaus GU. 2016. Where do we stand with super-resolution optical microscopy? Journal of molecular biology. 428(2 Pt A):308-322.

O'Leary DD, Chou SJ, Sahara S. 2007. Area patterning of the mammalian cortex. Neuron. 56(2):252-269.

Ott C, Martens H, Hassouna I, Oliveira B, Erck C, Zafeiriou MP, Peteri UK, Hesse D, Gerhart S, Altas B et al. 2015. Widespread expression of erythropoietin receptor in brain and its induction by injury. Molecular medicine (Cambridge, Mass). 10.2119/molmed.2015.00192.

Palay SL, Sotelo C, Peters A, Orkand PM. 1968. The axon hillock and the initial segment. The Journal of cell biology. 38(1):193-201.

Pan Z, Kao T, Horvath Z, Lemos J, Sul JY, Cranstoun SD, Bennett V, Scherer SS, Cooper EC. 2006. A common ankyrin-g-based mechanism retains kcnq and nav channels at electrically active domains of the axon. The Journal of neuroscience : the official journal of the Society for Neuroscience. 26(10):2599-2613.

Park KS, Mohapatra DP, Misonou H, Trimmer JS. 2006. Graded regulation of the kv2.1 potassium channel by variable phosphorylation. Science (New York, NY). 313(5789):976-979.

Peters A, Proskauer CC, Kaiserman-Abramof IR. 1968. The small pyramidal neuron of the rat cerebral cortex. The axon hillock and initial segment. The Journal of cell biology. 39(3):604-619.

Peters A, Proskauer CC, Ribak CE. 1982. Chandelier cells in rat visual cortex. The Journal of comparative neurology. 206(4):397-416.

Petersen AV, Cotel F, Perrier JF. 2016. Plasticity of the axon initial segment: Fast and slow processes with multiple functional roles. The Neuroscientist : a review journal bringing neurobiology, neurology and psychiatry. 10.1177/1073858416648311.

Petersen JD, Kaech S, Banker G. 2014. Selective microtubule-based transport of dendritic membrane proteins arises in concert with axon specification. The Journal of neuroscience : the official journal of the Society for Neuroscience. 34(12):4135-4147.

Pettigrew JD. 1974. The effect of visual experience on the development of stimulus specificity by kitten cortical neurones. The Journal of physiology. 237(1):49-74.

Preuss TM, Coleman GQ. 2002. Human-specific organization of primary visual cortex: Alternating compartments of dense cat-301 and calbindin immunoreactivity in layer 4a. Cerebral cortex (New York, NY : 1991). 12(7):671-691.

Prosser BL, Ward CW, Lederer WJ. 2010. Subcellular ca2+ signaling in the heart: The role of ryanodine receptor sensitivity. The Journal of general physiology. 136(2):135-142.

Rasband MN. 2010. The axon initial segment and the maintenance of neuronal polarity. Nature reviews Neuroscience. 11(8):552-562.

Rasband MN. 2011. Composition, assembly, and maintenance of excitable membrane domains in myelinated axons. Seminars in cell & developmental biology. 22(2):178-184.

Rossberger S. 2014. A novel combined structured illumination and single molecule localization microscope and its application to retinal structures [PhD Thesis]. [Heidelberg, Germany]: University of Heidelberg,http://www.ub.uni-heidelberg.de/archiv/17079

Rossberger S, Ach T, Best G, Cremer C, Heintzmann R, Dithmar S. 2013a. High-resolution imaging of autofluorescent particles within drusen using structured illumination microscopy. The British journal of ophthalmology. 97(4):518-523.

Rossberger S, Best G, Baddeley D, Heintzmann R, Birk U, Dithmar S, Cremer C. 2013b. Combination of structured illumination and single molecule localization microscopy in one setup. Journal Of Optics. Vol. 15, No. 9, 094003.

Saliba RS, Kretschmannova K, Moss SJ. 2012. Activity-dependent phosphorylation of gabaa receptors regulates receptor insertion and tonic current. The EMBO journal. 31(13):2937-2951.

Sammels E, Parys JB, Missiaen L, De Smedt H, Bultynck G. 2010. Intracellular ca2+ storage in health and disease: A dynamic equilibrium. Cell calcium. 47(4):297-314.

Sanchez-Ponce D, Blazquez-Llorca L, DeFelipe J, Garrido JJ, Munoz A. 2012. Colocalization of alpha-actinin and synaptopodin in the pyramidal cell axon initial segment. Cerebral cortex (New York, NY : 1991). 22(7):1648-1661.

Sanchez-Ponce D, DeFelipe J, Garrido JJ, Munoz A. 2011. In vitro maturation of the cisternal organelle in the hippocampal neuron's axon initial segment. Molecular and cellular neurosciences. 48(1):104-116.

Sanes JR, Masland RH. 2015. The types of retinal ganglion cells: Current status and implications for neuronal classification. Annual review of neuroscience. 38:221-246.

Sarmiere PD, Weigle CM, Tamkun MM. 2008. The kv2.1 k+ channel targets to the axon initial segment of hippocampal and cortical neurons in culture and in situ. BMC neuroscience. 9:112.

Sawamiphak S, Ritter M, Acker-Palmer A. 2010. Preparation of retinal explant cultures to study ex vivo tip endothelial cell responses. Nature protocols. 5(10):1659-1665.

Schafer DP, Jha S, Liu F, Akella T, McCullough LD, Rasband MN. 2009. Disruption of the axon initial segment cytoskeleton is a new mechanism for neuronal injury. The Journal of neuroscience : the official journal of the Society for Neuroscience. 29(42):13242-13254.

Schindelin J, Arganda-Carreras I, Frise E, Kaynig V, Longair M, Pietzsch T, Preibisch S, Rueden C, Saalfeld S, Schmid B et al. 2012. Fiji: An open-source platform for biological-image analysis. Nature methods. 9(7):676-682.

Schulien AJ, Justice JA, Maio RD, Wills ZP, Shah NH, Aizenman E. 2016. Zn -induced ca release via ryanodine receptors triggers calcineurin-dependent redistribution of cortical neuronal kv2.1 k channels. The Journal of physiology. 10.1113/jp272117.

Schwarz DS, Blower MD. 2016. The endoplasmic reticulum: Structure, function and response to cellular signaling. Cellular and molecular life sciences : CMLS. 73(1):79-94.

Sherk H, Stryker MP. 1976. Quantitative study of cortical orientation selectivity in visually inexperienced kitten. Journal of neurophysiology. 39(1):63-70.

Simpson PB, Challiss RA, Nahorski SR. 1995. Neuronal ca2+ stores: Activation and function. Trends in neurosciences. 18(7):299-306.

Sobotzik JM, Sie JM, Politi C, Del Turco D, Bennett V, Deller T, Schultz C. 2009. Ankyring is required to maintain axo-dendritic polarity in vivo. Proceedings of the National Academy of Sciences of the United States of America. 106(41):17564-17569.

Song AH, Wang D, Chen G, Li Y, Luo J, Duan S, Poo MM. 2009. A selective filter for cytoplasmic transport at the axon initial segment. Cell. 136(6):1148-1160.

Spacek J. 1985. Three-dimensional analysis of dendritic spines. Ii. Spine apparatus and other cytoplasmic components. Anatomy and embryology. 171(2):235-243.

Spacek J, Harris KM. 1997. Three-dimensional organization of smooth endoplasmic reticulum in hippocampal ca1 dendrites and dendritic spines of the immature and mature rat. The Journal of neuroscience : the official journal of the Society for Neuroscience. 17(1):190-203.

Strehl A, Lenz M, Itsekson-Hayosh Z, Becker D, Chapman J, Deller T, Maggio N, Vlachos A. 2014. Systemic inflammation is associated with a reduction in synaptopodin expression in the mouse hippocampus. Experimental neurology. 261:230-235.

Tarasenko AN, Isaev DS, Eremin AV, Kostyuk PG. 1998. Developmental changes in the expression of low-voltage-activated ca2+ channels in rat visual cortical neurones. The Journal of physiology. 509 (Pt 2):385-394.

Thome C, Kelly T, Yanez A, Schultz C, Engelhardt M, Cambridge SB, Both M, Draguhn A, Beck H, Egorov AV. 2014. Axon-carrying dendrites convey privileged synaptic input in hippocampal neurons. Neuron. 83(6):1418-1430.

Tian N. 1995. Development of retinal ganglion cell dendritic structure and synaptic connections. In: Kolb H, Fernandez E, Nelson R, editors. Webvision: The organization of the retina and visual system. Salt Lake City (UT): University of Utah Health Sciences Center.

Tian N. 2008. Synaptic activity, visual experience and the maturation of retinal synaptic circuitry. The Journal of physiology. 586(18):4347-4355.

Tian N, Copenhagen DR. 2001. Visual deprivation alters development of synaptic function in inner retina after eye opening. Neuron. 32(3):439-449.

Tremblay R, Lee S, Rudy B. 2016. Gabaergic interneurons in the neocortex: From cellular properties to circuits. Neuron. 91(2):260-292.

Trimmer JS. 1991. Immunological identification and characterization of a delayed rectifier k+ channel polypeptide in rat brain. Proceedings of the National Academy of Sciences of the United States of America. 88(23):10764-10768.

Umemiya M, Berger AJ. 1994. Properties and function of low- and high-voltage-activated ca2+ channels in hypoglossal motoneurons. The Journal of neuroscience : the official journal of the Society for Neuroscience. 14(9):5652-5660.

van Versendaal D, Levelt CN. 2016. Inhibitory interneurons in visual cortical plasticity. Cellular and molecular life sciences : CMLS. 10.1007/s00018-016-2264-4.

Van Wart A, Trimmer JS, Matthews G. 2007. Polarized distribution of ion channels within microdomains of the axon initial segment. The Journal of comparative neurology. 500(2):339-352.

Verbich D, Becker D, Vlachos A, Mundel P, Deller T, McKinney RA. 2016. Rewiring neuronal microcircuits of the brain via spine head protrusions--a role for synaptopodin and intracellular calcium stores. Acta neuropathologica communications. 4:38.

Vlachos A. 2012. Synaptopodin and the spine apparatus organelle-regulators of different forms of synaptic plasticity? Annals of anatomy = Anatomischer Anzeiger : official organ of the Anatomische Gesellschaft. 194(4):317-320.

Vlachos A, Ikenberg B, Lenz M, Becker D, Reifenberg K, Bas-Orth C, Deller T. 2013. Synaptopodin regulates denervation-induced homeostatic synaptic plasticity. Proceedings of the National Academy of Sciences of the United States of America. 110(20):8242-8247.

Wang L, Dumoulin A, Renner M, Triller A, Specht CG. 2016a. The role of synaptopodin in membrane protein diffusion in the dendritic spine neck. PloS one. 11(2):e0148310.

Wang Y, Zhang P, Wyskiel DR. 2016b. Chandelier cells in functional and dysfunctional neural circuits. Frontiers in neural circuits. 10:33.

Watanabe K, Al-Bassam S, Miyazaki Y, Wandless TJ, Webster P, Arnold DB. 2012. Networks of polarized actin filaments in the axon initial segment provide a mechanism for sorting axonal and dendritic proteins. Cell reports. 2(6):1546-1553.

Wefelmeyer W, Cattaert D, Burrone J. 2015. Activity-dependent mismatch between axo-axonic synapses and the axon initial segment controls neuronal output. Proceedings of the National Academy of Sciences of the United States of America. 112(31):9757-9762.

White LE, Coppola DM, Fitzpatrick D. 2001. The contribution of sensory experience to the maturation of orientation selectivity in ferret visual cortex. Nature. 411(6841):1049-1052.

Wong RO, Meister M, Shatz CJ. 1993. Transient period of correlated bursting activity during development of the mammalian retina. Neuron. 11(5):923-938.

Wong RO, Yamawaki RM, Shatz CJ. 1992. Synaptic contacts and the transient dendritic spines of developing retinal ganglion cells. The European journal of neuroscience. 4(12):1387-1397.

Woodruff AR, Anderson SA, Yuste R. 2010. The enigmatic function of chandelier cells. Frontiers in neuroscience. 4:201.

Wu C, Ivanova E, Cui J, Lu Q, Pan ZH. 2011. Action potential generation at an axon initial segment-like process in the axonless retinal aii amacrine cell. The Journal of neuroscience : the official journal of the Society for Neuroscience. 31(41):14654-14659.

Xu H, Tian N. 2004. Pathway-specific maturation, visual deprivation, and development of retinal pathway. The Neuroscientist : a review journal bringing neurobiology, neurology and psychiatry. 10(4):337-346.

Yoshimura T, Rasband MN. 2014. Axon initial segments: Diverse and dynamic neuronal compartments. Current opinion in neurobiology. 27:96-102.

Yu Y, Maureira C, Liu X, McCormick D. 2010. P/q and n channels control baseline and spike-triggered calcium levels in neocortical axons and synaptic boutons. The Journal of neuroscience : the official journal of the Society for Neuroscience. 30(35):11858-11869.

Zhang C, McCall MA. 2012. Receptor targets of amacrine cells. Visual neuroscience. 29(1):11-29.

Zhang C, Rasband MN. 2016. Cytoskeletal control of axon domain assembly and function. Current opinion in neurobiology. 39:116-121.

Zhang XL, Poschel B, Faul C, Upreti C, Stanton PK, Mundel P. 2013. Essential role for synaptopodin in dendritic spine plasticity of the developing hippocampus. The Journal of neuroscience : the official journal of the Society for Neuroscience. 33(30):12510-12518.

Zhang Z, Feng J, Wu C, Lu Q, Pan ZH. 2015. Targeted expression of channelrhodopsin-2 to the axon initial segment alters the temporal firing properties of retinal ganglion cells. PloS one. 10(11):e0142052.

Zhong G, He J, Zhou R, Lorenzo D, Babcock HP, Bennett V, Zhuang X. 2014. Developmental mechanism of the periodic membrane skeleton in axons. eLife. 3.

Ziskoven C, Grafweg S, Bolck B, Wiesner RJ, Jimenez M, Giacobino JP, Bloch W, Schwinger RH, Brixius K. 2007. Increased ca2+ sensitivity and protein expression of serca 2a in situations of chronic beta3-adrenoceptor deficiency. Pflugers Archiv : European journal of physiology. 453(4):443-453.